Selective Laser Melting of Nickel Superalloys for Aerospace Applications: Defect Analysis and Material Property Optimisation

Cong Liu

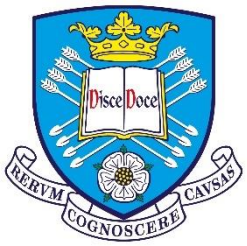

The University Of Sheffield.

A thesis submitted in partial fulfilment of the requirements for the degree of Doctor of Philosophy (PhD)

Materials Science & Engineering

University of Sheffield

May 2021

Abstract

Selective laser melting (SLM), as a main branch of additive manufacture (AM), is drawing increasing interest within both academia and industry, particularly in aerospace, owing to the ability to produce complex net-shape objects directly from designed files without expensive tooling. However, the knowledge on the influence of SLM processing parameters on defect and microstructure formation are limited. Therefore, this research investigates the SLM-fabricated nickel superalloys IN713C and LR8. IN713C is a commercially used γ' precipitation hardenable Ni-based superalloy, which can be limited by the high weld-crack susceptibility during processing. While LR8 is a newly designed material specific for AM, and thus the knowledge of its properties is very limited.

This research aims to establish a viable SLM processing route for both IN713C and LR8. Parametric studies are carried out to understand the influence of process variables on defects and microstructure. With the help of a melting pool simulation and defect classification script, the mechanism for defects and microstructures can be understood. The concepts of "laser travel time" and "apparent power" are introduced to analyse the effect of volumetric parameters, including part geometry and scan strategy. The effect of powder geometry on part quality was revealed in LR8 experiments, which need to be studied further.

The viable heat treatment (HT) for SLM-fabrication of IN713C has been investigated to refine the γ/γ' microstructure to determine if its mechanical properties can be improved. Scanning electron microscopy (SEM), electron back scatter diffraction (EBSD), and X-ray powder diffraction (XRD) were used to reveal the microstructure evolution through processing stages.

Mechanical tests (i.e., tensile strength, indentation hardness) were applied to compare SLM-fabricated and casted materials. The SLM IN713C generally shows better mechanical properties in all conditions. In general, both SLM-fabricated IN713C and LR8 show the potential to be used as aerospace components with proper processing parameters.

Acknowledgments

I would like to thank the many people who have helped and supported me during my postgraduate studies. I would like to take this opportunity to express my special thanks to those who have assisted me in different ways.

I would first like to give special thanks to my supervisor, Prof. Iain Todd, for giving me this opportunity, for providing valuable guidance and feedback throughout this project and for kindly giving me support when I became stuck and felt confused. I would also like to thank Dr Richard Thackray, my second supervisor, who gave me helpful advice and support.

I would also like to express my appreciation to all my colleagues and the technical staff at the University of Sheffield for their help and advice throughout this project: Dr Felicity Freeman, for providing and helping me with the MATLAB models; Dr Meurig Thomas, for providing and assisting me with the R language defect classification code; Dr Le Ma at the Sorby Centre, for assistance with sample preparation and electron microscopy; Neil Hind, for assisting me with the heat treatment experiment; George Maddison and Alister Lyle, for assisting me with the operation of the Aconity and Renishaw AM machines; and Lova Chechik, for assistance in processing the pyrometer data.

I would also like to thank all my friends for supporting me throughout this challenging period of my life. Most importantly, I would like to express my deep gratitude to my parents, Dayu Liu and Hong Zhang, for their love and support. All of this could not have happened without their support and kindness. I would like to dedicate this thesis to the memory of my late mother, who gave me constant love and encouragement and who I miss every day.

Contents

List of Figures

List of Tables

Nomenclature and Abbreviations

Symbol	Description	Units
*	Normalised quantity	-
a	Alloy constant	$s \cdot m^{-1}$
A	Surface absorptivity	-
a	Thermal diffusivity (= $\lambda/\rho C_p$)	$m^2 \cdot s^{-1}$
a_γ	Lattice parameter of γ	Å
$a_{\gamma'}$	Lattice parameter of γ'	Å
AC	Air cooling	-
A_h	Effective heat transfer area	m^2
AM	Additive manufacturing	-
APB	Antiphase boundary	-
A_s	Surface area of casting	m
b	Burgers vector	m
BCC	Body centred cubic	-
C_l	Cooling rate of part	$K \cdot s^{-1}$
C_{mp}	Cooling rate within a single melting pool	$K \cdot s^{-1}$
C_p	Specific heat capacity at constant pressure	$J \cdot kg^{-1} \cdot K^{-1}$
D	Diffusion coefficient	$m^2 \cdot s^{-1}$
d	Spot distance	m
DAS	Dendrite arm spacing	m
DDC	Ductility-dip cracking	-
DLD	Direct laser deposition	-
DoE	Design of Experiment	-
DSC	Differential scanning calorimetry	-
E	Energy density	$J \cdot m^{-3}$
EBSD	Electron backscatter diffraction	-
EDM	Electrical discharge machining	-
EDS/EDX	Energy dispersive X-ray spectroscopy	-

FCC	Face centred cubic	-
f_s	Solid Fraction	
G	Thermal gradient	$K \cdot m^{-1}$
h	Hatch space	m
HAZ	Heat-affected zone	-
HCP	Hexagonal close packed	-
HF	Heat flow	mW
HT	Heat treatment	-
K	Material constant	$K^2 s \cdot m^{-1}$
k	Distribution coefficient	-
L	Harmonic of perturbation constant	
l	Layer thickness	m
L_l	Laser welding track length	m
LoF	Lack of fusion	-
m	Mass	kg
n	Material constant	-
N_0	Nucleant density	$1 \cdot m^{-3}$
ODS	Oxide dispersion strengthened	-
PREN	Pitting resistance equivalent number	-
PWHT	post-weld heat treatment	-
q	Power of the laser beam	W
Q	Effective laser power	W
Q_a	Apparent power	W
Q_{act}	Activation energy for γ' precipitate	J
q_e	Heat flux	-
R	gas constant	$J \cdot K^{-1} \cdot mol^{-1}$
R	Solidification rate	$m \cdot s^{-1}$
r_B	Beam radius	m
SAC	Strain age cracking	-
SEM	Scanning electron microscopy	-

SLM	Selective laser melting	-
SPS	Spark plasma sintering	-
t	Exposure time	s
T	Total laser travel time	s
$\dot{\boldsymbol{T}}$	Cooling rate	$K \cdot s^{-1}$
T_0	Initial temperature	K
TGM	Temperature gradient mechanism	-
t_l	Laser travel time	s
T_L	Line tension of dislocation	$J \cdot m^{-1}$
T_{liq}	Liquidus temperature	K
T_m	Melting temperature	K
T_{sol}	Solidus temperature	K
u	Volume of casting	m^3
V	Solid growth rate	$m \cdot s^{-1}$
v	Laser scan speed	$m \cdot s^{-1}$
XRD	X-ray diffraction	-
Y	Depth of the overlapping portion	m
β	Heating rate	$K \cdot s^{-1}$
Γ	Gibbs-Thomson coefficient	-
γ_{APB}	Antiphase boundary energy	$J \cdot m^{-2}$
δ	Lattice misfit parameter	-
Δh_f	Latent heat of fusion	$J \cdot kg^{-1}$
ΔT_0	Equilibrium solidification temperature range	K
Δt_{HT}	Heat treatment time	s
Δt_x	Increment of time	s
λ	Thermal conductivity	$W \cdot m^{-1} \cdot K^{-1}$
$\sigma_{0.2}$	0.2% proof stress	MPa
ω	Microstructural parameter	-

Chapter 1 Introduction

With the continuous increase in the performance of aircraft engines, there is also an increased demand for high-performance alloys. The past 50 years have witnessed the evolution of superalloys in the aerospace industry, which can exhibit desirable properties under high-temperature and high-stress conditions. (John, 2009) However, owing to the nature of superalloys, the processing of their components in turbine engines is expensive, and the complexity of part geometry is limited by conventional techniques. (Han, 2017)

Additive manufacturing (AM) refers to technologies that deposit and join materials layer by layer to produce a three-dimensional object from a pre-designed file. The ability to produce complex objects with low material waste has been demonstrated as a potential route to effectively process jet engine components. Therefore, the AM of superalloys has drawn increasing interest in recent years. However, selective laser melting (SLM), which is the main branch in AM, has been reported to cause defects in superalloys during processing. (Syed et.al, 2018) Hence, it is imperative to investigate the defect mechanism and optimize processing to make AM a viable, alternative processing technique.

1.1 Aims and objectives of the project

- Understand the effect of processing parameters of SLM on materials, including their microstructure and mechanical properties and develop suitable SLM processing windows for nickel superalloys:
  - Explore the suitable processing window for SLM IN713C and LR8 using the existing processing map and Design of Experiment (DoE) method.
  - Characterise the microstructure response of nickel superalloys to processing parameters using sophisticated characterisation techniques.
  - Use mechanical tests to identify the mechanical behaviour of SLM nickel superalloys.
- Classify different type of defects in SLM-processed materials under different

processing parameters, understand the defect mechanism in SLM nickel superalloys and identify the potential factors that can affect defect formation during SLM:

- Characterise and classify possible defects resulting from SLM using K-NN machine learning method.
- Correlate the effects of the heat profile on defect formation using pyrometer and MATLAB modelling.
- Understand the main mechanism behind the defect formation during SLM.

- Understand the effect of heat treatment on SLM samples and the resultant microstructure and mechanical properties:
  - Characterise the microstructure response of IN713C to variable heat treatment conditions.
  - Investigate mechanical behaviour in heat treated SLM nickel superalloys using mechanical tests.

1.2 Thesis layout

Chapter 2 focuses on the literature review of nickel superalloys and AM.

- Characteristics of superalloys, including elements and phases, and fundamental of solidification.
- System of AM, including the characteristics of different AM techniques and workflow.
- The defect mechanism in nickel superalloys by variable processes from previous studies.

Chapter 3 provides an introduction of the experimental methodology employed in the project and associated investigation. In addition, the operation of the SLM system, analysis technique and equipment details are discussed.

Chapter 4 discusses the processing parameters of SLM IN713C on an Aconity3D Mini machine. Preliminary investigations focus on optimized processing windows and the effect of variable processing parameters on defect formation and mechanism. Meanwhile, the mechanical performance of as-built SLM IN713C samples is also

investigated.

Chapter 5 focuses on the effect of heat treatment on SLM IN713C samples. Several heat-treatment routines are applied to as-prepared samples to investigate the effect of heat-treatment conditions on the microstructure and mechanical properties.

Chapter 6 focuses on a novel material LR8, which is specially designed for SLM processing. A similar approach from Chapter 4 is applied to the investigation of optimized processing windows and material properties for SLM LR8. Owing to the relatively large and irregular size of LR8 powder, the effect of powder quality on build repeatability is also analysed.

Chapter 7 summarizes key research conclusions in this study and provides suggestion for further studies to investigate the AM of nickel superalloy for aerospace applications.

Chapter 2 Literature review

2.1 Nickel superalloys

2.1.1 Overview

Over the last century, the performance of aircraft engines has been continuously advanced. Therefore, the demand for materials that can withstand extreme working environmental elements, such as temperature, pressure, and stress, has consequently heightened. As shown in Figure 2.1, a common turbine jet engine can be divided into two sections: (1) the cold section, wherein gas intake and compression occur, which can be fabricated with lightweight Ti alloys because of the relatively low temperature and stress in this section, and (2) the hot section, whose material requirements must meet the following criteria: (Donachie, 2002)

- The material must maintain its mechanical performance under the operating temperature, which is close to the melting temperature ($T_{operation}/T_{melting} > 0.6$).
- The material must be resistant to mechanical degradation caused by loading over a long service lifetime, such as creep resistance and cyclic loading.
- The material must be functional in harsh environments, e.g., oxidation- and corrosion-resistant.

The development of nickel superalloys is aimed to satisfy these requirements for decades, and they have been widely used as materials for turbine disks and blades. Improving the performance of Ni superalloys is also paramount toward furthering the evolution of jet turbine engines.

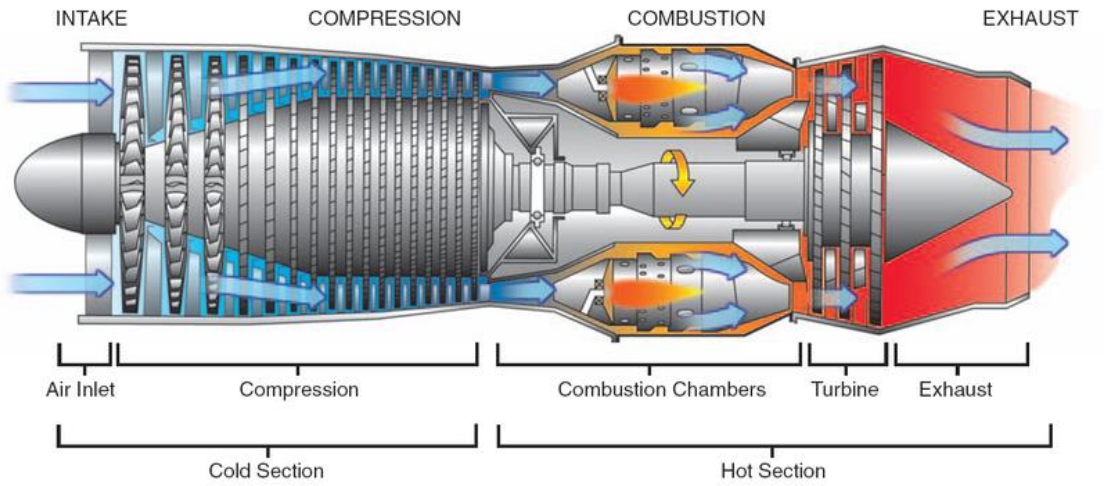

Figure 2.1 Diagram of a typical turbojet engine with all sections and key components labelled. (FAA, 2012)

2.1.2 Categories of superalloys

Superalloys are a category of metallic alloys that can be used at high temperatures, often in excess of 0.7 of their absolute melting temperatures. Superalloys can be further categorised into three main groups.

The first group comprises Fe–Ni-based superalloys. A typical commercial superalloy in this category is Incoloy 800. A high wt% of iron acts as the joint element with Ni; therefore, a solid-solution strengthening mechanism provides moderate strength. Compared with Ni-based superalloys, the precipitation of the strengthening γ' phase is more spherical than cuboidal. This type of superalloy is normally used as a wrought material. (Donachie, 2002)

The second group is Co-based superalloys, which use the strengthening of solid-solution elements and the formation of carbide to enhance the mechanical properties at elevated temperatures. Some elements can form an intermetallic phase (Co_3M), which is similar to the γ' phase in a Ni-based superalloy. (Donachie, 2002)

The third group comprises Ni-based superalloys, which are the most widely used superalloys in the aerospace industry. They have been developed and researched for over 70 years because of their ability to maintain the performance of parts under elevated temperature conditions, as well as the ability to function in harsh, corrosive working environments. Depending on the composition and strengthening mechanism,

it can be further categorised into three groups. (Donachie, 2002)

2.1.2.1 Solid solution-strengthened superalloys

Here, Ni and Fe or Cu are the main systems. Notably, IN625 and Hastelloy X are typical examples, wherein Fe and Cu are isomorphous; thus, a single-phase alloy can be produced. A solid solution-strengthened superalloy mainly contains some substitutional elements, such as Cr, Mo, and W, to improve the alloy performance and provide good corrosion resistance. It contains only a small amount of Al and Ti; therefore, it can only provide moderate strength. To achieve a higher strength level, precipitation hardening is required. (Lippold et.al., 2013)

2.1.2.2 Precipitation-hardened superalloys

The precipitation-hardened superalloy is a common type of alloy that is employed in aerospace applications because of its high strength in high-temperature environments. These superalloys generally contain a certain amount of Al and Ti (normally less than 10% of the total). With proper treatment, precipitates that are coherent with the austenite matrix can be formed to strengthen the austenite matrix. This microstructure is called gamma prime (γ'). Carbide and some substitutional elements can further enhance the high-temperature performance. The Al/Ti ratio can be critical to alloy stability and has a large impact on the microstructure. (Lippold et al., 2013)

2.1.2.3 Oxide-Dispersion-Strengthened (ODS) alloys

Unlike the previous two types of alloys, the ODS alloy contains a small amount of nanoscale oxide particles (normally less than 1% of Y_2O_3). The dispersion strengthening mechanism is due to the incoherency of the oxide particles within the matrix. Dislocations can only overcome the incoherent particle by climb rather than shear the particle directly. If the oxide particle precipitated within the grains, it can increase dislocation multiplication and causing more dislocation entanglement and prevent the movement which indirectly increasing "lattice friction". Therefore, the oxide particle can decrease dislocation and improve creep resistance. (Bhadeshia, 1997)

2.1.3 Advantages of the Ni superalloys

Generally, aerospace applications require high creep resistance and structural stability under high temperature conditions. The major face-centred cubic (FCC) phase in nickel superalloy has the highest diffusion activation energy with the lowest diffusivity in comparison with other microstructures at elevated temperature. The low diffusivity can cause a low thermally activated creep rate due to the relation between creep and diffusion activation energy. Therefore, FCC structures have better creep resistances compared with other structures, such as body-centred cubic (BCC) and hexagonal close-packed (HCP) structures. These properties make FCC Ni the best choice for an elevated temperature environment. The high cohesive energy generated from the strong cohesion provided by the electrons on the *d*-orbitals makes the FCC Ni tougher and more ductile than other structures (BCC and HCP). (Betteridge, 1984)

Moreover, the FCC structure of Ni superalloys can be maintained from room temperature to the melting temperature; thus, there is no major phase transformation during heating. Therefore, the risks of expansions and contractions induced by phase transformations can be minimised. Another transition element that exhibits the same crystal structure is Pt; however, its high density and high cost are inappropriate for industrial applications. (Fairbank, 2003; Cornish et al., 2009)

Have a comparison between FCC nickel and other crystal structure elements. For BCC structures, such as Cr, there is a ductile to brittle transition, which can cause a significant drop in toughness with a decrease in temperature. For HCP structures, Re and Ru are the same series as Pt, which are dense and expensive, as mentioned above. Notably, Os can be toxic, while Tc is radioactive. Therefore, only Co shows a similar performance with an acceptable cost. However, it is still more expensive than Ni superalloys.

2.1.4 Roles of phases in Ni superalloys

Generally, the microstructure of a Ni superalloy contains a combination of several different phases as listed below: (Lippold et al., 2013; Reed, 2006)

- γ phase: The gamma phase shows the FCC structure. It comprises the matrix of

the Ni-based superalloy

- γ' phase: The gamma prime phase represents the precipitates that act as a strengthening phase with an $L1_2$ FCC structure. Thus, it is often coherent with the γ phase.
- γ'' phase: In the Ni–Fe alloy system, the strengthening phase is the body-centred tetragonal phase with a D022 order.
- Carbide and boride: With a carbon level of 0.2 wt%, an MC type of carbide (M = Ti, Ta, Hf) can form on the grain boundary, and it can further decompose to an $M_{23}C_6$ or M_6C type of carbide (M = Cr, W, Co) during processing or service. Boride can also be formed on the grain boundary via the same mechanism.
- Topologically close-packed (TCP) and HCP phases: Some other phases, , such as TCP σ and μ phase, or Laves phase (HCP), can also occur in Ni superalloys. However, the alloy design is aimed at preventing the formation of these phases as they can have a negative effect on the mechanical properties.

2.1.5 γ/γ' Structure

2.1.5.1 γ/γ' Microstructure

The essential solutes in Ni-based superalloys are Al and Ti, which normally do not exceed 10 wt%. A two-phase equilibrium microstructure, which includes the γ matrix and the γ' phase, is generated. The fraction of the γ' phase is highly depending on the chemical composition and processing temperature as shown in Figure 2.2.

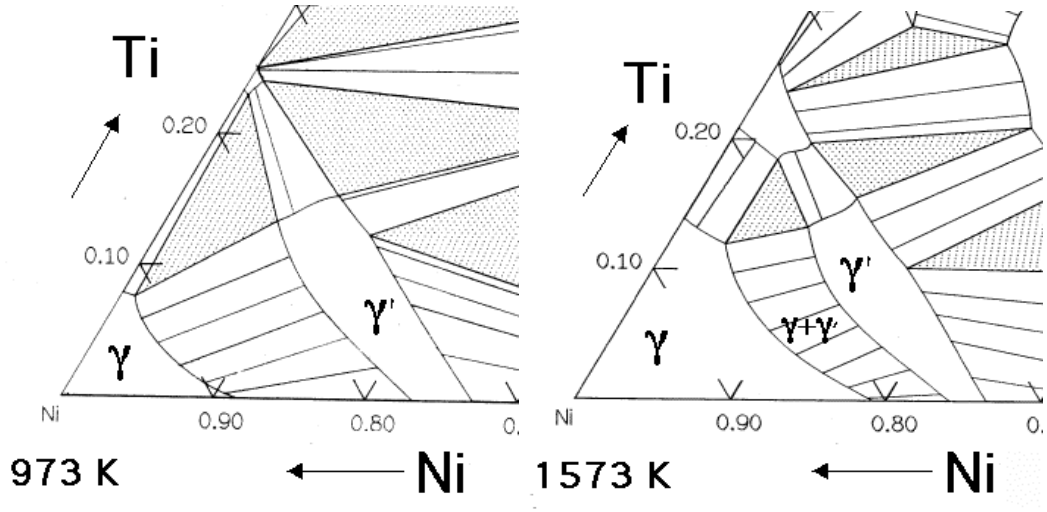

Figure 2.2 Part of the Ni–Al–Ti ternary phase diagrams showing that phase formation is related to the chemical composition and temperature. (Bhadeshia 2003)

For a given chemical composition, the fraction of γ' decreases as the temperature increases. Thus, the γ' phase can be dissolved at a sufficiently high temperature. With subsequent ageing at lower temperatures, a finer and more uniform dispersion of strengthening precipitates can be obtained. (Tancret et al., 2003)

The atomic structures of γ and γ' are depicted in Figure 2.3. The γ phase is a solid solution with an FCC lattice, whereas the γ' phase shows an ordered structure ($L1_2$ primitive cubic), wherein all the Ni atoms align at the centre of the faces, and Al or Ti atoms align at the corner of the lattices. This atomic structure, therefore, has a chemical formula of Ni_3Al, Ni_3Ti, or $Ni_3(Al, Ti)$. However, vacancies may exist in the sublattices or some of the Ni atoms may occupy the sites of Al and vice-versa. (Donachie, 2002)

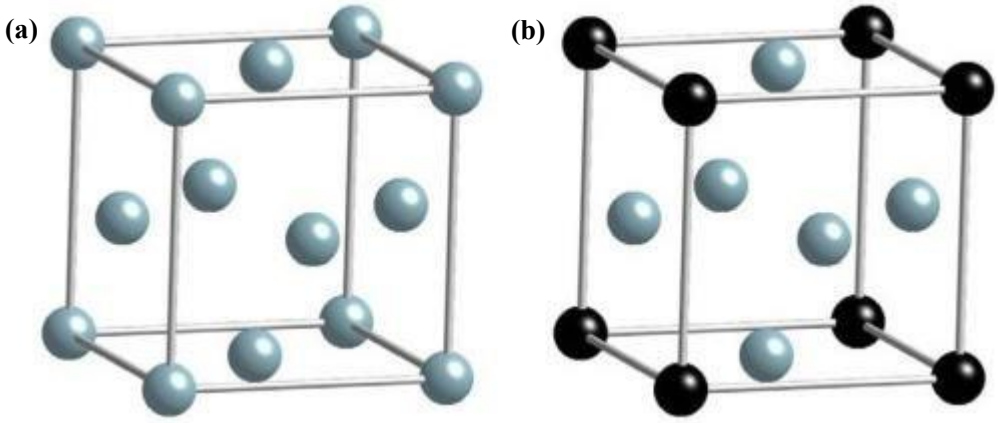

Figure 2.3 Diagram shows the FCC structure of (a) γ Ni phase and (b) γ' Ni_3Al phase, where grey particles represent the Ni atoms and black particles represent the Al atoms. (Sowa & Parlinska-Wojtan, 2016)

2.1.5.2 γ' precipitate strengthening mechanism

As shown in Figure 2.4, both γ and γ' have a cubic lattice and similar lattice parameters, whereby the γ' lattice is only 1.5% larger than the γ lattice. Therefore, the γ' phase can be coherent with the γ phase if the precipitate size is small. The dislocations in the γ phase are restricted by the formation of γ' precipitates. For the dislocations to penetrate the ordered γ' precipitates, it is essential that an antiphase boundary (APB) exists on the slip plane, as represented in Figure 2.5. The associated APB energy (γ_{APB}), as a barrier must be overcome to prevent particle cutting. The ½<110> dislocations must move in pairs through the particles. (Smallman & Ngan, 2014) According to Reed (2006), the particle cutting stress can be expressed as the order of γ_{APB}/b, where b is the Burgers vector, and the typical value of γ_{APB} is approximately 0.1 J/m^2, while b is 0.25 nm, and the cutting stress is approximately 400 MPa. Therefore, this indicates that the strengthening of ordered particles makes a substantial contribution to γ' particulate strengthening.

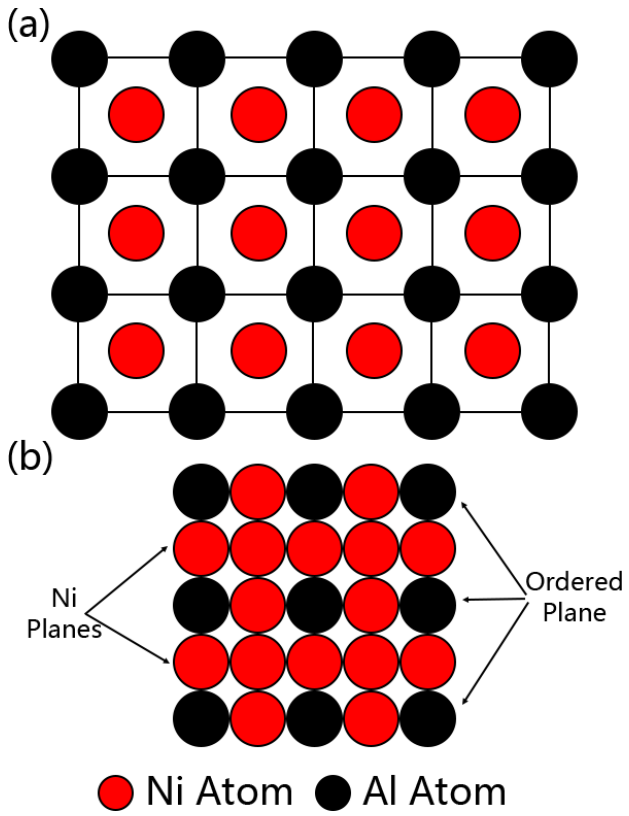

Figure 2.4 Diagram presenting the: (a) ordered plane of γ' lattice (b) compact structure of the ordered and Ni planes of γ' lattice; Figure is adapted from Carter (2013).

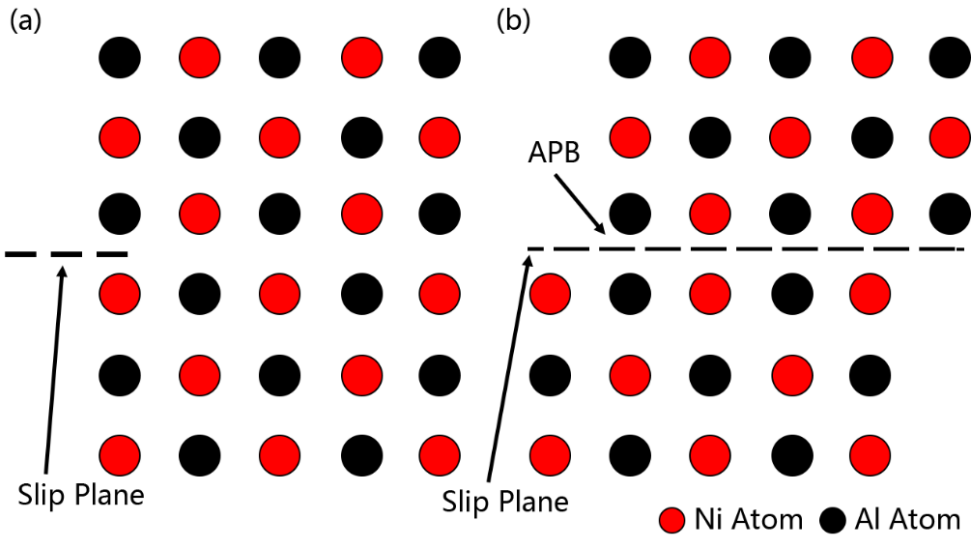

Figure 2.5 Diagram presenting the γ' particles (a) before and (b) after dislocation cutting and how it is associated with the slip plane and APB. Figure is adapted from Carter (2013).

For large particles, Orowan looping can be the mechanism for the dislocations to penetrate the precipitate particles. When the particle is sufficiently large, the energy required to loop the particle is less than that needed to shear it. (Smallman & Ngan, 2014) Thus, the dislocation will bypass the precipitate particles, as shown in Figure 2.6.

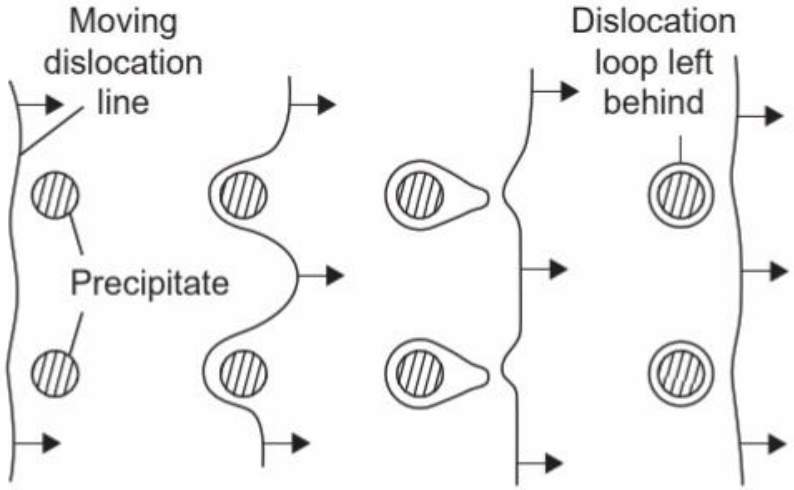

Figure 2.6 Diagram showing the Orowan looping mechanism around large precipitates. (Smallman & Ngan, 2014)

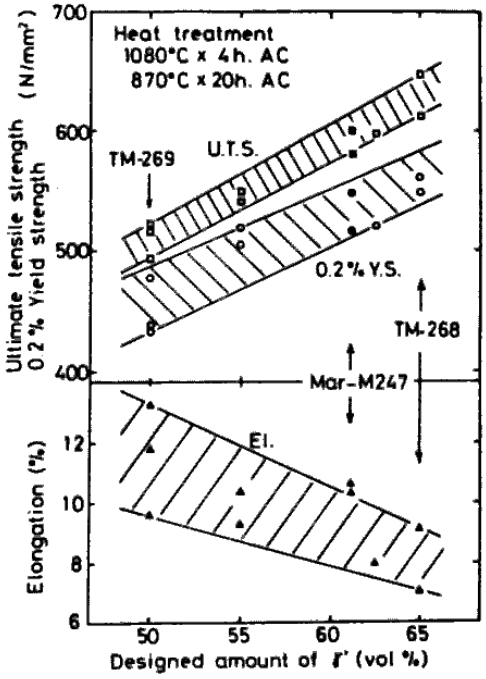

Figure 2.7 Diagram showing the linear dependence between the γ' volume fraction and all tensile properties. (Harada et al., 1982)

Generally, the volume fraction of γ' precipitates have a strong impact on the alloy strength. The increase in the amount of γ' precipitates can significantly elevate the tensile property. (Harada et al., 1982) As shown in Figure 2.7, the corresponding relationship between strength and γ' volume fraction is linear.

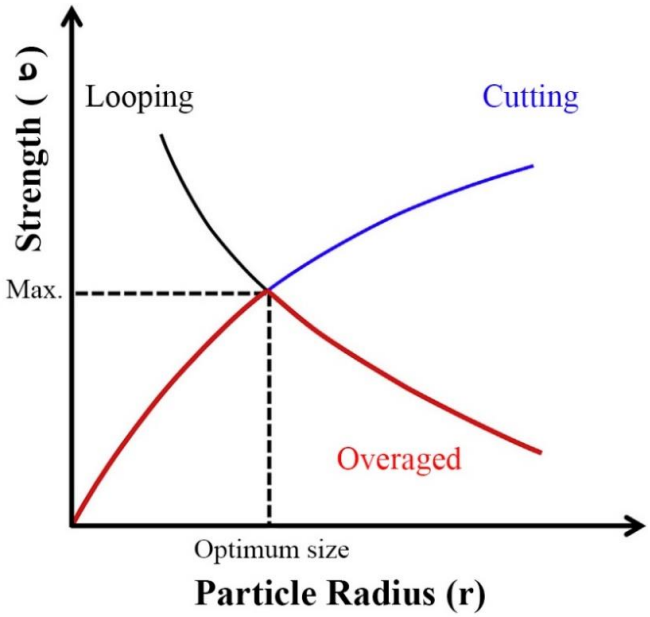

Figure 2.8 Material strength as a function of the radius of the γ' particle. The optimum particle size under the mechanisms of Orowan looping, dislocation shearing, and overageing. (Sun et al., 2016)

The literature shows that the tensile stress and ultimate tensile strength increase with the size of the precipitate particle to a maximum value and then drops upon further increase in the precipitate particle size, as illustrated in Figure 2.8. (Rifai et al., 1985) Thus, there is an optimum γ' particle size for the heat treatment of Ni superalloys. However, the ideal particle size is difficult to maintain owing to the growth of precipitates under service conditions in real-life applications.

2.1.5.3 Misfit of the γ' precipitate

The coherence of disordered γ and ordered $L1_2$ γ' phases in Ni superalloys can have a strong influence on the material properties. (Ricks et al., 1983) This strengthening effect can be described as the lattice misfit parameter of the γ/γ' interface; the expression is shown in Eq 2.1:

$$\delta = 2 \times \left[\frac{a_{\gamma'} - a_{\gamma}}{a_{\gamma'} + a_{\gamma}}\right] \qquad \textbf{Eq 2.1}$$

where δ is the lattice misfit parameter and a is the lattice parameter of γ and γ', respectively. A small misfit parameter can ensure a low γ/γ' interfacial energy, while a stable, coherent or semi-coherent lattice structure can be achieved, which is positive for high-temperature applications. Moreover, the misfit parameter can also directly influence the morphology of the precipitates. (Zhang, 2011) For a coherent γ/γ' matrix, the deformation-induced stress field depends on the particle size and misfit parameter. At some critical point, the stress field can be sufficiently large to deform the shape of the γ' particles. Ricks et al. showed that the sequence of γ' particles will be spheres, cubes, arrays of cubes, and eventually become solid-state dendrites under proper heat treatment conditions. (Ricks et al., 1983)

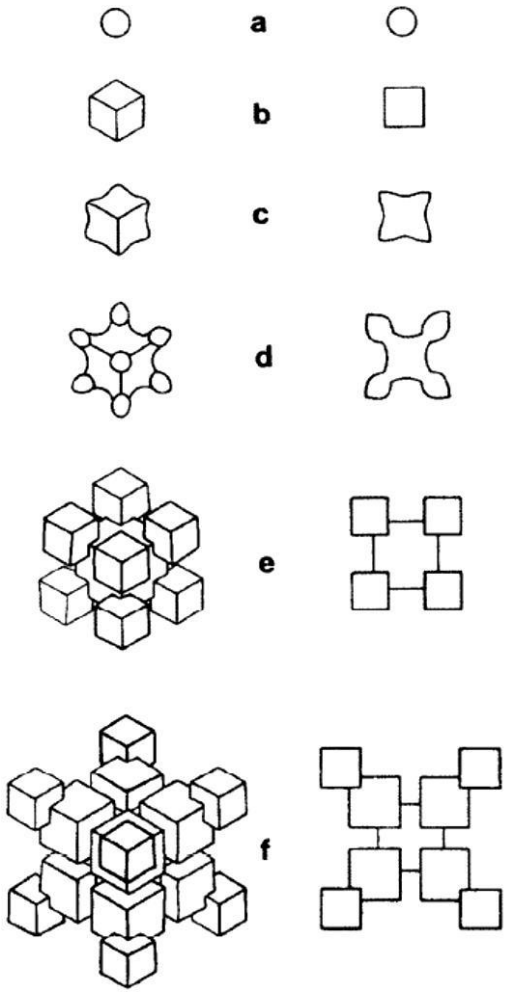

Figure 2.9 Evolution of particle shape from (a) spherical to (b) cuboidal to (c) arrowhead, and eventually to the (d, e, f) cuboidal array. (Ricks et al., 1983)

2.1.6 Carbides

Carbides can be formed when Ni superalloys contain 0.02 to 0.2 wt% of carbon. Carbides also contribute to the strength of the alloy to work at elevated temperatures. The carbides at the grain boundary can prevent or reduce grain boundary sliding, thereby strengthening the grain boundary. The fine carbide within the matrix can also potentially strengthen the material. The general form of carbides in Ni superalloys has the chemical expression of MC, $M_{23}C_6$, and M_6C. (Raza, 2015)

MC carbides are the most common type of carbides that can be observed in Ni superalloys at high temperatures. They can be observed as individual particles that are distributed randomly in the interdendritic area. At elevated temperature (Generally near 1100°C), MC carbide can slowly dissolve in the form of $M_{23}C_6$ and M_6C. (Donachie, 2002) The reaction can be expressed as:

$$MC + \gamma \rightarrow M_{23}C_6 + \gamma' \qquad \textbf{Eq 2.2}$$

$$MC + \gamma \rightarrow M_6C + \gamma' \qquad \textbf{Eq 2.3}$$

Moreover, $M_{23}C_6$ carbides tend to precipitate at the grain boundary and generally in the form of irregular discontinuous blocky particles. (Sims, 1966) However, with a high Cr content, plate carbides can also be observed. Their preferable location at the grain boundary can therefore prevent grain boundary sliding. (Doherty et al., 1971) However, the failure can initially occur at the location of the $M_{23}C_6$ carbides after a long service lifetime either by the fracture of the carbide particle itself or the decohesion of the carbide interface. (Engler-Pinto et al., 1996) Furthermore, M_6C has a complex cubic lattice, which can form at a slightly higher temperature than $M_{23}C_6$. Blocky M_6C carbides can be found in alloys with high W and/or Mo contents. Additionally, the M_6C carbide is preferably located at the grain boundary, which will also enhance the strength. (Bor et al., 2003)

2.1.7 The role of alloying elements

In general, Ni superalloys contain five to ten elements, and Ni is the major superalloy constituent. This kind of composition can result in a complex metallic system. Nickel

superalloys mainly contain Co, Cr, Al, and Ti. To improve some specific material properties, small amounts of W, Ta, Hf, Mo, Nb, and Zr (transition elements), as well as small amounts of non-metal elements (B and C) can be added to the alloy system. (Donachie, 2002)

2.1.7.1 The role of cobalt

Several studies have been conducted by Nathal et al. (1983). and Jarrett et al. (2012). to understand the effect of the Co content in the microstructure of Ni superalloys. The increase in the Co content can reduce the solvus temperature of the γ' phase and carbides. However, the transition temperature increases with the Co content, which also has a strong influence on the morphology of carbides. When the Co content is low, the carbides tend to be in thin film forms. As the Co content increases to 10 wt%, the carbides occur as normal particles on the grain boundary.

Tian et al. (2015). showed that the Co content had an inconsiderable effect on the overall fraction of γ' precipitates, which remained at approximately 46.5% as the Co level varied between 5 wt% and 23 wt%. However, the volume fraction of the primary γ' precipitates decreased with increasing Co content. Comparatively, the volume fraction of secondary and ternary γ' precipitates increased with the Co content. The γ' solvus temperature was higher in the alloy with low Co content. The amount of undissolved γ' precipitates within the grains can become primary γ' precipitates in low Co content alloys. This result shows that the addition of Co can be beneficial to the strength of Ni superalloys. (Tian et al., 2015)

The addition of Co decreases the stacking fault energy (SFE) within the alloy. For alloys with high SFEs, deformation microtwins form when the dislocations dissociate into Shockley partials and create a two-layer complex stacking fault (CSF) pseudo-twin structure owing to the shearing of the leading Shockley partials. Therefore, microtwins can occur with the reordering between Al and Ni atoms within the two-layer CSF. The deformation microtwins enhance the yield strength and strain-hardening ability. A large amount of secondary and ternary γ' precipitates can promote the transition of microtwins. (Karthikeyan et al., 2006; Cui et al., 2012)

2.1.7.2 The roles of other strengthening elements

Notably, Al, Ti, Cr, Nb, Mo, W, and Ta are common solid solution strengtheners in both the γ and γ' phases. Several studies have shown that the addition of Al and Cr can significantly improve the surface finishing and corrosion resistance. A protective oxide coating ($Cr_{2x}Al_xO_3$) can be formed on the exposed surfaces to prevent the reaction between the alloy and corrosive environment. Meanwhile, the formation of oxides can reduce the localised stress at the crack tip during fatigue failure, which means that the addition of Al and Cr can also improve fatigue resistance. However, the excess amount of Al could increase the volume fraction of the γ' phase, which would induce the formation of defects. (Pandey et al.,1986; Boismier & Sehitoglu, 1990; Sehitoglu & Boismier 1990; Gordon et al.,2007)

Nonetheless, Ti plays a role similar to that of Al in Ni superalloys, and Al atoms can be substituted by Ti in the γ' phase owing to the close misfit parameter. Under certain conditions, Ti can also form oxide particles (TiO_2) near the surface, which will degrade the adherence of Cr and Al oxides. (Rawlings & Staton-Bevan, 1975) The formation of TiO_2 particles can also be beneficial for hot corrosion resistance. The increase in Ti composition can also raise the volume fraction of the strengthening γ' phase, which can also improve the strength. However, an excess amount of Ti composition can cause a higher crack susceptibility. (Betteridge, 1984)

Both Nb and Ta are referred to as refractory elements, which can perform strengthening functions in Ni superalloys. Notably, Nb has been found to exhibit a finer γ' phase during solidification. However, it is believed that the excess composition of Nb over solubility can lead to the formation of the δ and η phases, which are harmful to the alloy properties. A high Nb concentration can also induce a high crack growth rate. With the ageing of high-Nb-based alloys, the fatigue resistance can be significantly improved. The Nb-containing alloy can also provide oxidation resistance by enhancing the kinetics of Cr_xO_3 oxide layer formation, while reducing the solubility and diffusivity of oxygen at the metal/oxide interface. (Christofidou et al., 2018) Furthermore, Ta can have a dramatic influence on the γ' phase. According to Morrison (2008), with 2 wt% of Ta addition, the volume fraction of γ' precipitates and solid solution strengthening

increased. This causes a 47±5 % increase in microhardness. Meanwhile, the increase in Ta concentration can change the morphology of the precipitates from a bimodal distribution of spheres to a cubic shape with round edges. (Booth-Morrison et al., 2008) The addition of Mo and W contributed to most of the non-oxidizing corrosion resistance in the Ni alloy. The corrosion resistance level can be represented by the pitting resistance equivalent number (PREN), which is mainly affected by the wt% of Mo and less by the wt% of W. (Zadorozne et al., 2012)

$$PREN = \%Cr + 3.3(\%Mo + 0.5\%W) \quad \textbf{Eq 2.4}$$

Several studies have shown that a certain amount of Mo concentration can be beneficial to creep resistance. (Tiearney & Grant, 1982; MacKay & Nathal, 1990; Zhang et al., 2004) After the creep test, the 2 wt% Mo concentration results in denser dislocation networks and a finer dislocation space. The networks act as a barrier, so the dislocations are difficult to slip or shear in the γ matrix. However, when the Mo composition exceed the saturation limit, μ precipitation is induced. According to Zhang et al. (2010)., μ precipitation can have a negative effect on creep resistance in three ways. First, the precipitate disturbed the regularity of the γ/γ' rafted matrix. The regular matrix is beneficial to the creep resistance because it interrupts the slip dislocation with the barrier. Second, the strengthening element is concentrated in the μ precipitation and causes the softening effect on the matrix. Third, the interface of the μ precipitation can be the initial onset of cracks and extend rapidly because of the brittleness. (Zhang et al., 2010) Notably, W had a similar effect as Ta. With a larger misfit parameter, alloys with high W contents can also provide decent creep resistance. (Tian et al., 2008)

2.1.7.3 The role of carbon and boron

The influence of carbon in the Ni superalloy is discussed in Section 4.2. Several studies (Davis, 1997; Tin, 2001; He et al., 2005) have shown that the fatigue life, creep resistance, and ductility can be affected by the size and morphology of carbides. Kotval et al. (1972) found that the addition of Hf can have a significant effect on the morphology of the carbide, thereby improving the ductility of the alloy. Boron worked in the same way as carbon. The formation of boride can improve the creep resistance.

Boride mainly preferred to grow at grain boundaries with a blocky or half-moon appearance. Therefore, the hard particle can prevent grain boundary sliding.

2.1.8 Solidification

Solidification is an important phenomenon that occurs when the material transitions from the liquid to the solid state. The solidification is mainly affected by the thermal profile and pressure. The solidification route can have a strong influence on microstructure formation and, therefore, the mechanical properties of the final products. By properly controlling the solidification path, specific grain texture and orientation can be achieved for the required application. (Campbell, 2015)

The extraction of heat energy induced by heat flux can cause a decrease in the enthalpy owing to the cooling of the material and the phase transformation from liquid to solid. Therefore, the cooling rate for an isothermal material can be expressed by Eq 2.5: (Kurz & Fisher, 1989)

$$\dot{T} = \frac{dT}{dt} = -q_e \left(\frac{A_s}{uC_p}\right) + \left(\frac{df_s}{dt}\right)\left(\frac{\Delta h_f}{C_p}\right) \qquad \textbf{Eq 2.5}$$

It shows that the cooling rate (dT/dt) depends on the heat flux (q_e), surface area (A) and volume (u) of the casting material. Solidification rate (df_s/dt), latent heat of fusion (Δh_f) and the specific heat capacity (C_p)The cooling rate of a known position and time correlates with the solid growth rate (V) and thermal gradient (G), as shown in the equation below: (Kurz & Fisher, 1989)

$$\dot{T} = GV \qquad \textbf{Eq 2.6}$$

Dendrite begin to grow when the accumulation of solute and heat was sufficient to induce the supercooling state of the liquid in front of the solidification front. The growth forms cells first and then dendrites, as shown in Figure 2.10. The cellular growth is parallel and opposite to the direction of the heat flux, while dendritic growth follows the preferred crystallographic orientation. (Losert et al., 1998)

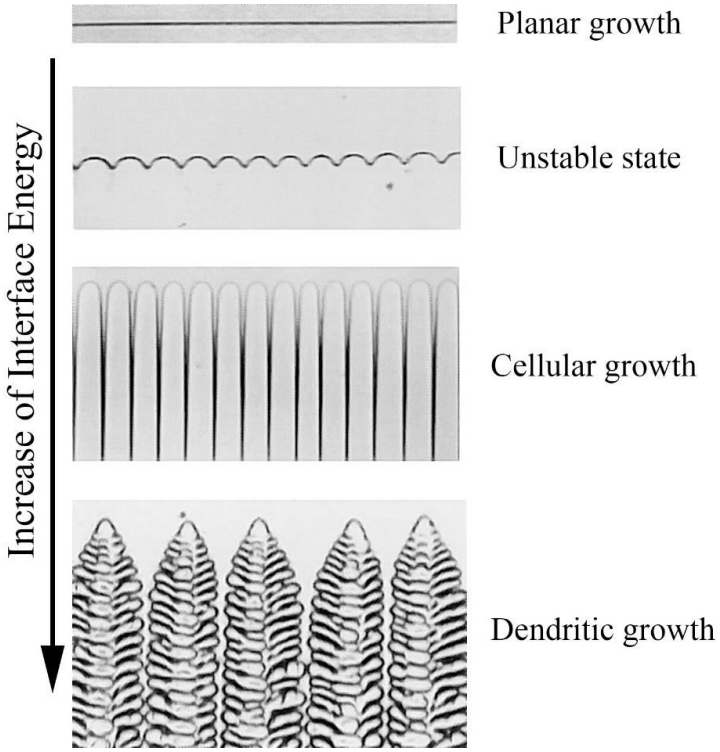

Figure 2.10 Evolution of growth pattern during solidification with an increase in the interface energy. (Losert et al., 1998)

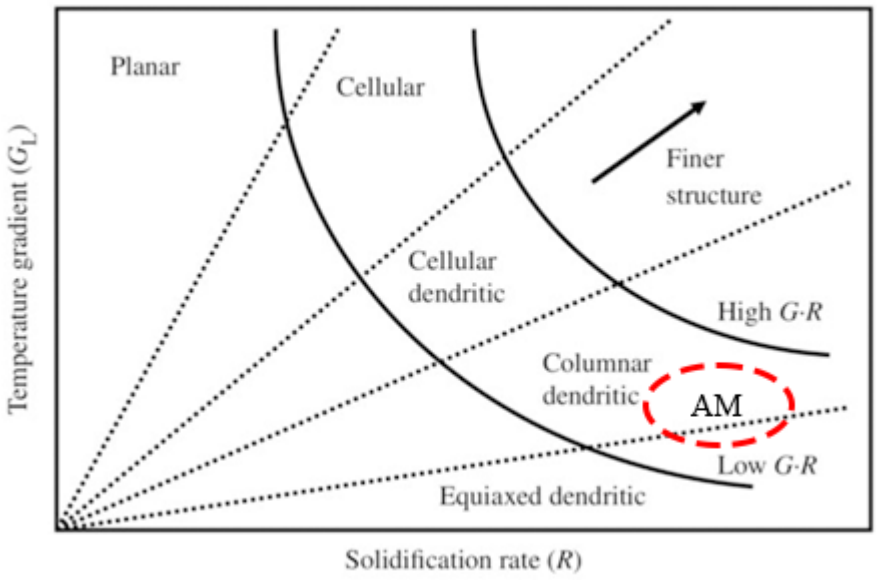

Figure 2.11 Effect of temperature gradient and solidification rate on dendrite growth morphology. (Lippold et al., 2013) The AM process generally produce columnar dendrites.

Therefore, the microstructure of the solidified material also depends on the solidification route. Different conditions can cause the grain to be equiaxed or columnar. Supercooling conditions induce heterogeneous nucleation, which leads to the formation

of equiaxed grains, while columnar grains are formed because of competitive growth. According to the research of Hunt (1984), the relationship between the morphology of the grains and solidification can be expressed by a columnar-to-equiaxed transition. As shown in Eq 2.3, the grain morphology also depends on G and V, where n is the material constant.

$$\frac{G^n}{V} > Cst \qquad \textbf{Eq 2.7}$$

Where,

$$Cst = \mathrm{a}(8.6\Delta T_0 \frac{N_0^{1/3}}{n+1})^n \qquad \textbf{Eq 2.8}$$

Under non-equilibrium conditions, dendritic growth is related to the non-equilibrium partition coefficient and the non-equilibrium solidification temperature range. Both Kurz–Fisher and Trivedi provided equations to calculate the primary dendrite arm spacing (PDAS), as shown below: (Kurz & Fisher, 1981)

$$\lambda = 4.3(\frac{\Delta T}{G})^{1/2}(\frac{D\Gamma}{VK\Delta T_0})^{1/4} \qquad \textbf{Eq 2.9}$$

$$\lambda = 2.83G^{-1/2}(\frac{\Delta T_0 LkD\Gamma}{V})^{1/4} \qquad \textbf{Eq 2.10}$$

Where, ΔT_0 is the equilibrium solidification temperature range, Γ is the Gibbs-Thomson coefficient, L is a harmonic of perturbation constant, D is the diffusion coefficient. K is the material constant and k is the distribution coefficient. The Kurz–Fisher model assumes that the dendritic tip radius is the same as the wavelength of the unstable solidification front, while the Trivedi model suggests that the dendrite tip is rather similar to a spherical shape. Previous research shows that the Kurz–Fisher model tends to overestimate the PDAS relative to experimental measurements. However, the Trivedi model underestimated the PDAS. Thus, the Kurz–Fisher and Trivedi models can be used as the upper and lower boundaries for PDAS prediction. (Kurz & Trivedi, 1994)

2.1.9 Rapid solidification

Rapid solidification can be defined as the short duration between the initiation and completion of the liquid–solid phase transformation. The fast cooling rate can lead to a high velocity of the solidification front, which can be within the range of 10^{-2} m/s and

10^3 m/s. In additive manufacturing (AM), the melting pool generally has a small size and is surrounded by a relatively cold solid. Therefore, the cooling rate can be up to 10^5-10^7 K/s with the solidification front velocities the same as laser scan speed (0.5-4 m/s). Thus, solidification during AM can be classified as 'rapid solidification'. (Cahn & Jones, 1999)

2.1.10 Specific metallurgy and properties of Inconel 713C (IN713C)

Inconel 713C (IN713C) is the primary Ni superalloy that is investigated in this thesis. The chemical composition range following the AMS 5391 standard is shown in Table 2.1:

Table 2.1 Chemical composition of IN713C. (Sandvik Osprey Ltd, 2015)

Element	Range (wt%)	Nominal (wt%)
Ni	Bal	Bal
Cr	12.0–14.0	13.0
Al	5.50–6.50	6.00
Mo	3.80–5.20	4.50
Nb	1.80–2.80	2.30
Fe	0.00–2.50	1.25
Ti	0.50–1.00	0.75
Si	0.00–0.50	0.25
Zr	0.05–0.15	0.10
C	0.08–0.20	0.14
Mn	0.00–0.25	0.125
Cu	0.00–0.50	0.25
B	0.005–0.015	0.010
S	0.000–0.015	0.0075

IN713C was first developed in the early the 1950s with the removal of Co to reduce the cost and density, while maintaining a certain level of mechanical performance. It is a typical γ'-precipitate-strengthened Ni-based superalloy. (Brinegar et al., 1984) The

grain structure of IN713C followed the discussion in the previous section, which included the coherence of the γ matrix with the γ' precipitate in a small amount of particulate carbide and boride located at the grain boundary, thereby strengthening the alloy. The IN713C also evolved into IN713LC, wherein 'LC' indicated a low carbon composition (0.08–0.20 wt% → 0.03–0.07 wt%). The effect of carbon content is discussed in Section 2.1.8.

The common manufacturing methods of IN713C are conventional casting, press forging, or extrusion, followed by certain heat treatment processes to produce the required grain morphology. In the cast condition, it is required for the AMS 5391(2014) that IN713C satisfies the following material properties:

Table 2.2 The tensile properties specification for IN713C.

Temperature (°C)	0.2% Yield Strength (MPa)	Tensile Strength (MPa)	Elongation (%)
25	680 minimum	760 minimum	3 minimum

Table 2.3 The stress-rupture properties specification for IN713C.

Temperature (°C)	Stress (MPa)	Life time (h)	Elongation (%)
25	680 minimum	760 minimum	3 minimum

Table 2.4 Hardness property specifications for IN713C.

Hardness Rockwell (C)	Density (g/cm^3)	Melting range (°C)
30–42	7.913	1260–1288

The tensile test results from the Nickel Institute show the corresponding relationship between temperature and tensile properties, as depicted in Figure 2.12. The sample was prepared by vacuum casting. When the temperature exceeded 750 °C, the strength reduced significantly. The elongation dropped between 500 °C and 800 °C.

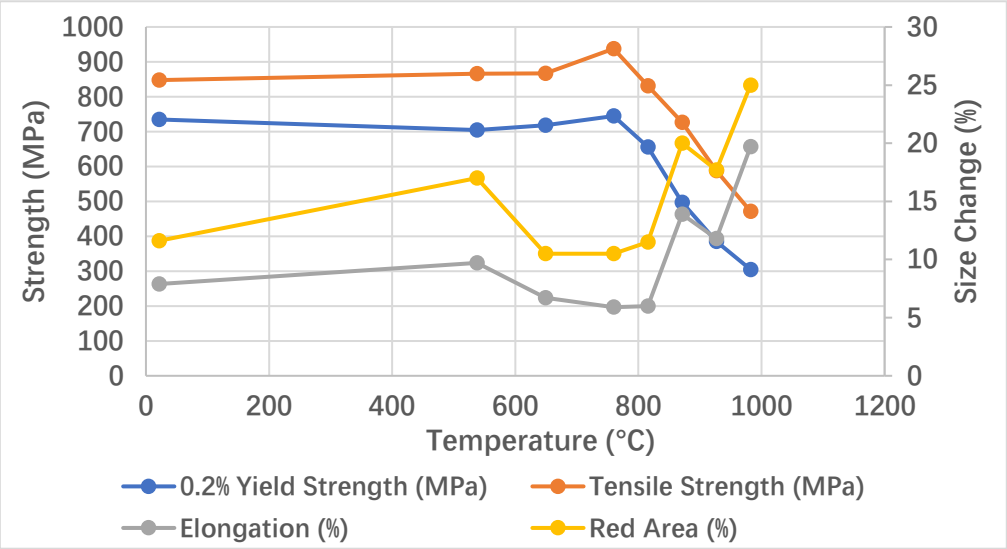

Figure 2.12 Tensile properties of IN713C as a function of temperature. The diagram is reproduced from the IN713C data sheet. (INCO, 1968)

The microstructure of as-cast IN713C is shown in Figure 2.13, wherein a typical cubical γ' phase exists within the γ matrix. In an enlarged scale, as shown in Figure 2.14, a 'chain-like' carbide can be found to be concentrated at the grain boundary location. Gasko et al. (1988). found that a decrease in the fractional percentage of the γ/γ' eutectic could increase the yield strength and decrease the ductility. This also explains the result shown in Figure 2.11. The dissolution of the γ' phase reduced the amount of the γ/γ' eutectic and caused a change in tensile properties.

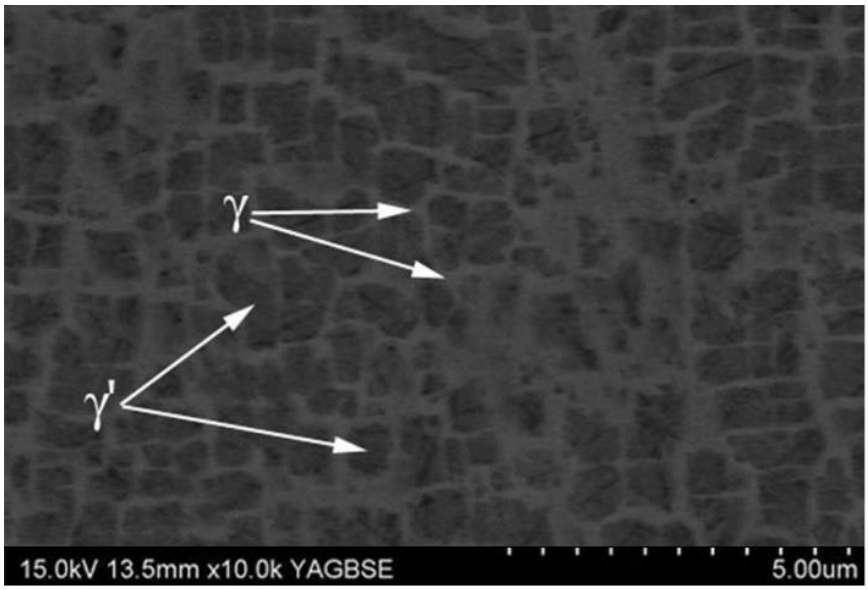

Figure 2.13 Morphology of the γ and γ′ phase matrix in the as-cast state IN713C superalloy. (Matysiak et al., 2014)

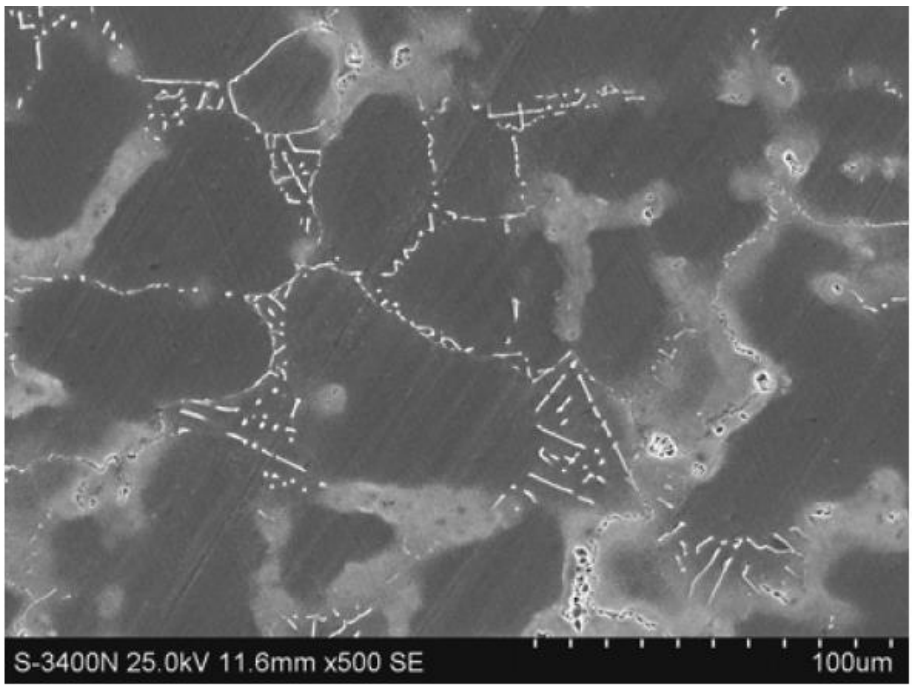

Figure 2.14 'Chain-like' MC-type carbide at grain boundaries in the as-cast state IN713C superalloy. (Matysiak et al., 2014)

2.1.11 Specific metallurgy and properties of LR8

LR8 is an experimental Ni–Co-based superalloy that is developed by Rolls Royce Inc. The chemical composition is shown in the table below:

Table 2.5 Chemical composition of the LR8 superalloy. (Rolls-Royce Inc, 2017)

Element	wt%
Ni	Bal
Co	33.6
Cr	13
Mo	3.2
W	8.4
Al	4.5
Ta	3.8
C	0.03
B	0.07
Zr	0.06

The main difference between the LR8 and the traditional Ni superalloy is the addition of a large amount of Co. The effect of Co in Ni superalloys has been discussed in Section 1.9.1. It can promote high-temperature strength by reducing the SFE in Ni. However, the density of the alloy will slightly increase with the amount of Co. A moderate amount of Al and no Ti content can ensure the achievement of reasonable mechanical properties while maintaining weldability. A typical γ/γ' matrix microstructure can be expected in an LR8 Ni–Co-based superalloy with common manufacturing methods, such as conventional casting and press forging.

As a newly designed material, the only commercial material which have a comparable chemical composition is ATI35N. ATI35N is a multi-phase nickel-cobalt-chromium-molybdenum alloy developed by ATI Metal (2016) which can achieve high strength, while maintaining good toughness, ductility and corrosion resistance with appropriate processing. Therefore, the performance of LR8 can be expect to be similar as ATI35N.

2.2 Additive manufacturing

2.2.1 Overview

Additive manufacturing is a relatively new manufacturing technology that has been developed since the late 1980s and early the 1990s due to the rising demand of produce complex parts with simplified procedures and cost. The early stage AM is also known as rapid prototyping (RP) technology. (Carter et al., 2014) All techniques start with a three-dimensional (3D) model normally in the form of a computer-aided design file. Thereafter, the model was processed into slices with fixed thickness values and transferred into the AM machine. A heat source assists the slices to connect and bond with the previous layer.

The first commercial AM machine (SLA-1) was invented in 1987 with stereolithography 3D printing. The solidification process was applied to an ultraviolet (UV) light-sensitive polymer by a laser source. The invention of SLA-1 leads to a fast and highly focused development of AM systems. It has evolved and blossomed into a plethora of manufacturing techniques, including selective laser melting (SLM), direct

laser deposition (DLD), electron-beam melting (EBM), and so on. In the mid-1990s, an AM process with metal was developed. In 1997, AeroMet successfully invented an AM system using a high-power laser and powdered Ti alloys. (Wohlers, 2015) Since then, the research on AM systems has mainly focused on the production of fully dense and functional parts. The two most commonly used AM systems are powder bed SLM (PB-SLM) and –blown powder DLD.

2.2.1.1 Powder bed selective laser melting system

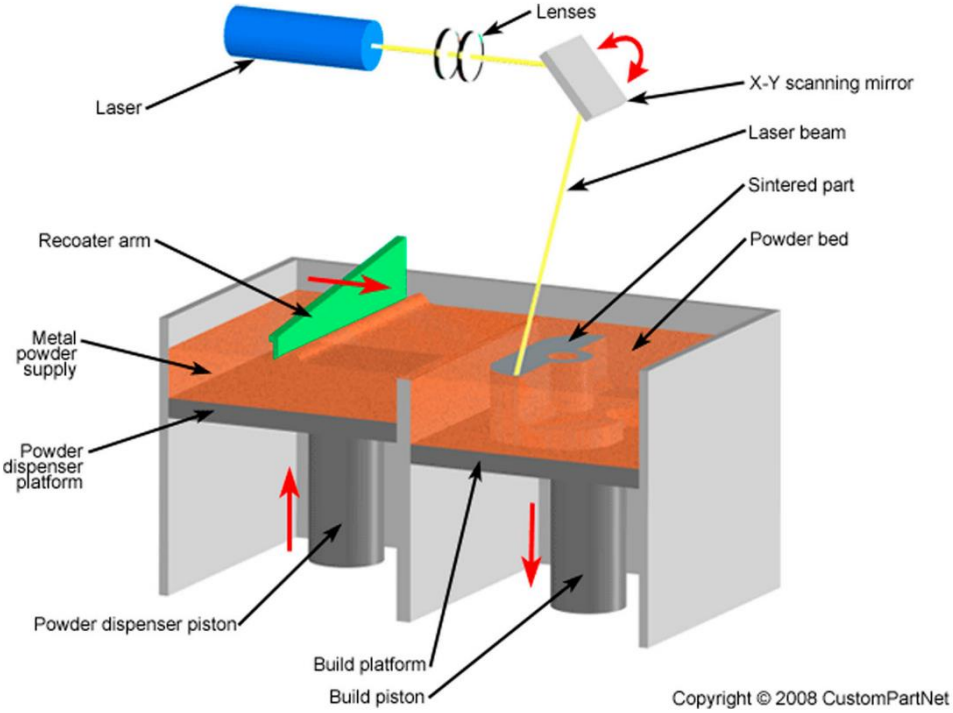

Figure 2.15 Schematic of the cross section of the SLM machine and melting process. (CustomPartNet, 2016)

The SLM powder-bed method has been developed since the early stage of AM technology development. (Carter et al., 2014) The schematic diagram of the SLM machine is shown in Figure 2.15.

There are two types of powder feeding approaches in the SLM system: the powder is stored either in a hopper or on a powder dispenser platform. For the hopper, a certain dose of powder is released at the start of the laser scanning of every layer, whereas for the powder dispenser platform, the piston rises to a certain height before the laser scanning of the layers. Typically, the SLM system requires a baseplate to build parts on

it, which also provides a mechanical and thermal substrate. A movable wiper with a soft blade then moves through the fabrication powder platform and deploys a layer of powder with uniform thickness on the baseplate. Generally, the SLM approach involves a laser system with lenses and an adjustable mirror to manoeuvre the position of the laser beam. Thus, the laser beam is scanned on the surface of the powder and melt selected position based on the model in the build file. During the melting process, the surface of the preceding layer is remolten by the laser to create a stronger bonding between layers. Once the selective melting of the current layer is completed, the fabrication bed declines a certain distance, which is the same as the layer thickness. All the above-mentioned steps are repeated until the entire component is finished. Thereafter, the fabrication bed rises to the top to remove the component from the stand. All unmelted powders can be recycled for the next build. (Carter et al., 2014) The parts were then cut off from the baseplate using wire electrical discharge machining (EDM). An alternative heat source for SLM is the electron beam, which works in a fundamentally different approach from the laser beam. An electron beam system requires a filament and magnetic coils to collimate and deflect the beam spatially. The electron beam then works like a high-power electron microscope and heats the exposed material. (Zenou & Grainger, 2018)

2.2.1.2 Blown powder direct laser deposition (DLD)

The blown powder DLD method has been developed since the late 1990s. (Thompson et al., 2015) The model and build file generation are the same as that of the SLM powder-bed method, while the build system is different from the SLM system. A schematic diagram of the SLM machine is shown in Figure 2.16.

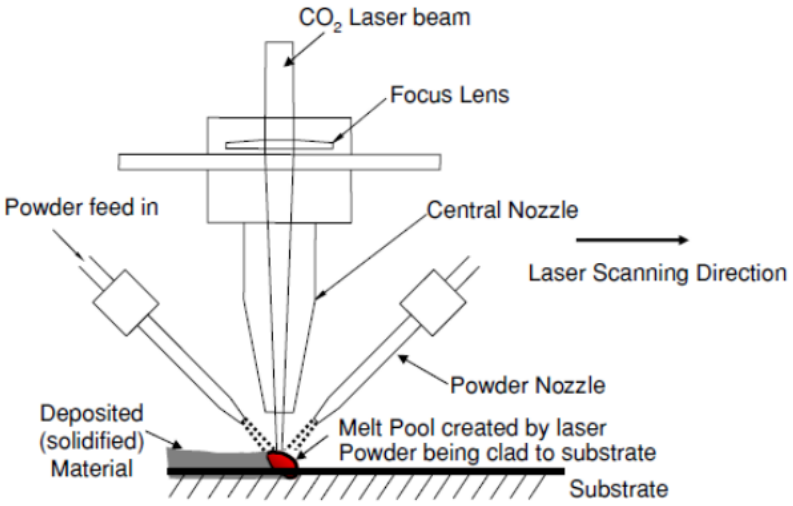

Figure 2.16 Schematic of the blown powder direct laser deposition machine. (Qi et al., 2009)

Similar to SLM, the DLD method also requires the powder stored in a hopper and a baseplate positioned in place as a substrate. Depending on the system, the baseplate can either be fixed (three-axis machine) or rotated (five- or more axis machines). The DLD method combines the powder delivery and laser melting systems. The powder nozzle can be coaxial or at an angle with a laser beam. Focused laser beam spots and melts the deposited material to create a melting pool. As one layer is finished, the stage will move or rotate to process the next layer. A multi-axis DLD system is capable of processing a much more complex geometry. Control of powder feeding is important in DLD systems. The powder flow rate must be checked regularly to ensure that the nozzle is unobstructed. (Thompson et al., 2015) After the build is complete, parts also need to be removed from the baseplate using wire EDM, similar to SLM parts.

2.2.1.3 Advantages of AM

Additive manufacturing is replacing conventional manufacturing methods, such as casting and subsequent machining. Compared with traditional manufacturing methods, AM has several advantages. First, it can be used to produce complex geometrical parts directly from a computational drawing. This means that the design of products will not be limited by the capability of the processing method. Second, AM can be a material-saving method compared to the conventional method. As powder is selectively melted

during the process, all unused powders can be recycled and ready for the next build. Third, near-net shape parts can be fabricated directly via AM; therefore, the expensive tooling cost and follow-up machining cost can be reduced. Furthermore, without subsequent machining, the processing time can be considerably reduced. Therefore, the fourth advantage entails time-saving related. There is no need to adjust the mould and tooling when changing between different build designs. Therefore, AM can be a very flexible solution for small-scale manufacturing. Summarily, AM can provide a new manufacturing system to the industry. It has a significant potential in terms of cost saving, design flexibility, and process simplification compared with conventional manufacturing. (Wang et al., 2015; Eisenhut & Langefeld, 2013; Pacurar, 2016

2.2.2 Defects and mechanisms

2.2.2.1 Laser melting mode

During the laser melting process, there are two types of melting mode base on the shape of melting pool. The shallow and hemispherical melting pool can be described as conduction mode while the deep and conical melting pool can be described as keyhole mode.

- **Conduction mode**

In conduction mode, the energy density is sufficient enough to melt the material. When energy is coupled into the powder layer, material is solely melted by thermal conduction within the limit of material thermal conductivity. The conduction mode can generally have a melting pool with a larger width than depth, as shown in Figure 2.17(a)

- **Keyhole mode**

Once the energy density increases to a threshold value where the heat energy cannot dissipate effectively, the residual temperature can raise above the vaporization point. Cunningham (2019) found the whole transition can be described by five characteristic stages. (1) material is melted by laser and exceed vaporization temperature. And cause (2) the formation and growth of vapor depression. With continuous heating (3) the

vapor depression become very instable and result in (4) the formation and growth of keyhole. (5) The vapor depression keeps penetrating through the melting pool can change the shape of melting pool. The final morphology of a keyhole melting pool can be like Figure 2.17(b)

Cunningham et al. (2019) also show that the linear dependent of depth of keyhole and power input in AM system. In general, the keyhole mode can be harmful to the as-build part due to the excessive porosity. The large number of pores in keyhole can be the initiators of cracks and reduce the part service life.

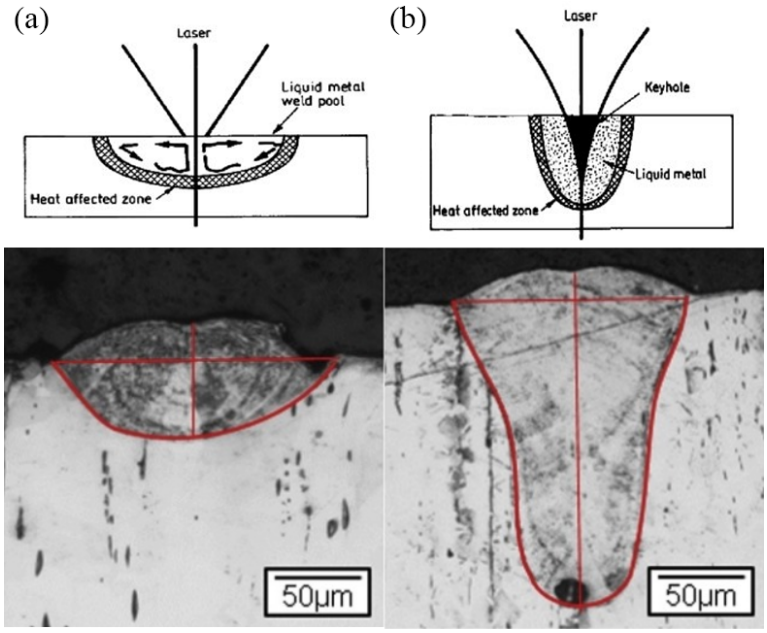

Figure 2.17 The morphology of (a) conduction melting pool (b) keyhole melting pool. Figure is adapted from Verma & Garg (2008) and Tenbrock et al. (2020)

2.2.2.2 Thermal residual stress

Because of the remelting of the preceding layer during laser fabrication, the grains considerably prefer to grow along the build direction and penetrate the boundary between layers. Thus, columnar grains can be formed in the laser fabrication products. However, the heat flow between the layers can induce thermal residual stress.

Residual stress is the stress that remains in the materials after being processed. Two different mechanisms can explain the formation of residual stress. According to the description of Kruth et al. (2006), the first mechanism is the temperature gradient

mechanism (TGM). The surface of the upper layer is rapidly heated up by the laser beam, while slower material heat conduction induces a steep temperature gradient. When the heated upper layer is expanded, it is restricted by the lower layer, which has a lower temperature and causes elastic compressive strains. At the cooling stage, the plastically compressed upper layer shrinks and forms a bending angle toward the laser beam direction. This causes tensile stress to form in the building direction.

The second mechanism is the cooling of the molten top layer. It shares a similar mechanism with the TSM; however, the shrinkage and formation of the bending angle is caused by thermal contraction during cooling. The temperature between layers causes the deformation to be restricted by the lower layers and induces tensile stress in the building direction. (Harrison et al., 2015)

2.2.2.3 Cracks

Carter et al. (2012). reported that laser AM can be considered to share a mechanism similar to that of the laser welding process. Thus, the weldability of alloys can be used as a reference for AM. The Al/Ti content causes an increase in γ' precipitation and induces high cracking susceptibility, as shown in Figure 2.18. It can be seen that IN713C is located in the difficult-to-weld region.

Several studies have reported four potential cracking formation mechanisms of Ni superalloys: solidification cracking, grain boundary liquation cracking, strain age cracking (SAC), and ductility-dip cracking (DDC).

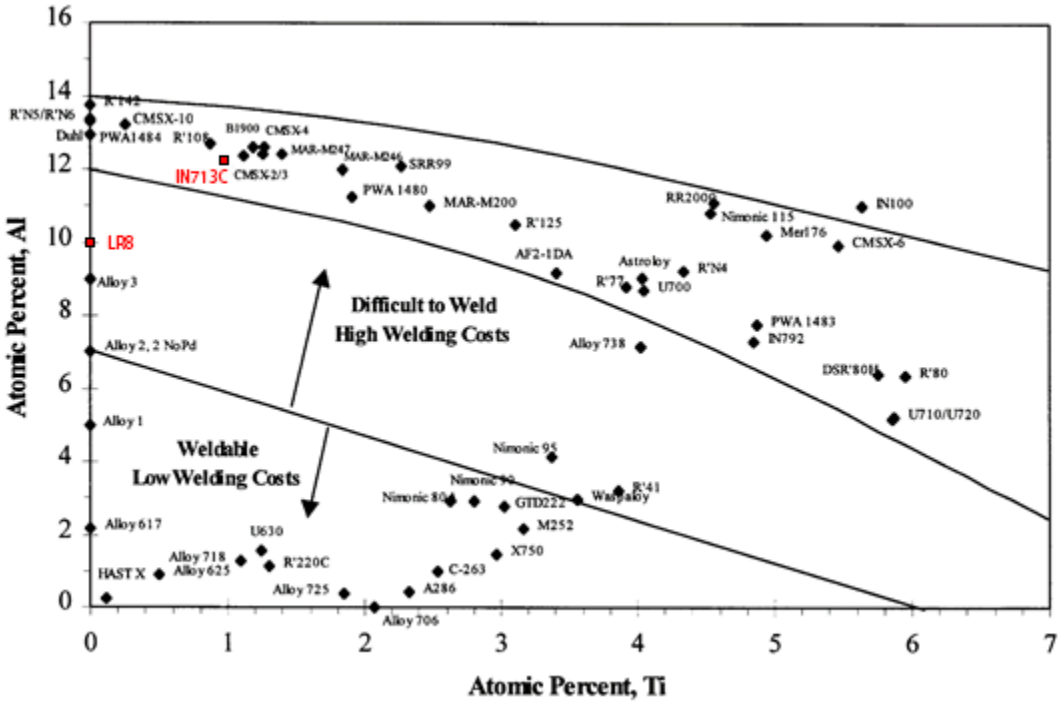

Figure 2.18 Weldability of various of Ni-based superalloys. (Simkovich & Whitney, 2001) Alloys used in this project is highlighted with red label.

- **Solidification cracking**

Generally, solidification cracking occurs when the two-phase solid–liquid region receives a tensile force during solidification. (Hemsworth et al., 1969) When the solid still occupies a low percentage during solidification, the solidification shrinkage and induced stress can be compensated by the liquid flow. However, when the solid occupies a high percentage (the solid fraction f_s is between 0.7–0.9), the formation of dendrites partially limits the flow of liquid material and forms an interdendritic structure. (Hunziker et al., 1999; Henderson et al., 2004) These positions can be separated if tensile stress occurs during progress and can become the initial locations of cracking. Figure 2.19 and 2.20 shows the macro and micrograph of the morphology of solidification cracks. (Carter et al., 2012) Several studies have reported that high power and small beam diameter tend to reduce the number of solidification cracks. (Yusof & Jamaluddin, 2014) Therefore, the high heat input can be linked to the elimination of solidification cracks.

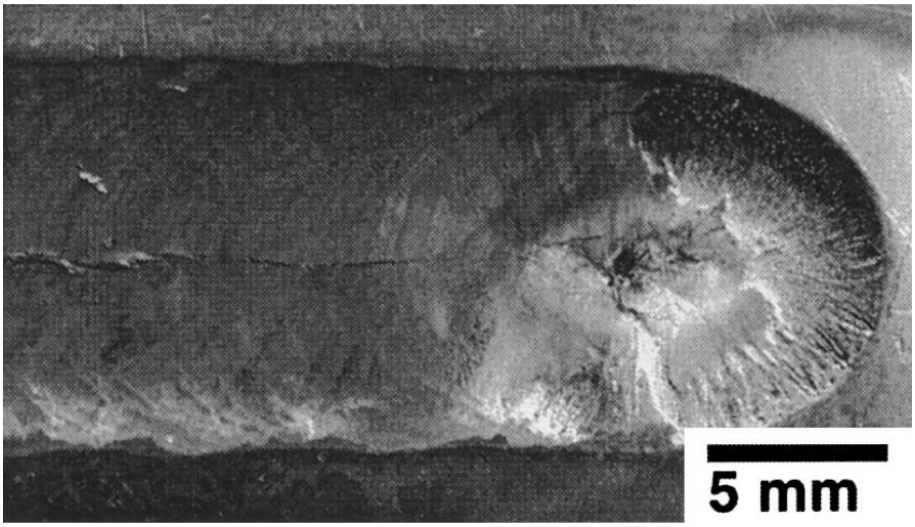

Figure 2.19 Optical micrograph of the solidification crack in a laser weld track. (Dye et al., 2001)

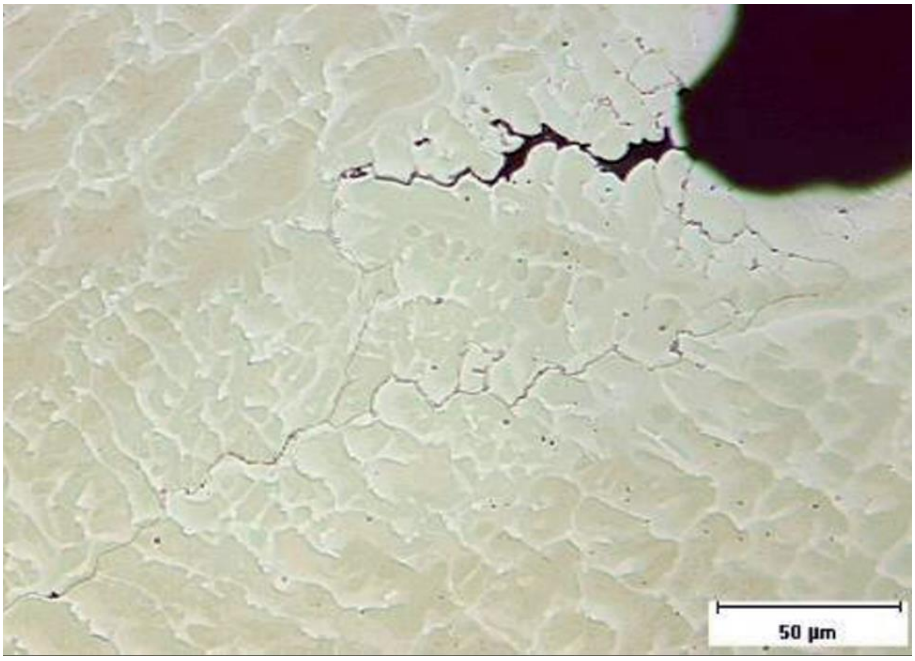

Figure 2.20 Morphology of the solidification crack in as-cast Haynes 230W alloy. (Lippold et al., 2008)

- **Grain boundary liquation cracking**

Grain boundary liquation cracking, also referred to as heat-affected zone (HAZ) fissuring, occurs in the HAZ near the molten pool. (Henderson, 2004) With a rapid heating condition, the material is heated to a temperature lower than the overall melting point of the bulk material, which causes insufficient dissolution of the grain boundary phases into solid solution. (Carter et al., 2012; Hemsworth et al., 1969) Therefore, the

carbides or nitrides can remain undissolved. The surrounding phases can be further melted and form a liquid film around, which can be the potential cracking initial point under a large residual or thermal stress, like displayed in Figure 2.21 and 2.22 (Dye et al., 2001) In solid solution strengthening alloys, liquation can be concentrated around carbides. In the γ' strengthening alloy, the liquation is concentrated around the γ' grain boundaries.

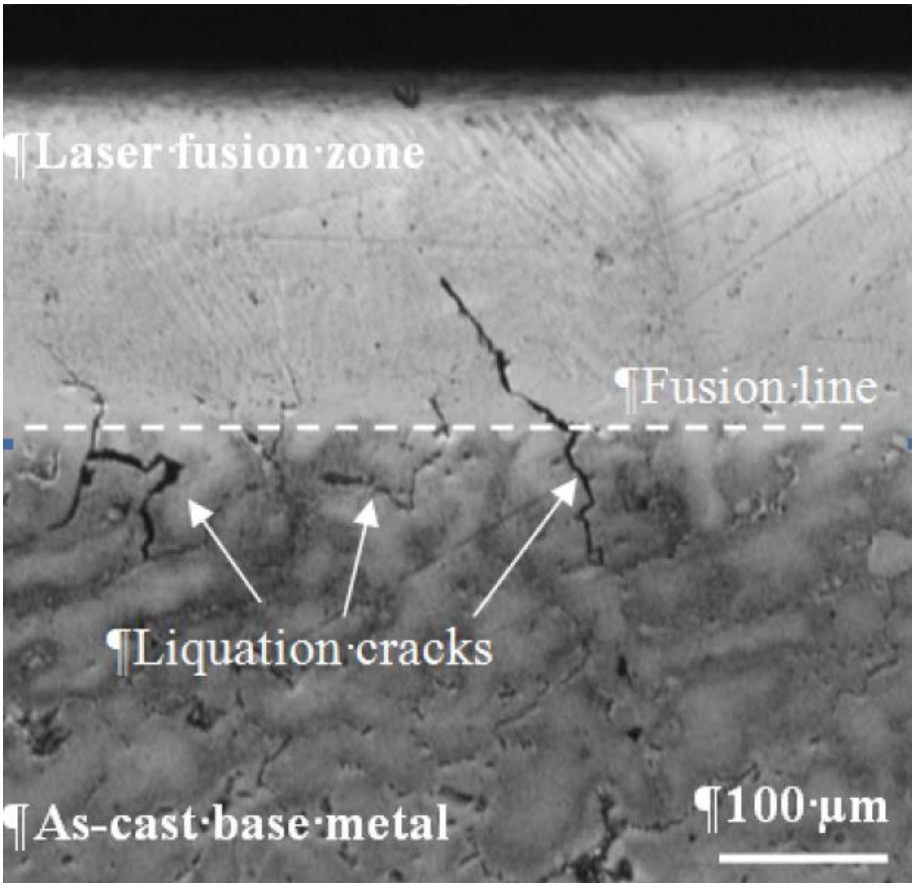

Figure 2.21 Morphology of liquation cracks in a laser melted as-cast IN738 alloy. (Mousavizade & Malek, 2011)

Mousavizade & Malek (2011) and Odabaşı et al. (2010). confirmed that the location of liquation cracks was in the HAZ. According to Odabaşı et al. (2010)., the liquation is more restricted in samples welded under lower energy. Thus, a lower energy input can be beneficial to prevent the formation of liquidation cracks.

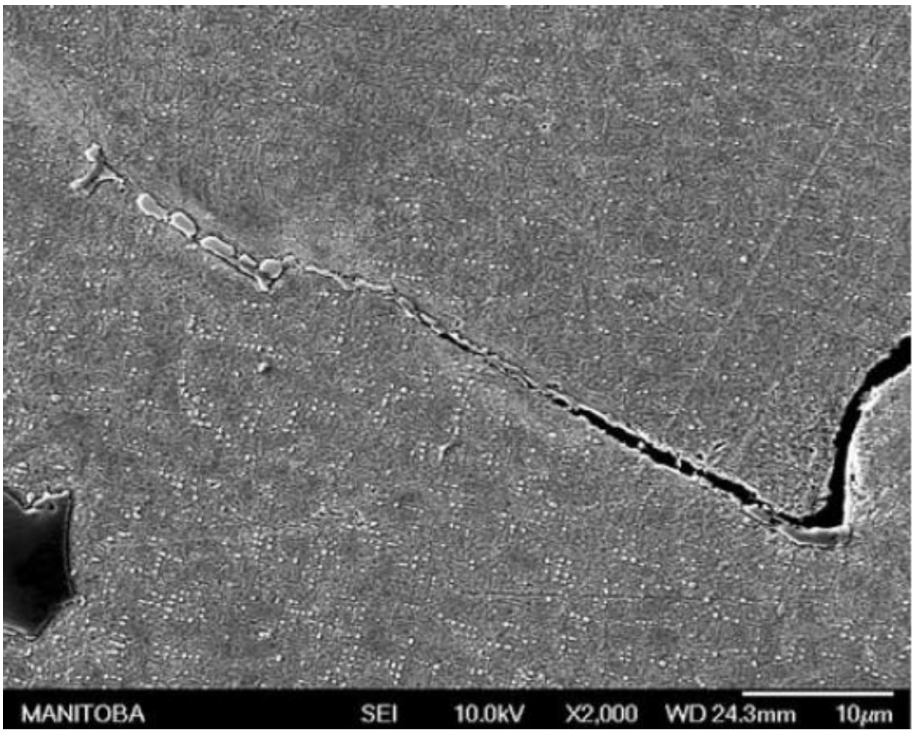

Figure 2.22 Morphology of HAZ liquation cracks in the laser AM-fabricated IN718 sample. (Odabaşı et al., 2010)

- **Strain age cracking (SAC) and post-weld heat treatment (PWHT) Cracking**

SAC can occur during the reheating of γ'- precipitate strengthening alloys. (Çam & Koçak, 1998; Henderson et al., 2004) If a large thermal stress occurs simultaneously, cracks can be formed. The remelting of preceding layers in AM is similar to this situation, which means that SAC can be a potential cause of cracking in AM. If post-weld heat treatment (PWHT) is applied within the aging range of the alloy, two competing actions can occur. The participation of the γ' phase leads to a slow relaxation of the residual stress. The stress release can increase the strength but reduce the ductility. However, an additional stress is induced when the volume of incoherent γ' precipitates is reduced in the solid solution. The superposition of the induced stress and remaining residual stress can result in an excess of strength limitation of the material, which can cause the crack to open. Henderson et al. (2004) showed that cracks could preferably start at grain boundaries with carbides acting as initial locations. The typical morphology of SAC is shown in Figure 2.23.

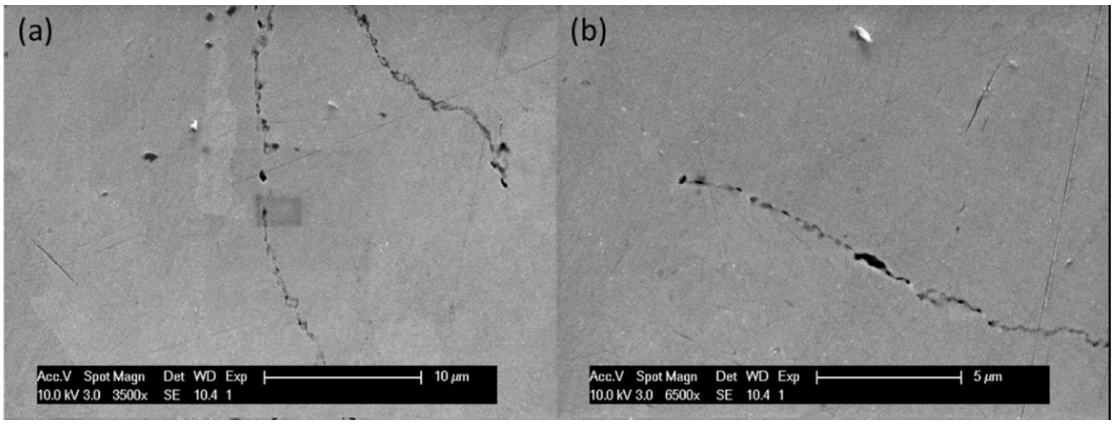

Figure 2.23 Morphology of strain age cracks at grain boundaries in post-weld heat treatment CM247LC (a) 960 °C, 2 h and (b) 960 °C, 2 h under SE. (Boswell et al., 2019)

- **Ductility-dip cracking (DDC)**

DDC has a vague definition in the literature, and is typically classified as 'reheat cracking' or 'hot cracking' with SAC together. Notably, DDC occurs at temperatures below the effective solidus temperature during solidification and causes a reduction in ductility. (Kim et al., 2011) In the intermediate temperature range (0.4–0.7 T_m), the grain boundary sliding induces stress concentration at the grain boundary, thereby resulting in the formation of voids and separation of grain boundaries. (Lippold et al., 2013) According to the research of Collins (2003: 2004) and Lippold et al. (2008), the stress is more concentrated at triple point boundary intersections, which increases the stress intensity at these locations. Thus, DDC is easier to initiate at triple point boundary intersections, like shown in Figure 2.24 and Figure 2.25 Type 1. The formation of cracks also highly depends on the grain boundary morphology, as a straighter grain boundary can induce a larger crack. The appearance of precipitates and the second phase can effectively restrict the grain boundary movement and, therefore, reduce the crack length. The high grain boundary angle can increase crack susceptibility.

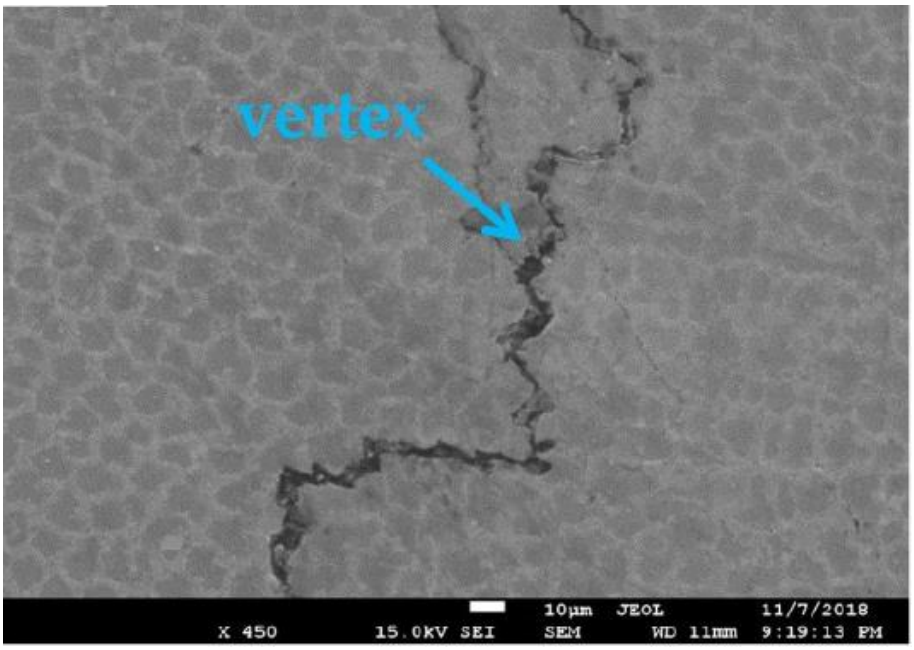

Figure 2.24 Morphology of a ductility-dip crack starting from the vertex of grains in laser forming repaired K417G Ni-based superalloy. (Liu et al., 2019)

The research of Young et al. (2008) provides a different explanation of the DDC mechanism. This suggests that the mechanism is similar to that of SAC and is caused by the precipitation of partially coherent carbides at the grain boundaries, which is shown as Type 2 in Figure 2.25. Carbides therefore impose a stress in the surrounding grains and cause voids at the grain boundaries, which can be the initiation point of cracks.

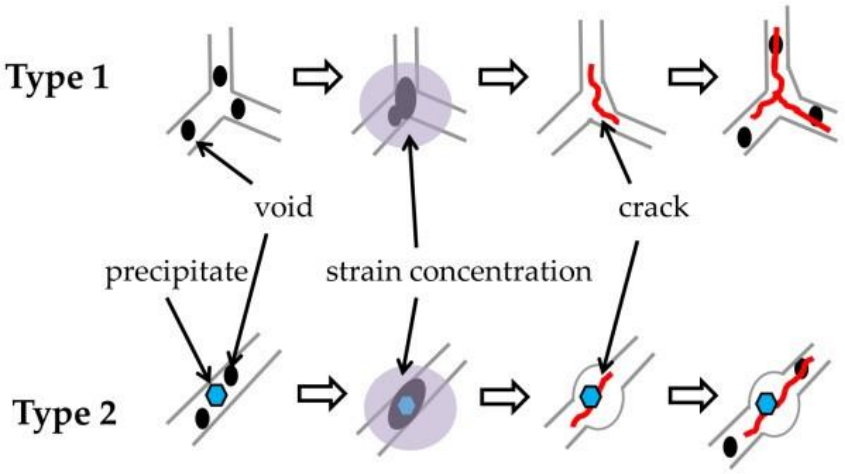

Figure 2.25 Schematic diagram of the formation mechanism of ductility dip cracking. Type 1 crack initiates at the vertex of three grains while type 2 crack initiates at the grain boundary precipitates. (Liu et al., 2019)

2.2.2.4 Porosity

Sames et al. (2014). showed the typical type of pores could be introduced inside Ni superalloy samples, as shown in Figure 2.26.

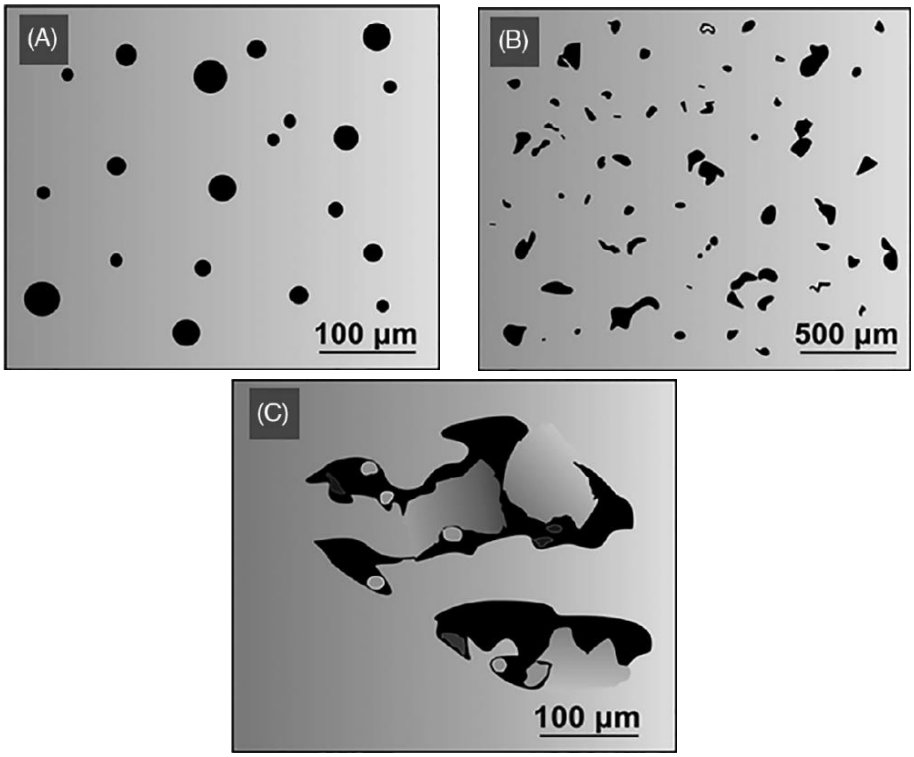

Figure 2.26 Schematic diagram of characteristic pores in selected laser melted parts: (a) entrapped-gas porosity, (b) melting-induced porosity, and (c) lack of fusion. (Sola & Nouri, 2019)

- **Gas-induced pores (Powder manufacture)**

The occurrence of regular spherical pores can be the result of entrapped gas in the powder particle. Gas was trapped in powder particles during powder manufacture. When powders containing internal pores are melted, gas will be released. However, fast solidification can lock gas inside to form pores. (Sames et al., 2016)

Another possible reason is the reaction between moisture and Al in the powder. Hydrogen gas can be formed by the following equation:

$$3H_2O + Al = Al_2O_3 + H_2 \qquad \textbf{Eq 2.11}$$

The reaction takes place at the interface of the solid and liquid during melting. Thus, hydrogen can be enriched in the molten alloy. Properly drying the powder before building can significantly prevent this problem. (Atwood et al., 2000)

- **Process-induced pores (AM)**

Some studies have reported that elongated and non-spherical pores can also be observed as defects in AM. One possible reason is the insufficient energy density, i.e., either insufficient energy input or improper hatch space and layer thickness. Insufficient melting can cause caves and voids around the melting pool. (Sames et al., 2016)

Another possible reason is that too much energy input induces over-fusion, which can cause the evaporation of low melting point elements. This type of porosity was defined as a keyholing behaviour by King et al. (2014). The excess energy input causes a significant melting pool depth in a keyhole mode compared with the normal conduction mode. Therefore, pores can be contained near the bottom of the melting pool owing to the formation of the vapour void after evaporation. During rapid solidification, surface tension forces acted on the surface of voids as shear forces. Thus, the surface of the keyholing porosity usually has wavy features, as shown in Figure 2.28.

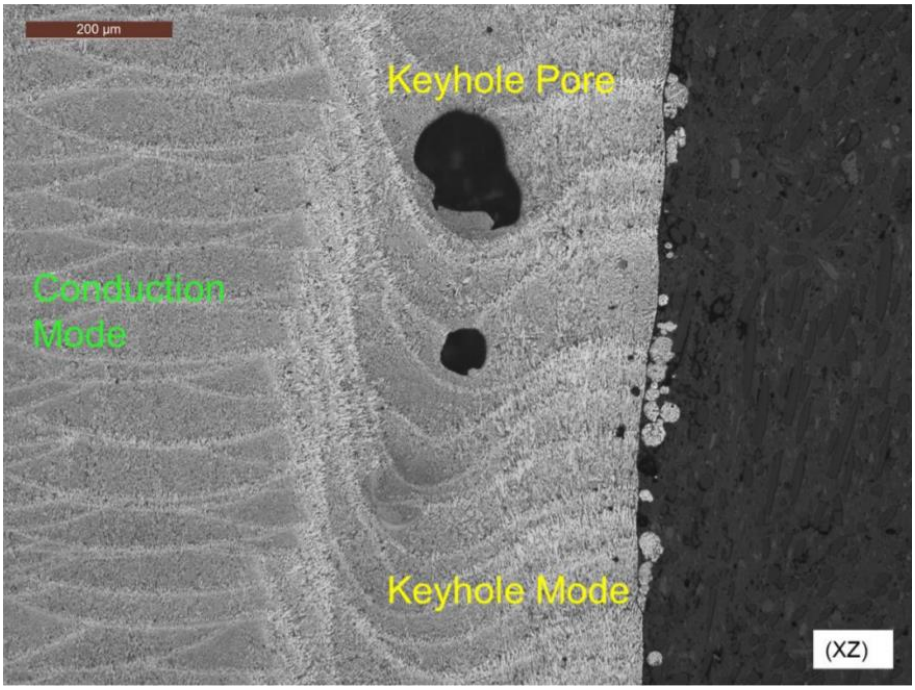

Figure 2.27 Laser powder bed fusion sample showing both the conduction and keyhole mode melting pools with keyhole porosities. (McFalls et al., 2018)

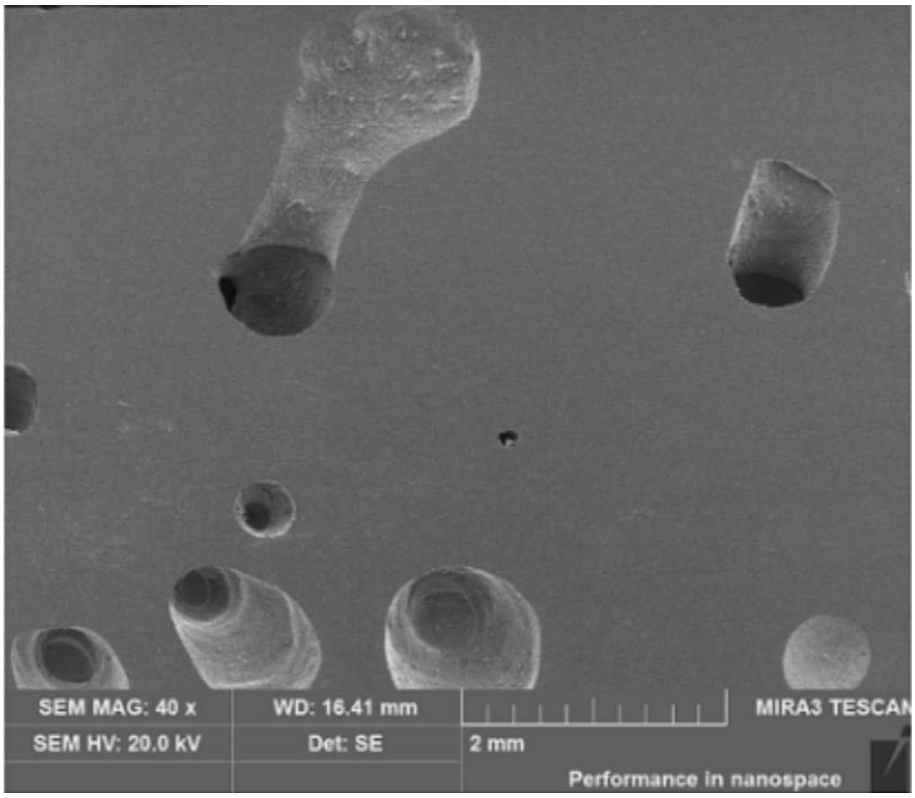

Figure 2.28 Morphology of the keyhole pores in laser arc melting 42CrMo steel. (Zhang et al., 2017)

2.3 Processing parameter map

When laser beam spots on the surface of materials, both beam characteristics and material properties are important variables that can have significant effects on product performance. Ion et al. (1992) defined two dimensionless groups to describe the processing parameters of a laser scanning system:

Dimensionless bean power:

$$q^* = Aq/[r_B\lambda(T_m - T_0)] \qquad \textbf{Eq 2.12}$$

where A is the surface absorptivity, q is the power of the laser beam, r_B is the beam radius, λ is the thermal conductivity, and T_m and T_0 are the melting and initial temperatures of the powders, respectively.

For the dimensionless beam velocity:

$$v^* = vr_B/\alpha \qquad \textbf{Eq 2.13}$$

where v is the traverse rate or velocity of the laser beam, and a is the thermal diffusivity. Therefore, the combination of q^* and v^* can control the thermal properties of

processing, including the peak temperature and heating rate. Considering the characteristics of AM technology, the mechanism can be described similar to the keyhole welding process, as shown in Figure 2.29.

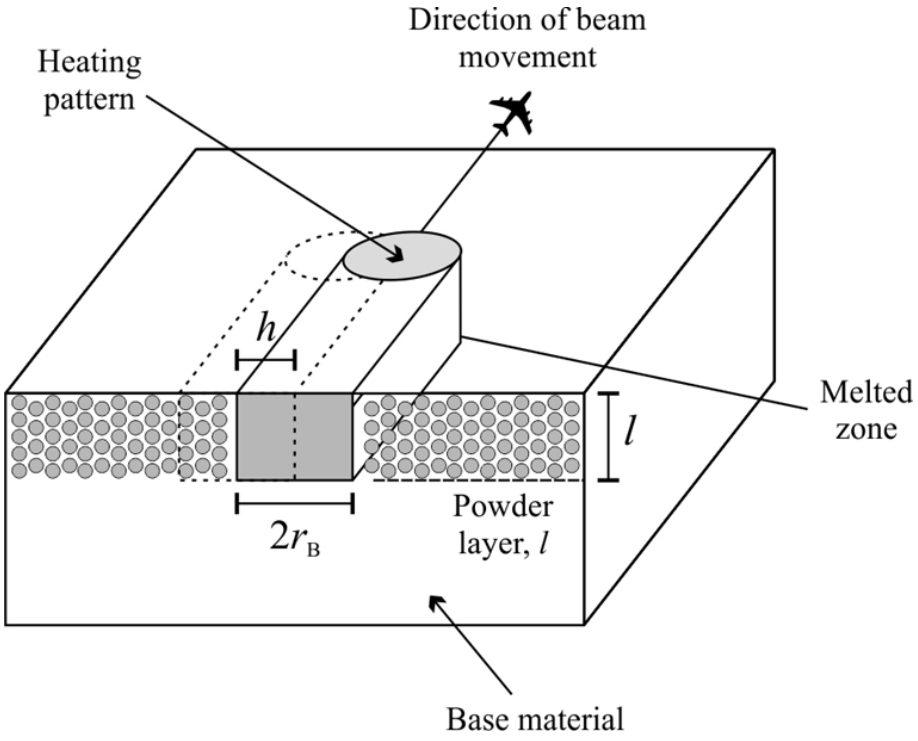

Figure 2.29 Scheme of heat flow pattern in SLM. (Thomas et al., 2016)

In this case, the laser spot area is $2r_Bl$, where l is the thickness of each powder layer and h is the hatch spacing between every spot. Therefore, the dimensionless layer thickness $l^* = 2l / r_B$. To ensure that the hatch spacing is comparable with the layer thickness, it can be represented in normalised form as follows (Thomas et al., 2016):

$$h^* = h / r_B \qquad \textbf{Eq 2.14}$$

The energy E input per unit volume to melt powder at a certain temperature can be represented as $q/2vlr_B$ when the energy per unit length is $q/2v$. As described by Thomas et al. (2016), with the combination of Eq 2.12 and Eq 2.13, a normalised equation of E^* can be defined thus:

$$E^* = q^*/v^*l^* = [Aq/(2vlr_B)][1/\rho C_p(T_m - T_0)] \qquad \textbf{Eq 2.15}$$

By using the two groups of normalised parameters, namely, the volumetric energy density (E^*) and hatch spacing (h^*), a laser process parameter map can be produced, as shown in Figure 2.30.

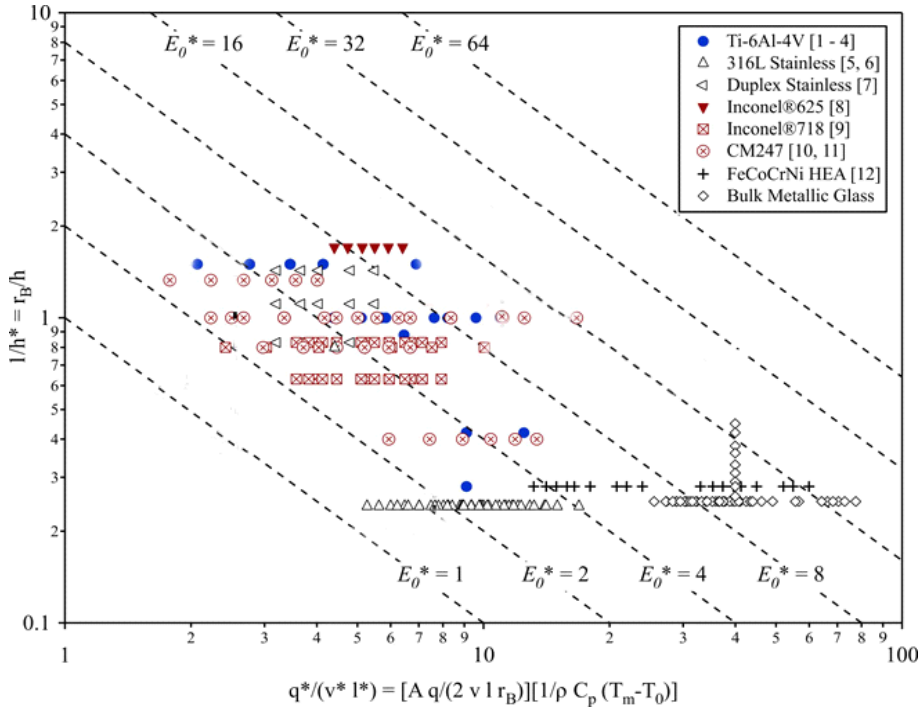

Figure 2.30 Normalised process maps for AM. Data from the literature are labelled in the legend. (Thomas et al., 2016)

Different types of powders with different product parameters can be displayed in the same figure, which has the benefit of converting all parameters into a normalised form. Here, E_0 is defined as the product of E^* and $1/h^*$, which can reflect the energy density and efficiency. A higher E_0 value refers to a higher energy input and/or longer duration. (Thomas et al., 2016)

2.3.1 Scan strategy

Scan strategy, which is also known as scan pattern, is an important feature in SLM systems. Several studies have shown that scan strategy can have a large influence on critical features, such as heat flow, microstructure and defect formation, as well as surface roughness and finishing. (Su & Yang, 2012; Calignano, 2014; Arısoy et al., 2017)

During the SLM process workflow, the workpiece model is digitalised and sliced into a certain number of layers. Each layer can also be divided into a stack of regions with specifically defined scanning directions. Generally, scanning directions can be unidirectional or bidirectional.

The scan strategy is important because it can strongly affect heat distribution and transfer. It also provides the flexibility to design different regions with different parameters. Therefore, the final properties and qualities are highly dependent on the scan strategy. Currently, many studies have demonstrated that four types of scan strategies are applied in SLM processing.

2.3.1.1 Stripe strategy

The stripe strategy is the most common scan strategy in SLM. It is defined by the length of the stripe and the hatch space between stripes. The gap or overlap between stripes in neighbouring blocks is also an important feature in the stripe pattern, as shown in Figure 2.31.

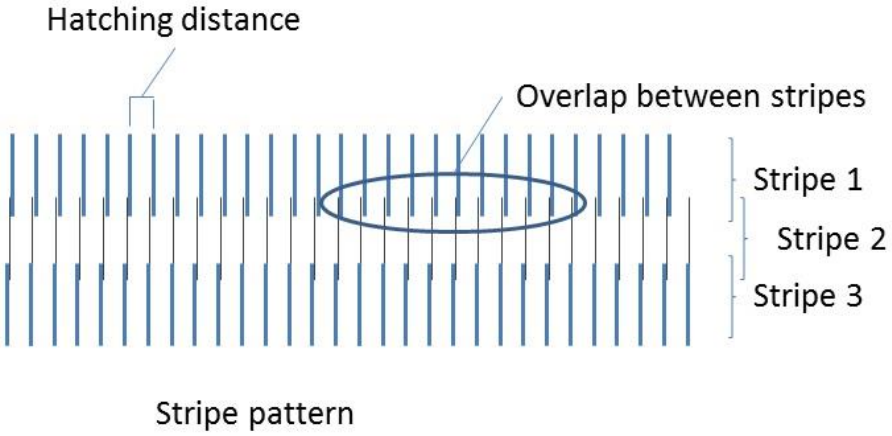

Figure 2.31 Schematic representation of the stripe scan strategy. (Inside Metal Additive Manufacturing, 2015)

2.3.1.2 Meander pattern

The meander strategy is developed from the stripe strategy. A stripe strategy does not rotate the scan direction through a build. A meander pattern will rotate by a certain angle after the scan on the previous layer is completed. Normally, a 67° rotation for each layer is performed to minimise the potential residual stress, like the present in Figure 2.32.

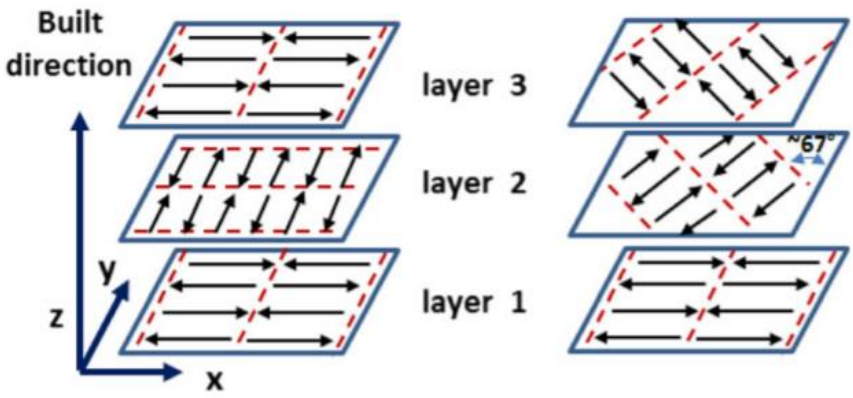

Figure 2.32 Schematic representation of the meander scan strategy. (Arısoy et al., 2017)

2.3.1.3 Chessboard pattern

The chessboard strategy is so-named because the divided square regions are similar to the shape of the chessboard, as the present in Figure 2.33. As with a chessboard, the squares can be divided into two groups: a black square and a white square. White squares are scanned first, followed by the black squares. Within every square, it can be considered as a small stripe pattern. The chessboard scan strategy can be defined by the size of an individual square and the overlap between neighbouring squares.

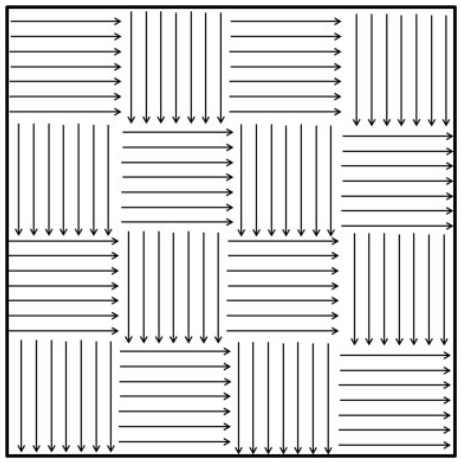

Figure 2.33 Schematic representation of the chessboard scan strategy. (Sing et al., 2016)

2.3.1.4 Island pattern

The island scan strategy is a modified chessboard strategy, as detailed in Figure 2.34. Instead of dividing all the squares into two groups, every square was treated as an individual part. Therefore, each square is scanned with a random order across the layer.

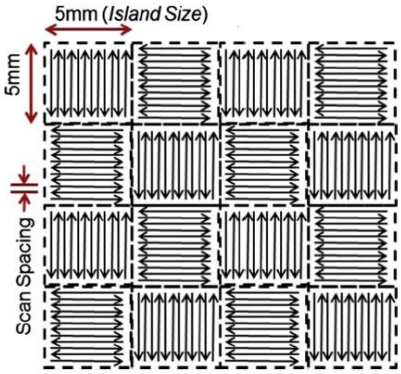

Figure 2.34 Schematic representation of the island scan strategy. (Carter et al., 2014)

2.3.1.5 Contour scan

A separate hatch line outside the edge of the workpiece can be applied after or before the scan of the main body for every layer, as can be seen from Figure 2.35. This is referred to as the contour scan, which can be applied to all scan strategy. Generally, it can provide a better surface finishing.

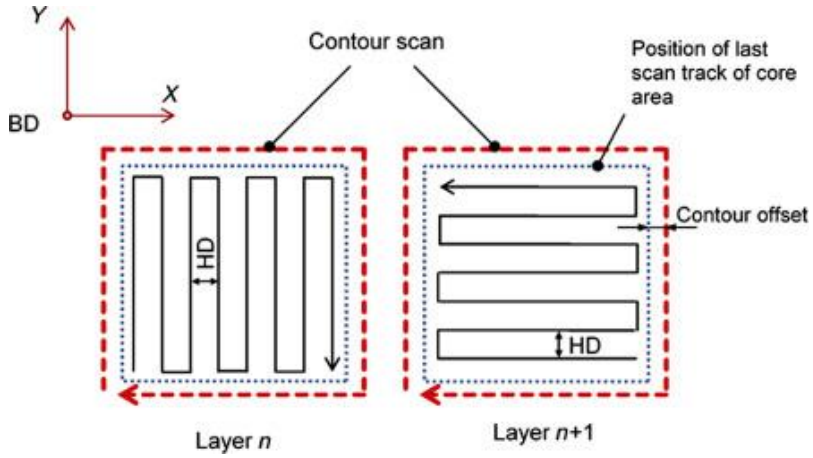

Figure 2.35 Schematic representation of the Contour scan. (Chen et al., 2019)

2.4 Heat treatment

Heat treatment is a common post-processing technique in metallurgy to further refine the microstructure of an alloy and modify its mechanical properties. For Ni superalloys, heat treatment generally involves solution treatment and ageing treatment.

Solution treatment is also known as annealing in metallurgy. The metal was heated to a specific temperature (above recrystallisation temperature), held for a short duration, and

then cooled in air or with a furnace with a low cooling rate. The microstructure can be refined by annealing. The residual stress generated during AM can also be relieved after annealing. (Callister, 1997)

In the generic term, ageing treatment followed the solution treatment as a second-stage heat treatment step. The two-stage heat treatment is also known as precipitation hardening. Fine particles can be formed in the precipitated phase owing to the variation in solid solubility with temperature. Yield strength can be improved after ageing treatment. (Sims et al., 1987)

In a simple Ni system, the desired γ/γ' structure can be achieved by heat treatment. Figure 2.36 shows an Al–Ni binary diagram. The alloy can be heated above the γ' solvus temperature such that the γ' phase can be completely dissolved into a solid solution. A certain duration can allow the microstructure to be homogenised and stress to be relieved. With air cooling afterwards, both coarse primary γ' and fine secondary γ' can be precipitated. In the subsequent ageing treatment, the alloy is heated to a temperature below the γ' solvus temperature. Therefore, the γ' particles can continue to grow by diffusion, and carbide can be precipitated at the grain boundaries. (Chen et al., 2011)

In a Ni superalloy system, the involvement of multiple elements can be too complicated to be presented in a one-phase diagram. Therefore, the result from a heat treatment procedure may not exactly follow the outcome from the phase diagram.

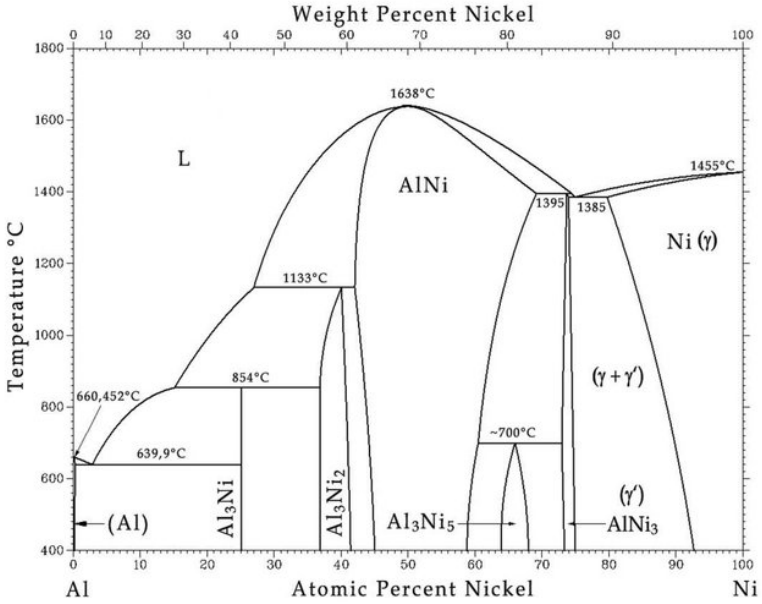

Figure 2.36 Binary phase diagram of the Ni–Al system. (ASM, 1992)

2.5 Summarising remarks

Owing to their beneficial properties, Ni-based superalloys are extremely attractive in high-temperature aerospace applications in comparison conventional alloys. IN713C with a high γ′ ($Ni_3(Al,Ti)$) precipitate content renders excellent strength and creep resistance; however, the high content of γ′ precipitate content also leads to high crack susceptibility and difficult processing. On the other hand, properties of LR8, which is a newly designed alloy, have not been investigated considerably. With the addition of Co and W, the low content of γ′ precipitate element. LR8 is expected to exhibit better high-temperature performance as well as better weldability.

The existing literature reveal that AM is complex as multiple factors can affect microstructure and material behaviours. (Carter, 2013; Freeman, 2018; Boig, 2019) The processing map is a beneficial tool for effectively evaluating and developing suitable processing parameter for a material. However, it is difficult to analyse the change factor of individual processing parameters. Previous studies reveal similarities between a welding process and a laser AM process. (Lippold et al., 2013; Carter et al., 2012; Freeman, 2018) Therefore, the defect mechanism in AM can be expected to be mainly solidification cracks and SAC. Therefore, processing parameters also contribute to the tendency for defect formation. Based on previously reported results (Carter, 2013; Galizoni et al., 2019), post-processing can clearly refine the as-fabricated microstructure; hence, the mechanical properties can be improved further.

In this study, effects of individual processing parameters and thermal profiles are investigated by a parametric study and DoE. The main defect mechanism with the change in processing parameters can be fully understood. Defect classification is possible by newly developed computer science and technology, such as machine learning. The mechanical test results will provide better understanding of SLM Ni-based superalloys as well as the effect of post-processing routes.

Chapter 3 Experimental Methods

3.1 Powder analysis

3.1.1 Powder size distribution

This analysis is aimed at measuring the particle size distribution of LR8 powders, and the results can help to understand if the powder size affects the formation and size of cracks. The test was carried out with the Mastersizer 3000, which used laser diffraction to measure the size of particles with high accuracy. The dry separation method was used for metallic powders to feed powders into the instrument at a certain feeding rate. The compressed air then passed through and blew the powder samples through the object area. A laser beam interacts with the passing samples. Six detectors with different angles were placed on the other side. The powder size was then measured by the degree of diffraction of the laser beam when passing through the samples. Large particles cause a small amount of diffraction because light glances off their surface, while small particles cause a large diffraction angle. Therefore, the powder distribution can be calculated using the diffraction angle and pre-set powder model. The average value of 10 measurements was taken to reduce the error.

3.1.2 Internal defect analysis

To observe the internal defect in powder particles, a special sample preparation process is required. The powder samples were mounted in an EpoFix resin; 8 g of the powder sample was mixed with 150 g of EpoFix resin and continuously stirred until the powder was uniformly mixed with the resin. The mixed resin was evenly divided into six portions and poured into six moulds. All the samples were left in a Struers CitoVac vacuum chamber for 5 min. Bubbles in the resin escaped and all powder particles were deposited at the bottom of the moulds. The samples were then incubated at room temperature for 24 h to allow the resin to solidify.

3.1.3 Powder density analysis

This analysis is aimed at analysing the density of powders. The experiment was carried out using the Micromeritics AccuPyc II 1340. The machine used the gas displacement method to measure the volume and density with high accuracy. A certain weight of the powders was put in a small cap and placed in a sealed instrument compartment. With helium gas as the displacement medium, it was passed through the chamber and filled the sample chamber with pressure to reach the equilibrium state. Thereafter, the gas flowed into the second chamber to allow measurement of the powder solid phase volume. Helium gas can rapidly fill gaps and pores around the powders, and only the solid-phase powders can displace gas. Therefore, the actual weight divided by this volume value can provide an accurate gas displacement density. To reduce the error, an average value of 20 measurements was taken.

3.1.4 Powder thermal analysis

3.1.4.1 Differential scanning calorimetry (DSC) Test

Here, the differential scanning calorimetry (DSC) test was used to understand the critical temperature of phase transfer in materials, as well as the specific thermal conductivity of materials. The temperature gradient was set to 10 k/min. The temperature range for the DSC test was between room temperature and 1400 °C.

3.1.4.2 Thermal conductivity test

The thermal conductivity test was carried out at Merrow Scientific Ltd. The C-Therm TCi analyser was used to measure the thermal conductivity at room temperature. Five measurements were taken to reduce the error.

3.2 Selected laser melting (SLM) technology

3.2.1 Renishaw AM 125

The Renishaw AM 125 machine at the Mercury Centre of the University of Sheffield is an advanced AM system that produces a highly dense metal workpiece. The modulated Ytterbium fibre laser system can provide a maximum 200 W output and 70 mm beam diameter on the powder surface. The laser system in the Renishaw AM 125 is a pulsed laser system that can provide a scan speed of up to 2000 mm/s. The layer thickness can be adjusted between 20 and 100 μm.

The build chamber contains an argon atmosphere to prevent oxidation during building. Argon is pumped into the build chamber and continues to flow at a certain rate across the platform during the build. It can not only avoid oxidation but can also blow away the oxidised or partially sintered particles. Before the build processing, the chamber was vacuumed to remove air from the chamber. Once the pressure in the chamber reached 945 mBar, Ar gas flows into the chamber and reduces the oxygen level. Oxygen sensors are located on both the top and bottom of the chamber to provide accurate readings. The build automatically starts when the oxygen level drops below 1000 ppm (parts per million). Argon flow is kept at a certain rate to maintain the chamber atmosphere during the building process.

3.2.2 Key parameters in Renishaw AM 125

These key parameters can have a strong effect on the microstructure and phase formation, thereby affecting the mechanical properties. The influence of these key parameters will be investigated in this project:

- Laser power (q_R): The value of power input to melt the powder with its unit in W. The maximum power of the Renishaw AM 125 was 190 W to prevent the machine from running at full load.
- Exposure time (t): The dwell time of each laser spot.
- Spot distance (d): The distance between every spot. The scan velocity can be

calculated by the exposure time and spot distance:

- Layer thickness (l_R): The thickness of each powder layer is delivered on the build platform. The layer thickness is controlled by the descent distance of the build platform after the melting on every layer is finished. Normally, the layer thickness is between 20 and 40 μm.
- Scan strategy: As discussed in Section 4.6, a scan strategy is selected for the build. The scan track is controlled by the movement of the mirror pivoting system in front of the laser generator.
- Hatch space (h_R): The distance between neighbouring scan tracks. It can have a significant influence on the grain size and microstructure.

3.2.3 Aconity3D Mini

The Aconity3D mini in the Mercury Centre at the University of Sheffield is an advanced laboratory AM system. The system has a high expansibility, which allows the attachment of various components, such as a pyrometer and camera. Unlike Renishaw 125, the Aconity3D mini has a continuous laser system, which can create a narrow laser track, like detailed in Figure 3.1. The laser system is a single-mode laser that provides a maximum power output of 200 W with a spot size of up to 80 μm. The maximum usable powder size in the Aconity3D mini is 100 μm to prevent the blockage of filter overflow.

The Aconity3D mini also requires shield gas to prevent oxidation. Argon was chosen to maintain the same chamber environment as Renishaw 125, and it can be substituted for Helium. Once the oxygen level dropped below 1000 ppm, the chamber pressure was set to 50 mbar. The machine is equipped with a pyrometer to monitor and record the thermal profile of the build.

These key parameters in Aconity3D mini are slightly different from those in Renishaw 125:

- Laser power (q_A): The value of the power input to melt the powder with its unit in W. The usable power of the Aconity3D mini ranges between 70 W and 190 W.

- Scanning speed (v_A): The refers to the speed of laser scanning on the powder surface. Generally, it is slower than 3000 mm/s to prevent a massive splatter of powder.

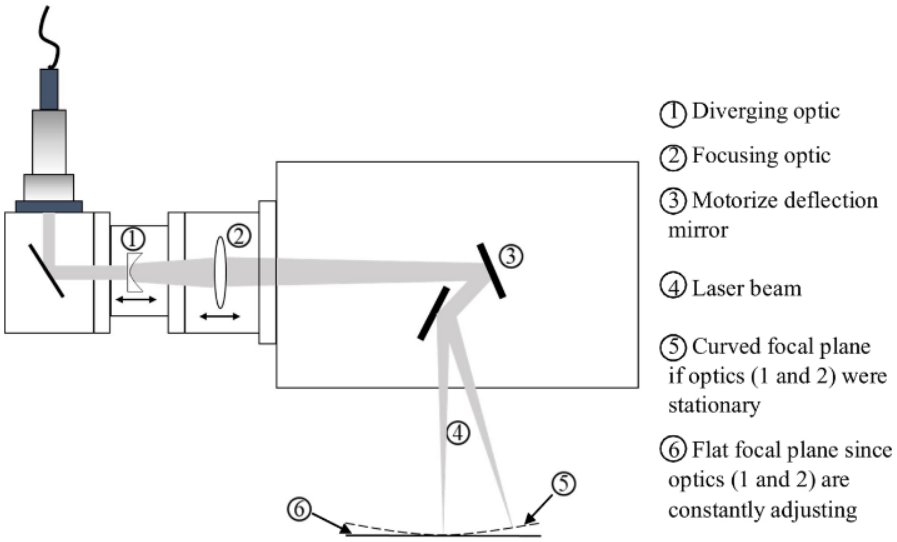

Figure 3.1 Schematic diagram of a 2D laser scanning unit in SLM system. (Uddin, 2018)

3.2.4 Design of experiment

Design of Experiment (DoE) is a powerful tool to efficiently control, collect and analyse the test data in order to evaluate the effect of parameters on the experiment objects. The necessary numbers of samples with associated value combinations can be provided using the DoE. Various DoE approaching have been developed, the simplest and intuitive way is named 2^k Factional Design. It is particularly useful for the parametric studies and early-stage experiment. The "k" represents the number of factors that is introduced in the experiment. For example, a 2^2 design will include two factors ('A' and 'B') with two level of values ('high' and 'low'). With the help of Minitab 17 software, the DoE value combinations can be established, like the shown in Figure 3.3. To reduce the effect of thermal distribution on the samples, the running order in the build is randomly distributed.

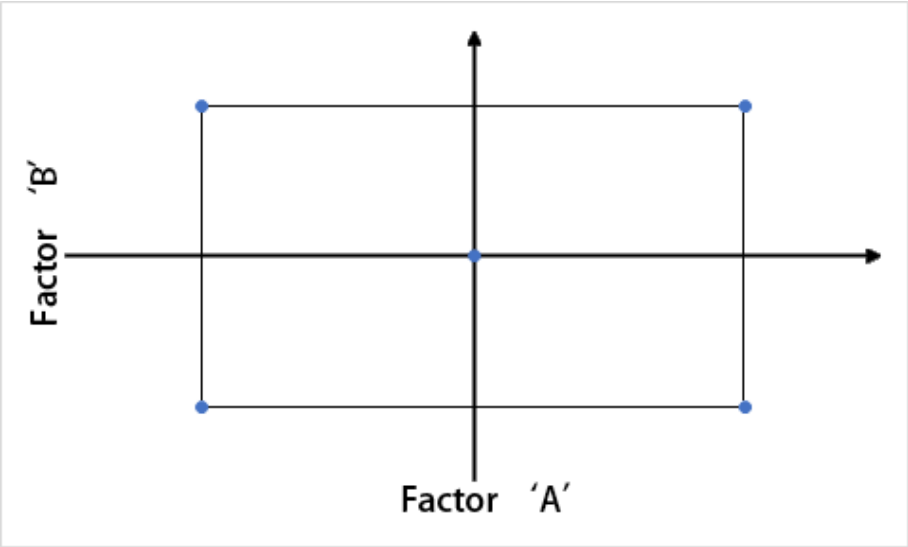

Figure 3.2 Schematic diagram show the 2^2 Factional Design.

3.3 Pyrometer

The pyrometer can record the thermal profile during laser scanning. Figure 3.3 shows the basic structure of the pyrometer. A heated object can emit infrared radiation, which can be captured and focused by the fibre optics in the lens unit. The aperture is set to block unwanted rays that are mixed with infrared rays.

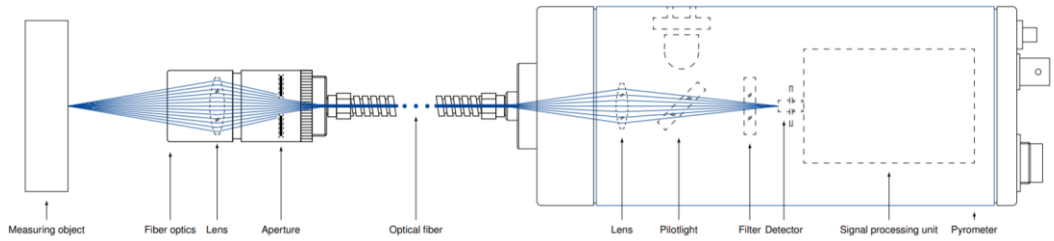

Figure 3.3 Schematic diagram of a Kleiber KG 740-LO pyrometer. (Kadlec, 2009)

The infrared radiation is then transmitted to the pyrometer unit via optical fibres. The lens behind the optical fibre collects the radiation again and guides it to the filter, which allows only the desired spectral range to enter the detector. The radiation is transformed into an electric signal at the detector. The signals are then linearised by the signal processing unit and transferred into a displayable and readable output signal to be written into a hard drive.

A Kleiber KG 740-LO 07401–12400 pyrometer was attached to the Aconity3D Mini.

It can sense radiation ranging between 1580 nm and 1800 nm. The measuring range is 500–2500 °C The output unit is in mV, which is linear, corresponding to the actual temperature, as shown in Figure 3.4. The coversion equation can be written as:

$$T\ (°C) = 500 + 0.2V \qquad \textbf{Eq 3.1}$$

where V is the voltage reading (mV) from the pyrometer. The temperature unit is in °C.

3.4 Microstructural characterisation

3.4.1 Sample preparation

To gain a better understanding of the microstructure inside the sample, each sample was required for sample preparation. All the samples were cut through to observe the cross section along the build direction. The cutting process was carried out using a Struers Secotom 50 cut-off machine. The Secotom 50 is capable of precision cutting for a variety of materials. Based on previous experimental experience and guide booklet, a Buehler IsoCut CBN HC cutting disk was used. To prevent damage to the cutting surface, as well as overloading the motor, the total output load should be within 20% to protect the motor. In this case, a cutting speed of 1500 rpm with a feed speed of 0.03 mm/s was used.

To examine the sample cross sections, all the after-cut samples were hot mounted in conductive Bakelite in a mount press machine. The mounted samples are approximately 40 mm high with a diameter of 23 mm.

The mounted samples were ground and polished to obtain a flat, scratch-free surface. The grinding and polishing sessions were carried out on a Struer Tegramin 20 machine. While, the grinding and polishing procedures are based on experimental experience and the Struer standard preparation guide booklet for Ni superalloys.

After proper grinding and polishing, the sample surface should be flat and clean without scratches. Otherwise, the polishing can be repeated until the surface is clean and scratch-free. After polishing the sample need to be cleaned with water for 10 min. All the polished samples need to be properly dried with isopropanol to prevent surface corrosion by agents or suspensions.

3.4.2 Etching

Etchants were used to reveal the microstructure of the samples. Glycerygia can be considered as the mildest etchant for Ni superalloys. It is a mixture of glycerol, hydrochloric acid (HCl), and nitric acid (HNO_3) at a ratio of 3:2:1. Glycerygia can attack the martensite and sigma phases; therefore, it will outline the ferrite and austenite (γ/γ' phase) and reveal the structure of carbides and grain boundaries. As Ni superalloys generally have great corrosion resistance, the best way to apply an etchant is by swabbing it on the surface of the superalloy with cotton soaked in the etchant. Swabbing can be performed between 1 and 2 min, depending on the corrosion resistance of the sample. After etching, the sample is placed in water to halt the reaction. The etchant can only be used when it is fresh, and it needs to be discarded when the colour turns orange.

3.5 Optical microscopy

Optical microscopy is widely used in various areas for scientific analysis. In this project, microstructural analysis was carried out using an Olympus optical microscope with CLEMEX software. The combination of optical scope and digital zoom can provide a magnification ranging from 50× to 500×.

3.6 Scanning electron microscopy (SEM)

Scanning electron microscopy (SEM) is a type of microstructural analysis procedure that produces high resolution. Focused electron beam scans the surface of the sample. Atoms in the sample interact with the electron beam and generate various signals that contain information on sample morphology. The SEM session was carried out with a Nikon Inspect F in secondary electron mode. For the powder and built samples, voltages of 20 kV and 5 kV, respectively, were used.

3.7 Defect classification

To classify the defects, image analysis was used to obtain the key particle measurements. Images from the optical microscope were analysed using the ImageJ software. The image analysis process is as follows:

1. The scale set based on the scale bar from the microscope image.
2. Images are converted into an 8-bit image format.
3. The threshold value is adjusted to separate the defects from solid parts.
4. Various measurements are taken using the 'Particle Measurement' function.

The key parameters to measure are described below: (ImageJ, 2020)

- Area: the project area of object (μm^2).
- Major and minor axis lengths: the distance of longest line that can be drawn through object (major axis) and the distance of the longest line perpendicular to the major axis (minor axis).
- Circularity: a dimensionless measurement of how close the shape of an object is to a perfect circle; "1" is a mathematically perfect circle, while "0" indicates that the shape is more irregular.
- Aspect ratio: a measurement of the ratio of the object height and width. A high value indicates a more elongated shape.
- Feret diameter: this refers to the longest distance of two parallel planes on the boundary of the object.

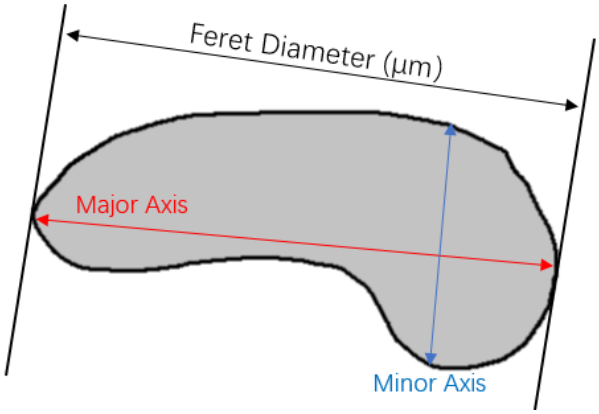

Figure 3.4 Schematic of a particle showing the key measurements used in the defect classification.

Defect classification is carried out with a script using the R language. The script was modified from that provided by Dr. Meurig Thomas. (2018) Based on the key parameters, the machine learning function can automatically distinguish the types of defects. To achieve this, a database is collected using the analysis results from CM247, IN713, and LR8 experiments.

3.8 The melting pool simulation

The melting pool simulation was developed by Felicity Freeman (2019) based on the Eagar equation for a continuous Gaussian laser beam. The code is modified to fit the thermal properties of IN713C and the input parameters, and is run in MATLAB. A small step size is set to obtain finer results. The output of the simulation is the dimension of the melting pool and the corresponding cooling rate and thermal gradient. Figure 3.5 shows the melting pool geometry and thermal profile.

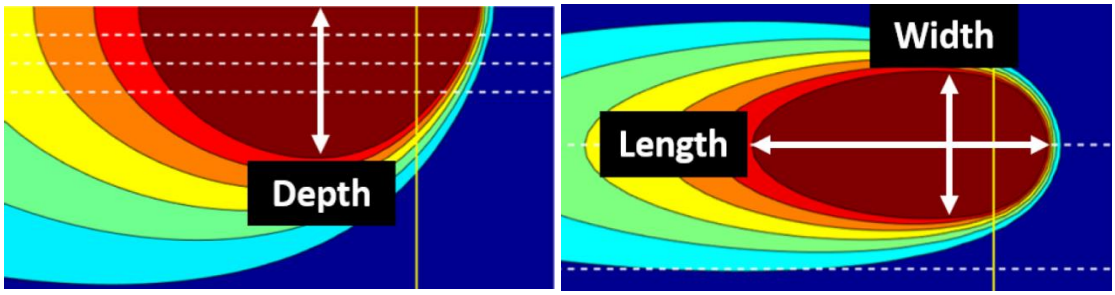

Figure 3.5 Top and Side view of the melting pool from Freeman's melting pool simulation. Colours show different temperature grades. (Freeman, 2018)

3.9 X-ray diffraction (XRD)

X-ray diffraction (XRD) is a non-destructive analytical technique used to identify the phase of a crystalline material, as well as the unit cell dimensions. A Bruker D2 Phaser was used to measure the XRD pattern for all the samples.

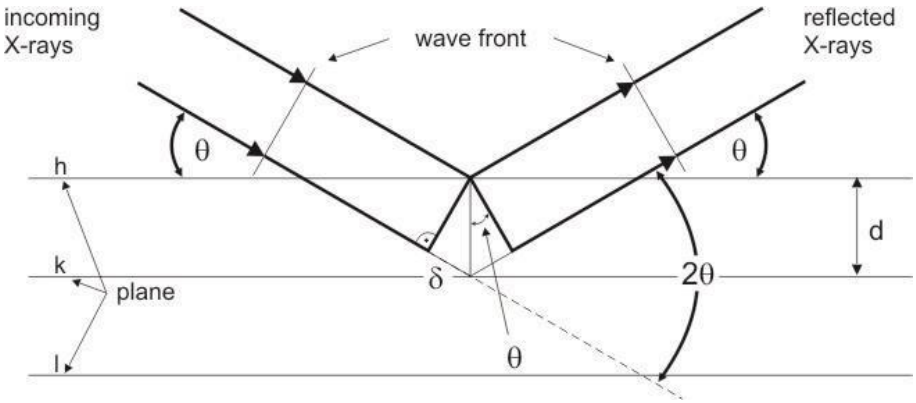

Figure 3.6 Schematic diagram of the X-ray diffraction (XRD) mechanism. (Kumar, 2016)

X-ray diffractometers generally contain three main components: X-ray beam, sample holder, and X-ray detector. In the cathode ray tube, a filament is heated to produce electrons, which are then accelerated and bombard the target material; the most common target material is Cu. Once electrons have sufficient energy to remove the electrons in the inner shell, characteristic X-ray spectra $K_{\alpha 1}$ and $K_{\alpha 2}$ can be generated. Thereafter, the specific wavelength is filtered by foils to produce monochromatic radiation. X-rays will then be collimated by the target and directed toward the sample surface. In most cases, a Cu target is used for single-crystal diffraction with CuK_{α} radiation = 1.5418 Å. The interaction of the incident X-ray spectra with the sample can produce constructive interference with an intensity peak if the condition satisfies Bragg's law ($n\lambda = 2d\sin\theta$). (Bish & Post, 1989) The detector can therefore capture and process the X-ray signal to a figure, as shown in Figure 3.6.

3.10 Energy dispersive X-ray spectroscopy (EDS)

Energy dispersive X-ray spectroscopy (EDS or EDX) is a widely used analysis technique for the composition characterisation of elements with atomic number $n > 3$. The EDS system was integrated into SEM microscopy. The EDS system has a sensitive EDS detector fit into the chamber of the SEM to collect data. The most commonly used detector is made of Si(Li) crystals; thus, the detector can operate at low voltages to achieve high sensitivity. A high-energy beam spots on to the surface of the sample. In

the normal state, the atom contains unexcited electrons that have discrete energy levels. Once the beam spot falls on it, the electron from the inner shell can be excited and escape from the shell such that an electron–hole pair can be created. An electron from the outer and higher energy shell will then fill the hole. The energy difference between two different energy level shells, therefore, will be emitted in the form of X-rays. The intensity of the X-ray emitted can be detected by the detector. As the emitted energy levels vary for different atom structures, the composition of different elements can be measured. (Goldstein et al., 2003)

3.11 Electron backscatter diffraction (EBSD)

Electron backscatter diffraction (EBSD) is a commonly used microanalytical technique for SEM to obtain information about grain morphology, grain boundary structure, and the orientation of grains and textures. With the help of processing software, more features can be analysed. To obtain accurate results, the sample needs to have a flat, fine-polished surface.

The EBSD technique is based on the Kikuchi band electron diffraction phenomenon of the focused electron beam. When the electron beam strikes the specimen surface, electrons are diffracted on crystallographic planes and leave the sample surface as backscattered electrons. Therefore, the backscattered signal is modulated by Bragg's law and the specimen-to-phosphor screen distance to generate a Kikuchi band that is specific for the local crystal structure and its orientation. The electrons hit the fluorescent screen of the fast EBSD to produce light. To obtain a high contrast of diffraction patterns, the yield of diffracted electrons can be maximised by the high tilt of the sample. Therefore, the sample in the SEM chamber is tilted at 70° towards the EBSD detector for most of the SEM or FIB-SEM process. The light can be captured by a charge-coupled device (CCD) or silicon intensified target (SIT) camera behind the screen and converted into an image using a specific software. (Oxford Instruments, 2019)

3.12 Mechanical tests

3.12.1 Tensile test

Samples with desired shape were built using the Aconity3D mini system, as depicted in Figure 3.7. Tensile tests were carried out using a Zwick Z100 tensile test machine by Special Testing Ltd, Sheffield, UK. All tensile tests were performed in accordance with the ASTM standard (ASTM-E8/E8M-16a). The samples were machined to a standard M8 threaded cylindrical dog-bone piece.

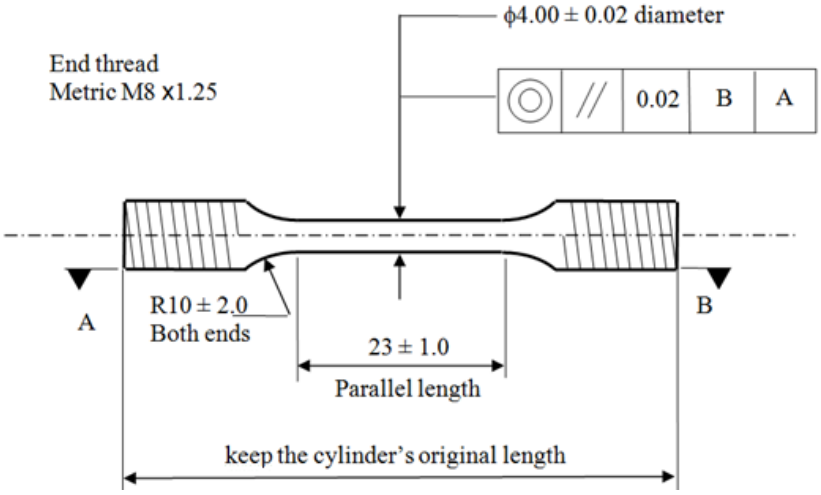

Figure 3.7 Geometry and dimension of an ASTM M8 tensile test specimen. (ASTM, 2016)

All the samples were set at a strain rate of $10^{-4}s^{-1}$ at room temperature, following section 7.6.3.3 of the ASTM standard. Furthermore, 0.2% of the proof stress and ultimate tensile stress (UTS) were recorded. The elongation rate was also calculated.

3.12.2 Hardness test

Hardness tests were carried out using a Durascan 70 hardness indentation machine at the University of Sheffield micropreparation laboratory. Samples were mounted in bakelite and well-polished. The sample also needs to be fixed on a test platform with plenty of mounting resin surrounding the sample to obtain accurate results. All the samples were tested via Vickers hardness test method. The diamond indenter is in the shape of the right pyramid with an angle of 136°, as shown in Figure 3.8.

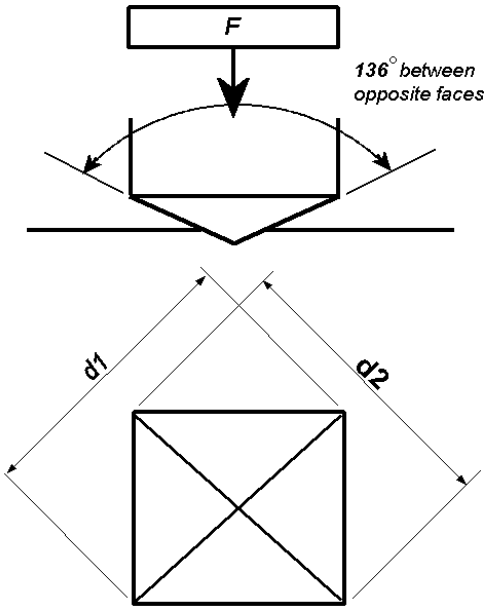

Figure 3.8 Schematic of Vickers hardness test. The d1 and d2 are the diagonal length of the indentation mark. (Darmawan et al., 2012)

The dwell time of the load was 15 s, while the load was set at 0.5 kgf force for all tests. An indentation mark can be left on the surface of the material after load removal. The hardness is then calculated using the following equation:

$$\mathrm{HV} = \frac{2F\sin\frac{136°}{2}}{d^2} \approx 1.854\frac{F}{d^2} \qquad \textbf{Eq 3.2}$$

where F is the load of the indenter, and d is the average of two diagonals $d1$ and $d2$. (Darmawan et al., 2012)

3.13 Heat treatment

Performing heat treatment on the AM-fabricated samples can modify the γ' microstructure and, therefore, the mechanical properties. Heat treatment was carried out at the Quarrel lab at the University of Sheffield. All samples were processed in a furnace under vacuum. The sample was air-cooled after heat treatment. The temperature was monitored by an in-situ thermocouple with an error of ±1 K. The heat rate was set at 10 k/min according to previous literature.

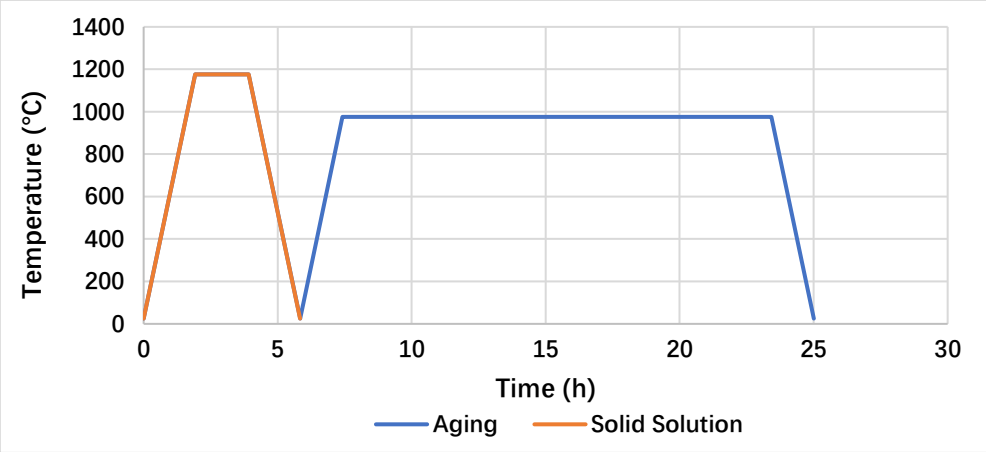

Figure 3.9 Example of the heat treatment route for cast IN713C. Reproduced from the IN713C data sheet. (Pratt & Whitney's Aircraft, 1965).

Chapter 4 Process Development of IN713C: The Influence on Microstructure and Defects

The chapter is focused on the parametric study to understand the influence of processing parameters on AM IN713C part density and defect formation. Additionally, the concept of "laser travel time" is introduced to deeply understand the relationship between local heat energy and defect formation. Mechanical properties of as-built IN713C components are compared with conventional cast samples to understand the capability of AM technique to become an alternative technique for aerospace industry.

4.1 Powder analysis

4.1.1 Powder size analysis

Figure 4.1 shows that the IN713C provided has a relatively good size distribution. The particle size distribution ranges between 9 μm and 90 μm. The result suggests that although the maximum particle size is approximately 80 μm, which is higher than the suggested powder size (20–60 μm), the powder size distribution generally falls well within the limit level. The results from 5 different batches of powder show a high consistency. The measurements and shape of plot suggest the powder size is close to a normal distribution. The following experiments show a successful deployment and ease of deployment of the powder during AM process indicated the powder quality is acceptable.

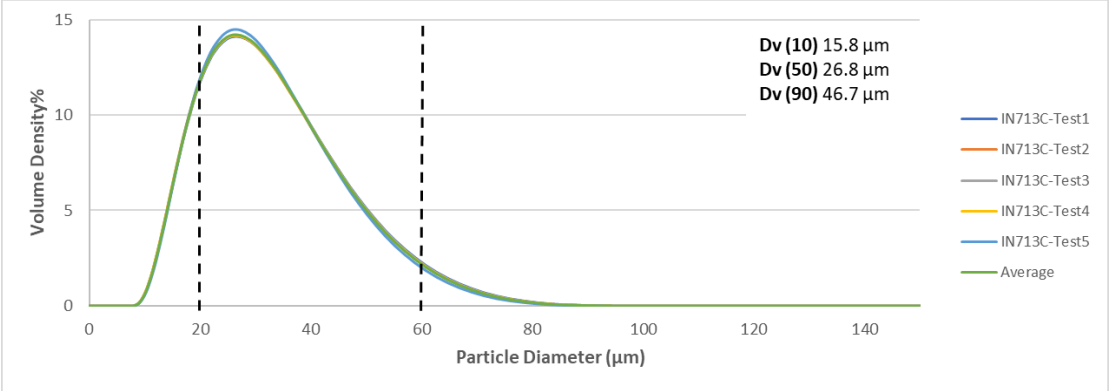

Figure 4.1 Powder size distribution of the IN713C alloy; Black dash lines indicate the ideal powder size distribution for AM. Key size parameters are shown in the figure.

4.1.2 IN713C thermal analysis

The thermal analysis graph is shown in Figure 4.2. The key temperature values obtained from the DSC curve are shown in Table 4.1. The measures and plots confirmed the powder as a typical IN713C superalloy in comparison with literature measurements (Binczyk & Śleziona, 2009; INCO, 1968). The solidification and phase transformation value will be used in melting pool simulation.

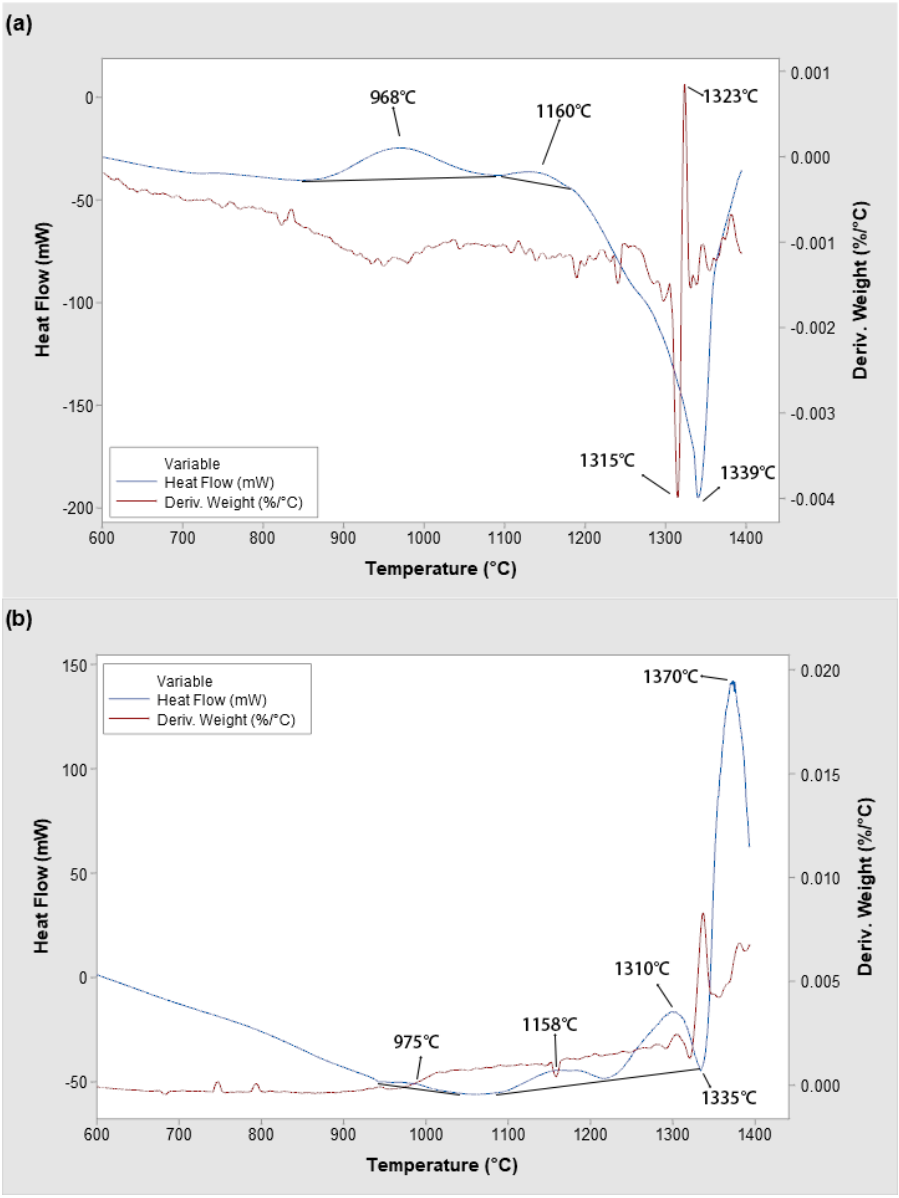

Figure 4.2 Plotted DSC curve of the IN713C superalloy. (a) heating (b) cooling. Key peaks measurements are labelled in plots.

Table 4.1 Key temperature values of the IN713C alloy solidification taken from the DSC curve.

Liquidus temperature	1370°C (1643K)
γ phase solidification temperature	1335°C (1608K)
Solidus temperature	1310°C (1583K)
γ' solvus temperature	1158°C (1431K)

4.2 Weld track analysis of the IN713C alloy

IN713C is a hard-to-weld material that can easily induce defects. A weld track test can provide a brief understanding of the melting and solidification behaviour during processing. The applied processing parameters based on previous literature are shown in Table 4.2.

Table 4.2 Parameters used to produce samples for weld track analysis of the SLM-fabricated IN713C alloy; Red group: high energy, Yellow group: moderate energy, Green group: low energy.

Power (W)	Speed (mm/s)					
	600	1000	1400	1800	2200	2600
190	Not build					
160						Not build
130						Not build

All samples are inspected using microscope, the depth of field level is not able to be adjusted due to the limitation of equipment. Samples in the high energy density group generally have a wide track width, and although the laser is continuous, it still shows a deep discontinuous melting pool. The melting pool depth difference within the same track is large; therefore, the energy absorption on the surface is non-uniform. Cracks can be observed in the middle of the melting pool, as shown in Figure 4.3. Therefore, for AM, the high energy density group can cause overmelting and internal defects.

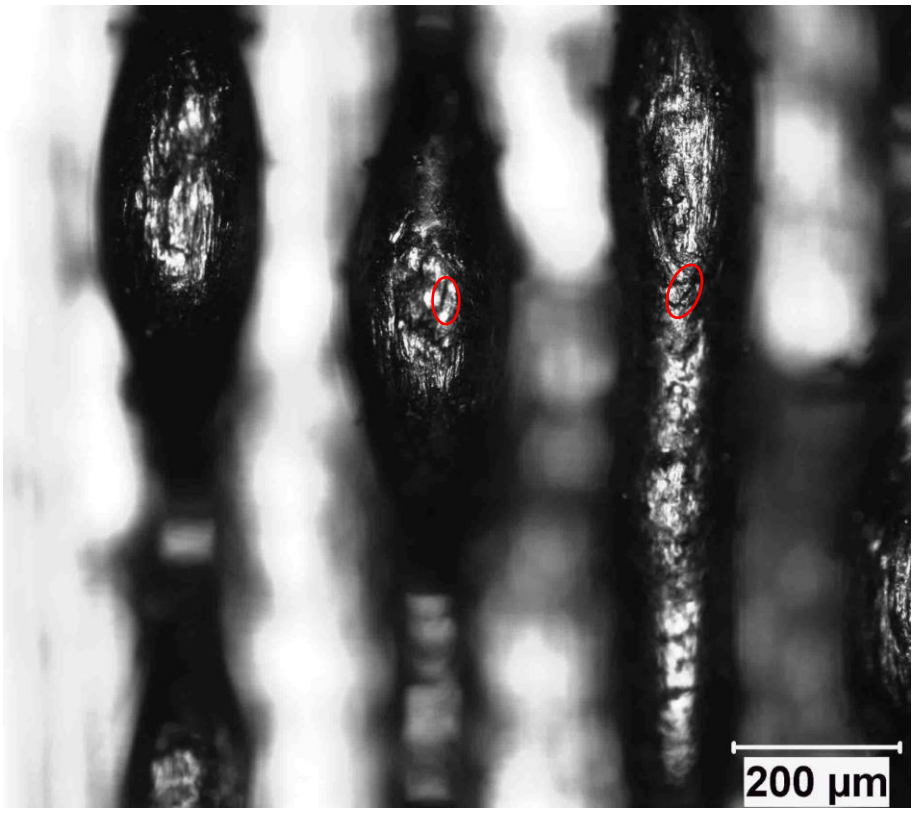

Figure 4.3 Top view of the bottom of weld track with high energy parameters. Cracks at the bottom of melting pool are labelled.

Samples in the moderate energy density group showed a similar track width with a high energy density group, but the width was inconsistent across the track. The track shows a more discontinuous feature compared with the other groups. Cracks can still be observed inside the melting pool, as shown in Figure 4.4. Therefore, the moderate energy density group for AM can cause non-uniform melting across the layer and internal defects.

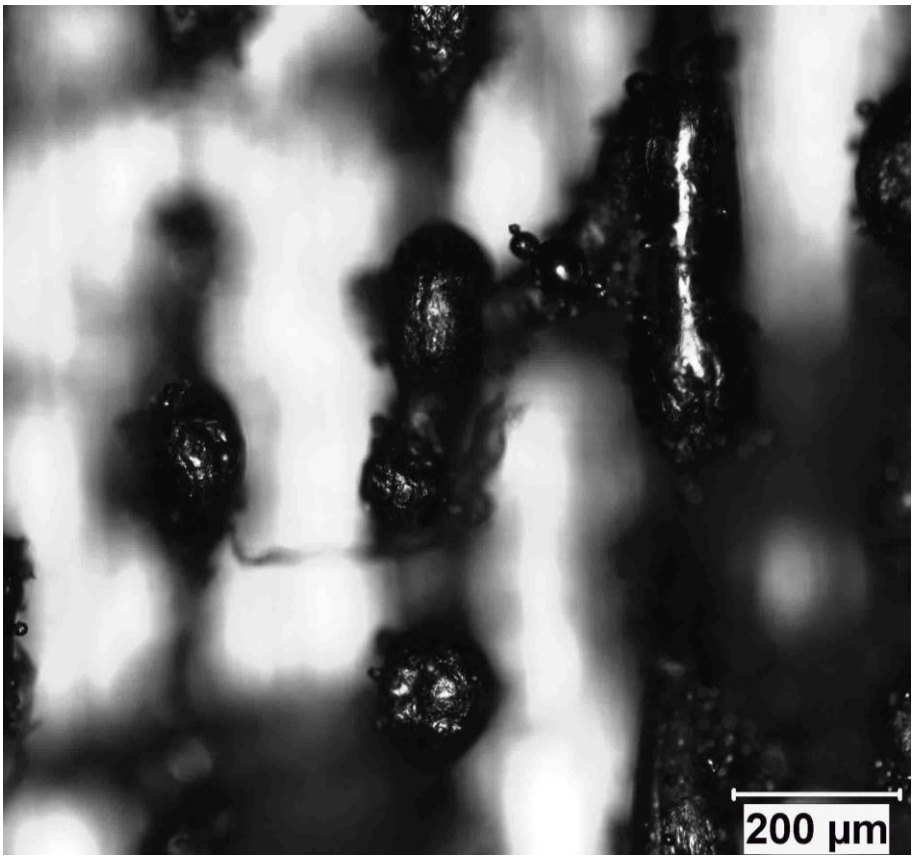

Figure 4.4 Top view of the bottom of weld track with moderate energy parameters showing large altitude difference and cracks.

Samples in the low energy density group show an evident continuous laser track with a constant width (approximately 70 μm), which is basically the same as the laser spot diameter. As shown in Figure 4.5, no defects were observed within the melting pool. Splatters can be observed on the surface, which can be the potential origins of cracks during processing. In general, the parameters of the low energy density group can produce a very smooth weld track.

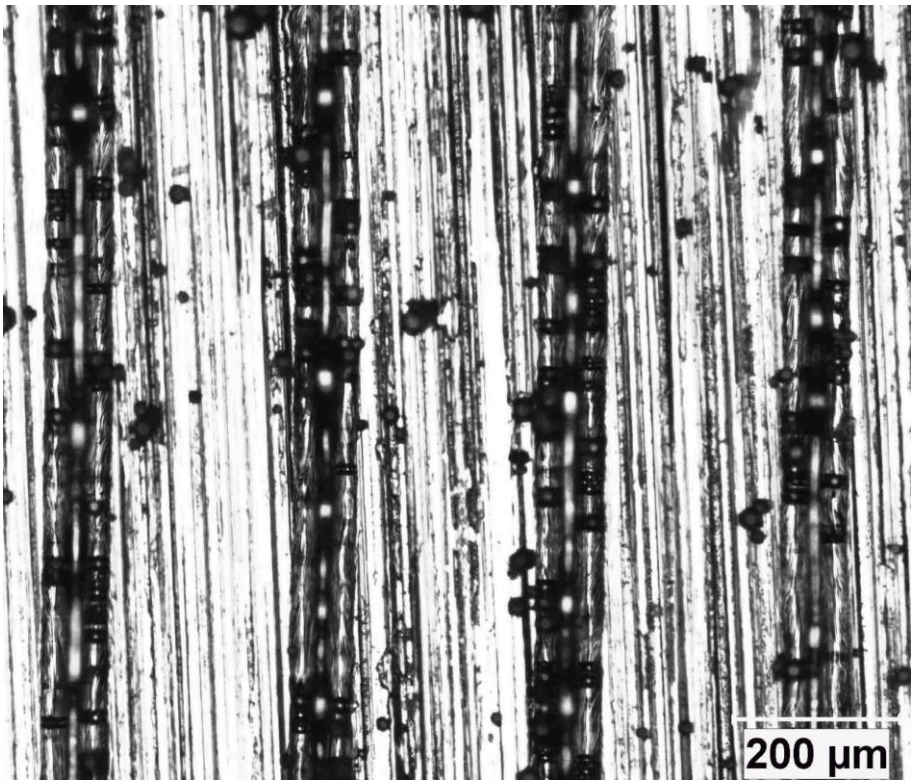

Figure 4.5 Top view of the weld track with low energy parameters showing clear tracks with few powders stack on the track.

4.3 Parametric study of the IN713C sample

The parametric study is designed based on the results of the weld track test. To understand the effect of both the input energy density and hatch space, a build with a series of cubic subjects is performed on the Aconity3D mini system. The processing parameters are presented in the table below. The processing window generally covered the area suitable for additive-manufactured CM247 from the literature (Cooper et al., 2013; Carter et al., 2014).

Table 4.3 Parameters used to produce samples for analysis within the parametric study of SLM-fabricated IN713C sample.

Sample ID	q (W)	v (m/s)	h (µm)	q*/ (v*l*)	1/ (h*)	q*/ (v*.l*.h*)
1-A	190	2.200	40	4.21	0.875	3.68
1-B	190	2.200	80	4.21	0.438	1.84
1-C	190	2.200	60	4.21	0.583	2.46
2-A	190	2.600	40	3.31	0.875	2.90

2-B	190	2.600	80	3.31	0.438	1.45
2-C	190	2.600	60	3.31	0.583	1.93
3-A	160	2.200	40	3.55	0.875	3.10
3-B	160	2.200	80	3.55	0.438	1.55
3-C	160	2.200	60	3.55	0.583	2.07
4-A	130	1.800	40	3.96	0.875	3.47
4-B	130	1.800	80	3.96	0.438	1.73
4-C	130	1.800	60	3.96	0.583	2.31
5-A	130	2.200	40	2.88	0.875	2.52
5-B	130	2.200	80	2.88	0.438	1.26
5-C	130	2.200	60	2.88	0.583	1.68
6-A	110	1.000	40	5.36	0.875	4.69
6-B	110	1.000	80	5.36	0.438	2.35
6-C	110	1.000	60	5.36	0.583	3.13

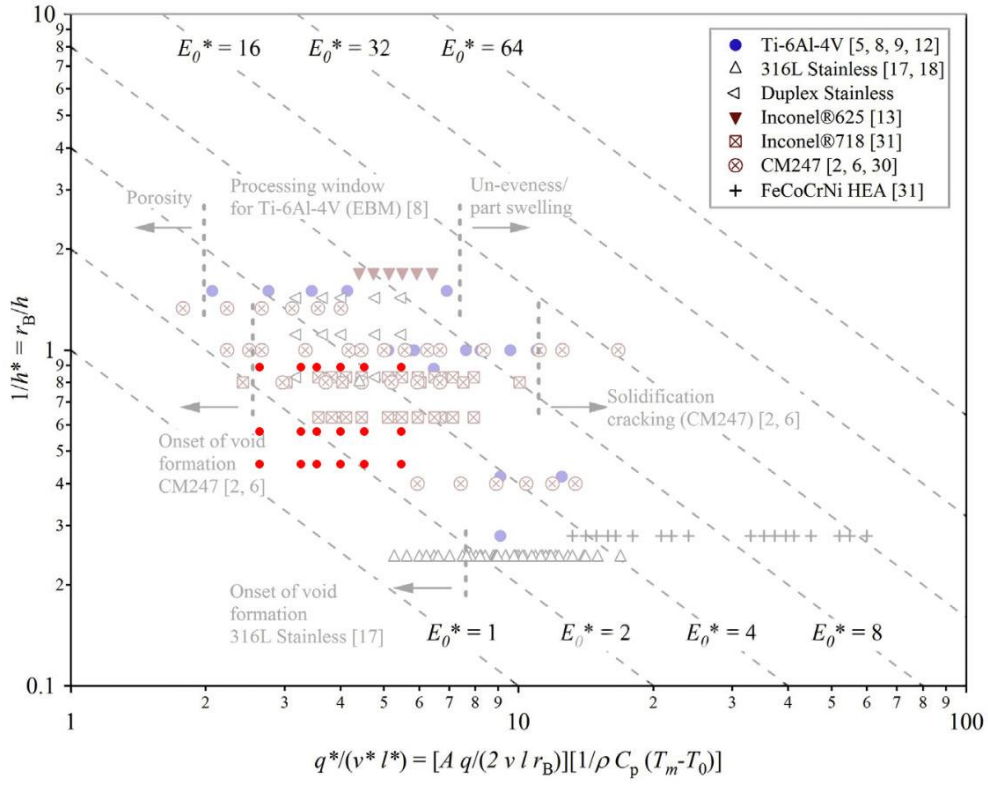

Figure 4.6 Distribution of processing parameter set of IN713C in the normalised energy density map. The processing window covered the area suitable for additive-manufactured CM247 from the literature. (Cooper, 2013; Carter, 2014).

The effect of energy density on the part density is depicted in Figure 4.7. The results show that the large variation between the highest (98.46%) and lowest (87.13%) densities shows that energy density has a strong influence on part density. With a higher energy density, the part density can be significantly improved. However, once the energy density exceeds a threshold point (q*/(v*.l*.h*)≥2), the density tends to reach a maximum density level (approximately 98%). In general, the volume energy input has (q*/(v*l*)) the strongest impact on part density. A larger energy input tends to heat a large area which creates a larger heating volume. The hatch space will have the most effective impact when the volume energy input is low. With the energy input increase for unit volume, the effect of hatch space becomes less obvious. As the space between hatches can be compensated with the large heating area. The difference in density is mainly induced by internal defects, which will be analysed in the next section.

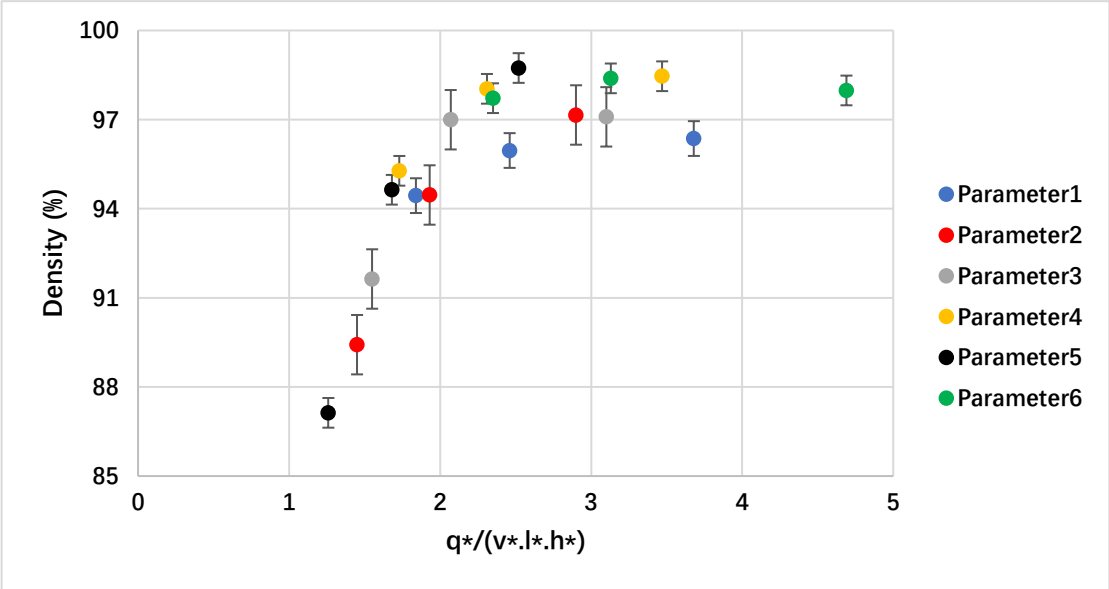

Figure 4.7 Plot showing the normalised energy density versus part density (%). The data group labels are referred to Table 4.3

4.4 Melting pool geometry and simulation

Literature reveals that the morphology of the melting pool can be affected by the energy input. The melting pool geometry can be analysed by measuring the width and depth of each melting pool, as expressed in Table 4.4.

Table 4.4 Measured geometry of melting pool with different parameters.

q	V	q*/(v*.l*.h*)	Average Width	Average depth
(W)	(m/s)		(μm)	(μm)
190	2.2	3.68	150.22	53.52
190	2.6	2.90	142.66	36.50
160	2.2	3.10	148.82	40.23
130	1.8	3.47	143.92	46.20
130	2.2	2.52	147.52	39.33
110	1.0	4.69	157.18	37.62

All samples had a width of approximately twice the diameter of the laser beam (70 μm). At a constant speed, the higher power input creates a deeper melting pool with a slightly greater width. It can be seen that at the same power input, a fast speed can form a relatively shallow melting pool. Conversely, a slow speed can create a deeper melting pool with minor changes in width. A slow speed can cause longer exposure at a site and higher energy absorption; thus, the melting pool will be relatively narrower and deeper. When the speed remains constant, a higher power indicates more simultaneous energy absorption. Therefore, the laser penetrates deeper into the object and creates a deeper melting pool, which can be classified into two types. The high energy input can create a deep narrow melting pool which can be identified as “keyhole” melting pool, while the low energy input can create a shallow melting pool with the least remelting of previously processed layer, which can be identified as “conductive” melting pool. However, owing to the nature of AM, the previously processed layer can be partially remelted by the next layer, which can cause uncertainty in depth measurement. The overlap between hatches can cause some uncertainty in the width measurement. Nevertheless, the melting pool depth and width generally increase with a decrease in the laser scan speed or an increase in the power input.

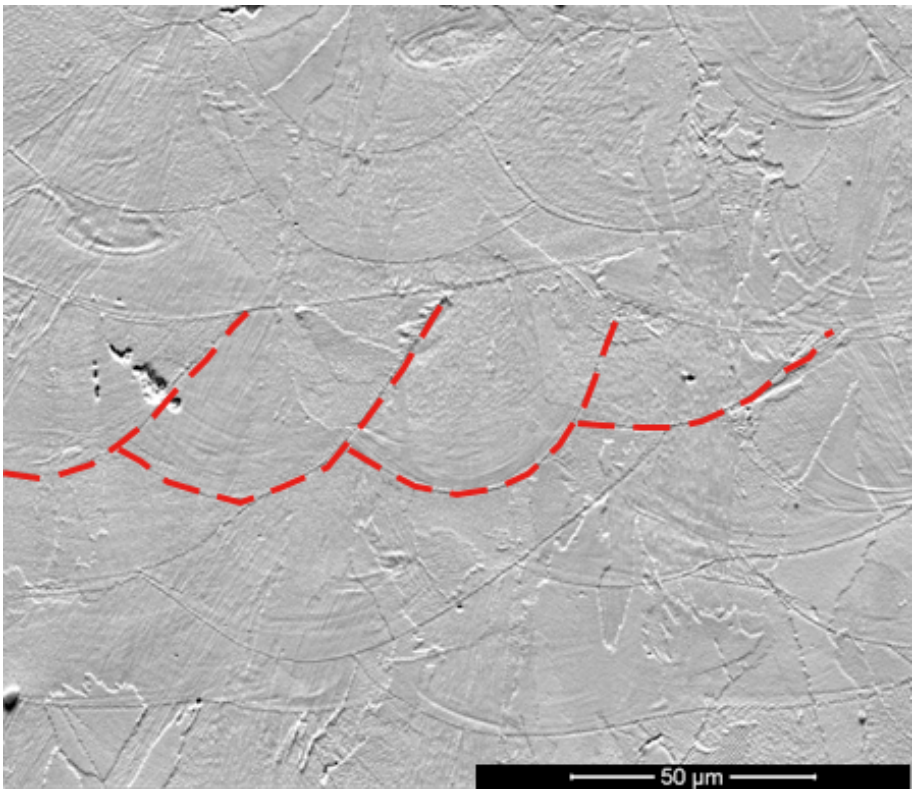

Figure 4.8 SEM micrograph of the etched cross section of the IN713C sample with q*/(v*.l*.h*) = 2.52. Overlaid melting pools can be observed. The melting pool geometry can be classified as "conductive" mode.

As the laser is continuous, the length of the melting pool can only be obtained by means of simulation. The same result as the melting pool width and depth can be observed in Figure 4.9. At the same scan speed, a higher power can create a longer melting track, while at the same power level, the slow speed can create a slightly longer melting track, but is not as effective as the variation of power. Although the effect of the hatch space is hard to analyse, the high hatch space induces severe lack of fusion (LoF), which makes the melting pool hard to identify.

Both the measurement and simulation results show that power is the dominant parameter that affects the size of the melting pool. As shown in Figure 4.9(f), the sample has the highest energy density, but the size of the melting pool is still the smallest owing to the lowest power input. Thus, the morphology of the melting pool does not linearly depend on the normalised unit energy input. It confirmed that power is the most dominant factor among all parameters.

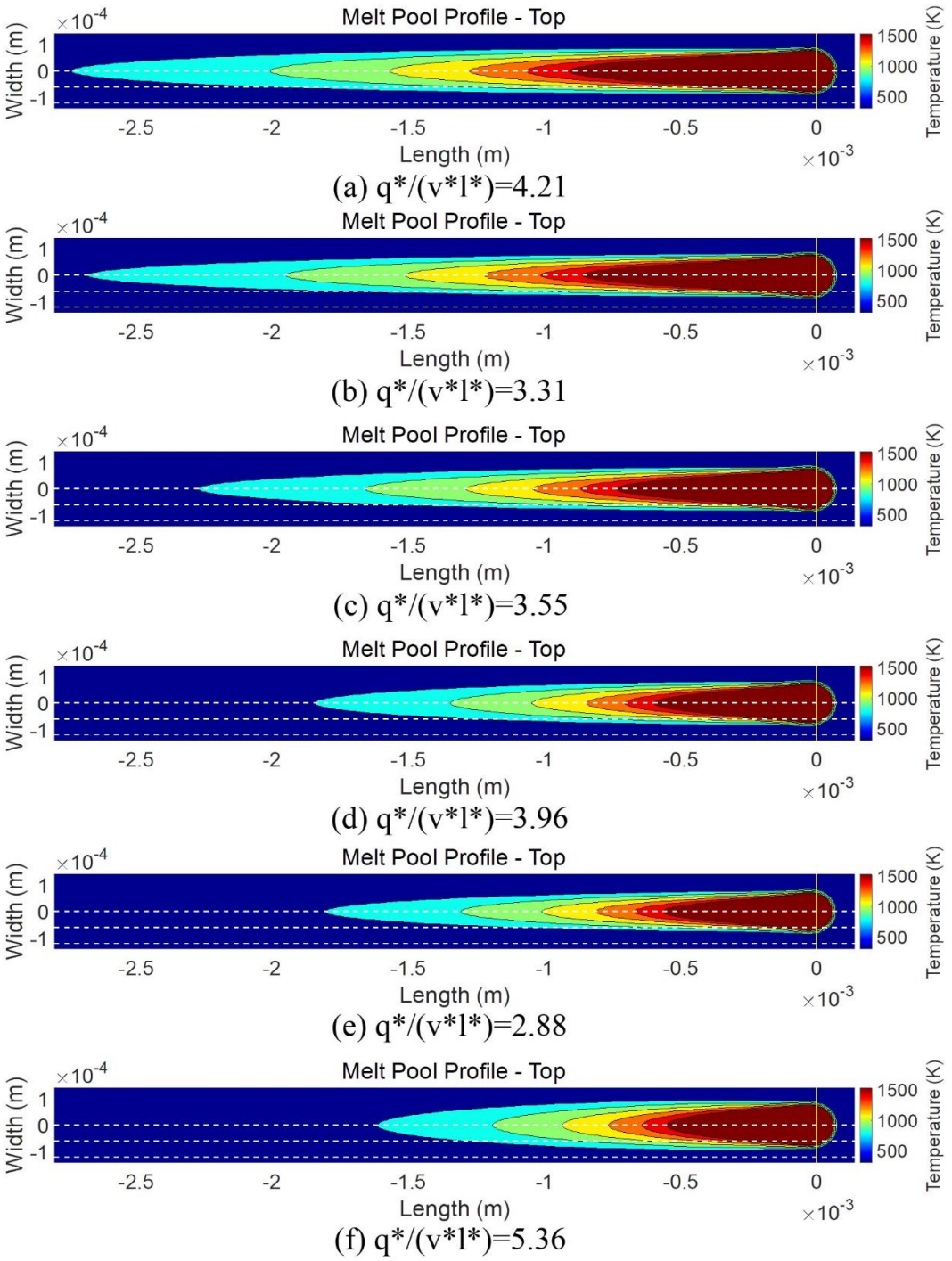

Figure 4.9 Top view of the melting pool with MATLAB simulation using the parameters given in Table 4.3. Different level heat affect areas are labelled. (a) 190W, 2.2 m/s; (b) 190W, 2.6 m/s; (c) 160W, 2.2 m/s; (d) 130W, 1.8 m/s; (e) 130W, 2.2m/s; (f) 110W, 1.0m/s. The HAZ zone (light blue) is defined at 50% of solidus temperature. It can be seen that the power has higher impact on melting pool geometry.

4.5 Defect analysis

Based on the research and development of the machine learning (ML) algorithm developed by Kathryn (2020), the effect of energy input on different types of defects can be analysed, as depicted in Figures 4.11–4.14. The defects are analysed using ImageJ as described in Section 3.7. The example of a defect selection is shown in Figure 4.10. The defect threshold method is used for the better contract, the result of all different threshold methods is listed in Appendix A. When the particles are smaller than a threshold size, the characteristics of the defects can be hard to distinguished. Therefore, to reduce the potential noise data generated from the small defects, the defect smaller than 5μm are removed from the analysis. For a better comparison, the scale of the defect length axis is identical in all four figures.

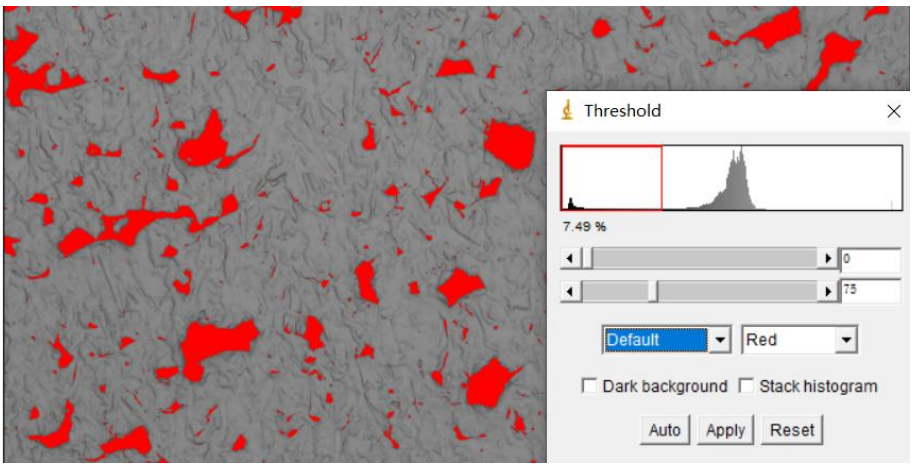

Figure 4.10 threshold setting in ImageJ. Red area are defects included in analysis.

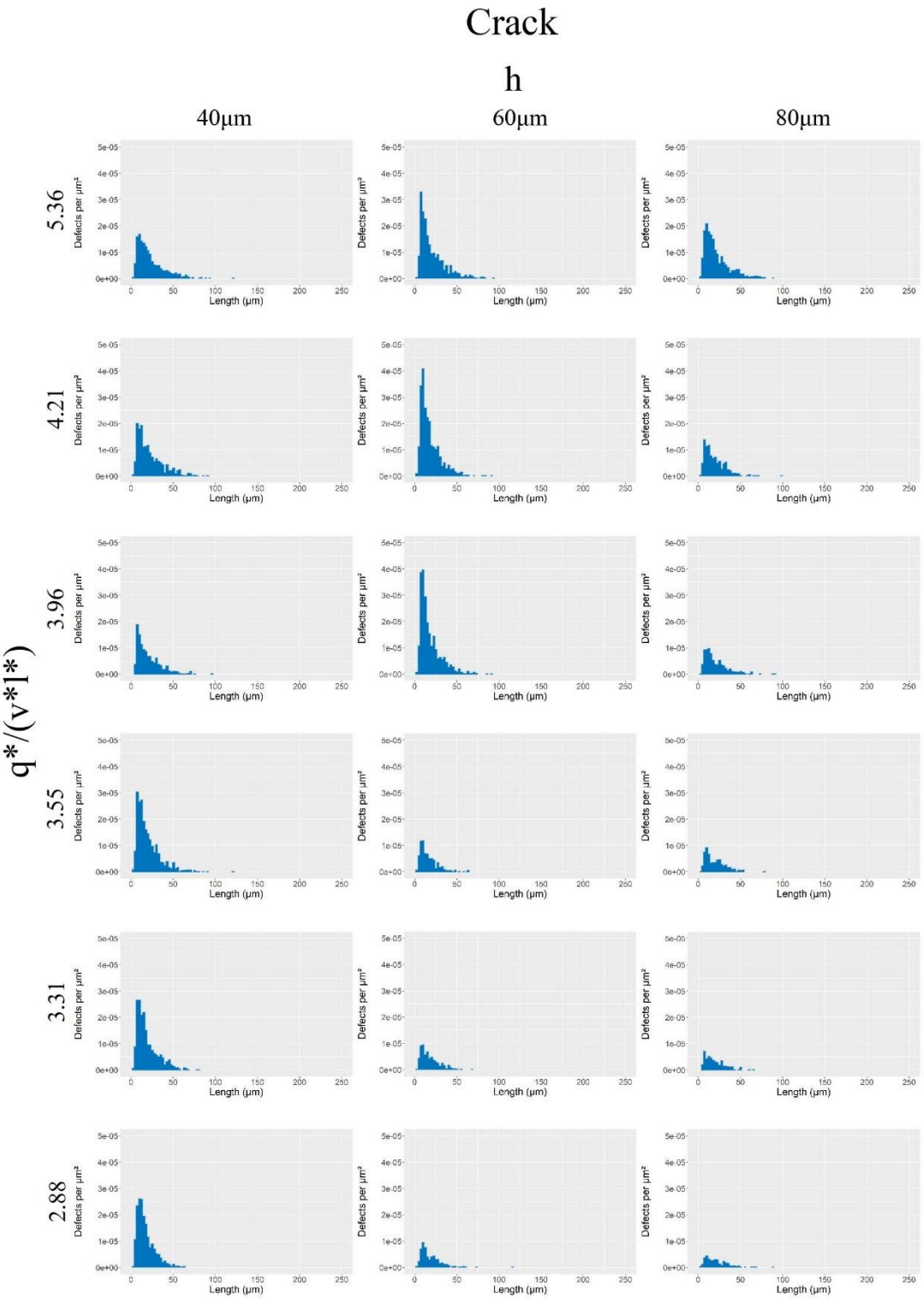

Figure 4.11 Size distribution of cracks in the IN713C samples with the parameters given in Table 4.2. The normalised energy density is labelled at the left-hand side, while the hatch space is labelled at the top.

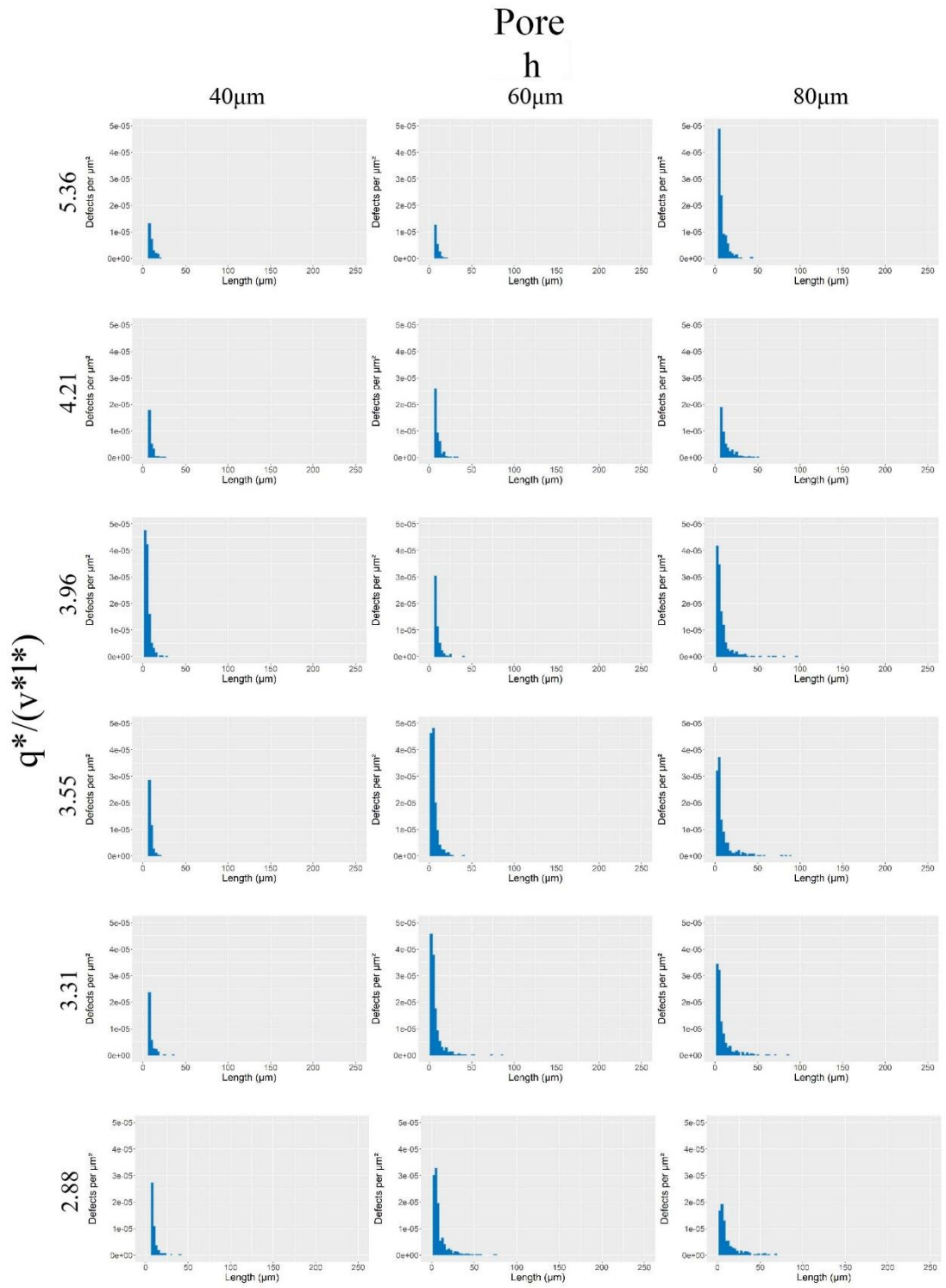

Figure 4.12 Size distribution of pores in the IN713C samples with the parameters shown in Table 4.2. The normalised energy density is labelled at the left-hand side, while the hatch space is labelled at the top.

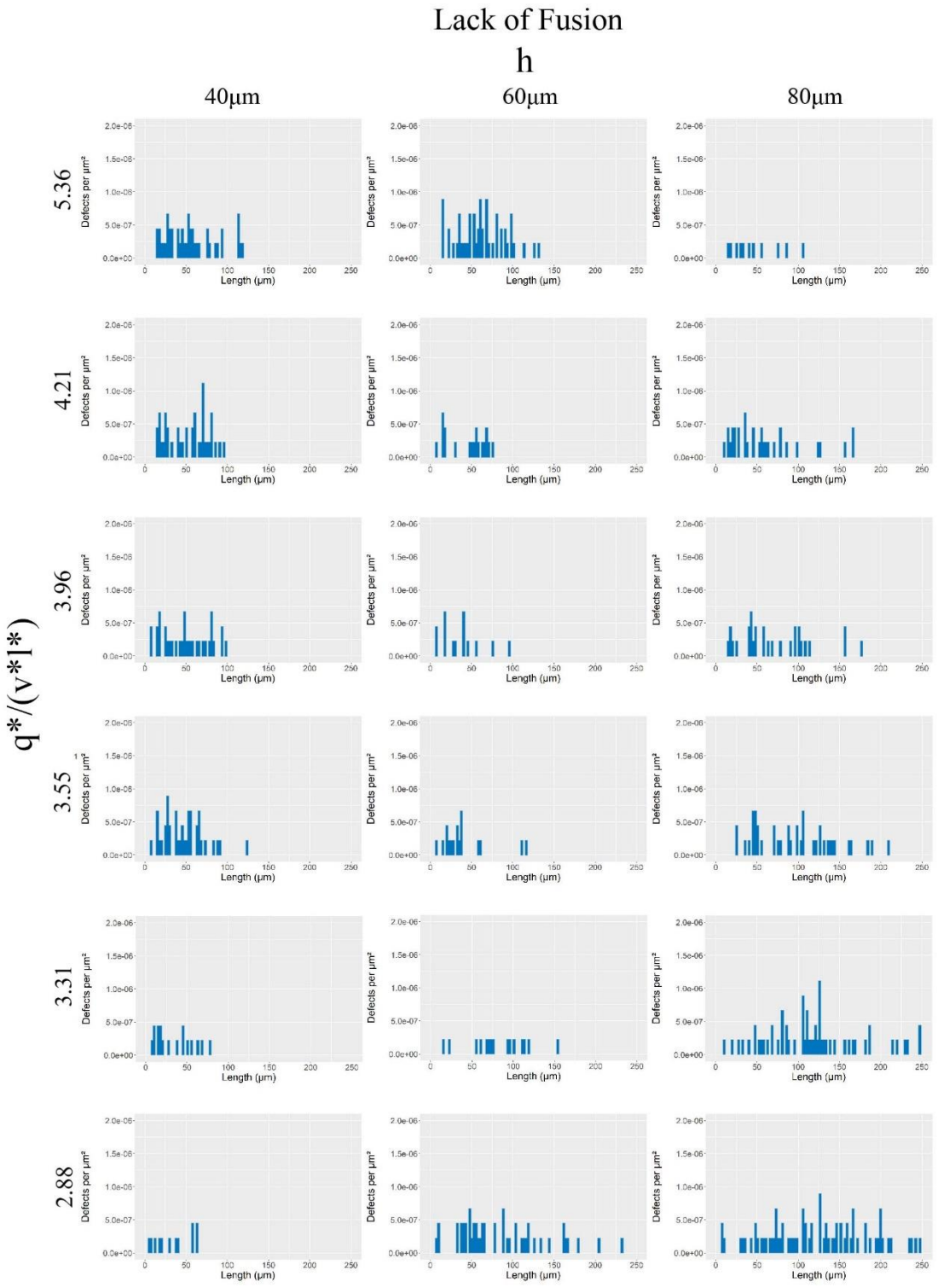

Figure 4.13 Size distribution of lack of fusion in the IN713C samples with the parameters shown in Table 4.2. The normalised energy density is labelled at left-hand side, while the hatch space is labelled at the top.

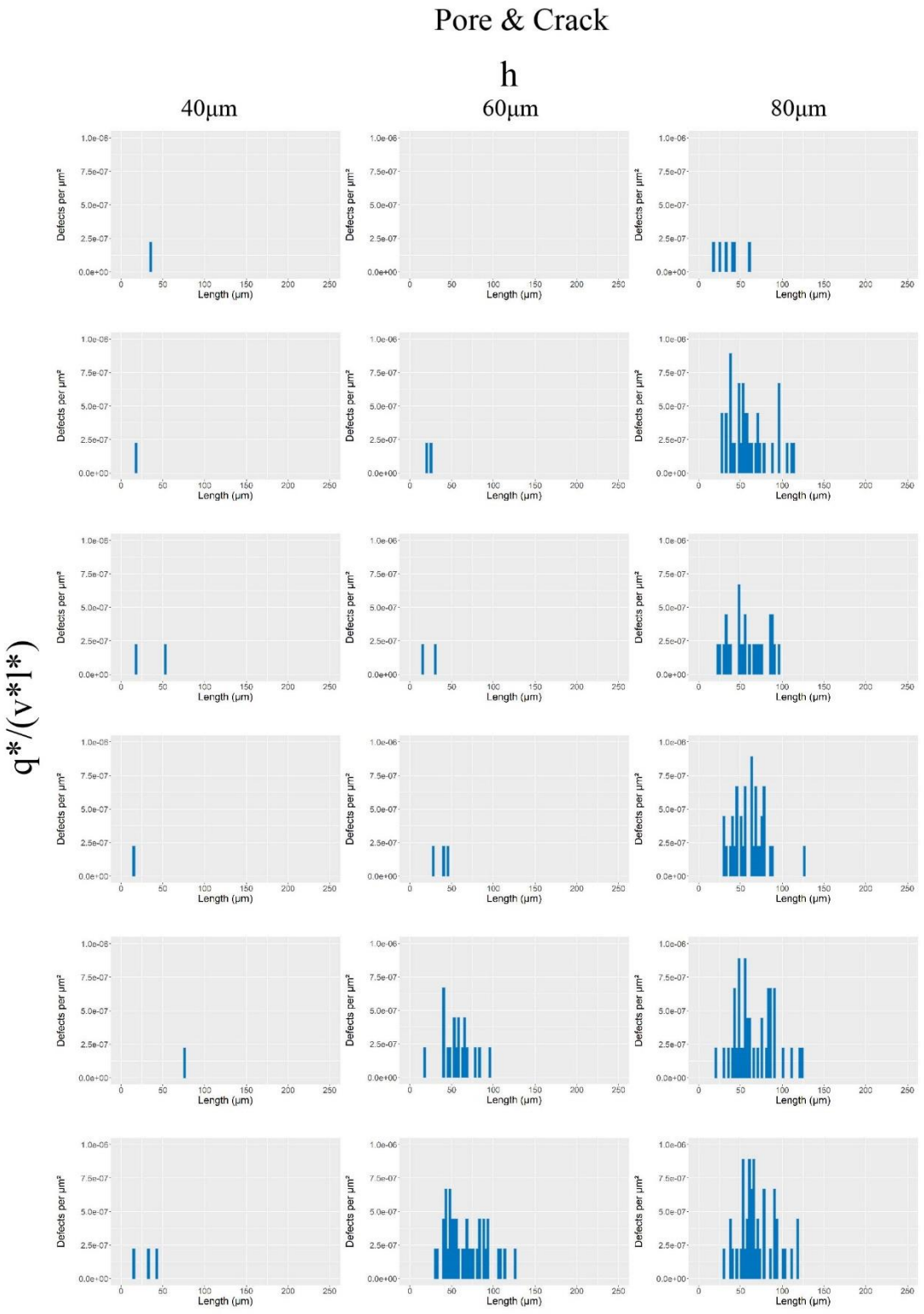

Figure 4.14 Size distribution of pores with cracks in the IN713C samples with the parameters shown in Table 4.2. The normalised energy density is labelled at the left-hand side, while the hatch space is labelled at the top.

Through data analysis, the results from the micrographs are generally confirmed. It can be seen that the crack sizes are generally less than 50 μm. More cracks can be found in the high-energy input group (top left in Figure 4.11). The close hatch space (40 μm) consistently causes numerous cracks. The high energy density is excessive for the local region with a small hatch space.

Porosity can be found in all samples, while more can be found in the low energy input and wide hatch space samples. The wide hatch space and low energy input cause insufficient melting. The powder cannot be completely fused together; thus, voids can be produced. In high energy density samples, the pores are rounder, and this is induced by the trapped gas, which is hardly eliminated.

The result shown in Figure 4.13 shows that the LoF is highest in the low energy input sample with a large hatch space (bottom right). However, several defects are recognised owing to an LoF in the high energy with close catch space (top left). Lack of fusion should only exist in samples, where the energy input is not sufficiently enough to fuse the powder together. Therefore, the high energy density sample should not have LoF type defect. Furthermore, it can be seen that the defects generated owing to the LoF in the high-energy density sample generally have a smaller size (< 100 μm). There can be a possible erroneous judgement of the keyhole porosity, as this has similar analysis parameter characteristics with LoF.

The pores with cracks represent the type of defects that have single or multiple cracks on the edge of a pore. It can be seen that this type of crack only occurs in the low energy input sample and wide hatch space. Because a lower energy input leads to a higher cooling rate, a higher residual stress is induced. The edge of the pores is a preferred initial location for residual stress cracks.

4.5.1 Defect morphology and mechanism

The micrographs generally confirmed the analysis results from ML scripts. Cracks can be found in all samples, which confirms that IN713C is a high-crack-susceptible superalloy. Cracks are generally reduced with energy density reduction. However, the large-scale porosity with an irregular morphology starts to appear in the sample, which

can be identified as an LoF.

4.5.1.1 Cracks

The morphology of cracks at low and high energy density conditions are different. In the low and moderate energy density groups, the cracks were strongly aligned in the build direction and penetrated through the layers. Upon considering the crack at higher magnifications, the edge of the cracks is quite sharp and clean. It can also be seen that in the etched sample, cracks generally lay along the build direction. The clean crack edge indicates that defects were most likely formed in the solid state, as presented in Figure 4.15. Based on the understanding of the crack mechanism in Chapter 2. Ductility-Dip cracking, corresponding to strain age cracking, can be the main mechanism behind this type of crack. The reheat during laser melting introduces a large residual stress due to the temperature difference between the layers. Meanwhile, the reheat of each layer could cause sliding of the grain boundaries. Because of the relatively low reheat temperature, the grains were not recrystallized. Therefore, the crack is relatively sharp and clean.

In the high energy density group, the morphology of cracks is completely different from that of the low energy group. The crack grows both horizontally and vertically along the build direction with a ‘zigzag’-like shape, as shown in Figure 4.16. In the etched sample, it can be seen that all these types of cracks followed the grain boundary orientation. The dendritic protrusions can be found inside cracks when cracks are observed under high magnification, as shown in Figure 4.17. The dendritic protrusions indicated that this type of crack is most likely formed during solidification rather than during the reheating stage. The stress was directly introduced by the laser beam during scanning. When the material solidified after scanning, the remaining liquid between the grains and dendrites could act as the initial point of cracks. The concentrated residual stress combined with the shrinkage of solidification can tear the boundaries away and form wide-open cracks.

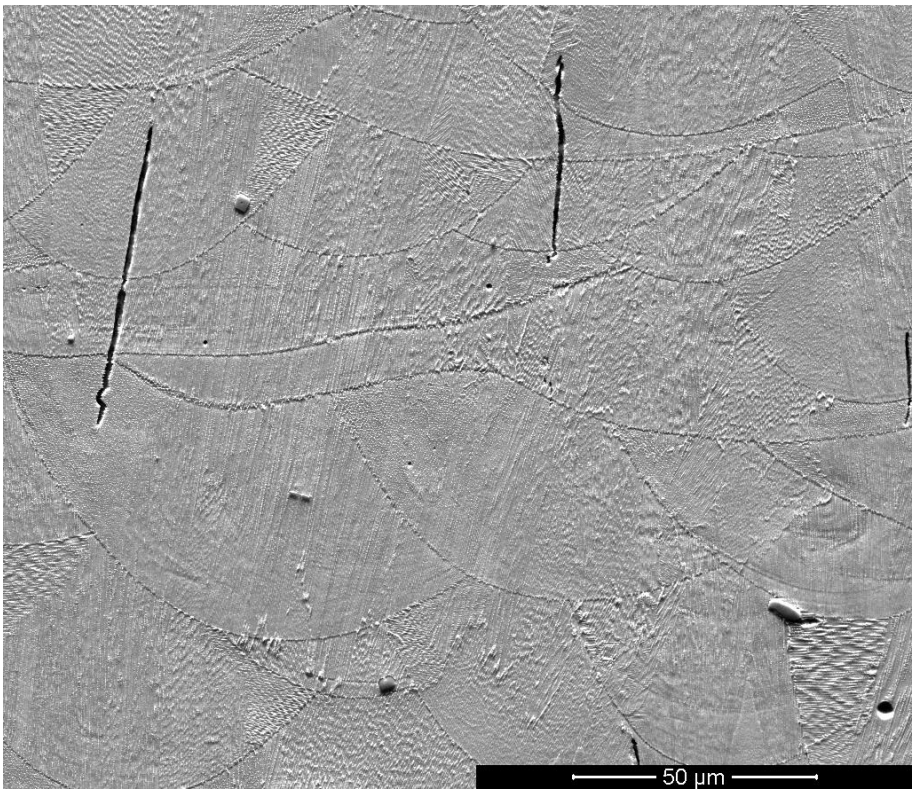

Figure 4.15 SEM image of a low energy sample (130 W, 2.2 m/s, 60 µm) showing clean sharp cracks. Strain age cracking, can be the cracking mechanism.

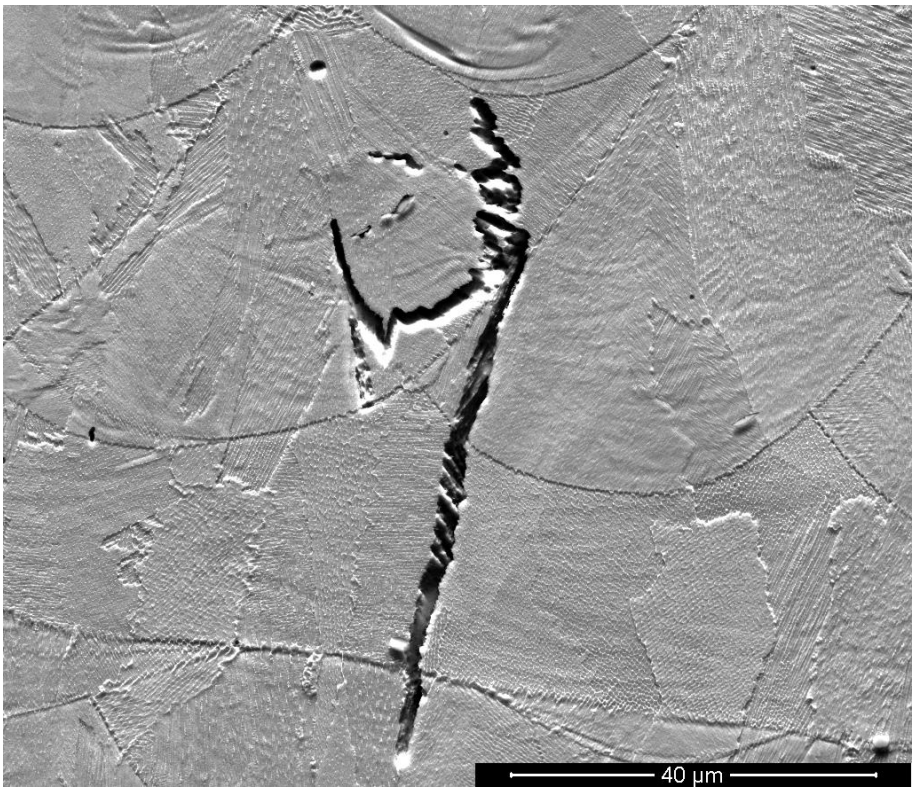

Figure 4.16 SEM image of a high energy sample (190 W, 2.2 m/s, 40 µm) showing large 'zigzag'-like cracks. Solidification cracking can be the cracking mechanism.

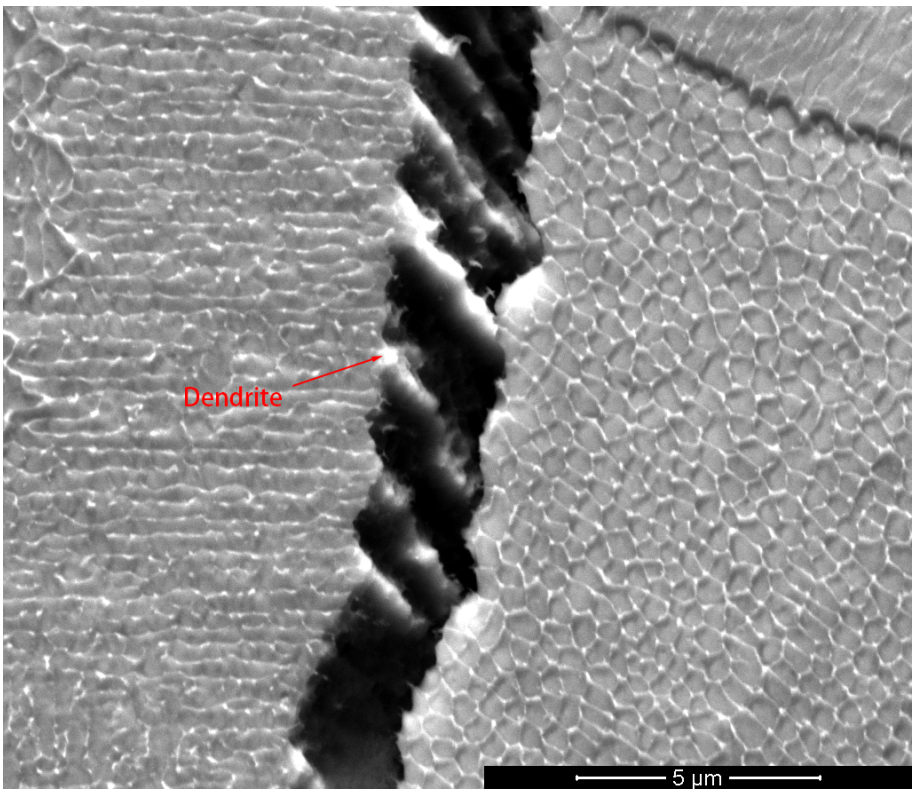

Figure 4.17 SEM detail of a 'zigzag'-like crack. Dendrite structure can be seen at the edge with a size less than 1 µm.

4.5.1.2 Porosity

As shown in Figure 4.18, the pores are generally elongated with no preferred direction with a size range of 50–500 µm. At a higher magnification, partially melted powder particles can be observed owing to the low energy input and sintering together. This can mainly be induced by insufficient melting during the process. The gap between particles can become the void that can remain inside after solidification. The internal porosity can be observed under higher magnification. The outline of the powder particles can still be seen at the edge of the porosity. The surface of a partially melted particle can also be seen inside the porosity. Owing to these features, this type of porosity can be classified as an LoF.

The internal surface also provides a concentration point for residual stress. Therefore, cracks can also be found start at some LoF type of porosities. Therefore, the 'pore with crack' type of defects can be found in low to moderate energy density samples.

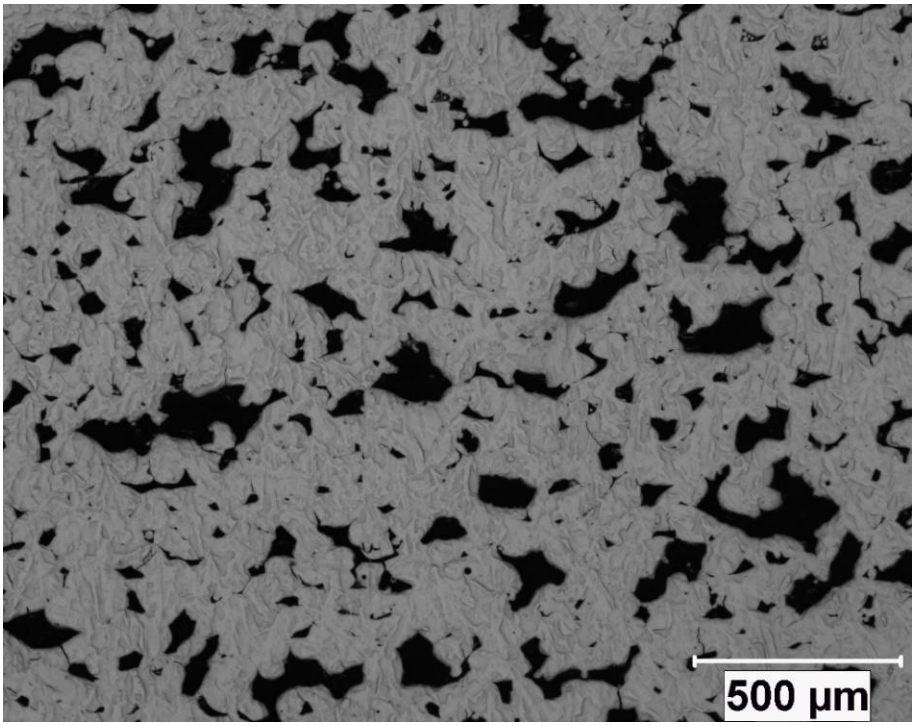

Figure 4.18 Optical microscopy image of a low energy sample (130 W, 2.2 m/s, 80 µm), with a large amount of lack of fusion distribute uniformly across the sample.

With visual inspection under a microscope, no LoF type of defects was observed in the high energy density sample. However, a small amount of irregular porosity can be observed, as shown in Figure 4.19. Unlike the LoF, the porosity is generally small and lies at the bottom of each melting pool. It is confirmed that keyhole melting due to high energy density input is responsible for this type of porosity, and the ML script failed to distinguish it from the LoF owing to the similarity of the morphological characteristics.

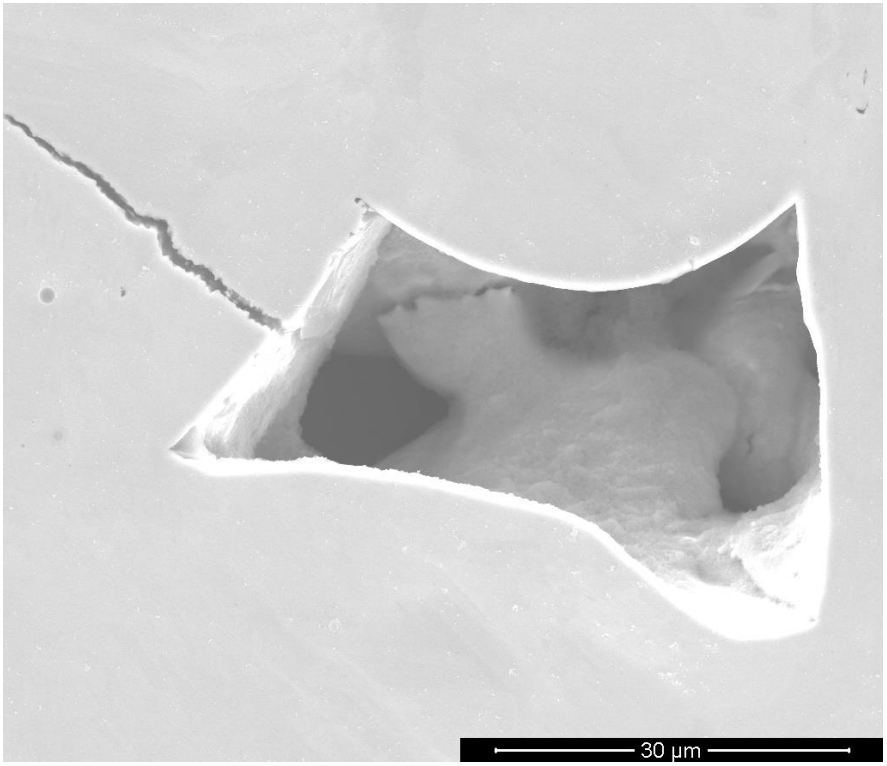

Figure 4.19 Zoom-in image of one lack of fusion pore; partially melted powder particles can be seen in the pore. A crack is on the edge of the pore due to thermal stress.

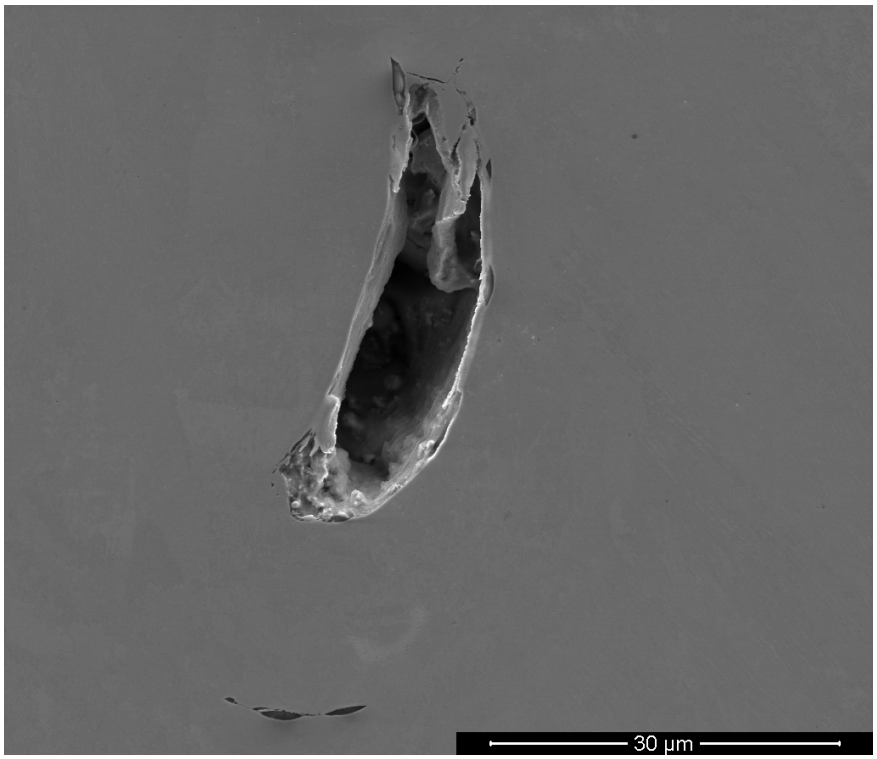

Figure 4.20 SEM image of a high energy sample (110 W, 1.0 m/s, 40 µm) showing the irregular 'keyhole' pore.

4.5.2 The effect of melting pool volume on defect formation

When the laser heats the powder layer, the temperature within the melting pool can be different owing to the heat transfer. The outer area has a temperature less than the melting temperature and is still sufficiently high to alter the microstructure (50% of solidus temperature), which can be referred to as the HAZ. The middle area is where the material can be fully melted. The core area is that which is directly exposed under the laser beam. The residual temperature can be close to the boiling point; thus, it can be regarded as an overheated area. The relation between the ratio of the overheated volume to the melting volume and the defects is shown in Figure 4.21. The ratio of the overheated and melting volumes indicated the heat transfer with different parameters. Heat transfer can directly affect defect formation. As evident in the sample with a wide hatch space, the amount of three types of cracks decreases with an increase in the volume ratio. The only exception is the number of cracks in the close hatch space sample. A large volume ratio with a close hatch space means that the melting pools are heavily overlaid with each other, thereby leading to a high local heat distribution, while the excess heat input results in hot cracking. Thus, the cracking level linearly increases with the volume ratio in the melting pool.

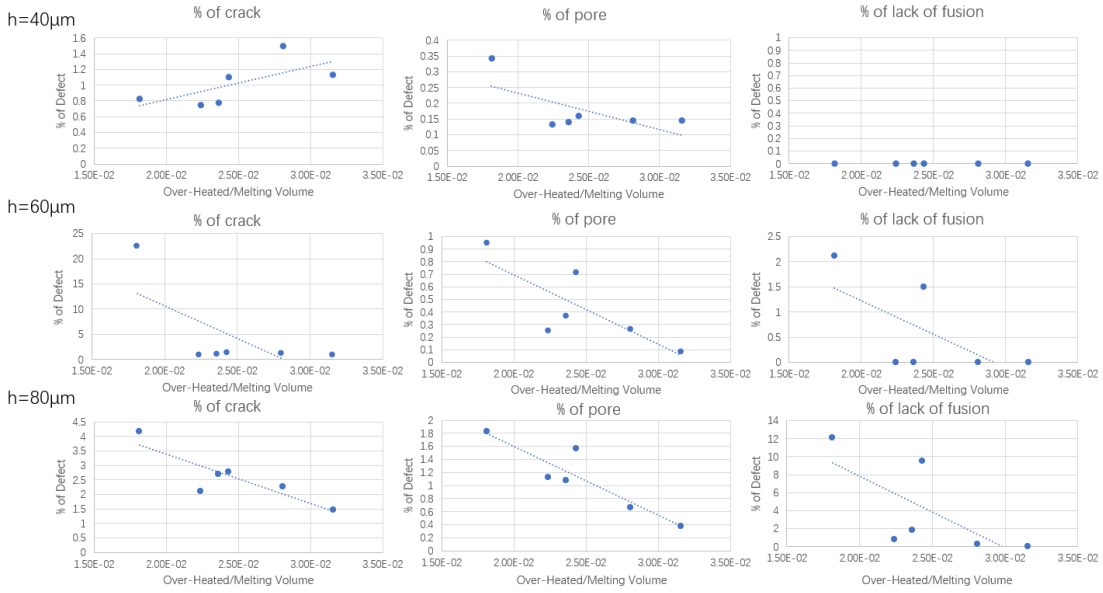

Figure 4.21 Plotted graphs show the variation in the defect densities for an SLM-fabricated IN713C sample with different melting pool volume ratios.

4.5.3 The effect of laser travel time on defect formation

In selective EBM, the laser return time is a key parameter defined as the time taken to get from the middle of the melt line to the middle of the adjacent one. Therefore, a similar measurement can be set for the SLM process, which is the laser travel time, i.e., the time taken to get from the top of the laser track to the bottom of the same laser track. Thus, the laser travel time (t_l) can be calculated as follows:

$$t_l = L_l / v \qquad \textbf{Eq 4.1}$$

where L_l is the length of the laser welding track. In general, the difference in time can mainly affect the heat loss during cooling. Thus, it can affect the microstructure and defect formation.

To investigate the effect of laser travel time, all the parameters were fixed, except the sample length, as depicted in Figure 4.22. The laser scan direction is fixed from top to bottom without interlayer rotation. A pyrometer was used to monitor the temperature during processing. The parameters are presented in Table 4.5.

Table 4.5 Fixed parameters with varying sample lengths for analysis within the laser travel time study on the SLM-fabricated IN713C sample.

q (W)	v(m/s)	q*/(v*.l*.h*)	Laser track length (mm)	laser travel time (ms)
130	2.200	4.81	5	2.27
130	2.200	4.81	10	4.55
130	2.200	4.81	15	6.82
130	2.200	4.81	20	9.09
130	2.200	4.81	25	11.36
130	2.200	4.81	30	13.64
130	2.200	4.81	40	18.18
130	2.200	4.81	50	22.73
130	2.200	4.81	60	27.27

The pyrometer data can be converted using the MATLAB script to plot a thermal map for each layer, as shown in Figure 4.22. To reduce the effect from the environment, the thermal map of a median layer is used in the research. It can be seen that the local temperature in the short laser track area is generally higher than the temperature in the long laser track area. It is also evident that the temperature is generally slightly higher at the top and bottom edges because the laser beam will turn back and scan the next hatch instead of starting a new hatch. The edges will be immediately reheated, while the centre can have time to cool down. Thus, the temperature at the centre is slightly lower than that at the edges.

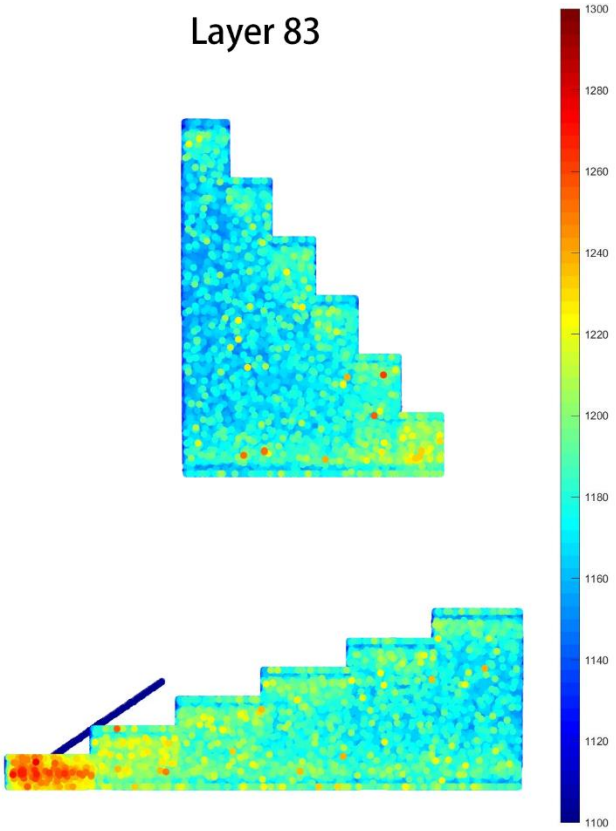

Figure 4.22 Thermal map of the median layer converted from the pyrometer data for the laser travel time sample. Colour indicated the residual temperature captured by pyrometer. Short length/travel time have higher residual temperature.

The corresponding relationship between temperature and travel time is presented in Figure 4.23. According to the datasheet of the pyrometer, the actual temperature is proportional to the voltage output. It can be seen that the temperature gradient is steeper

for a short laser track, which is equivalent to a short travel time. For a long laser track, the average temperature tends to be stable at approximately 1160 mV (732°C).

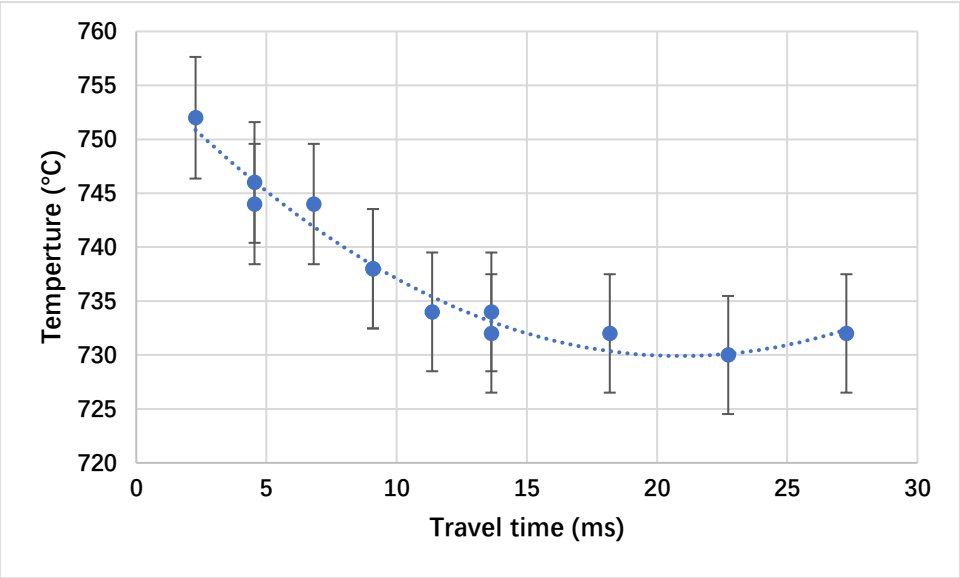

Figure 4.23 Plotted graph showing the variation of temperature with the laser travel time. The residual temperature tends to be stable at approximately 730°C when travel time is longer than 10 ms.

The influence of travel time on defect formation can also be analysed using CLEMEX and the ML script. The trend of each type of defect is listed in Figure 4.24. The increase of cracks density generally happened with the decrease of pore density which are similar to the result of parametric study. A longer travel time led to a lower processing temperature, and therefore induced a small amount of lack of fusion. Meanwhile, a lower temperature can slightly reduce the temperature gradient between the layers. Therefore, the number of cracks is reduced in large objects. With a fast travel time, the temperature is higher, such that a slower cooling rate can induce more hot cracking. The total defects can be maintained at a relatively low level (approximately 1%) with a travel time of approximately 10 to 15 ms and the residual temperature is about 740°C.

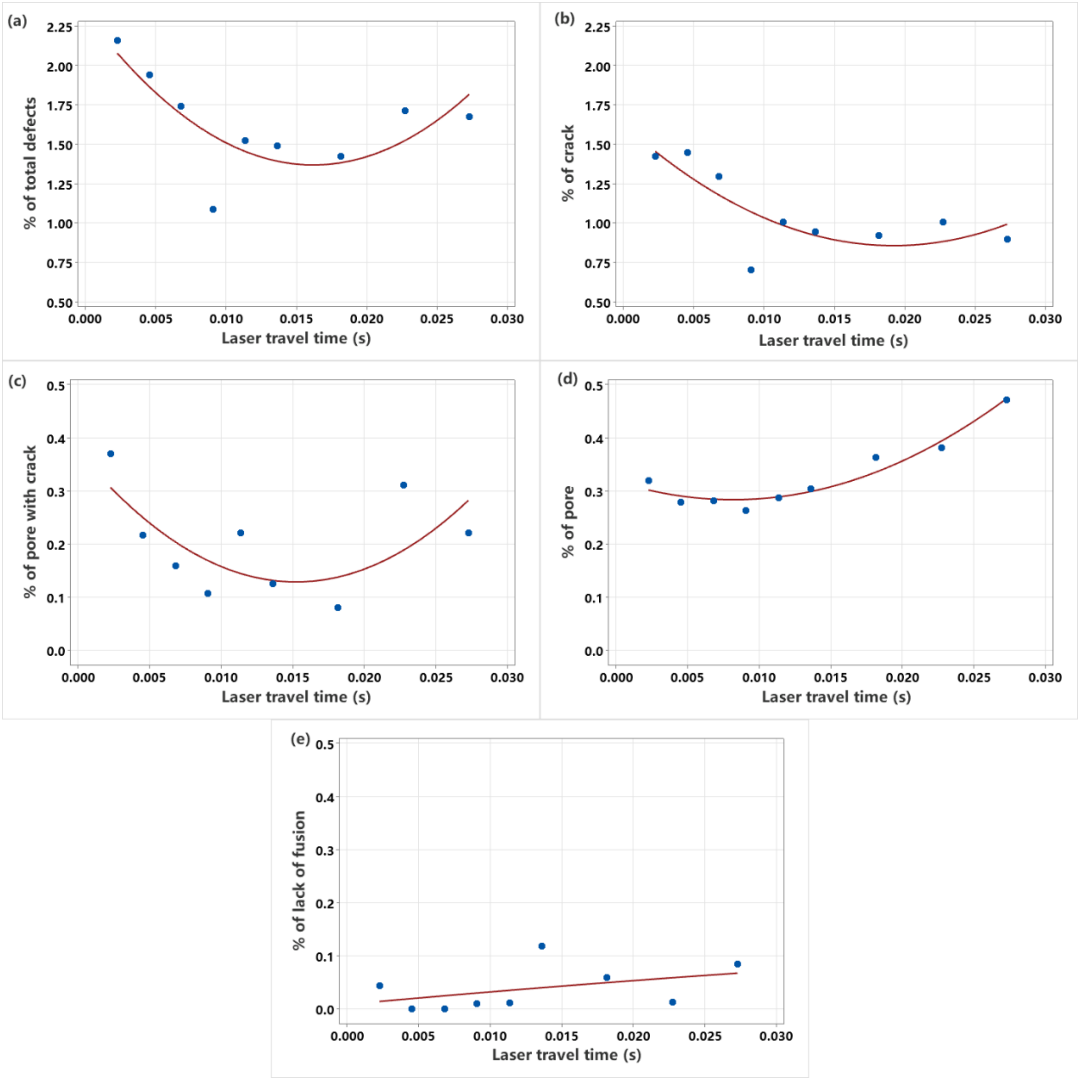

Figure 4.24 Plot showing the trend of density of each type of defect with different laser travel times. (a) total amount of defects (b) cracks (c) pore with cracks (d) pores and (e) LoF. Corresponding trend of cracks and pores can be seen.

4.5.4 The effect of travel time on melting pool geometry

The melting pool simulation results for the travel time samples are elongated and shallow. The cooling rate within a single melting pool (C_{mp}) can be calculated using the following equations:

$$G = (T_{liq} - T_{sol})/L \qquad \textbf{Eq 4.2}$$

$$C_{mp} = G * V \qquad \textbf{Eq 4.3}$$

where G is the thermal gradient; while T_{liq} and T_{sol} are the liquidus and solidus temperatures, respectively; and L is the distance between two temperature marks

directly behind and in line with the beam. (Yilmaz & Kayacan, 2018) This shows that the return time has a limited effect on the melting pool geometry and cooling rate for a single melting pool. The critical thermal recovery time before completely cooling down is approximately 0.367 ms for all samples in Table 4.5, which is much shorter than the travel time, which is between 2 ms and 28 ms. Thus, the previous hatch has a limited effect on the thermal profile of the following hatch with general AM build parameters.

4.6 The influence of processing parameters on the mechanical properties

4.6.1 Tensile properties

The mechanical properties of the Ni superalloy can be significantly affected by the microstructure based on the results from the literature (Tian et al., 2015; Carter, 2013; Lapin et al., 2009). The microstructure can be changed by altering the processing temperature. Therefore, the processing parameters may potentially affect the mechanical properties. Three samples with different applied laser powers and speeds were tested. Owing to the limitation of the build platform, the tensile samples were all horizontally built. The tensile test results at room temperature are shown in Table 4.6. The tensile data presented by Galizoni et al. (2019) for investment cast IN713C sample for comparison are also shown in Table 4.6.

Table 4.6 Measured tensile properties of the SLM as-built parameters with the reference cast sample.

Sample ID	Power (W)	Speed (m/s)	0.2% proof strength (MPa)	Tensile strength (MPa)	Elongation (%)	Reduction in Area (%)
1	120	2.03	747	837	1	3
2	130	2.20	742	826	1	3
3	140	2.37	758	803	1	3
Cast Ref (Galizoni et al., 2019)			689	758	2–3	6–7

With a fixed energy density, there is no significant difference between different parameter groups. The fast scan speed tends to slightly reduces the tensile strength, even with a higher power input. Considering the potential defects in samples, there is no clear evidence that the change of processing parameters under a fixed energy density can have impact on tensile properties. All the AM as-built samples exhibited a better tensile strength and 0.2% proof strength than the as-cast sample, with a lower elongation rate.

4.6.1.1 Fracture surface analysis

Figure 4.26 shows the fracture surfaces of all the three tensile samples. It is evident that these samples show a mixture of the dimple-type and cleavage-type surfaces with tear ridges. Only a small amount of ductile dimple can be found in low power input samples as presented in Figure 4.25 (a)(b). The large amount of cleavage surface confirmed the brittle property from Table 4.6. With increasing power and speed, the cleavage fracture surface becomes smoother and flatter. There is no visible boundary between cleavage faces. This indicates that a fast scan can cause a lack of bonding between hatches and layers, which confirms the tensile result presented in the table above. A small amount of tear ridges can be found in all three samples indicating some ductile deformation also occurred in the sample. With a higher magnification, the dendrite structure can be found on the fracture surface in all the three samples. Owing to the rapid cooling involved in AM processes, strengthening phases cannot be formed in the sample, No participate particles can be found to prevent the dislocation. The only structure that prevents tensile failure therefor is the cell structure. Open cracks with a length less than 100μm can be observed on all the sample fracture surfaces. It can be concluded that the exsited cracks in as-built samples are the main sites for fracture to initiate.

A large porosity with numerous partially melted powder particles stuck on the surface can be found in sample 3, as shown in Figure 4.25 (c). This internal defect can be considered as the main reason sample 3 has the lowest tensile strength among the three samples. A faster laser scan speed can bring more impact on deployed powder layer and cause the powder splash out. Therefore, the partially melted powder can be spatter-

powder inserted into the melting pool during laser scanning.

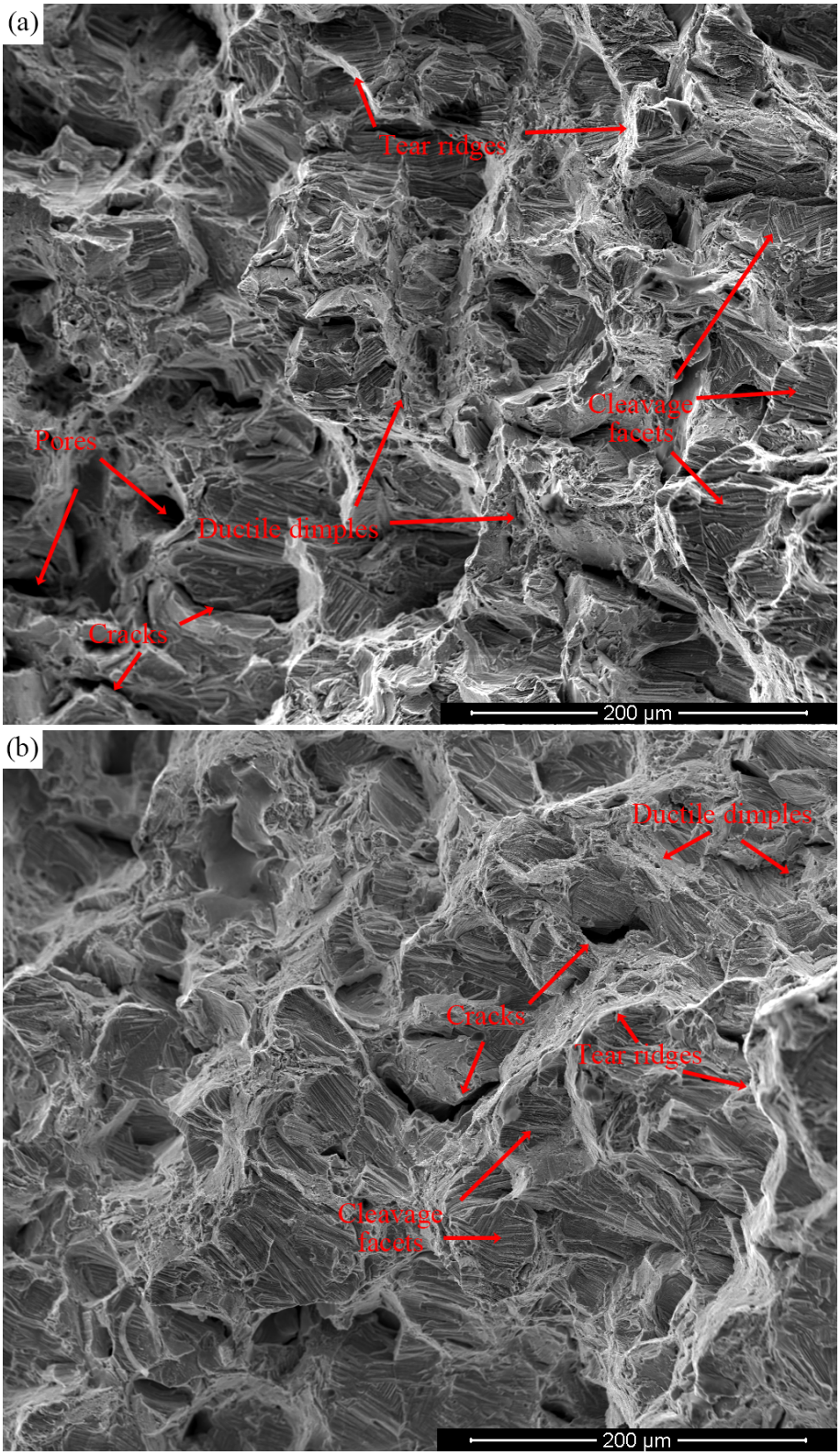

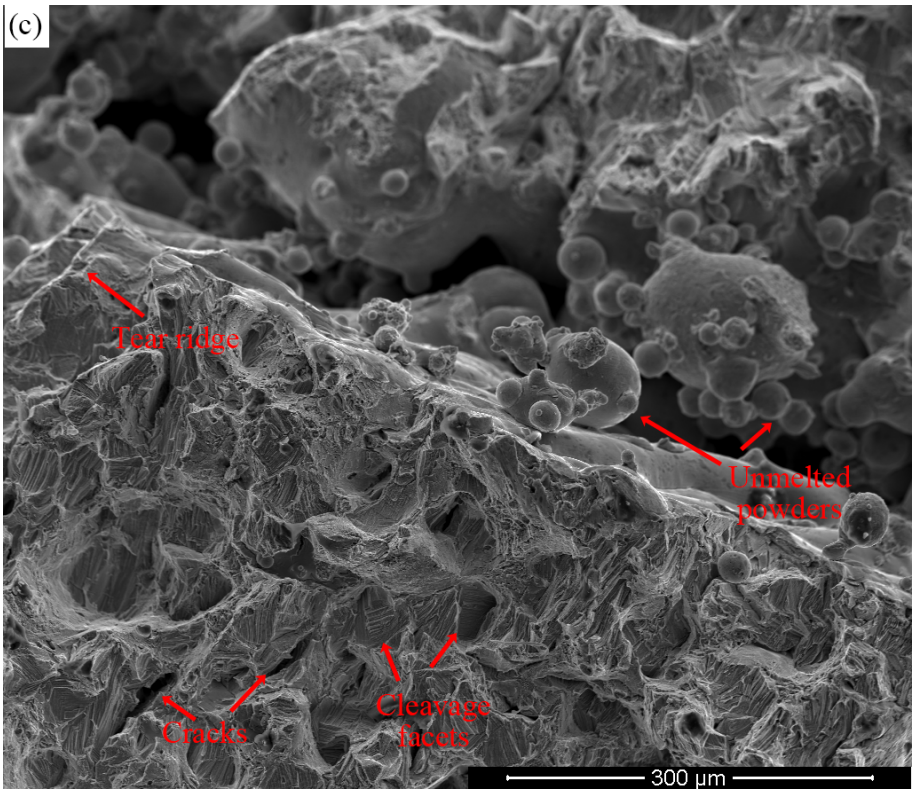

Figure 4.25 Fracture surface of the tensile samples: (a) 120 W, 2.03 m/s, (b) 130 W, 2.2 m/s, and (c) 140 W, 2.37 m/s. Different fracture features can be observed on the fracture surface.

4.6.2 Hardness tests

The hardness test was performed on the cross section of the build direction and the laser scan direction. The results are presented in Table 4.7. Apparently, at a constant laser power, the hardness tends to decrease with an increasing laser scan speed. While, the hardness also decreases with the decrease of power.

Table 4.7 Measured hardness test of the IN713C as-built sample from parametric studies.

Sample ID	Q (W)	V (m/s)	q*/(v*.l*.h*)	Hardness ($HV_{0.5}$)
1-A	190	2.2	3.68	359.64
2-A	190	2.6	2.90	343.84
3-A	160	2.2	3.10	356.13
4-A	130	1.8	3.47	359.6
5-A	130	2.2	2.52	346.73
6-A	110	1	4.69	376.44

In general, it can be seen from Figure 4.26(a) that the hardness reduces when more layers are deposited onto the substrates. As the heat energy can be quickly dissipated by both the substrate plate and the surrounding environment, with an increase in the deposition height, heat energy is dissipated through the substrate with more difficulty. Thus, the cooling rate is lower than at the region close to the substrate. Therefore, with the thickness increase, the grain can growth coarser than bottom part which lead to a reduce of hardness. The thermal profile for the bottom part is more similar to a quenching procedure and produce fine grains, which can increase the hardness.

The hardness on the XY plane in Figure 4.26(b) show no evident trend, which means that the laser scan direction on the XY plane has a limited effect on hardness. This considerable deviation mainly ensues owing to the difference in microstructure between the HAZ and the melting pool. In the previous section, it was demonstrated that fine equiaxed cells could be found, and the area of interaction between hatches, as well as the cell in the centre of the melting pool was more elongated. Defects beneath the test surface can also cause a lack of strength; therefore, the hardness can be lower than the average value at some sites.

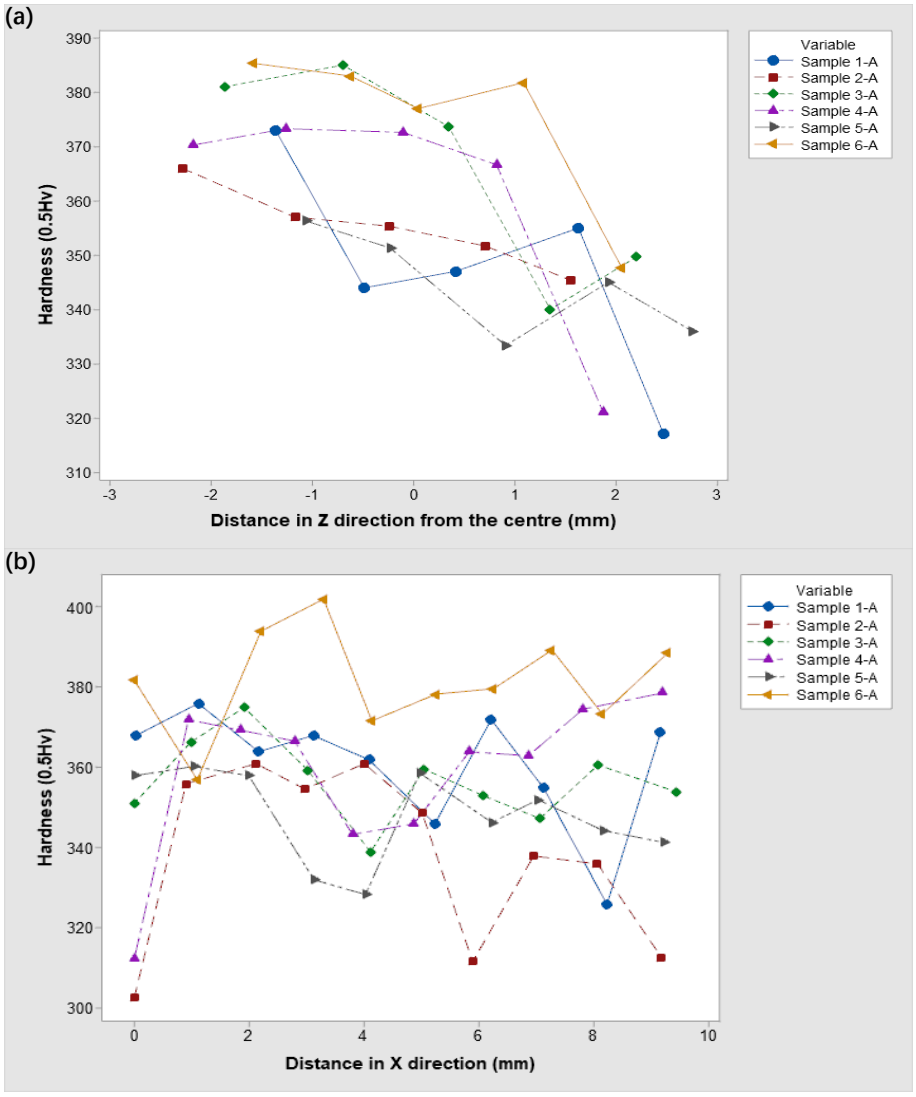

Figure 4.26 Hardness of samples from parametric studies group A: (a) along build direction (Z) with the zero point at centre and (b) horizontal direction (X).

4.7 Discussion

4.7.1 Microstructure and defect mechanism in IN713C AM-fabricated samples

The columnar cell microstructure was observed in all the AM-fabricated samples. The cell orientation exhibits a strong preference along the build direction owing to the rapid cooling of the AM process. Fine, equiaxed cells can be found in the melting pool-overlaid area. The laser can partially remelt the previous hatch; the local cooling rate is

lower than in the other areas. Therefore, the cell can continue to grow and form relative equiaxed cells.

In a low energy density sample, incomplete consolidation causes a small melting pool and induces an LoF. The fast cooling rate also introduces high thermal stress within samples, such that cracks can also be found on the edge of the pores, which are generally sharp and clean. Therefore, the SAC mechanism is responsible for this type of defect.

The zigzag-like crack is the main type of defect can be found in the high energy density sample. Cracks generally lie on the grain boundaries with an apparent dendritic feature on the crack surface. Therefore, the possible mechanism that causes cracks is DDC.

The LoF can be eliminated by increasing the energy input. Owing to the high crack sensitivity of the IN713C sample, a minimum level of cracks (~1% with the highest density of ~99%) always remains. Post-processing approaches, such as hot isostatic pressing (HIP), can be helpful to completely eliminate defects in the AM-fabricated IN713C samples.

The result of the LoF analysis shows the limitation of the two-dimensional (2D) image analysis. Owing to the similar morphology of the LoF and keyhole porosity, the ML code could not distinguish the difference. However, the 2D defect analysis provides a good general relationship between the processing parameters and defects.

The impact of the normalised energy density on the total defect density is depicted in Figure 4.27. The total number of defects was much higher in the low energy density group, which confirmed the result from the density test. When the energy density exceeds the threshold point ($q^*/(v^*.l^*.h^*)\geq 2$), the total amount of defects can be significantly reduced to a level of approximately 2%. Owing to the crack-sensitive nature of IN713C alloys and trapped gas within the powder, the minimum achievable defect is 1.5~2%.

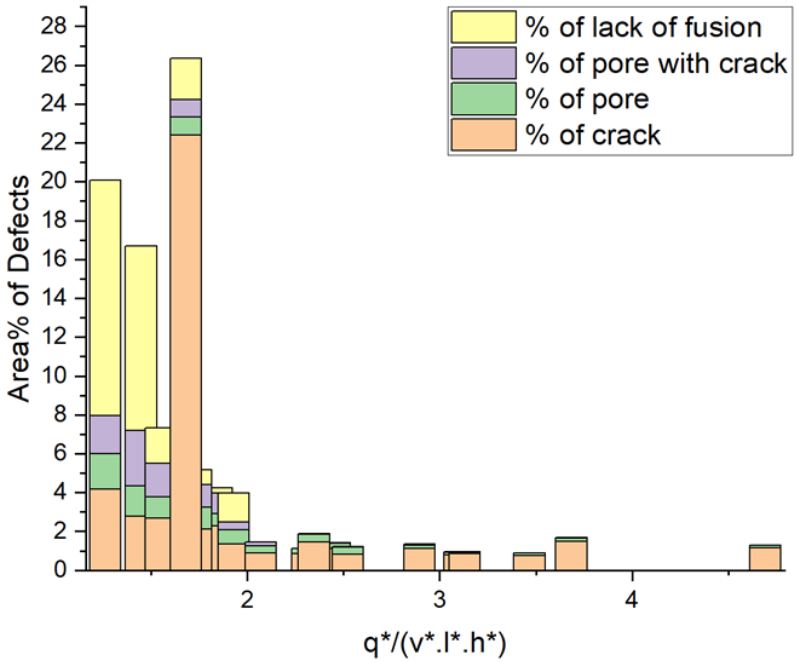

Figure 4.27 Variation of defect density with different normalised energy densities. Crack is the dominated defect type in as-built IN713C. LoF only occurred in low energy density sample.

4.7.2 The optimised parameters for IN713C alloys

The results of the parametric study show that the energy input apparently dominates the solidification process and defect behaviour. The AM-fabricated samples processed at higher energy densities show better densification and lower defect levels. The normalised energy density is a useful tool to identify the optimised processing parameter window; however, the individual parameters have different levels of influence on defect formation.

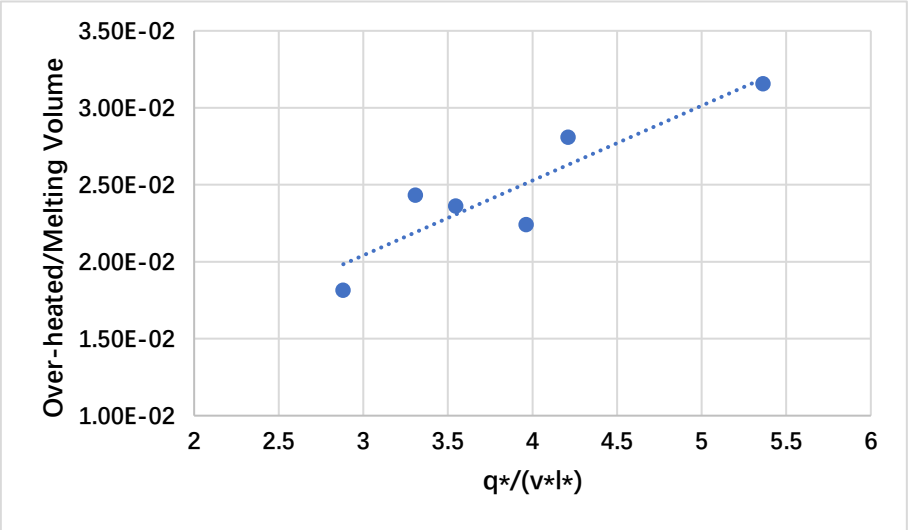

Figure 4.28 Plot showing the linear dependence of the overheated and melting volume ratio with normalised energy input.

Laser power and hatch space have the strongest influence on the melting pool morphology, as well as defect formation. Figure 4.28 shows that the change in the processing parameter directly changes the thermal profile of the melting pool, and, therefore, the melting pool morphology. The laser melting processing in AM is rather complex. The processing parameters are not the only factors that can have an impact on consolidation. Literature shows that the layer thickness, laser spot size, and laser scan strategy can also have an impact on the part qualities. (Carter 2014, Shi 2016, Bean 2018) This parametric study managed to show a processing parameter to minimise defect formation to create a near-fully dense part. The processing window is presented in Table 4.8. With a similar defect behaviour, the large hatch space can reduce the total processing time.

Table 4.8 Optimised processing parameter for the SLM-fabricated IN713C alloy with Aconity3D Mini.

Laser power (W)	**Scan speed (m/s)**	**Hatch space (µm)**	**q*/(v*.l*.h*)**
130	1.6–2.2	40–60	2.3–5.5

***Meander scan strategy; layer thickness = 30 µm, part geometry = 10 mm × 10 mm × 10 mm.**

4.7.3 The effect of laser travel time on the AM-fabricated IN713C sample

The monitor data from the pyrometer show that the laser travel time has a significant influence on the residual temperature of the part. At the same scan speed, it took the laser more time to travel in a large sample than in a small sample; thus, the residual temperature was higher in the short laser travel time sample. The difference in laser travel time directly affects defect formation, as depicted in Figure 4.24. Therefore, the residual temperature, which varies with laser travel time can be a useful parameter to indicate the heat absorption level. For SLM-fabricated IN713C samples, the appropriate processing temperature range is approximately 730–745°C. Because the parts in the parametric study are all 1 cm cubes, it is suggested that the input energy density should be increased for parts with a track length larger than 1 cm and reduced for smaller parts. The model (Freeman, 2019) is designed to predict the melting pool geometry and heat distribution for one laser spot. The results show that the effect of the laser travel time on the single melting pool is negligible. Therefore, the research reveals the limitation of the melting pool simulation. The factor that can affect the cooling rate is complex, including geometry, surrounding and substrate conditions, and the cooling rate can be further expressed as:

$$C_l \propto A_h/(q^*t_l) \qquad \textbf{Eq 4.4}$$

where C_l is the cooling rate of part and A_h is the effective heat transfer area. The q^*t_l function indicates the energy input level; thus, the cooling rate reduces with higher energy input. For large samples, a large surface area can lead to a faster heat transfer rate. Therefore, the residual temperature in the long travel time sample is lower due to the higher cooling rate by geometry.

4.7.4 The effect of processing parameters on precipitation and in-situ heat treatment

During the AM processing, the following laser scan can have heat effect and reheat the previous melting pool, the following layer will also reheat the previous layer to a certain level. The reheat effect is reduced when the laser source is away from the observed site until the heat effect can be negligible. The temperature profile of a certain site during the build can be demonstrated as Figure 4.29. Therefore, when the temperature profile is in the range between the solidus temperature and the γ' solvus temperature can be considered as an in-situ solid solution heat treatment. However, the different temperature levels will have a different magnitude of heat treatment effect. To understand the effective time of heat treatment effect during the build, the Equation 4.5 developed by Higginson (2002) can be used to convert the increment of time Δt_x at any temperature T_x to the heat treatment time Δt_{HT} and associated heat treatment temperature T_{HT}.

$$\Delta t_{HT} = \Delta t_x exp \frac{Q_{act}}{R} (\frac{1}{T_{HT}} - \frac{1}{T_x}) \qquad \textbf{Eq 4.5}$$

Where, Q_{act} is the activation energy for γ' precipitate and R is the gas constant (8.431J/mol.K). The effective heat treatment time is therefore the sum of all equivalent heat treatment time Δt_{HT} for every laser track that is sufficient to have effect on the observed site.

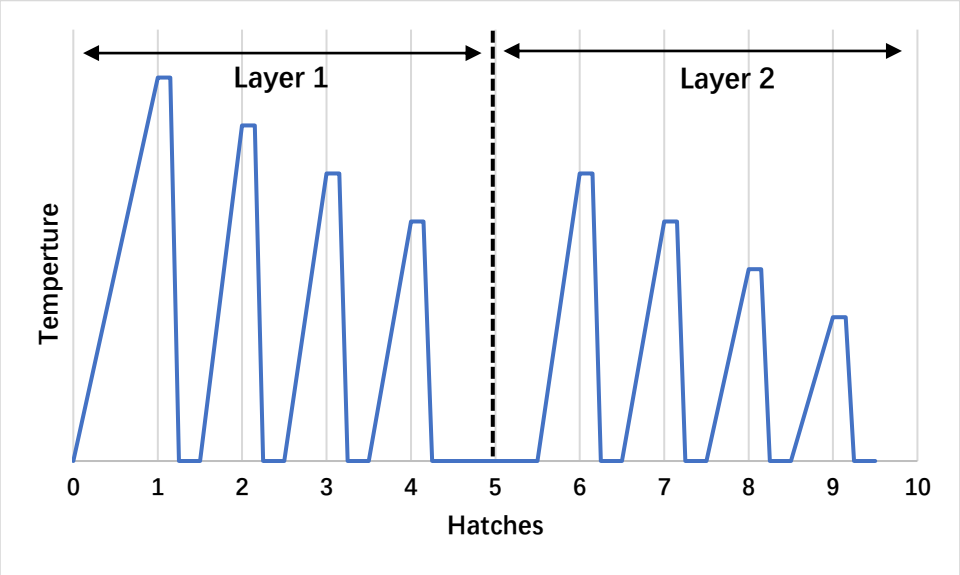

Figure 4.29 A schematic plot demonstrated the reheat effect of following hatches and layers. The effect is reducing with the increasing distance between the observed site and laser source.

In this case, the DSC result from Section 4.1 revealed that the γ' solvus temperature is about 1158°C. The activation energy value of γ' precipitation for IN713C is similar to the value for Waspaloy (Masoumi et al., 2016), owing to the similar element content, although the absolute value of activation energy may not be accurate. Within the same material system, the change in the trend of effective heat treatment time change with energy density can still be revealed. The time is an exponential function of temperature, while the residual temperature is proved in Section 4.3 to be directly affected by energy density and cooling rate. Therefore, the effective heat treatment time as Figure 4.30 and 4.31 presented is exponential depending on the energy density and cooling rate. It can be seen that the highest and lowest energy density is differing with a factor of 1.86, while the effective heat treatment is more than 40 times difference. Although the time duration is only in the unit of microsecond, it may be still sufficient enough to start a very small effect like solid solution treatment. In general, the high energy density can bring much higher heat treatment effect.

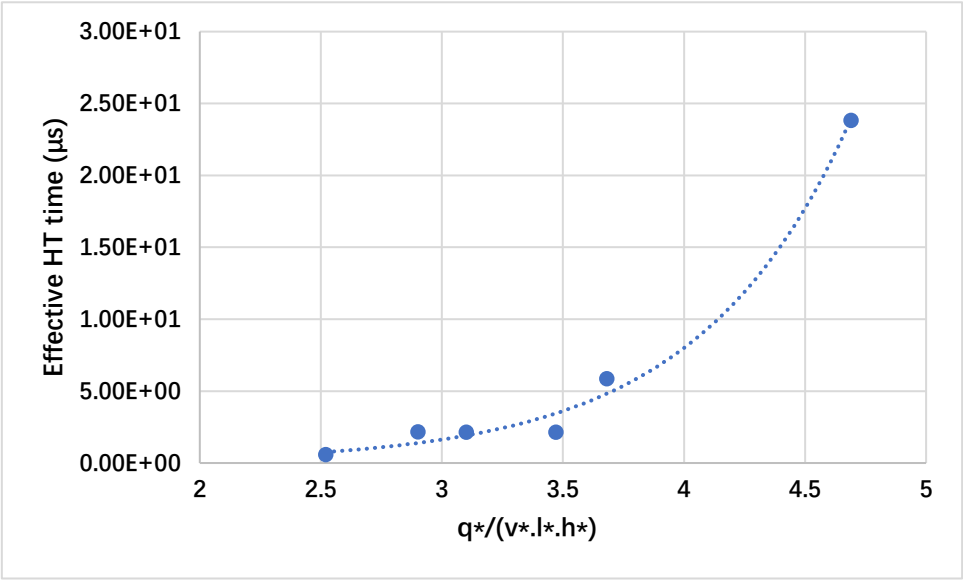

Figure 4.30 The effect of normalised energy density on effective heat treatment time from simulation result.

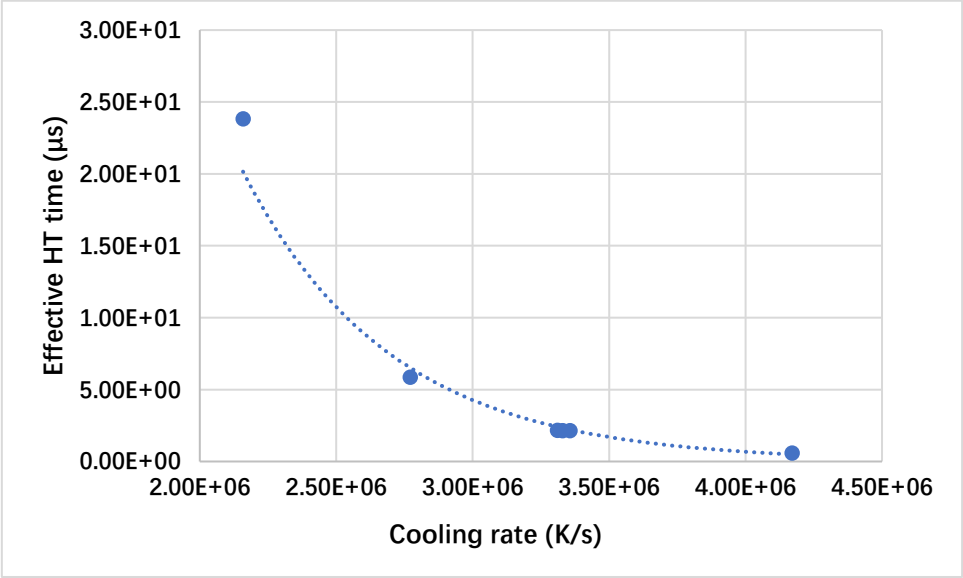

Figure 4.31 The effect of cooling rate on effective heat treatment time from simulation result.

Meanwhile, it can be seen that the high energy density generally reduced the cooling rate, which means the time duration for γ' precipitation is longer. With the limited result, it can be predicted that precipitation is already initiated during the build, while more precipitates can exist in high energy density samples. However, the precipitation time duration is also with a unit in microsecond, the amount of γ' precipitates is not enough to be observed as a major second phase.

4.7.5 The mechanical properties of AM-fabricated IN713C samples

Compared to conventional cast IN713C samples, the SLM-fabricated IN713C samples have better tensile properties in terms of 0.2% proof strength and UTS. With a constant energy density, the tensile result only changes slightly with different laser powers and scan speeds. Moreover, the SLM-fabricated samples generally contain small cell structures within a grain, generally between 500 nm and 2 μm, as shown in the previous section. The small cell structure increases the ratio of surface area to volume. which correlates with a greater ratio of the cell boundary to dislocations. The dislocation can be more difficult to move, thereby leading to a higher strength. However, the elongation rate is much lower than that of the as-cast sample. The fracture surface analysis showed that the main reason for the low ductility compared with the conventional cast sample was the internal cracks. When tensile force is applied, internal cracks can be the fracture initiation. The as-built IN713C sample has a high yield strength but only a moderate UTS relative to other common Ni superalloys, as shown in Table 4.9.

Table 4.9 Tensile properties of the SLM as-built IN713C sample and other common Ni superalloys.

SLM material	0.2% proof strength (MPa)	Tensile strength (MPa)	Elongation (%)
IN713C	747	837	1
IN718 (Aydinöz et al., 2016)	580	845	20
CM247LC (Wang et al., 2017)	792	980	3
IN625 (Rivera et al., 2017)	380	900	58

The hardness of the AM-fabricated IN713C sample is highly influenced by the energy density and cooling rate. The hardness of the sample block decreases with increasing scan speed and decreasing power. Therefore, the hardness of the AM-fabricated IN713C

sample generally exhibits a linear trend, as shown in Figure 4.32.

As Figure 4.33(a) presented, the variation of hardness could be understood as inversely linear with cooling rate. hardness increases as precipitation occurs, thus: the hardness increases with lower cooling rate, which is consistent with the trend of precipitate formation. As a low cooling rate can provide a greater opportunity for γ' precipitation to be initiated. Equally, a higher in-situ heat treatment time can be seen in the low cooling rate sample with more precipitates which can potentially increase the hardness. However, the limited range of the experiment is not enough to cover this discussion conclusively. This would require further research which is beyond the scope of this project. Moreover, the increase of hardness with normalised energy density can be the result of less LoF and pores in high energy density samples. However, as Section 4.5.1 discussed, the excess energy density can induce cracks and key-hole pores, which can also lower the hardness level. The wide distribution of data point with a low coefficient of determination therefore can be caused by the internal defects which is difficult to be qualified.

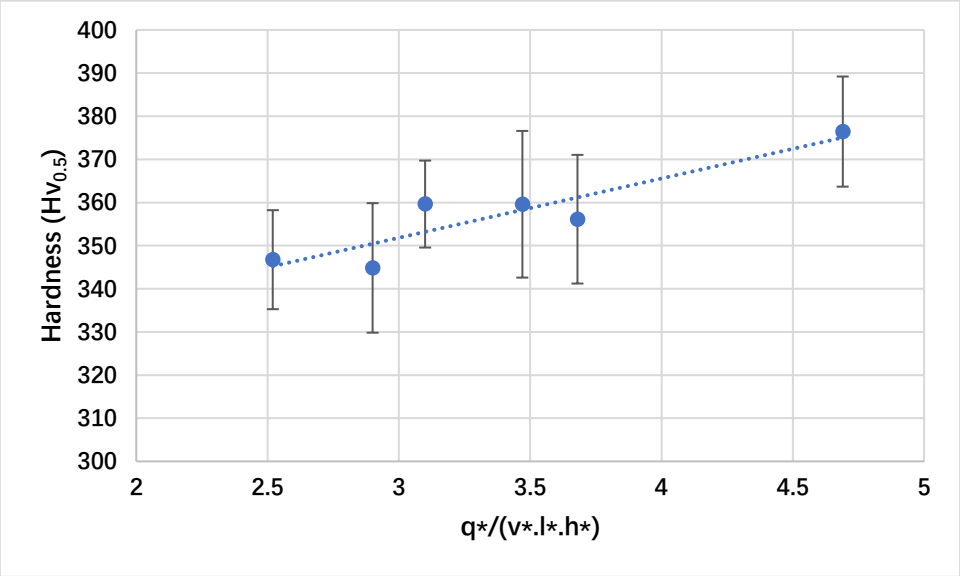

Figure 4.32 Plot showing the linear dependence of hardness with normalised energy density.

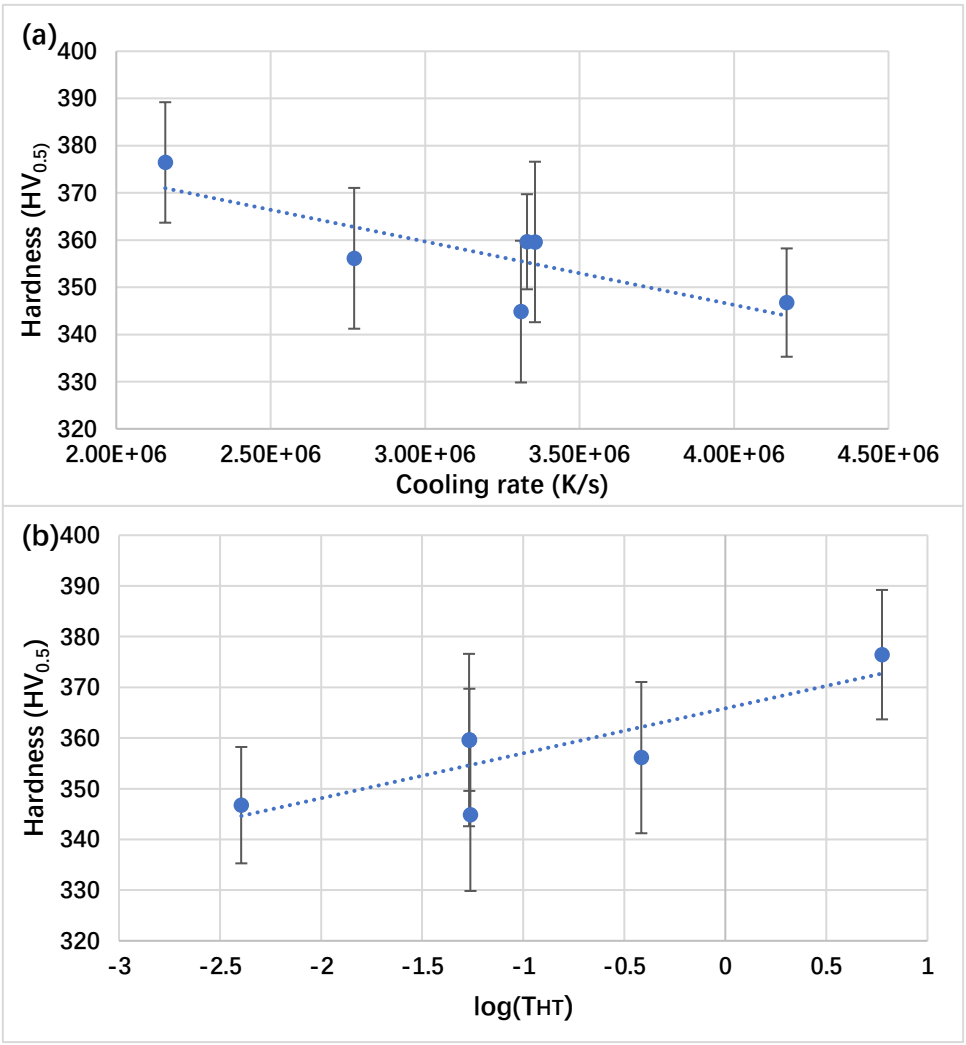

Figure 4.33 Plot showing the non-linear dependence of measured hardness with (a) cooling time (b) effective heat treatment time. The wide distribution of data points is the effect of internal defects.

The mechanical test results generally show that good mechanical properties can be achieved by the as-fabricated IN713C sample, despite the presence of a small number of defects in the sample. The AM IN713C is quite competitive in comparison with other AM nickel superalloys. While literature shows the mechanical properties can be further improved by proper heat treatments.

4.8 Summarising remarks

- A parametric study has shown that the consolidation and defect formation are highly related to the processing parameters.

- The defects in the SLM-fabricated IN713C sample cannot be completely eliminated owing to the high content of γ' precipitates. Under the optimised processing parameters, the main type of defects is cracking on the grain boundary, so the DDC and SAC can be responsible for the defect formation.
- Further research shows that the laser travel time can significantly affect the residual temperature, thereby influencing the defect formation and melting pool morphology. The optimised processing temperature is approximately 730–745°C.
- The simulation and experimental data show the possible recovery and γ' precipitation in as-fabricated samples. The effect is exponential and depends on normalised energy density.
- Hardness can show linear dependence on cooling rate and in-situ heat treatment time. However, the limited experimental data is not enough to cover this discussion conclusively
- Mechanical tests show that the as-built IN713C sample can provide a decent level of mechanical properties compared to the conventionally cast material. Further improvement of the mechanical properties can be achieved by post processing.

Chapter 5 Influence of Heat Treatment on SLM-fabricated IN713C Samples: Microstructure and Mechanical Properties

Results from the previous chapter shows that AM-fabricated IN713C have limited improvement on mechanical properties. This chapter focuses on the effect of heat treatment (HT) on AM-fabricated IN713C alloys. The influence of different heat treatment conditions on microstructure and mechanical properties are investigated. The goal is to produce fine cuboidal γ/γ' microstructure to improve the mechanical properties. Additionally, the experimental results are compared against literature values of conventional cast HT samples to understand the feasibility of HT AM-fabricated alloys.

5.1 Establishing the heat treatment routine for SLM-fabricated IN713C alloys

Notably, IN713C is hardened by the precipitation of secondary phases. To induce the precipitation of these phases (Ni–Al, Ni–Ti, Ni–Nb), heat treatment was conducted at temperatures ranging between 600 and 950 °C. To properly form the second phases, the stabilising elements have to be completely dissolved in substitutional solid solution in the FCC γ matrix; otherwise, the precipitate element may form other phases or combine with other elements. A different precipitation can alter the microstructure and reduce the effect of strengthening. To maintain the proper precipitate function, it is essential to perform a solution heat treatment process as the first step.

The results from the DSC test show that solidus temperature is around 1323 °C, and the temperature of γ' solvus temperature is approximately 1158 °C. The heat treatment performed for the IN713C sample is shown in Table 5.1. All samples were built with the same processing parameter (Table 4.3 (5-A)) HT3 and HT4 was performed to explore the heat treatment effect below γ' solvus temperature

Table 5.1 Heat treatment routine applied to the SLM-fabricated IN713C samples (130 W, 2.2 m/s, 40 μm)

Sample	Solution Treatment	Ageing Treatment
HT1	1176 °C for 2 h (AC)	-
HT2	1176 °C for 2 h (AC)	895 °C for 16 h (AC)
HT3	1076 °C for 2 h (AC)	-
HT4	1076°C for 2 h (AC)	795°C for 16 h (AC)

5.2 The effect of heat treatment on the microstructure

5.2.1 The microstructure of the as-built sample

The columnar grain structure can be observed in all the samples. The grains in the AM-fabricated samples have a preference for growth towards the build direction (Z-direction). The grain continuously grew through the deposited layers. When the laser partially melts the previous layer, the grain provides an easy crystallographic growth orientation along the build direction. The newly deposited material therefore solidifies epitaxially across the layers. Figure 5.1 shows that, unlike in the conventional processing method, the grains in the AM-fabricated samples contain finer elongated cellular microstructures with a width of approximately 2–3 μm. The orientation of cells generally followed the grain orientation, but the growth was impeded by the grain boundaries.

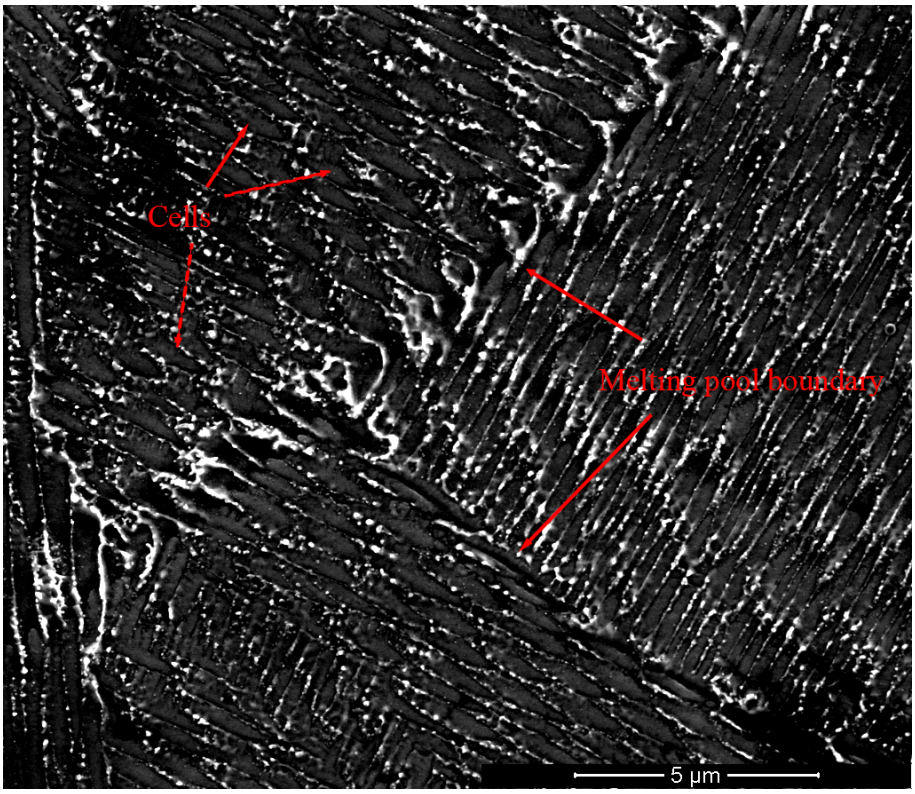

Figure 5.1 SEM of the fine cell structure and melting pool boundaries in the SLM as-built IN713C sample.

The XRD results of the as-built sample are presented in Figure 5.2. Peaks were detected at 2θ = 43.5°, 50.8°, 74.7°, and 91.1°. Thus, the as-built samples only exhibited FCC structures, which were the γ/γ' phase with different lattice parameters. No carbides or other phases were detected. Moreover, AM can be classified as a rapid solidification process. The solution elements, such as Cr, Mo, and Nb, are trapped within the Ni matrix under rapid solidification conditions; thus, the phase transition is difficult to initiate. However, carbides are also difficult to aggregate and precipitate within a short duration.

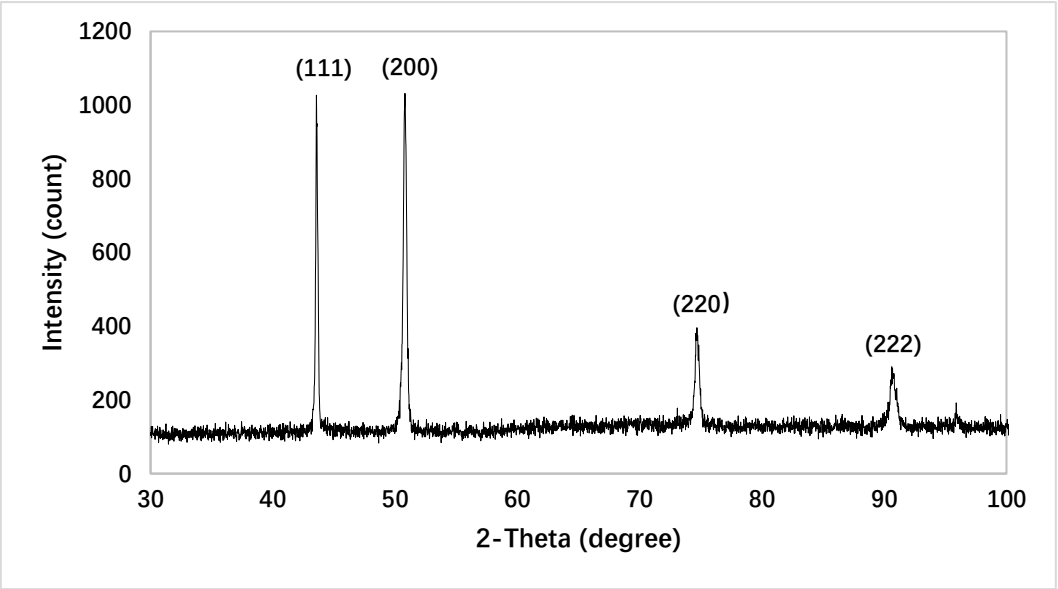

Figure 5.2 XRD profile of the SLM as-built IN713C alloys; labelled peaks are the typical γ/γ' values.

The SEM image and EDS map indicate that no visible γ' phase can be observed in the as-built samples. Some light precipitates can be found at the cell boundary, while the EDS map shows that these are fine borides and carbides. The EDS map in Figure 5.3 shows no excess of γ' phase. However, owing to the rapid cooling rate, no γ/γ' matrix can be found in the as-built sample.

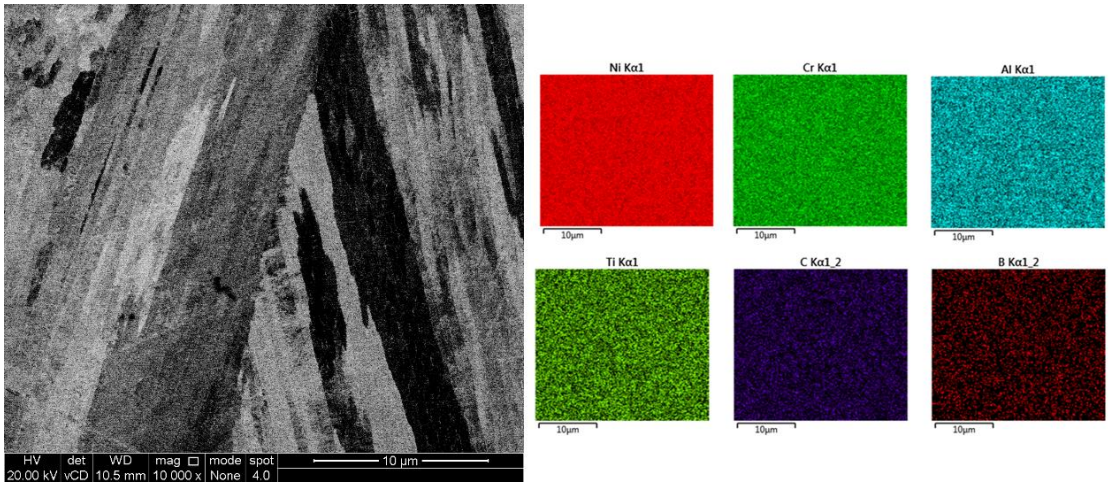

Figure 5.3 BSE-SEM micrograph of elongated grains in the SLM as-built IN713C alloys and the EDS mapping analysis. EDS results show no significant precipitation and segregation across the map.

5.2.2 The microstructure of the 1176 °C/2 h sample

The SEM image of the etched sample shows a typical γ/γ' matrix structure. Both coarse and fine γ' particles can be seen in Figure 5.4. The coarse primary γ' particles tended to be more spherical, while the fine secondary γ' particles showed a more cubic-like morphology. The secondary γ' have a size range between 50-150 nm can be found uniformly distributed around primary γ' within the grains. Large irregular γ' with a size between 1-2 μm can be found preferably precipitated at the grain boundaries White precipitate particles are found on the grain boundary, which can be MC-type carbides with a size range between 0.3-0.6 μm. With only solid solution HT, the dissolution of γ' participates is very limited, the morphology of γ' participates can be seen similar to the pattern in conventional cast nickel superalloy (Huang et al., 2004; Yoo et al., 2020)

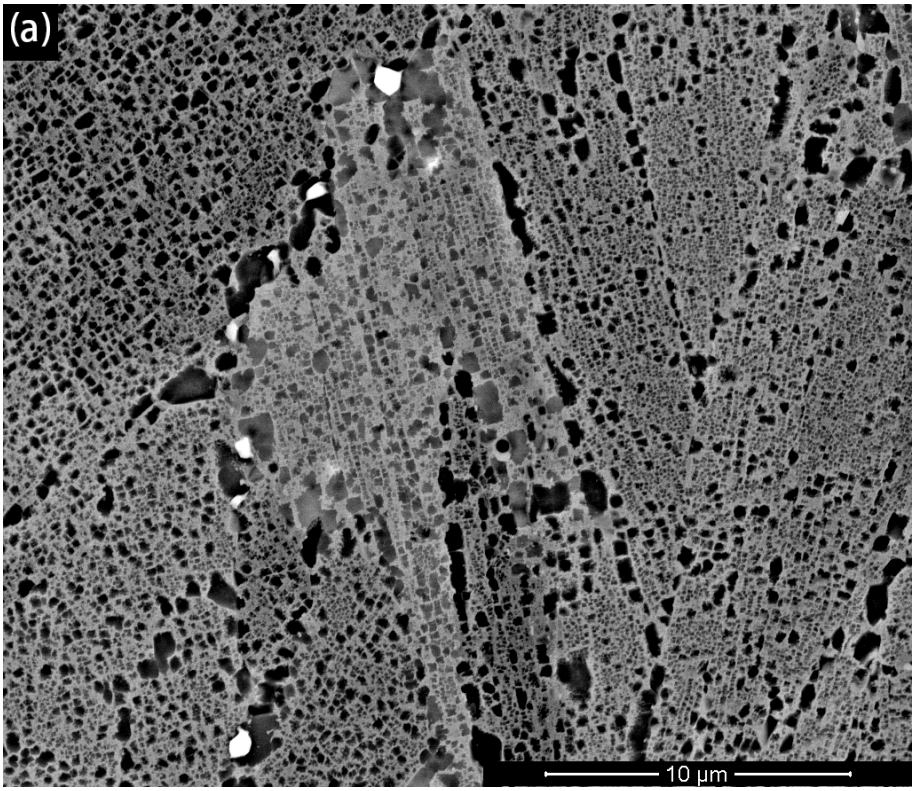

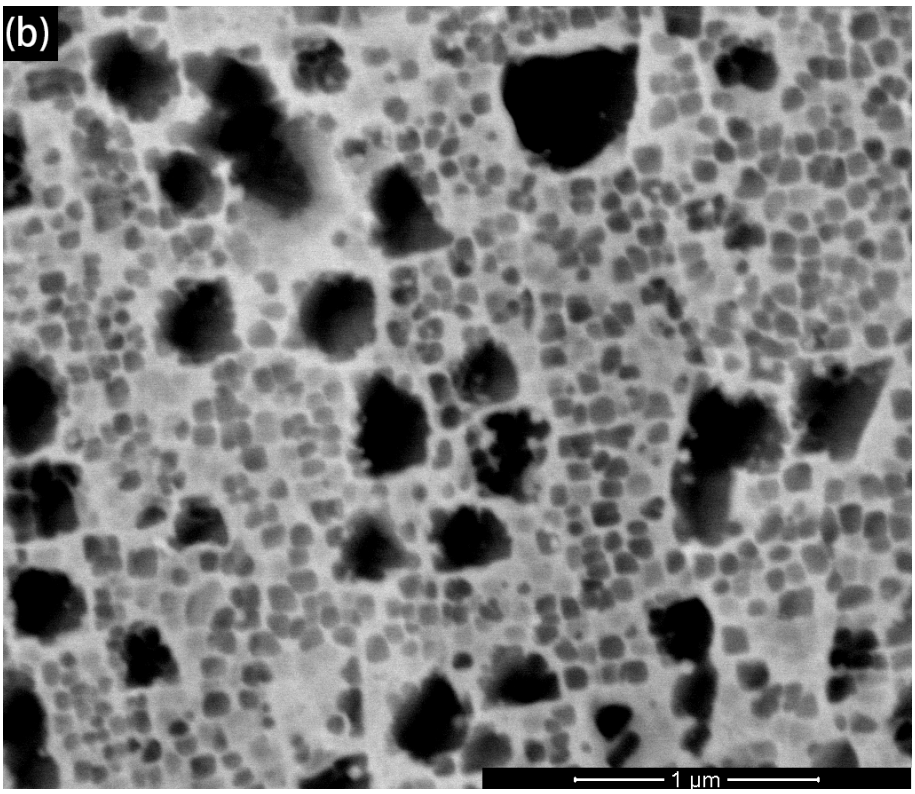

Figure 5.4 SEM micrograph of the etched, heat-treated SLM-fabricated IN713C sample (1176 °C/ 2 h) (a) low magnification image shows typical γ/γ' matrix with white carbide particle on grain boundaries (b) high magnification image shows spherical primary γ' and cuboidal secondary γ'.

The EBSD map shows that the coarsening effect started in the sample. Low-angle boundaries started to dissolve into the grains, while the high-angle grain boundaries remained. Figure 5.6 shows 3 weak off-axis peaks in {100} and 1 weak peak in {111}, as the microstructure of the HT1 sample is more cubic-like. However, the grain orientation was still generally towards the build direction with a relatively elongated morphology.

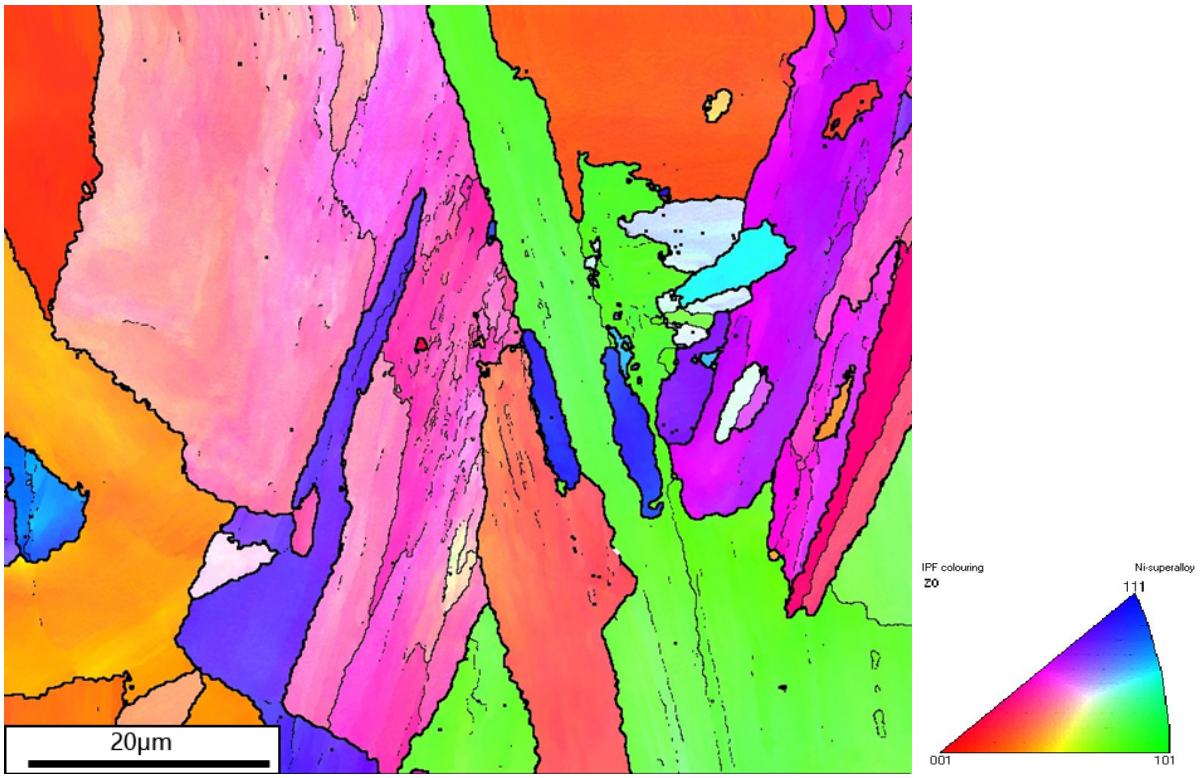

Figure 5.5 EBSD orientation map of the heat-treated SLM-fabricated IN713C sample (1176 °C/2 h) in the build direction (X-Z plane). Grain coarsening effect started.

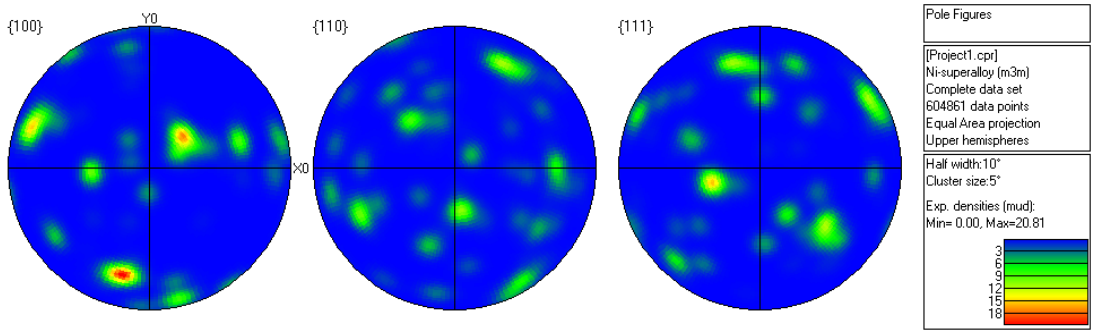

Figure 5.6 Pole figures corresponding to Figure 5.5 showing off-axis peaks in {100}{110}{111}.

5.2.3 The microstructure of the 1176 °C/2 h + 895 °C/16 h sample

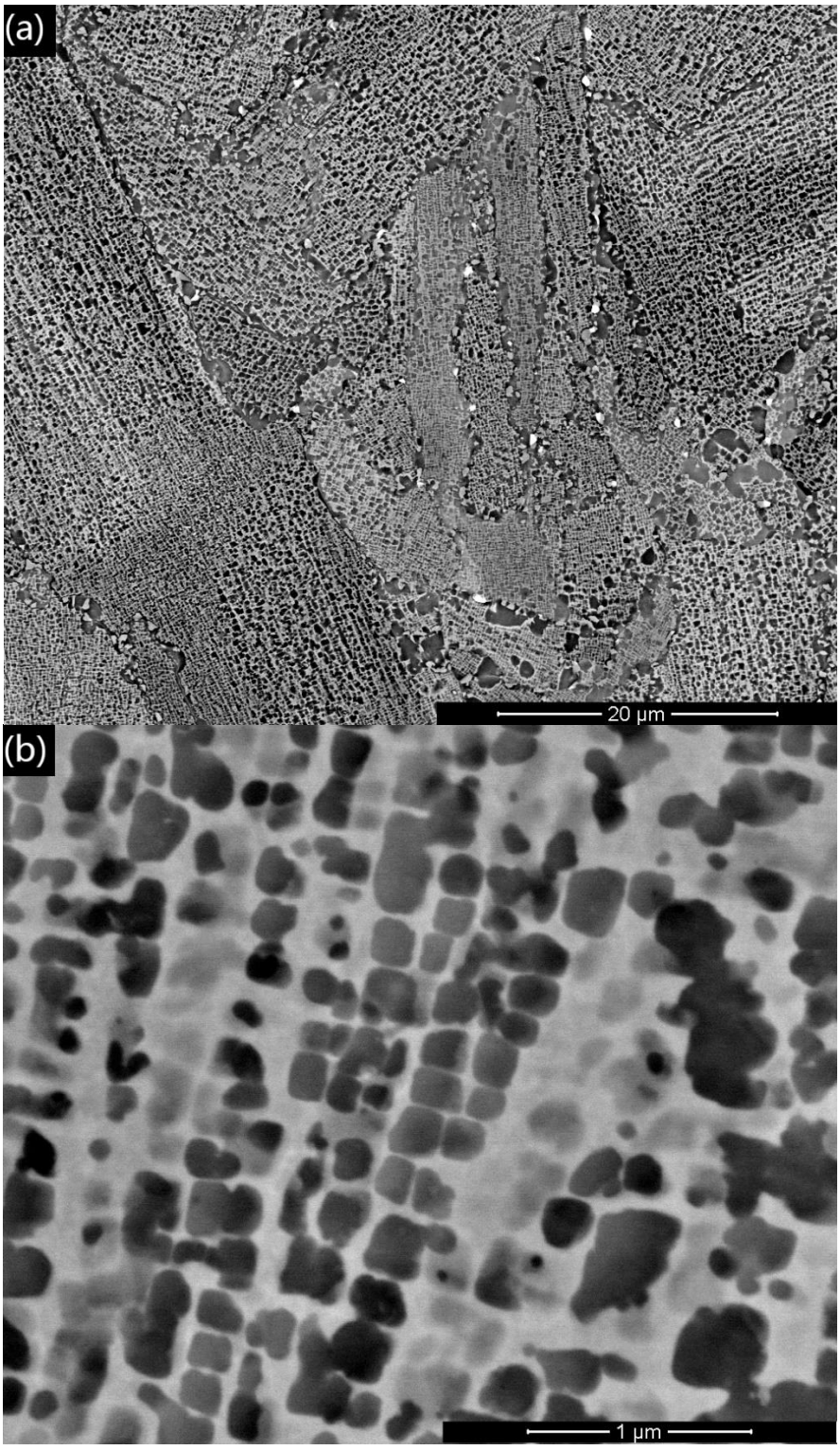

Figure 5.7 SEM micrograph of the etched, heat-treated SLM-fabricated IN713C sample (1176 °C/2 h + 895 °C/16 h) (a) low magnification image shows fine γ/γ' matrix with white carbide particle on grain boundaries (b) high magnification image shows homogeneous fine cuboidal γ'.

With the ageing heat treatment, uniform cubic-like γ' particles become evident in the etched sample. The array of cuboidal γ' precipitates can be seen in Figure 5.7 (b). The size of the γ' particles tend to be homogenous cubic-like with a length approximately 100 nm. Large irregular γ' precipices can still predominantly grow at the grain boundaries. Owing to the dissolution of grain the size of γ' precipices at boundaries increases to 5-7 μm. Fewer white carbide precipitates can be observed in the sample. The carbides are still mainly located at grain boundaries with a size range between 0.4-0.6 μm.

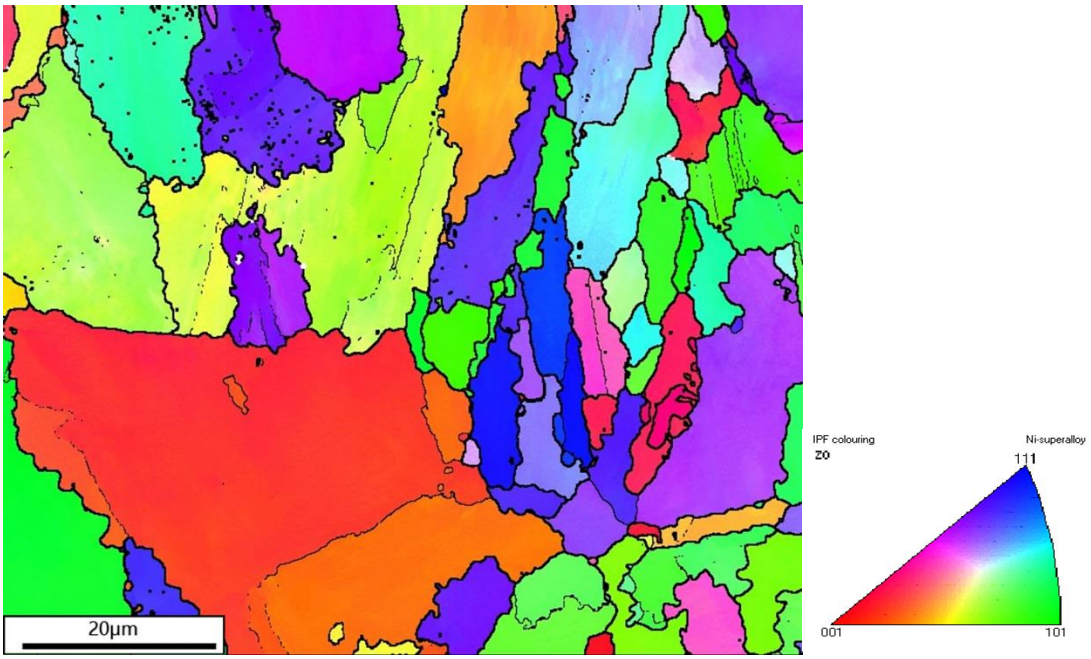

Figure 5.8 EBSD orientation map of the heat-treated SLM-fabricated IN713C sample (1176 °C/ 2 h + 895 °C/1 6 h) in the build direction (X-Z plane).

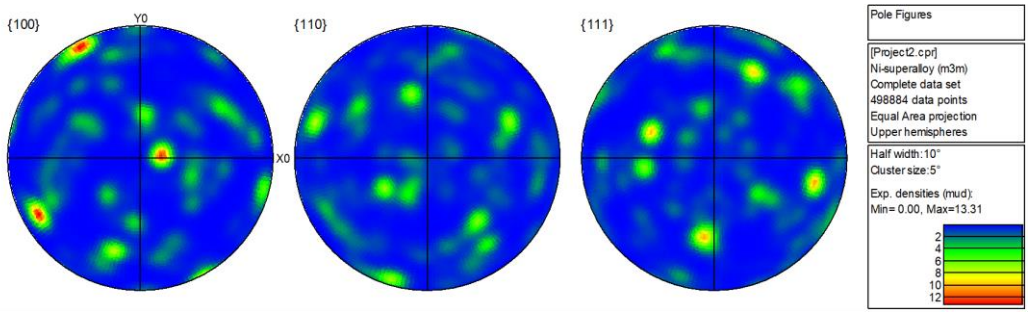

Figure 5.9 Pole figures corresponding to Figure 5.5 showing off-axis peaks in {100}{110}{111}.

The EBSD results show that after long ageing, all the low-angle boundaries are

dissolved into grains. The long ageing time also drove grains to become less elongated, similar to the as-built sample. The pole figure still shows a very strong on-axis peak on the {100} plane. However, some variations in orientation start to show, as several weak off axis peaks is shown in the three planes.

5.2.4 The microstructure of the 1076 °C/2 h sample

With a heat treatment temperature below the γ' eutectic point, the γ' particles showed more abnormal growth. Extremely fine γ' particles can be found between the coarse primary γ' particles. The particles which can be identified as secondary γ′ particles tend to be more spherical in comparison with the particles in HT1 sample. The size of secondary γ′ particles is measured between 30-50nm. More white particles can be observed at the grain boundaries with a size less than 1 μm, which can be identified as carbide. The carbide is more globular than the high-temperature heat-treatment sample. Unlike HT1 sample, the smaller carbide can also be found within grains. The chain-like primary γ′ particles that predominantly growth at the grain boundaries have size around 1 which is smaller than the particles in HT1 sample.

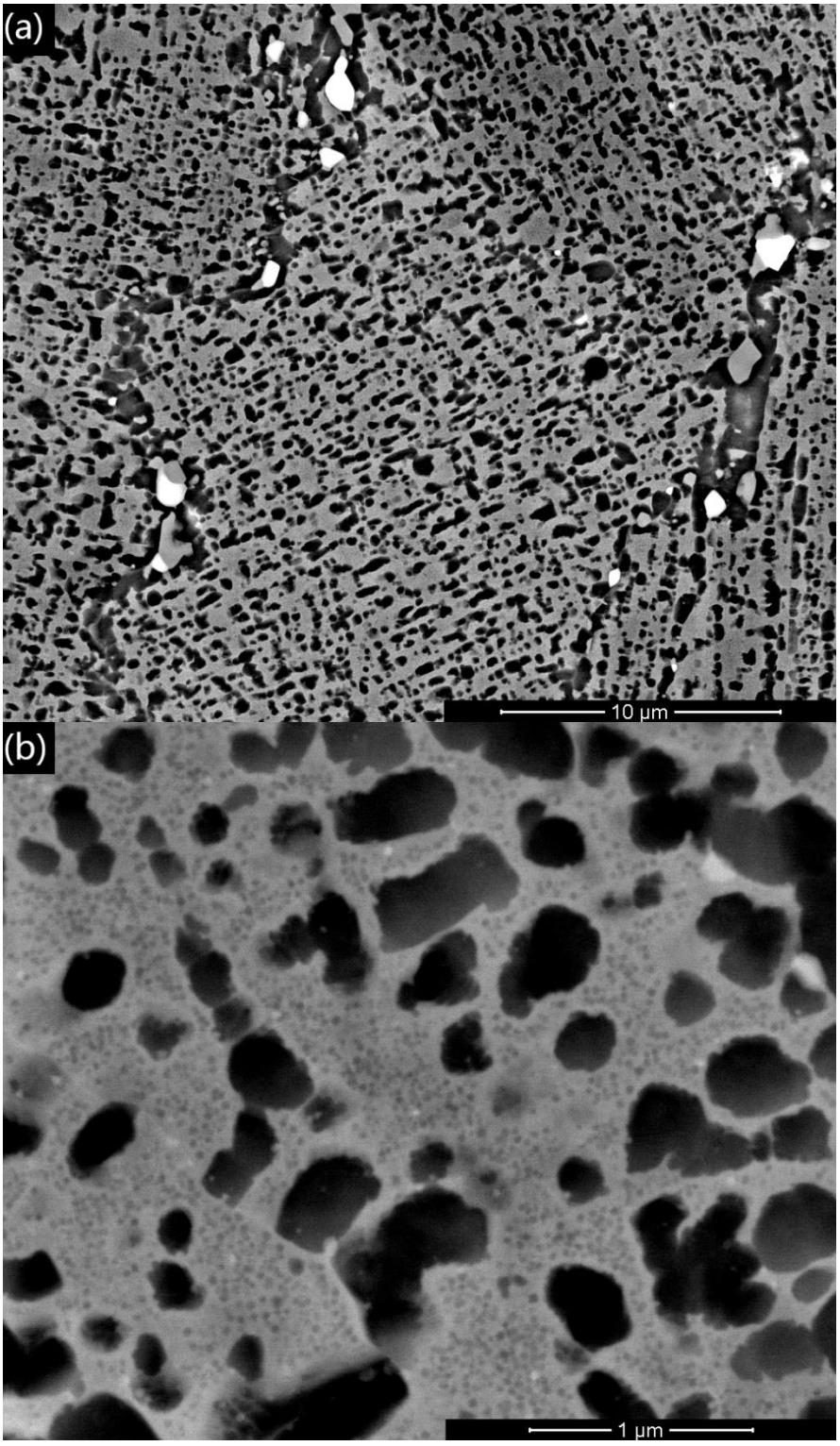

Figure 5.10 SEM micrograph of the etched, heat-treated SLM-fabricated IN713C sample (1076 °C/ 2 h) (a) low magnification image shows wide spaced large irregular γ/γ' matrix with white carbide particle within both grains and grain boundaries (b) high magnification image shows irregular primary γ' and extremely fine spherical secondary γ'.

5.2.5 The microstructure of the 1076 °C/2 h + 795 °C/16 h sample

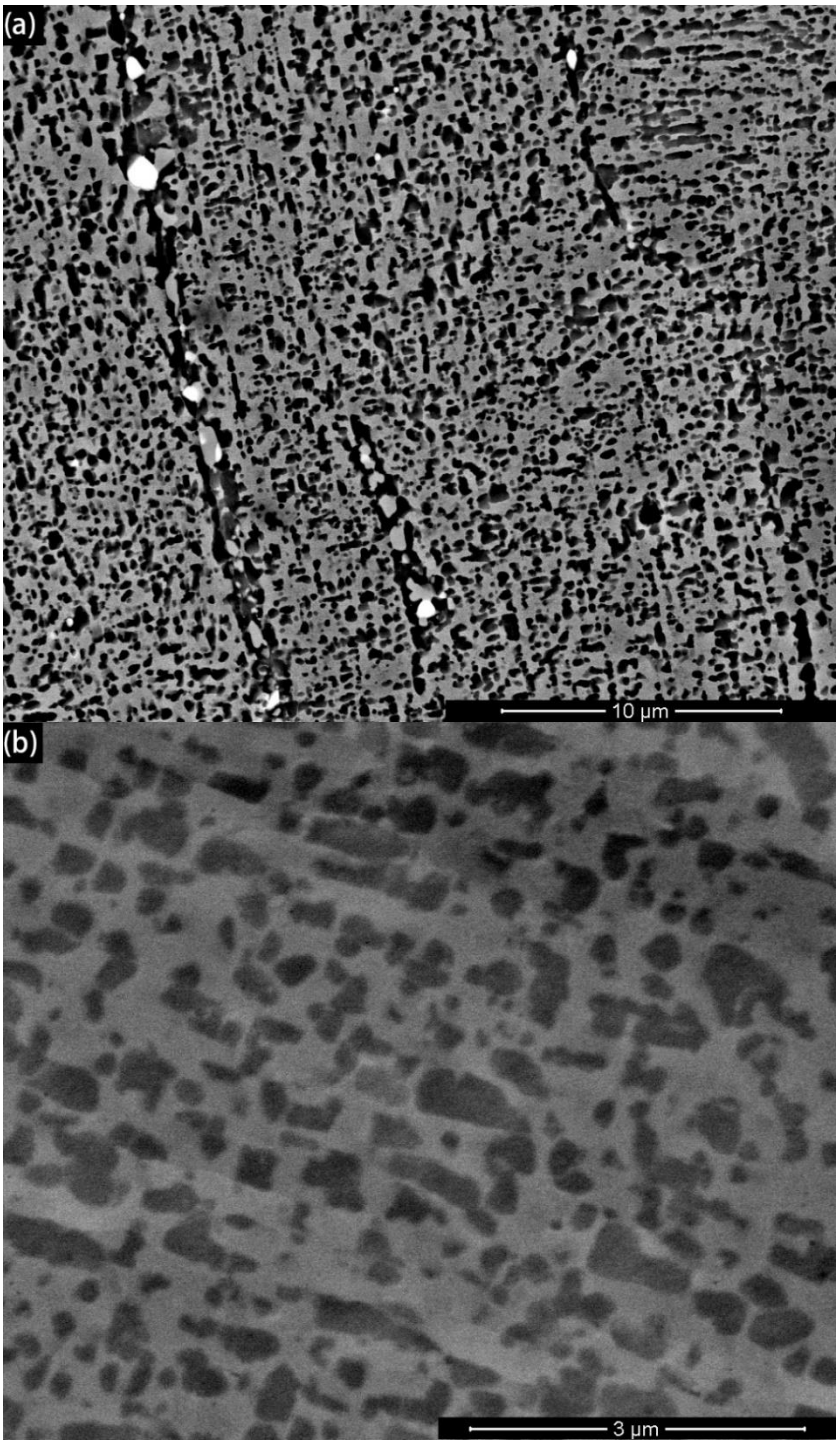

Figure 5.11 SEM micrograph of the etched, heat-treated SLM-fabricated IN713C sample (1076 °C/2 h). (a) Low magnification image shows the γ' particles are still in large irregular shape with wide space. Large carbides can be found within both grain and grain boundary (b) High magnification image shows that some γ' particles start to be more cubic-like.

The effect of γ' dissolving with a low temperature second heat treatment which is very limited compared with the high-temperature heat treatment sample. Non-uniform distribution of γ' precipitates can be observed within grains, as shown in Figure 5.11, ranging from 150 nm to 600 nm in size. Owing to the low ageing temperature, the shape of the γ' particles is more irregular compared to the high-temperature heat treatment sample. The amount of the white carbide was approximately the same as that of the solution heat treatment sample; however, the size of the carbides reduced to 300-500nm, thereby indicating that the carbide was slightly dissolved with long-time ageing. However, the carbides within grains are still not sufficiently dissolved.

5.2.6 Discussion

The areal fraction of the phases in the heat treatment samples is presented in Figure 5.12. It can be seen that the areal fraction of the γ' phase is higher after 16 h of ageing. Both samples with only solution treatment show a coarse and abnormal distribution of the γ' phase. This means that γ' is not completely dissolved within the γ matrix during the solution treatment. With a solution treatment temperature below the γ' solvus point, the areal fraction of the γ' phase in the HT3 sample increased from 37.9% to 41.1% compared with HT1. The average size of γ' increased from 0.54 μm to 0.70 μm. The long-time ageing provides homogenization and re-precipitation of γ' particle. Furthermore, particle agglomeration can be observed in most of the grains, while some fine γ' particles can be found around the primary γ' particle. The above-mentioned results indicate that γ' can hardly be dissolved in this condition. Less carbide can be found in the high-temperature sample, which all concentrate at grain boundaries. In general, with proper heat treatment, carbide can dissolve into base alloy and precipitates at grain boundaries during cooling. However, carbide can be found both in the grains and at the grain boundaries in the low-temperature HT sample, which means the HT3 and HT4 condition can not sufficiently dissolve the intragranular carbides. The existence of intergranular carbide can increase the intergranular embrittlement and reduce the creep resistance.

The γ' particle size and distribution are presented in Table 5.2. It can be seen that, with

an ageing treatment, the γ' particles are more homogenous compared to the solution treatment sample. The average particle size of the ageing sample is higher than that of the solution treatment one, as shown in Table 5.2. This indicates the general coarsening of γ' particles during long-term ageing. This means that a lower ageing temperature also suppresses the growth of the γ' particles.

In general, the melting pool boundaries can be completely dissolved with all heat treatment conditions. No harmful phases are observed in all HT samples. The examination of solution heat treatment temperature shows that the γ' phase can only be sufficiently dissolved into the γ matrix when the temperature is higher than γ' solvus temperature. Thus, the columnar morphology can still be observed in the HT3 sample. The aspect ratio analysis shown in Table 5.2, where the higher aspect ratio represented a more elongated columnar microstructure, and the value of 1 shows a perfect equiaxed grain. The lower grain aspect ratio values for HT1 in comparison with the HT3 sample further confirm the equiaxed development under HT1 condition. Meanwhile the heat treatment temperature below γ' solvus temperature results in larger incoherent γ' particles with a wider inter-particle spacing. Therefore, the solution heat treatment temperature below γ' solvus temperature (HT3) has limited effect on achieving a desired microstructure. The following ageing with HT4 condition only shows limited refinement of γ' morphology, only a small amount of γ' particle start to transfer into cubic structure which means the HT4 ageing condition is much less efficiency than the HT2 condition.

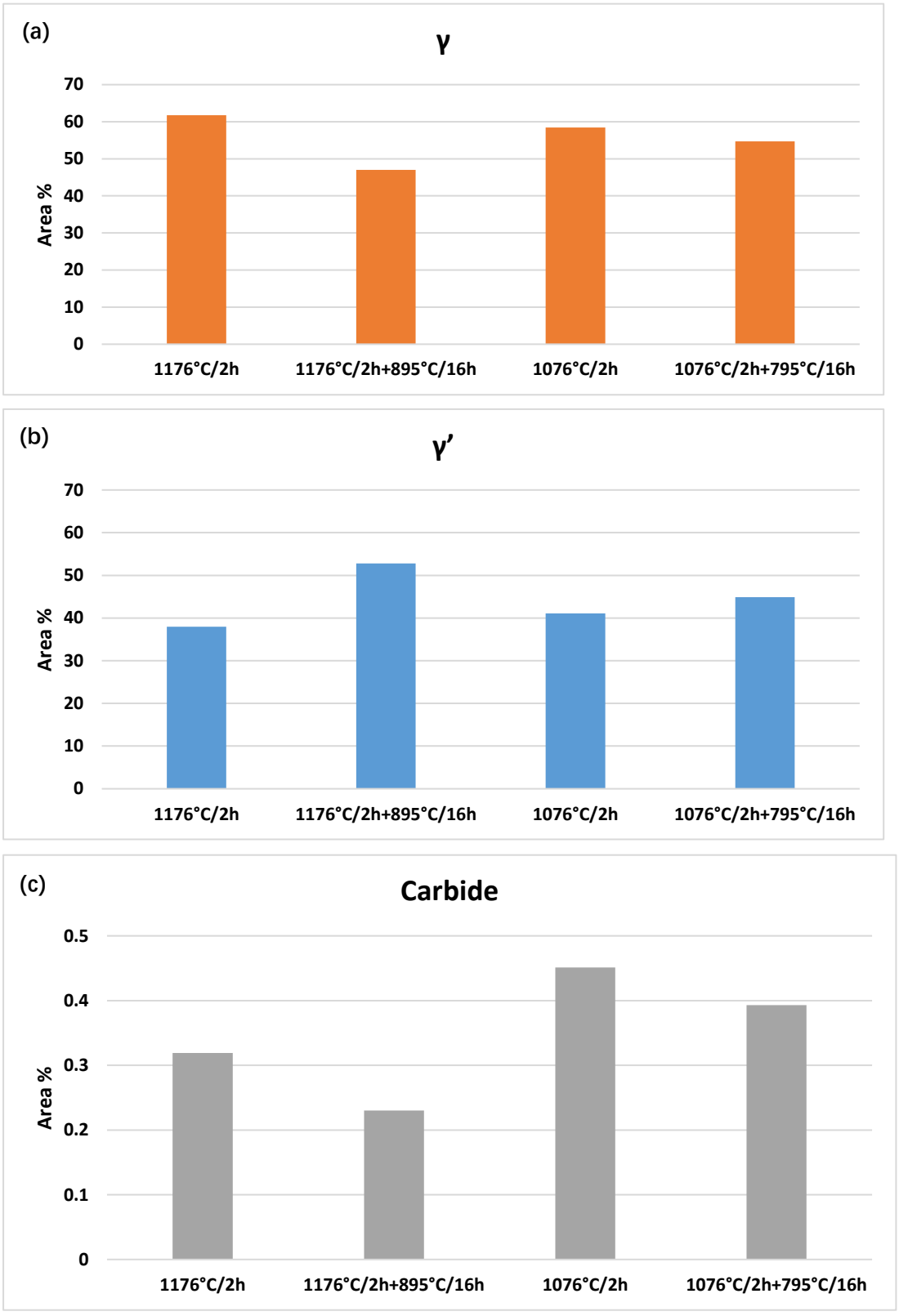

Figure 5.12 Fraction of phases in the heat-treated samples: (a) γ, (b) γ', and (c) carbides.

Table 5.2 Measured particle parameters of the γ' phases in the heat-treated SLM-fabricated IN713C samples.

Heat Treatment	1176 °C /2 h	1176 °C/2 h+ 895 °C/16 h	1076°C /2 h	1076 °C/2 h +795 °C/16 h
Mean particle length (μm)	0.543	0.639	0.703	0.754
Mean particle size (μm^2)	0.153	0.210	0.258	0.302
Mean aspect ratio	1.794	1.940	1.914	1.926

The internal defects of all the heat treatment samples were analysed using the same method for the as-built samples in Section 4.5. The results are shown in Table 5.3. It is difficult to conclude that heat treatment has an effect on defect elimination. The minor change in the defect level in different samples could be related to the individual differences in the origin of the defects in the samples prior to heat treatment.

Table 5.3 Defect densities of the SLM-fabricated IN713C samples after heat treatment.

Sample	% of crack	% of pore	% of pore with crack	% of lack of fusion	% of defects
As-built	0.83	0.34	0.034	0	1.21
1176 °C/2 h	0.81	0.15	0.054	0	1.01
1176 °C/2 h + 895 °C/16 h	1.02	0.18	0.079	0	1.02
1076 °C/2 h	0.96	0.25	0.059	0	1.27
1076 °C/2 h + 795 °C/16 h	0.96	0.22	0.126	0	1.28

5.3 The effect of heat treatment on mechanical properties

5.3.1 Tensile tests

Owing to the limitation of the build platform, the tensile samples were all horizontally built. The UTS, 0.2% proof strength and elongation can be plotted as shown in Figure

5.13 and 5.14. The tensile data presented by Galizoni et al. (2019). for the investment cast IN713C sample are also shown in the figure for comparison.

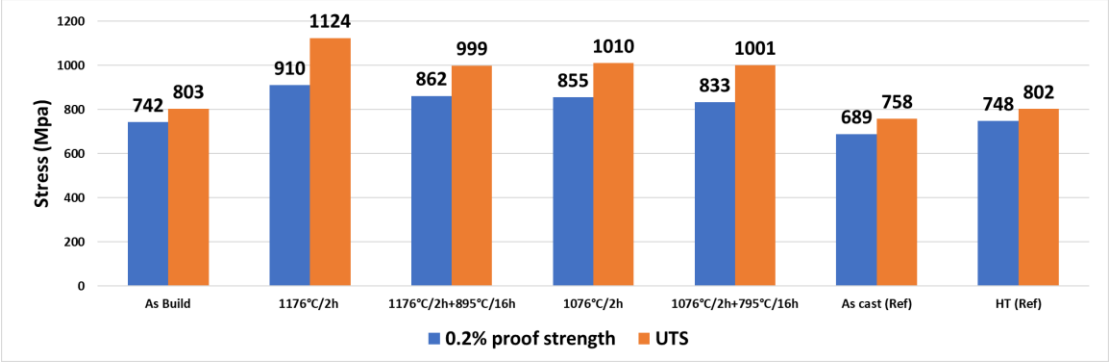

Figure 5.13 Tensile strength of the SLM-fabricated IN713C sample under as-built and heat-treated conditions compared with the cast IN713C sample from the literature.

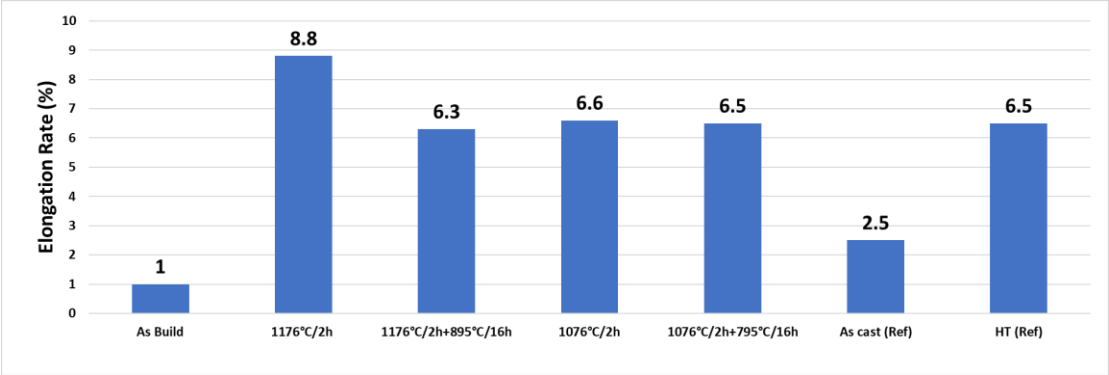

Figure 5.14 Elongation of the SLM-fabricated IN713C sample under as-built and heat-treated conditions compared with the cast and heat-treated IN713C sample from the literature.

Both the 0.2% proof stress and UTS of the AM-fabricated sample are higher than those of the as-cast sample. The cells within grains in the AM-fabricated sample introduce more barriers to prevent deformation when load is applied. It is evident that the as-built sample exhibits a similar trend with a slightly less plastic deformation range compared with the as-cast sample. In general, the as-built sample exhibits a more brittle behaviour than the cast sample, which can be because of the internal defects in the as-built sample. The defects within the sample can easily become the initial point of failure. When the load exceeds the elastic region, the existing cracks can continue to grow and cause the

fracture of the sample.

However, defects still existed in the heat treatment samples. The tensile properties of all the heat treatment samples were still significantly higher than those of both the as-built and as-cast samples. In general, the HT1 sample has the best tensile properties among all the heat treatment routes. The heat treatment at 1176°C brings a significant increase in stress, ductility and hardness. This can attribute to the microstructure refinement with HT temperature above γ' solvus point. The ageing treatment in the HT2 sample caused a decrease in both 0.2% proof stress and UTS after HT1 solution treatment. Ageing treatment can cause coarsening of γ' particles; therefore, fewer grain boundaries exist to strengthen the structure.

The solution treatment HT3 sample with a temperature lower than the γ' solvus temperature showed less improvement in tensile strength. The elongation rate of the HT3 sample is also less than that of the HT1 sample. The areal fraction of the γ' phase of the HT3 sample is only slightly higher than that of the HT1 sample, but the average size of the γ' particles in the HT3 sample is more than 30% compared with the HT1 sample. Therefore, the areal fraction of the γ' particles have a limited effect on the tensile stress. An ageing treatment for the HT3 sample slightly reduced both the 0.2% proof stress and UTS. Ageing treatment at different temperatures (HT2 & HT4) did not cause a significant difference in the tensile properties.

The elongation rate of the AM-fabricated sample is poorer than that of the cast sample owing to the internal defects and elongated grains. However, heat treatment can significantly improve the elongation rate, which means that heat treatment can also improve the ductility of IN713C. More internal defects can be found in the HT3 and HT4 samples. Defects can be the initial point of fracture, which can lead to early failure. Therefore, the 0.2% proof stress of the HT3 and HT4 samples is slightly lower than that of the HT1 and HT2 samples. In general, the tensile properties depended more on the shape and size of the γ' particles. Fine cubic-like γ' particles can benefit from the tensile stress.

5.3.2 Hardness tests

Table 5.4 shows the average hardness data of the as-built and heat-treated samples. The hardness data presented by Galizoni et al. (2019). for the investment cast IN713C alloy are also shown in the table for comparison.

Table 5.4 Average value of the measured hardness for SLM-fabricated IN713C samples under heat-treated conditions compared with the value of the as-cast and heat-treated IN713C samples from the literature.

Sample	Hardness ($HV_{0.5}$)	Standard deviation
As-built	346.76	16.33
HT1	437.23	8.65
HT2	428.68	7.69
HT3	423.19	9.2
HT4	420.59	8.49
As-cast (Galizoni et al., 2019)	343	9.09
Cast - HT1(Galizoni et al., 2019)	392	9.09
Cast - HT2 (Galizoni et al., 2019)	362	9.09

It can be seen that the hardness of the as-built sample is similar to that of the cast samples. Heat treatment can significantly increase the hardness of the samples. The HT1 sample presented the largest improvement in hardness at 437.23 HV. Solution treatment can refine the size of γ' particles. Higher solution treatment temperatures are better for refining coarse particles with finer sizes. The fine particle as impurity phase prevents the movement of defects and dislocations. Therefore, the hardness of the HT1 sample is higher than that of HT3. The application of ageing treatment causes the coarsening effect of γ' particles. Therefore, the hardness of the HT2 sample is lower than that of the HT1 sample, while that of the HT3 sample is slightly higher than that of the HT4 sample. Moreover, the sample with ageing treatment had a lower standard deviation of hardness. This means that the hardness across the ageing sample is more consistent compared with the solution treatment sample. During the ageing treatment, smaller particles dissolved into large particles follow the Ostwald ripening theory. The grain size after the coarsening effect is more uniformly distributed, so the hardness

properties are more isotropic.

Figure 5.15 and 5.16 displays the effect of the γ' particle size and areal fraction of the γ' phase. The increase in the γ' particle size also causes a decrease in hardness. However, when the particle size is larger than a threshold point, it has a limited effect on hardness. With an increase of γ' particle size, the interaction between dislocation and γ' particles transform from shearing to Orowan looping. The threshold point can be the point where the transform starts, which request a TEM analysis to further confirm the result in the future research. The threshold point of the particle size in IN713C is approximately 0.6 μm, and the effect of the γ' areal fraction is not evident.

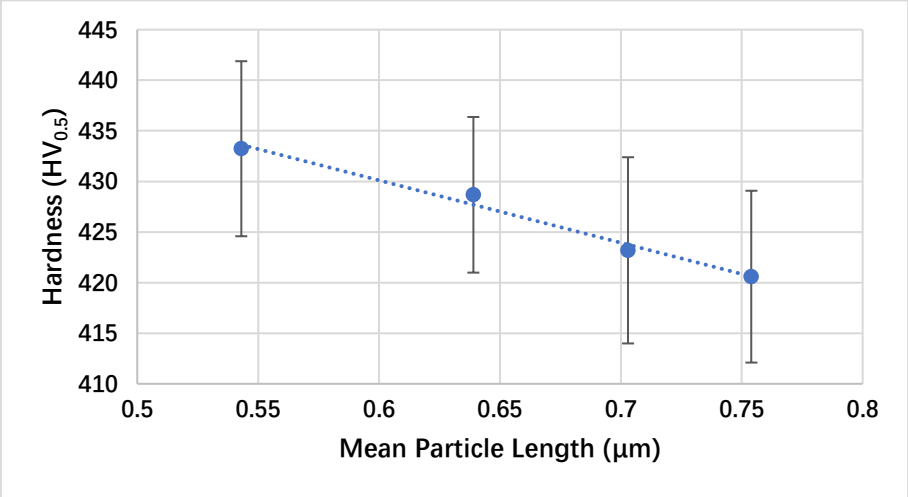

Figure 5.15 Plot showing the hardness versus γ' particle length in SLM heat-treated IN713 samples.

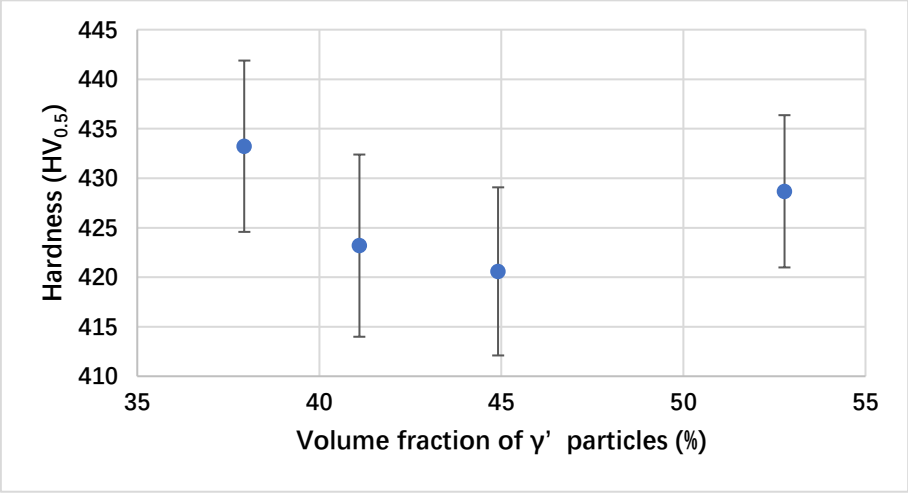

Figure 5.16 Plot showing the hardness versus volume fraction of γ' particles in SLM heat-treated IN713 samples.

5.3.3 Discussion

5.3.3.1 Tensile tests

No obvious γ' precipitates are presented as a second phase in as-fabricated samples; therefore, the strength is only enhanced by grain boundaries and solid solution strengthening. While the formation of γ' precipitates as a second phase can be found in all samples with different heat treatment conditions. The γ' precipitates can further strengthen the sample and improve the yield strength and UTS in comparison with as-fabricated samples. The fine cubic γ' precipitates in HT1 condition can provide better resistance to dislocation therefore enhance the tensile strength. The formation of carbides at the grain boundaries combine with the equiaxed γ/γ' matrix provides the higher elongation in compare with as-fabricated samples. The carbide precipitates on grain boundaries during cool down also prevent the movement and dislocation, because the carbides are too difficult to deform. Although the microstructure of HT2, HT3, HT4 conditions are all different, the room temperature tensile values are close. The difference may be revealed with an elevated temperature tensile test. In general, the influence of each factor on tensile properties is very difficult to differentiate in a complex alloy system.

Owing to the lack of tensile data of conventional cast IN713C with the same routine, the heat treatment data from the research of Yoo et al. (2020) were used as the HT reference sample. It can be seen that all the heat-treated SLM samples have better yield and tensile strength compared with the heat-treated conventional cast sample. As the grains in the SLM-fabricated samples are still elongated towards the build direction, less grain boundaries can be the initial point of fractures.

5.3.3.2 Hardness tests

The hardness of the SLM-fabricated IN713C sample was significantly improved compared to that of the cast IN713C sample under the same heat treatment conditions. The improvement of hardness is also attributed by the appearance of γ' precipitates. In

general, finer grain structures can provide better hardness performances. The coherent fine γ' particles in HT1 condition leave more grain boundaries with a smaller mean free path. Accordingly, when force is applied on the same area, it can be more effective to block the dislocation and form the antiphase boundaries APB. Hence, both the volume fraction of the γ' particles and particle length influence the hardness; The exist of internal defects can still reduce the hardness, as Section 4.7.5 discussed. However, the amount of defect in heat treatment are very close, thus the effect of internal defects on each sample can be considered as the same magnitude.

5.3.3.3 Order strengthening

The ordered coherent γ' precipitates can create APB on the slip plane of the precipitate to strengthen the structure when dislocation occurs. The contribution of the order strengthening effect on shear stress (τ) for heat treatment samples can be calculated using the equation below: (Cahn et al., 1993)

$$\tau = 0.7\sqrt{\frac{\omega T_L V_P \gamma_{APB}}{b^2 a}} \approx A\sqrt{\frac{V_p}{A}} \qquad \textbf{Eq 5.1}$$

Where, ω is the microstructural parameter, T_L is the line tension of dislocation. A is the constant. With the experimental data, a linear dependence of hardness and 0.2% yield strength corresponding to the volume fraction and size of γ' precipitates can be revealed, as shown in Figure 5.17. Therefore, the hardness increases with a higher fraction of the γ' precipitates or finer particle size.

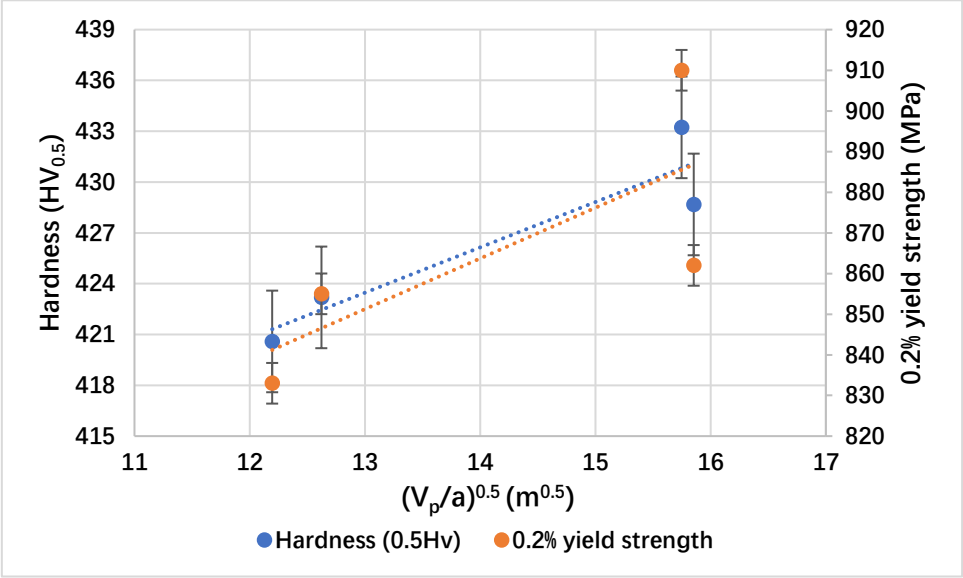

Figure 5.17 Dependence of hardness and 0.2% yield strength on volume fraction and particle size of the γ' phase in SLM heat-treated IN713C samples.

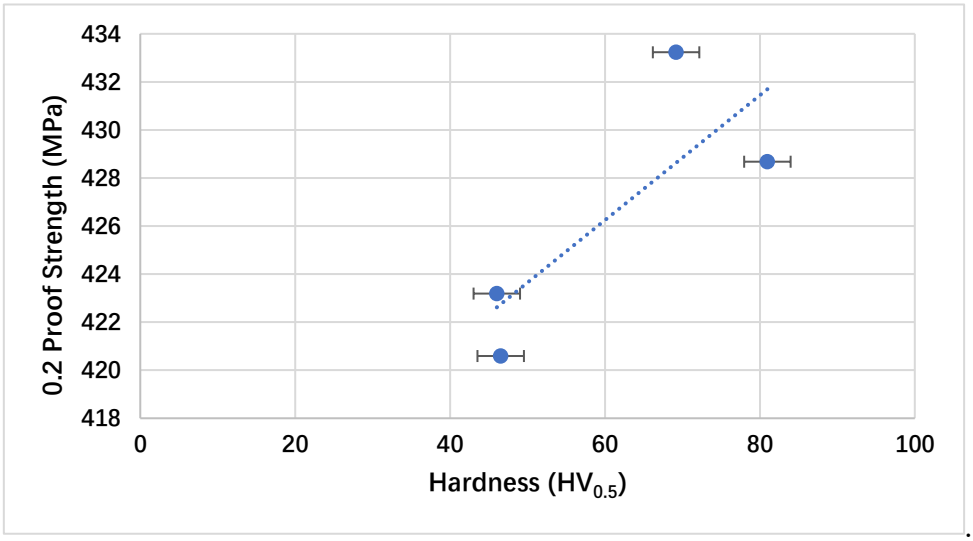

Figure 5.18 Linear dependence of hardness and 0.2% proof strength in SLM heat-treated IN713C samples.

According to Lapin et al., a linear relationship exists between the 0.2% proof stress and hardness in CMSX-4. (Lapin et al., 2009) The above-mentioned result shows that a similar trend can be found in IN713C. Figure 5.18 shows that the yield stress of HT samples can be found to linearly increase with the hardness. The linear regression equation can be calculated as follows:

$$\sigma_{0.2} = 5.4073HV - 1440.8 \qquad \textbf{Eq 5.2}$$

The correlation coefficient of this fit was $R^2 = 0.89$. While the trend of elongation between yield stress and UTS are not clear. Therefore, the equation can be used as a

simple prediction tool to indicate the yield strength from the hardness result for the heat-treated SLM-fabricated Nickel superalloy sample at room temperature.

5.4 Summarising remarks

- The fine γ/γ’ matrix can be found in all the heat treatment samples. The grain morphology is generally oriented towards the build direction. Long-term ageing leads to a coarsening effect of the γ’ particles and the dissolution of carbide. The sizes of the γ’ particles are more homogenous after long-term ageing.
- The heat treatment temperature can have a significant effect on the microstructure and mechanical properties. The γ’ precipitate solvus temperature is a key threshold point in heat treatment. The heat treatment below γ’ solvus temperature has limited effect on microstructure refinement
- Heat treatment has a limited effect on defect elimination. Notably, HIP is necessary to completely eliminate internal defects.
- Heat treatment can significantly improve the mechanical properties of SLM-fabricated IN713C samples. With a solution treatment of 1176 °C/2 h, the samples exhibited the best mechanical properties. The creep property can be researched in the future to fully understand the effect of heat treatment
- Comparatively, the tensile and hardness results of the heat-treated SLM sample are better than those of the heat-treated conventional cast sample. Therefore, the AM-fabricated part is capable of replacing the conventional cast part and provides better mechanical properties.

Chapter 6 Process Study of a Novel Ni superalloy (LR8) and the Associated Challenges

As, LR8 is a newly designed material for AM, the characteristics of the material powder were first determined via a series of tests. The parametric study could then be conducted to acquire an understanding of the processing window suitable for SLM-fabricated LR8. Meanwhile, owing to the defect mechanism in parts, the printability of LR8 via AM can be determined. Because of the powder size limitation of the Aconity3D mini system (maximum 100 μm), the experiment was carried out using Renishaw 125. Therefore, the effect of continuous and pulsed lasers on the AM-fabricated part can also be studied using the melting pool modelling of IN713C and LR8.

6.1 Powder analysis

6.1.1 Powder size distribution

The powder size distribution of LR8 powders, as measured by the Mastersizer 3000, is displayed in Figure 6.1. The particle size distribution range is between 40 μm and 150 μm. The D10 and D90 values suggest that the majority size distribution range of particles is between 68.8 μm and 140 μm. The D50 value suggests that the median particle size is 99.1 μm. There are still some powders with diameters less than 40 μm. These particles can be satellite particles around larger powder particles. Particles with a diameter greater than 150 μm can be as a result of the fusion of several regular particles during powder manufacturing or the excess reuse of the powder after AM. Comparatively, the commercial IN713C powder for AM has powder sizes ranging between approximately 40–60 μm, as shown in Chapter 4.

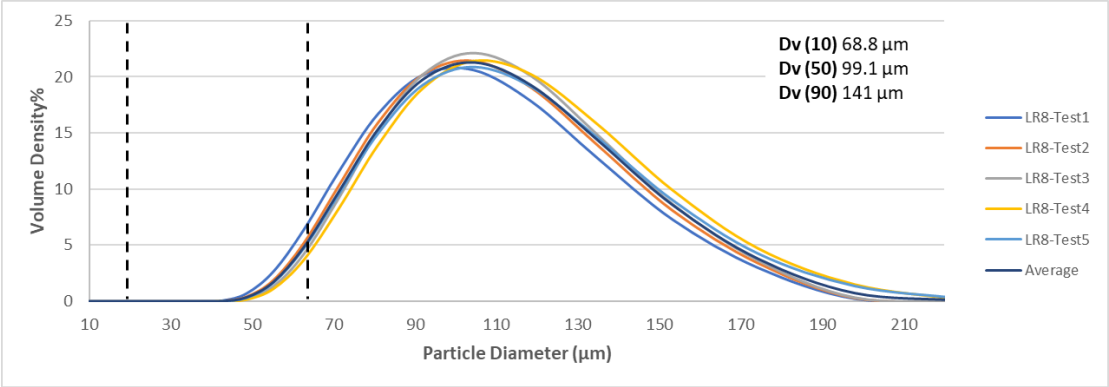

Figure 6.1 Powder size distribution of the LR8 Ni superalloy powder. Black dash lines indicate the ideal powder size distribution for AM. Key size parameters are showing in the figure.

6.1.2 Powder morphology

The powder morphology was analysed using the CLEMEX software. Ideally the roundness and sphericity of AM powder should be between 0.9 and 1. The results in Figure 6.2 show that the powder has relatively low roundness and sphericity. This indicates that the powders are not ideal solid spheres. Strondl et al. (2015) studied that irregular morphology could have influence on the layer densities. A low layer density can introduce more void and therefore potentially reduce the part quality.

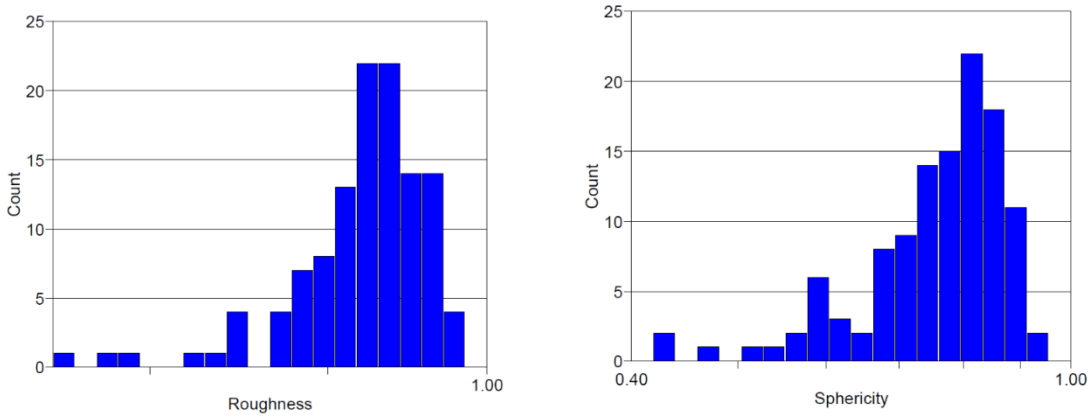

Figure 6.2 Bar charts showing the (a) roughness and (b) sphericity of LR8 powders for SLM. Result indicates the irregular morphology of LR8 powders.

The powder morphology obtained via SEM confirmed the result from the CLEMEX analysis. Numerous irregular particles can be observed in the powders, as shown in the red area in Figure 6.3(a). On the spherical particle surface, an apparent dendritic

structure can be observed, which is formed during rapid cooling. The SEM image also confirmed the results of the powder size distribution session. These extremely small particles are satellite particles around larger powder particles. Several powder particles fused together to form extremely large particles. This phenomenon can be introduced by the inapposite flow rate during powder atomisation or through the reuse of the powder after laser melting experiments.

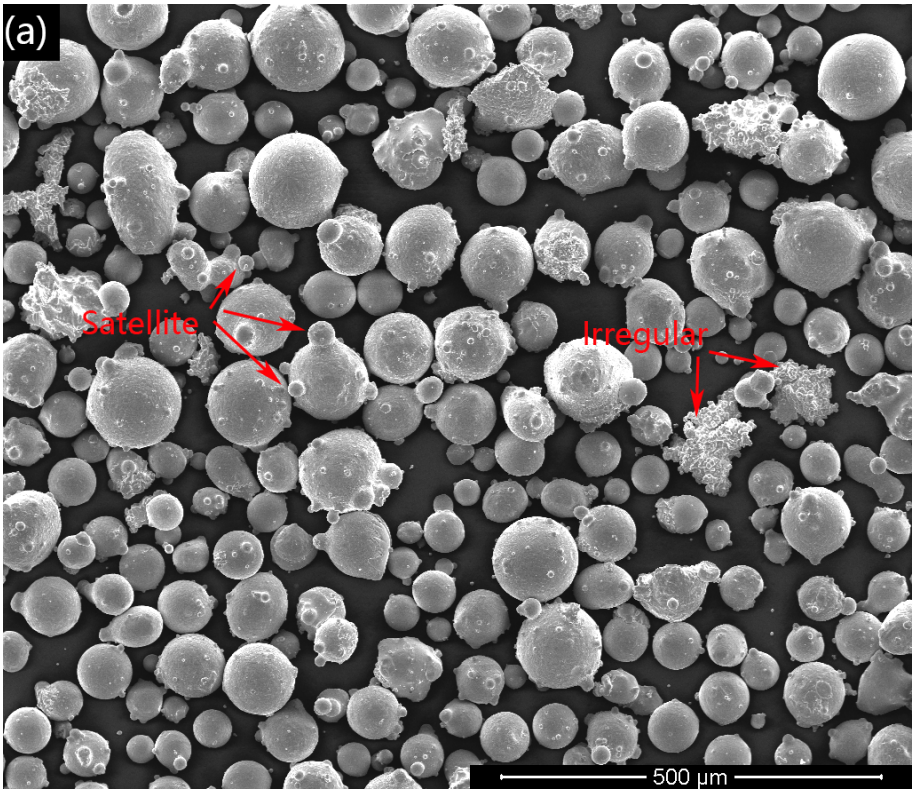

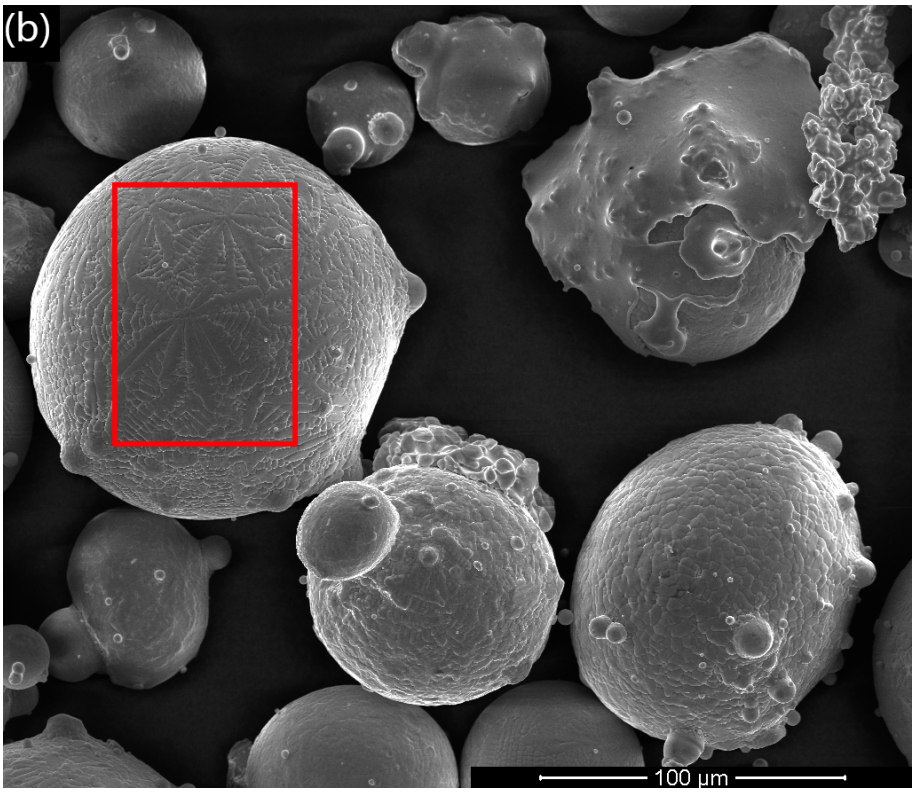

Figure 6.3 Secondary SEM micrographs showing powder particle morphologies: (a) Low magnification image shows satellite powders and irregular powder morphology (b) High magnification image reveal the surface dendrites in red area.

By observing the cross section of the powder under an optical microscope, it is evident that various particles are hollow. These hollows could be entrapped gas or porosity that formed because of shrinkage during rapid cooling. The analysis from CLEMEX shows that the hollowness occupies approximately 20% of the volume in a powder particle.

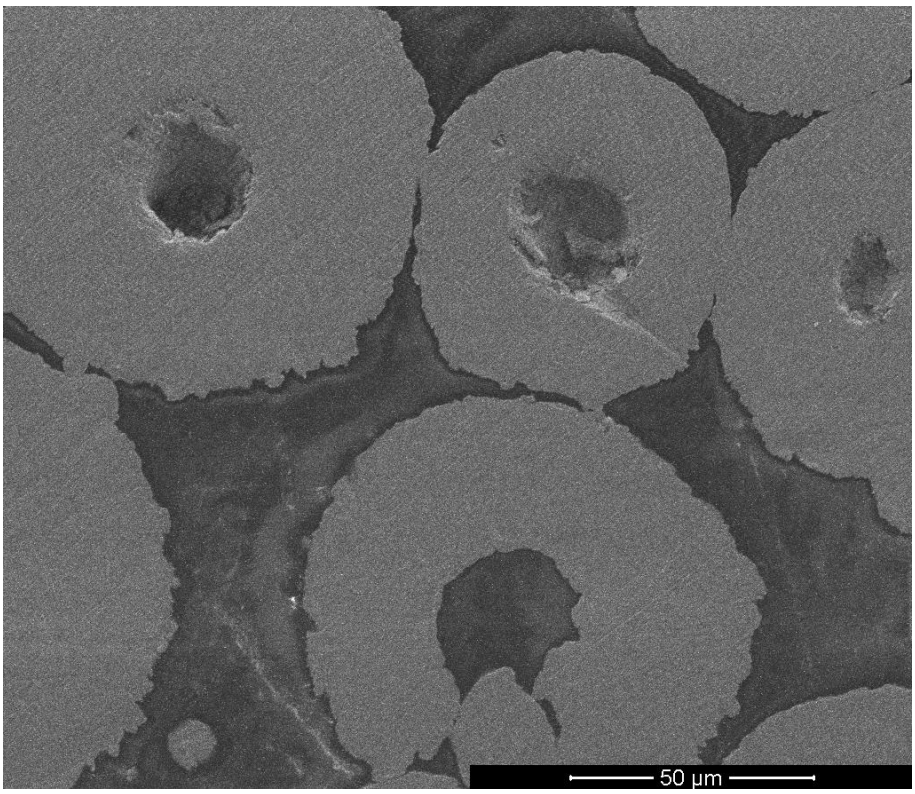

Figure 6.4 Secondary SEM showing the cross section of ground and polished powder particles. Hollow features are showing in most powders.

6.1.3 Powder density

The measured powder density of LR8 was 8.423 g/cm^3. Compared with other Ni superalloys, such as IN718 (8.192 g/cm^3), IN713C (7.941 g/cm^3), and ATI35N (8.41 g/cm^3), the density of LR8 is rather close to that of ATI35N, with a similar chemical composition. The density of the powder is also a good reference for calculating the condensation level for built parts by comparing the density of the as-built parts.

6.1.4 Powder thermal properties

Based on the heat flow results from the experiment, the calculation of specific heat capacity C_p can be written as:

$$C_p = \frac{HF}{m * \beta} \qquad \textbf{Eq 6.1}$$

where HF is the heat flow, m is the mass of the sample, and β is the heating rate. Thermal diffusivity α can be calculated using the equation below:

$$a = \frac{k}{C_p * \rho} \qquad \textbf{Eq 6.2}$$

where k is the thermal conductivity and ρ is the density of the material. The comparison of thermal properties between LR8 and other alloys is displayed in Table 6.1. It can be seen that LR8 has a significant increase in thermal properties compared to Ni-base superalloy.

The introduction of tungsten content provides high heat conductivity and diffusivity, which means the heat can dispersing fast in LR8, while a relatively high specific heat capacity indicates that LR8 requires more energy input to heat the material compared with the two Ni base superalloy reference. The LR8 solidification simulation from Thermo-Calc shows a high melting point in comparison with other alloys owing to the high content of tungsten and molybdenum. In a general sense, more energy input needs to be used for AM-fabricated LR8.

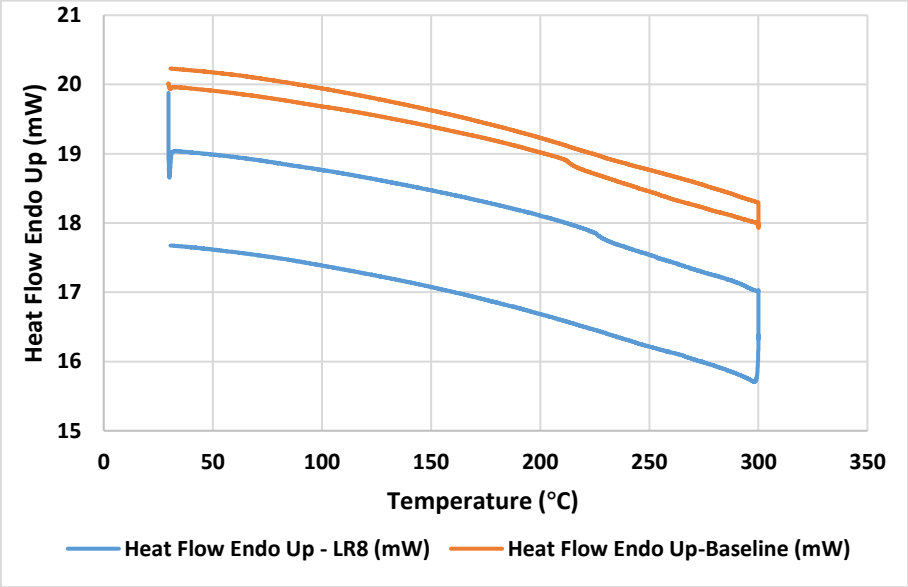

Figure 6.5 Heat flow profiles of LR8 powders with a baseline reference.

Table 6.1 Measured thermal properties of LR8 compared with other common Ni superalloys.

Thermal properties	LR8	IN713C (INCO, 1968)	ATI35N (ATI, 2016)	IN718 (Agazhanov et al., 2018)
Specific heat capacity (J/K.s)	530 ± 10	444	753	435
Thermal conductivity (W/m.K)	16.75 ± 0.18	9.82	13.4	11.4
Thermal diffusivity (mm^2/K)	3.76 ± 0.02	2.78	2.18	3.20
Melting temperature (K)	1690*	1547	1650	1663

***The melting temperature of LR8 is an estimated value from Thermo-Calc (TCNI8: Ni-Alloys V8.2)**

6.2 The difference between continuous and pulsed lasers

The pulsed laser system in Renishaw 125 has a different emission mode compared to the continuous laser in Aconity3D. The intermittent operation of the laser results in an energy profile like that shown in Figure 6.6(b). when laser exposure on a spot, it will ramp up to the pre-set power and hold for a period. When the galvanometric mirror moves the laser to next spot there will be a short idle time between points. Therefore, the energy input with pulsed laser will have a periodic change during the scanning. One complete cycle of ramp up, exposure and laser switch can be referred as “duty cycle”. So, the effective energy of a pulsed laser is lower than the continuous laser within the same period of time. The level of energy input can be directly affected by point space (D) and laser travel speed (V_t).

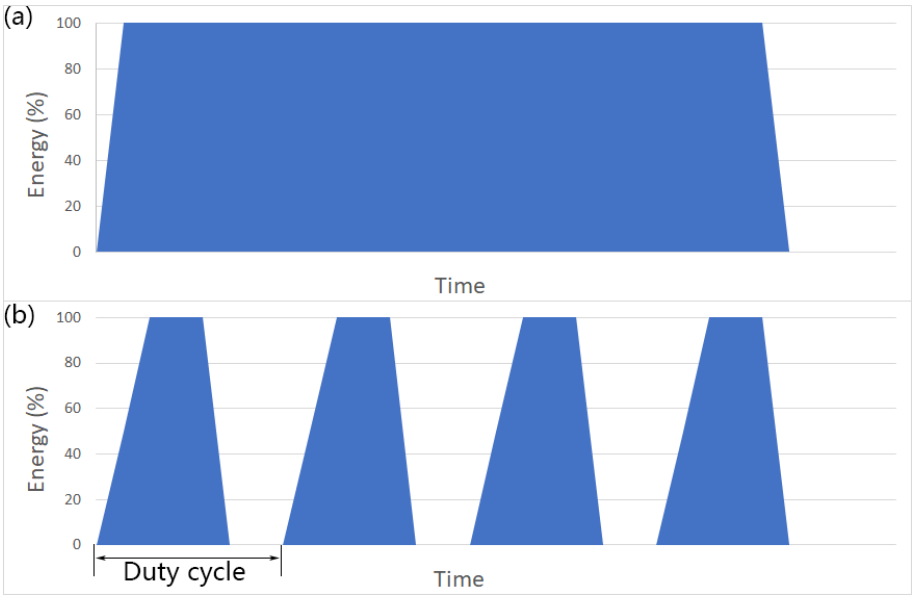

Figure 6.6 Energy profile of different scan mode with same peak power input within the same time (a) continuous laser (b) pulsed laser with a complete 'duty cycle' labelled.

Concerning the difference in emission mode, a melting pool simulation for IN713C with both continuous and pulsed laser is done with same energy input and speed. The material properties applied for simulation are taken from Table 6.1. Figure 6.7 shows the melting pool geometry of IN713C and LR8 with different laser setting. It can be seen that, under the same parameters, the melting pool of the pulsed laser is narrow and elongated. While, the melt pool after 1 pulse from the laser can be considered as a hemisphere, as the laser moves to the next spot, the heat effect of previous melting pool still exist and cause a significant affect to the following melting pool. As presented in Figure6.6 (b)(c). However, Figure 6.7 (c)(d) has demonstrated that the melting pool shapes are identical after 50 and 100 pulses. Thus, the heat effect can eventually reach steady state after more points are included. Therefore, the melt pool becomes the more familiar, and expected, "teardrop shape" we normally associate with a moving laser source rather than the hemispherical shape that would result from a stationary laser. Because there is a duty cycle - given by ratio between the interaction time and total time (Interaction plus travel time between spots), more energy input is required to achieve the same melting volume. The melting pool and HAZ is still much smaller than

a continuous laser, as shown in Figure 6.7 (c)(d). In common, the melting pool shape should be similar for the same material with same energy input. Therefore, it can be concluded that the input parameter from continuous laser AM cannot be directly applied to pulsed laser AM.

With the same processing parameter, the effective melting pool volume of IN713C is approximately 4-6 times larger than LR8 with continuous laser owing to the significant difference in thermal properties between them as discussed in Section 6.1, with the most significant difference being in thermal conductivity. The energy input required to process LR8 with the same melt pool volume as IN713C is therefore expected to be up to 100% higher based on the simulation data.

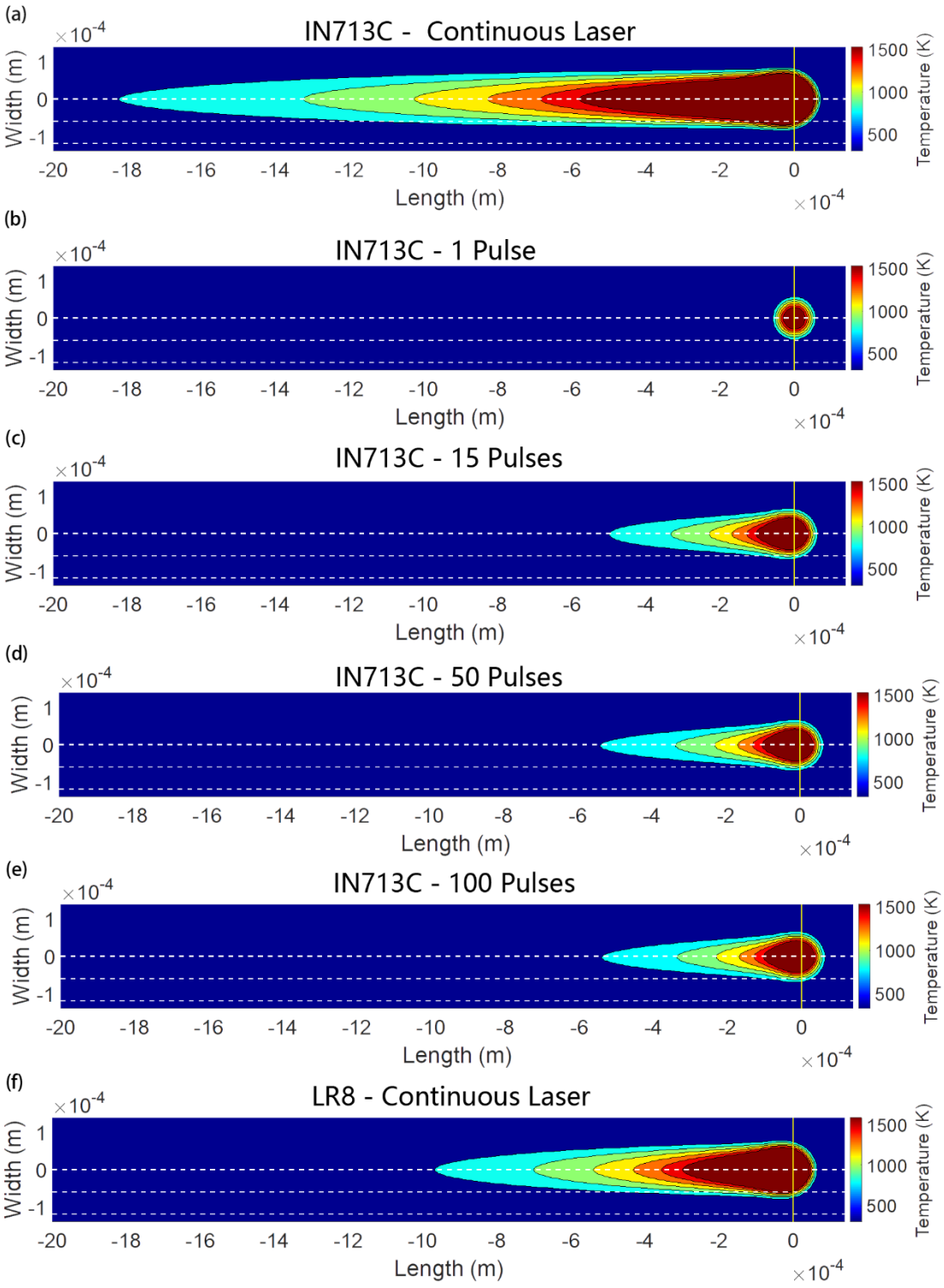

Figure 6.7 Melting pool of the IN713C with (a) continuous laser (b) 1 pulse (c) 15 pulses (d) 50 pulses (e) 100 pulses; and LR8 with (f) continuous laser (q=130W, v=2.0m/s).

6.2.1 The conversion of parameters between Renishaw 125 and Aconity3D mini systems

Owing to the different behaviours of the pulsed and continuous lasers, the parameter cannot be directly transferred to the other machine without conversion. For a pulsed laser, the travel speed (V_t) between points for the Renishaw 125 system is 4 m/s based on data from previous experiments. The total time (T) can be expressed as:

$$T = t + d/V_t \quad \textbf{Eq 6.3}$$

Thus, the average speed (V) for the pulsed laser can be expressed as:

$$V = d/T \quad \textbf{Eq 6.4}$$

The conversion of effective laser power (Q) from nominal power (q) is:

$$\mathrm{Q} = \mathrm{q} \times \frac{t}{T} \quad \textbf{Eq 6.5}$$

Therefore, the parameter for the pulsed laser can be converted into average speed (V) and effective laser power (Q) for the continuous laser. The hatch space and layer thickness can be kept the same. With the conversion of effective power, the 130W power used in continuous laser system in section 6.2 is equivalent to only 65W in pulsed laser system. The corrected continuous laser melting pool can be presented in Figure 6.9. It can be seen that with same effective power, the melting pool geometry of both systems become nearly identical. Therefore, the effective power needs to be fully considered in a parametric study for pulsed laser.

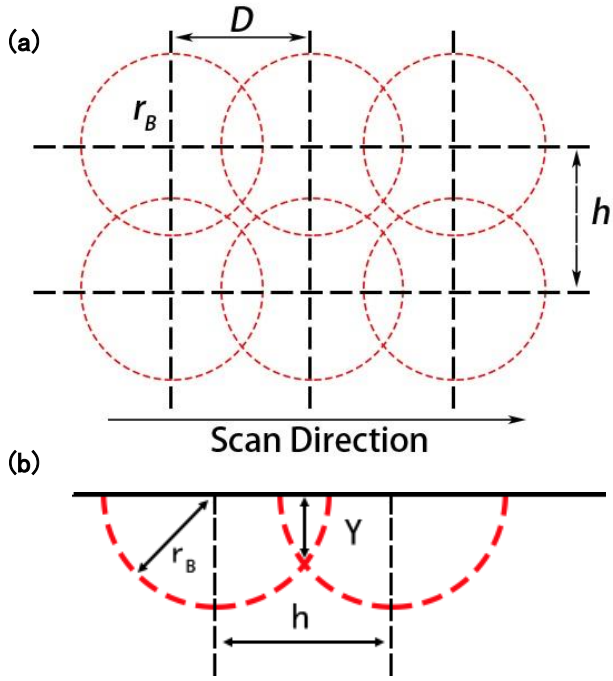

Figure 6.8 Schematic diagram showing the scanning path of the pulsed laser in the Renishaw system. (a) top view (b) front view.

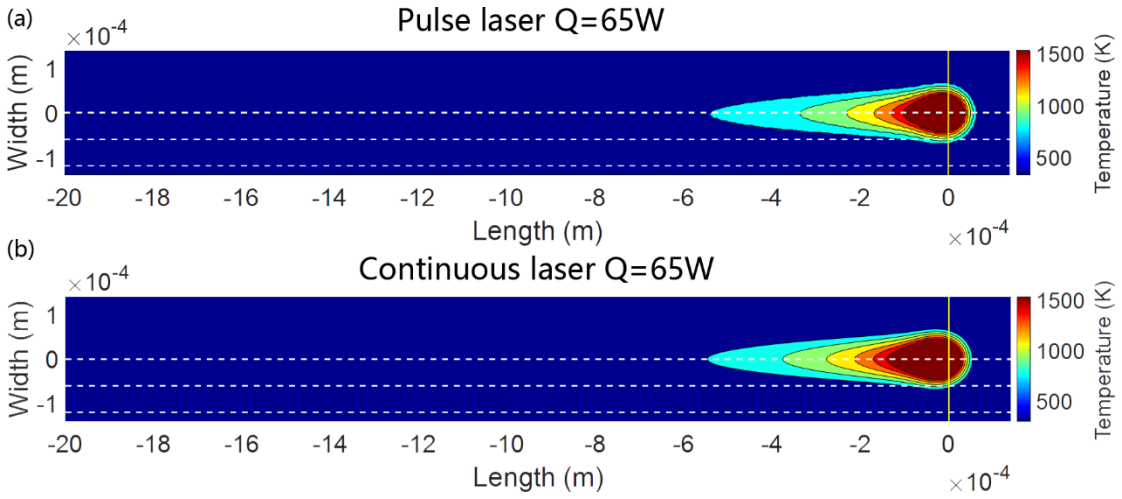

Figure 6.9 Melting pool of IN713C with (a) Pulse laser (b) Continuous laser. With effective laser power (Q), The melting pool of pulser and continuous laser show the nearly identical geometry (Q=65W, V=2.0m/s).

Meanwhile, the point space can have a significant impact on the quality of the parts. As shown in Figure 6.8, if the point space is large, there can be an unexposed area between laser spots, which can also cause an LoF. As the laser spot is round, the

overlapping area therefore can be calculated from laser spot size (r_B), point space (D), and hatch space (h).

For the overlap area between points:

$$A_p = 2(\cos^{-1}\left(\frac{d}{2r_B}\right)(r_B)^2 - \frac{d}{2}({r_B}^2 - \left(\frac{d}{2}\right)^2)^{\frac{1}{2}}) \quad \textbf{Eq 6.6}$$

A same trend can be established for the overlap area between hatches:

$$A_h = 2(\cos^{-1}(\frac{h}{2r_B})(r_B)^2 - \frac{h}{2}({r_B}^2 - \left(\frac{h}{2}\right)^2)^{\frac{1}{2}}) \quad \textbf{Eq 6.7}$$

The void area in the centre of four spots is

$$A_v = \frac{3\pi}{4}dh - (A_p + A_h) \quad \textbf{Eq 6.8}$$

Boig (2019) had an investigation of the depth of the overlapping portion (Y), which can be expressed as:

$$Y = (R^2 + \frac{h^2}{2})^{\frac{1}{2}} \quad \textbf{Eq 6.9}$$

However, the overlapping calculation will be invalid if the melting volume are not predicted to be overlapped. Therefore, both the point space and hatch space cannot be higher than 2 r_B.

6.3 The parametric study of LR8

The processing parameter is designed base on the experiment data from IN625 and CM247 (Cooper et al., 2013, Carter et al., 2014). With a spot distance fixed at 40 μm, the laser travel time for pulse laser AM-fabricated LR8 is 10 μs. The distribution of the processing parameter set on the normalised energy density map is shown in Figure 6.10. Cubical samples were built on a stainless-steel substrate with a 4 × 4 distribution. The gap between every sample was 5 mm, and every sample was built with an identical dimension (5 mm × 5 mm × 5 mm). The effective AM method for large particle powders can be determined with a list of processing parameters, as shown in Table 6.2 below:

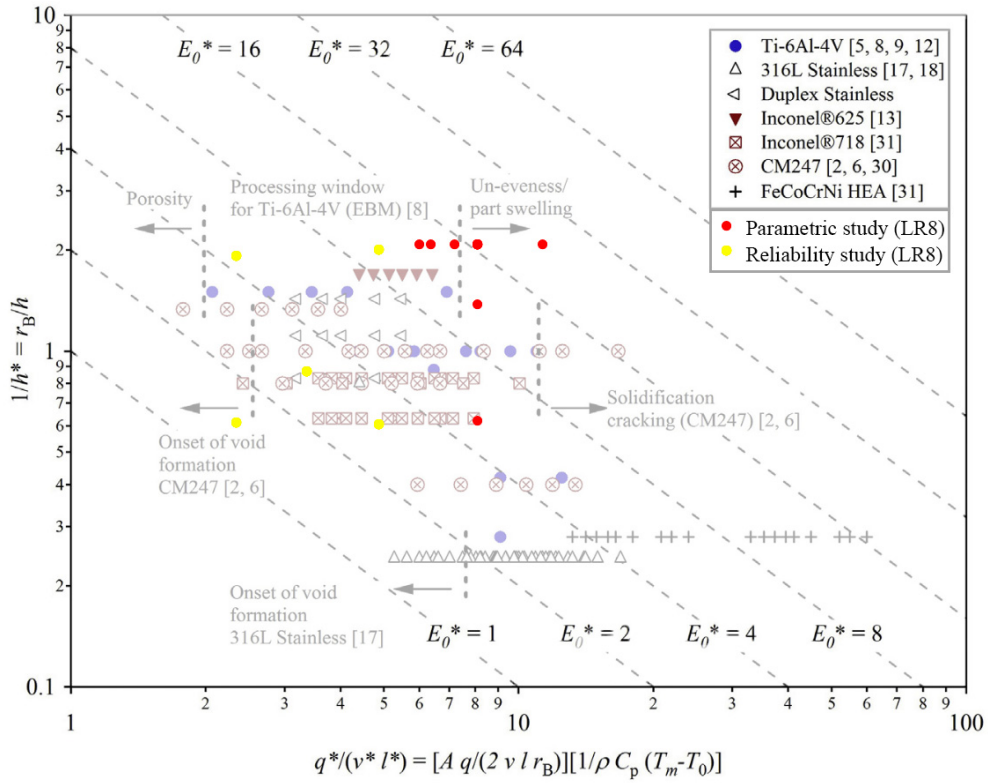

Figure 6.10 Distribution of processing parameter set of LR8 in the normalised energy density map; parametric study is labelled with red dots and reliability study is labelled with yellow dots.

Table 6.2 Parameters used to produce samples for analysis within the parametric study of SLM-fabricated LR8. Sample ID1 was set as a baseline for the following analysis

ID	q	Q	v	h	Overlap	Rotation
	(W)	(W)	(m/s)	(μm)	(mm)	(°)
1	190	154.2	0.755	13.3	0	0
2	190	154.2	0.755	13.3	0.01	0
3	190	154.2	0.755	13.3	-0.01	0
4	150	121.7	0.755	13.3	0	0
5	190	154.2	0.755	13.3	0	0
6	170	137.9	0.755	13.3	0	0
7	190	154.2	0.755	13.3	0	66.6
8	190	154.2	0.755	13.3	0	90

9	190	154.2	0.755	13.3	0	45
10	190	145.8	0.93	13.3	0	0
11	190	159.8	0.635	13.3	0	0
12	190	154.2	0.755	40	0	0
13	190	154.2	0.755	20	0	0

Figure 6.11 shows the variation of the part density with the energy density q*/(v*.l*.h*). In general terms, the AM LR8 shows the potential to achieve a near-full density (>99%) with proper parameters. Sample 1 with a relative part density 99% is set as the baseline for the following analysis. From Figure 6.11, it can be seen that power can have the strongest impact on part density. A 21% reduction in power input can lead to an approximately 7% to 10% decrease in the part density. The change in scan speed and hatch space only led to a variation of part density within 3%. The energy density required to build fully dense LR8 part is therefore about 2 times higher than parameters from previous literature for IN713C (Boig, 2019) owing to the two facts that LR8 powder have a higher specific heat capacity and the oversize irregular morphology.

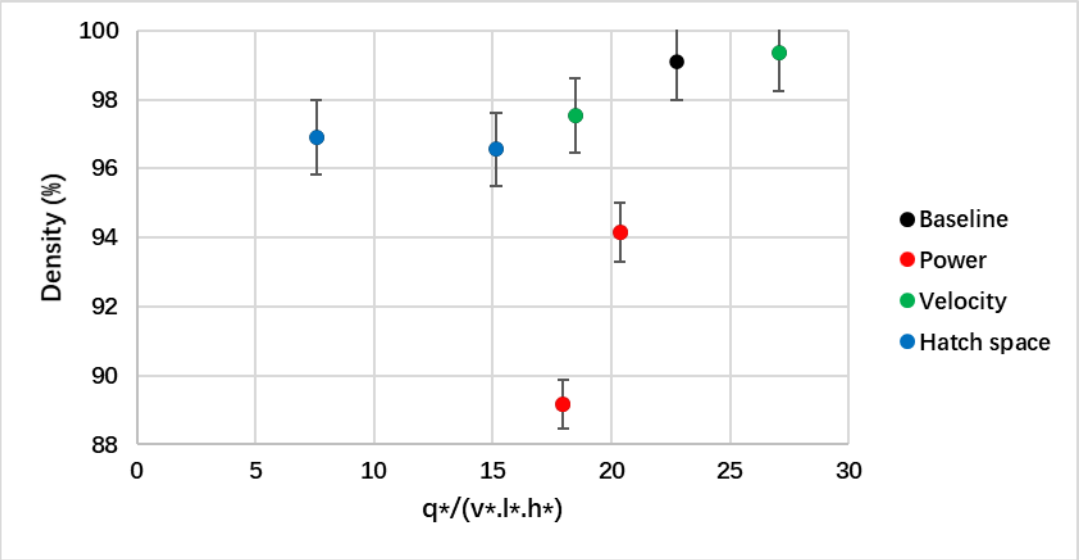

Figure 6.11 Plot of the as-built part density against normalised energy density. Baseline parameter can achieve >99% part density. All factors show certain degree of impact on part density. Power shows the largest influence on part densities.

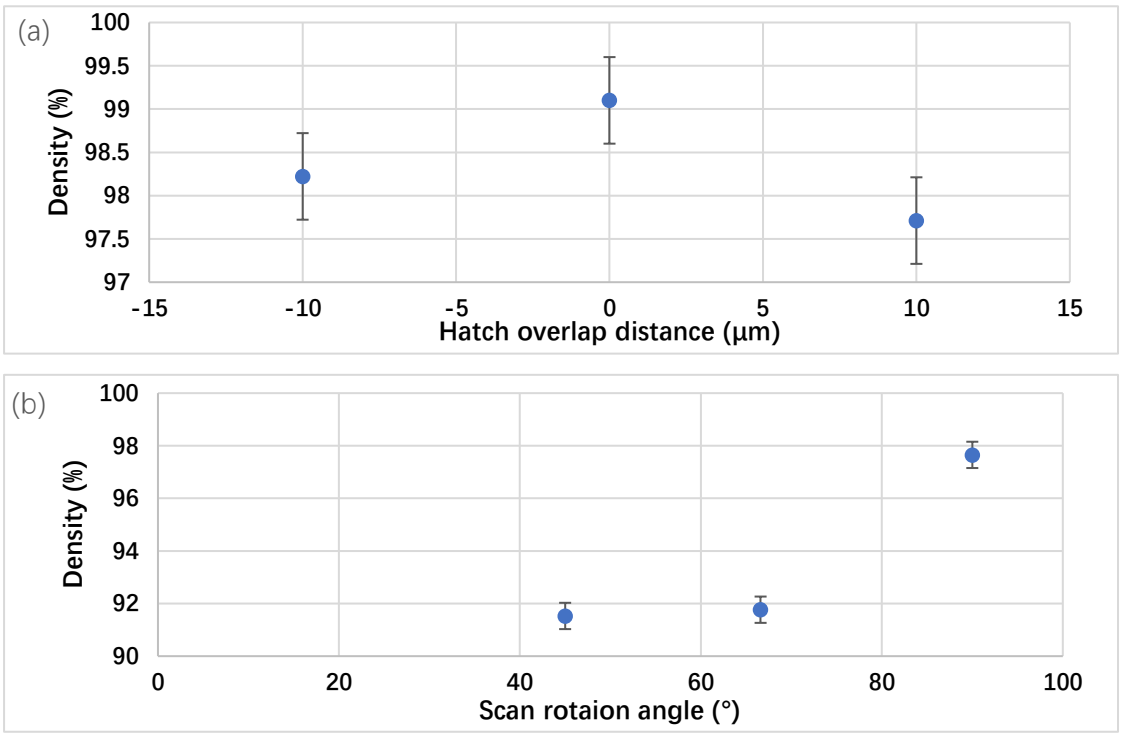

Figure 6.12 Effect of scan strategy on the as-built part density with fixed energy density. (a) overlapping distance in stripe scan strategy (b) rotation angle in Meander scan strategy.

The scan strategy can also cause a considerable difference in the part density. Figure 6.12(a) shows that either an overlap or gap between hatches can slightly reduce the part density. The effect of hatch overlap on local energy input can be represented with normalised hatch length (L_s*) for stripes scan strategy

$$L_l^* = L_s/(L_s + L_{overlap}) \qquad \textbf{Eq 6.10}$$

Where L_s is the set length for a single stripe and $L_{overlap}$ is the overlap value between two stripes When there is a gap between hatches, the local energy input at the end of the hatches is insufficient to melt the powder and induce an LoF. An overlap of hatches can induce excess energy input on the overlap area and cause crack formation.

Figure 6.10 (b) shows that the rotation angle has a minor influence on the part density. The main character of Meander scan strategy is a constantly changing laser travel time. To fully understand the effect of rotation angle, the normalised laser travel time (t_l*) for meander scan strategy can be calculated

$$t_l^* = L_n/L_{max} \qquad \textbf{Eq 6.11}$$

For a cuboid part, the nominal hatch length (L_n) is equal to the side length. The maximum hatch length (L_{max}) is the maximum length of a laser track in a layer during the Meander rotation.

As shown in Table 6.3, the difference in maximum laser travel time can be up to 41.3% with different rotation angle. The difference in laser travel time induces an uneven melting across a layer with meander scan strategy. With the same energy input, a shorter travel time can significantly concentrate local heat input to reduce the LoF. The sample with the stripe scan strategy can be approximately 8% higher than that of meander samples. The meander scan strategy performance is worse than the simple stripe scan strategy even with the same laser travel speed. The large powder particles require more constant energy to penetrate, while the constant rotation scan strategy cannot provide a stable heat input at the same location.

Since the scan strategy can directly influence the local heat input, an 'apparent power' (Q_a) is introduced to further analyse the effect of scan strategy. The apparent power is defined as the product function of normalised scan strategy factor and effective power (Q):

The apparent power (Q_a) for stripes scan strategy:

$$Q_a = L_l^* \times Q \qquad \textbf{Eq 6.12}$$

The apparent power (Q_a) for Meander scan strategy:

$$Q_a = t_l^* \times Q \qquad \textbf{Eq 6.13}$$

As Figure 6.12 presented, with the increase of rotation angle from 45° to 90°, the maximum hatch length is closer to the part side length. Therefore, the local heat input is closer to the baseline energy and improved the part density. The overlap length is a minor change in this experiment, therefore the effect on part density is very limited.

With the help of the apparent power, the effect of scan strategy can be qualified and compared with other nominal parameters, as presented in Figure 6.12. Here it can be seen that power input is still the dominant factor that affects part density. However, the rotation angle also brings a significant impact on part density when the Meander scan strategy is used. The overlapping in stripe scan strategy can only have limited impact

when the overlap ratio is less than 5%. In general view, the original power parameter (q) is still the dominant factor which affects the part density.

Table 6.3 The effect of rotation angle in meander scan strategy on laser travel time (V= 0.755 m/s, layer size 10 mm × 10 mm) (a) Meander scan strategy (b) Stripe scan strategy with overlapping.

(a) Meander scan strategy.

Rotation angle (°)	Maximum hatch length (mm)	Maximum Laser travel time (ms)	Normalised travel time (%)	Apparent power (w)
66.6	13.72	18.17	72.89	112.35
45	14.14	18.72	70.72	109.02
90	10	13.25	100	154.15

(b) Stripe scan strategy with overlapping.

Hatch overlap (mm)	Hatch length (mm)	Normalised hatch length (%)	Apparent power (w)
0	2.5	100	154.15
0.01	2.5	99.6	153.53
-0.01	2.5	100.4	154.77

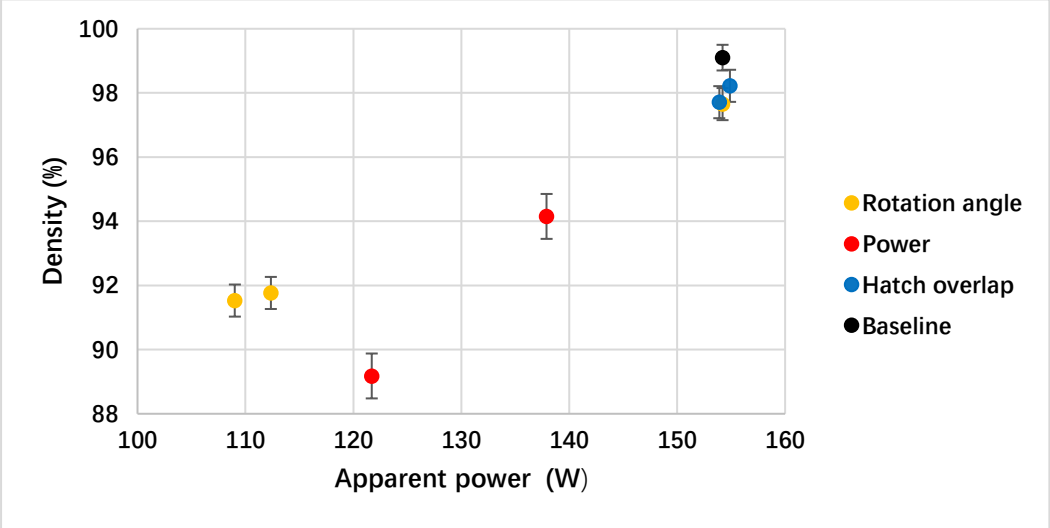

Figure 6.13 Plot of part density against apparent power. The effect of scan strategy can be transferred to apparent power. The actual power parameter is still the dominant factor affecting part density.

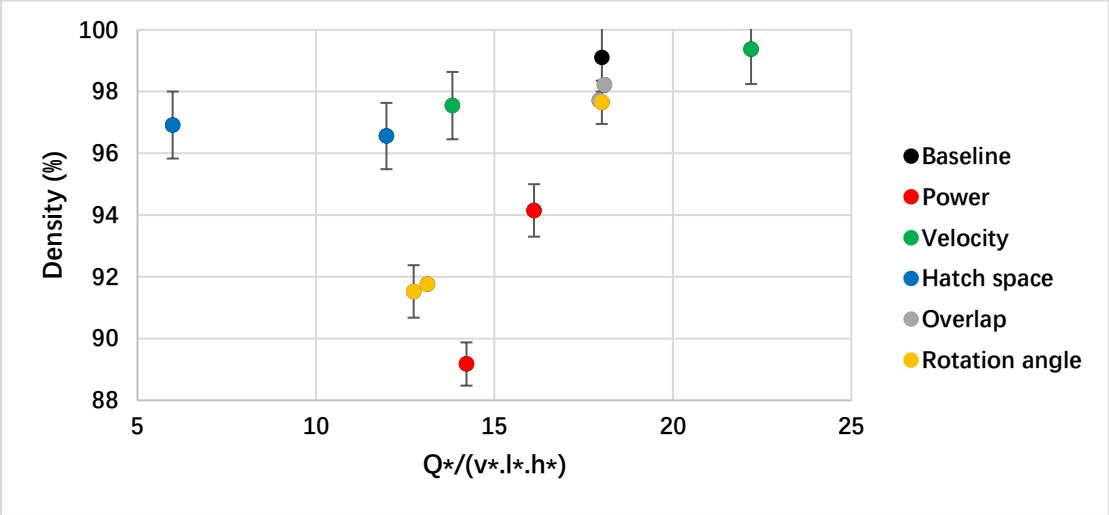

Figure 6.14 Plot of part density against all factors after correction with effective power. Power still shows the largest influence, followed by the Meander rotation angle.

6.4 Defect Classification and Mechanism

6.4.1.1 Porosity

- **Gas porosity**

Gas pores can be observed in a high-energy density sample with a diameter of less than 30 μm. This can be the gas trapped in the melting pool. Owing to the rapid cooling feature of AM, the gas within the melting pool has no time to escape and is sealed inside. The effect of surface tension makes all these types of pores have a perfectly round shape.

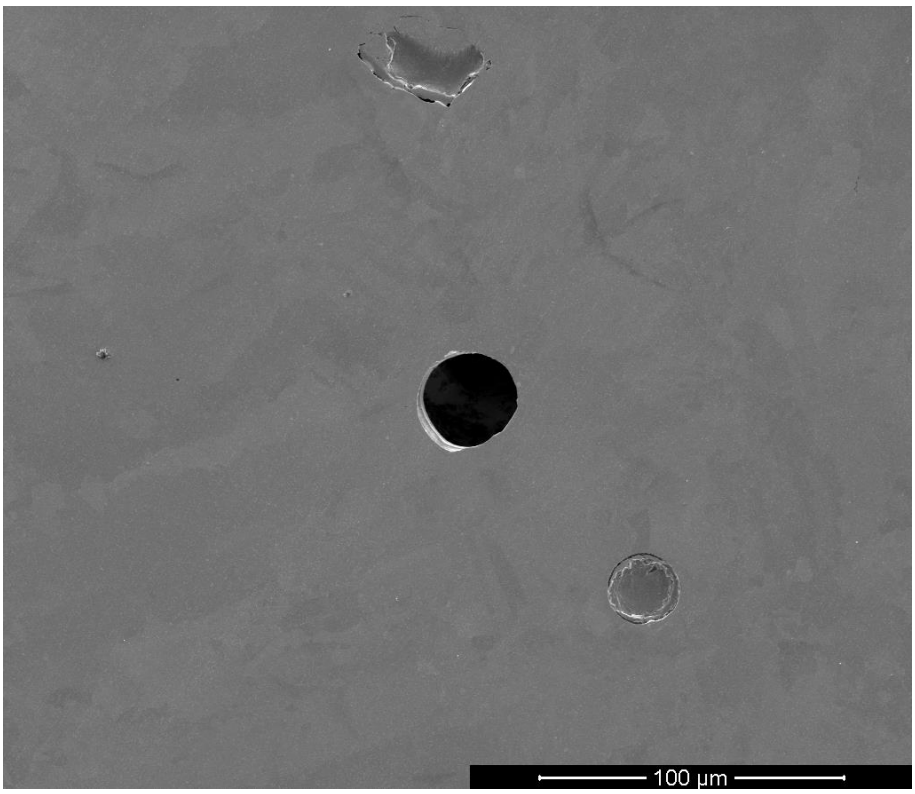

Figure 6.15 SEM image from the as-built samples (moderate energy) showing large gas pore and inclusions (X–Y plane).

- **Keyhole pores with crack**

Figure 6.16 shows the morphology of a typical irregular pore in the high energy density sample, similar to the IN713C sample. The excess energy boiled the core of the melting pool and caused the irregular pore. Cracks can be found on the edge of the pore due to the thermal stress. The excess energy boiled the core of the melting pool and caused the irregular pore.

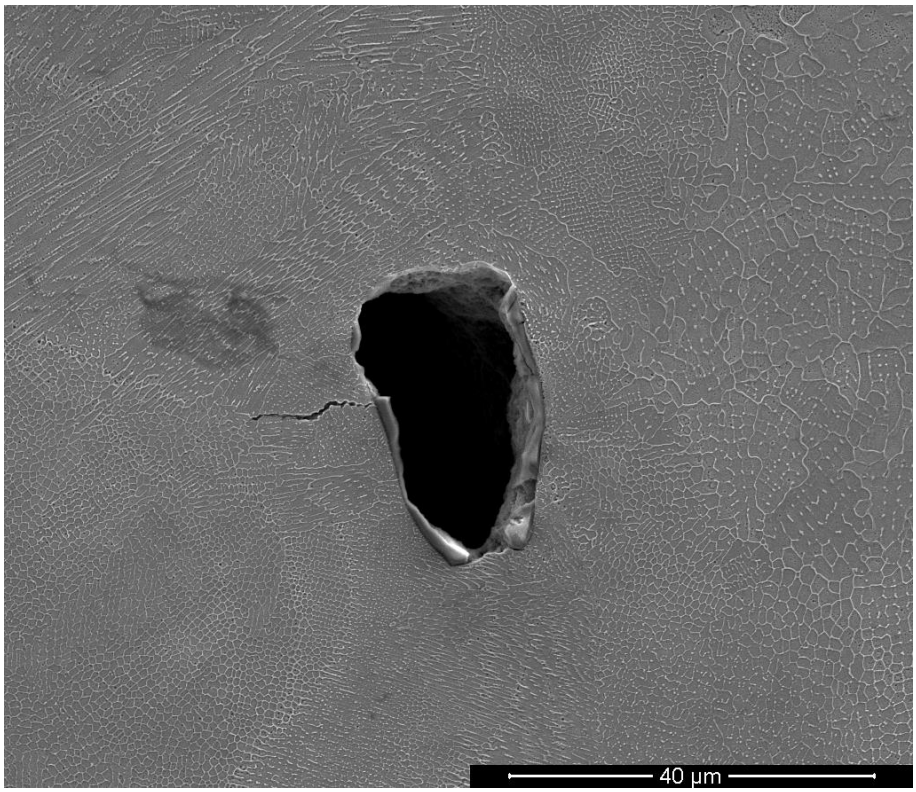

Figure 6.16 Secondary SEM of a typical high energy density sample showing the keyhole mode pore (X–Z plane).

- **Lack of fusion (LoF)**

With the energy density reduced to a certain level ($q^*/(v^*.l^*.h^*)<10$), a large amount of LoF started in the sample. As shown in Figure 6.13, the LoF typically has a size larger than 100 µm. Compared with the IN713C sample, the LoF in LR8 generally has an elongated direction along the layer direction. Therefore, the LoF can be introduced by the insufficient melting and uneven deployment of powders. With a higher magnification, the unmelted powder can be found within some of the LoF defects.

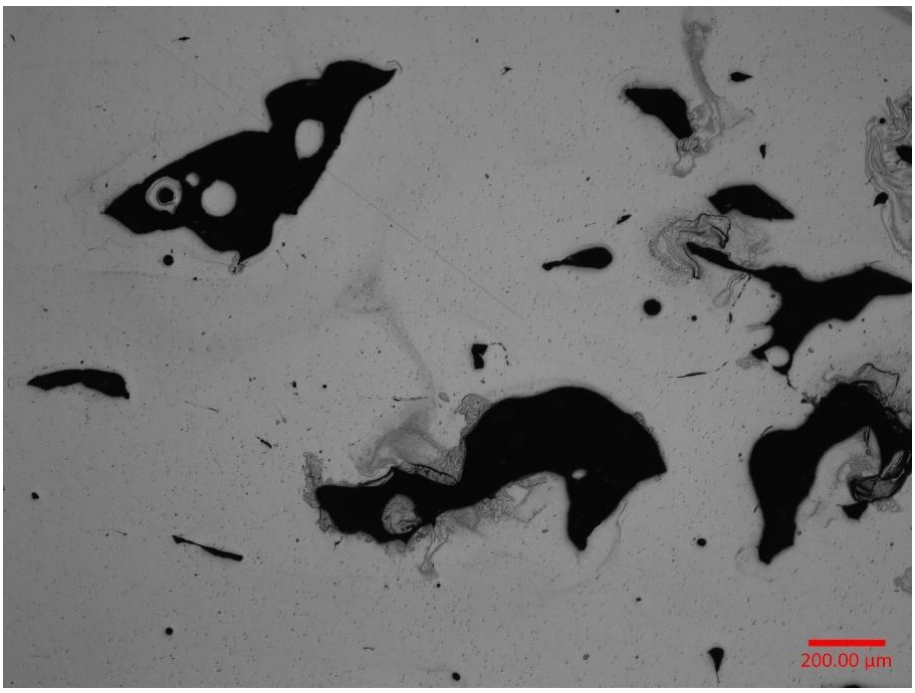

Figure 6.17 Secondary SEM of a typical low energy density sample showing the LoF (X–Z plane); unmelted powder can be seen inside the pores.

6.4.1.2 Cracking phenomena

According to Carter et al. (2014) and the result from Chapter 4, there are three potential cracking mechanisms that can be observed in SLM-fabricated samples. Figure 6.18 shows a typical crack similar to the AM-fabricated IN713C sample, which can only be found in high energy density samples (q*/(v*.l*.h*)>20). Cracks generally follow the build direction, as well as the orientation of grains and dendrites. Meanwhile, the edge of cracks is generally jagged-like, the surface of dendrites can be seen at the edge. As discussed in Chapter 4, this is a typical characteristic of solidification cracks. The formation of dendrites during solidification blocks the capillary flow of the remaining liquid in the interdendritic region. Therefore, a considerable amount of thermal stress can concentrate in the interdendritic region and pull the primary dendrite arms apart.

No cracks are observed in the low energy density sample; however, large-scale pores occur as mentioned in the previous section. No evident liquidation cracking or DDC was found in the samples.

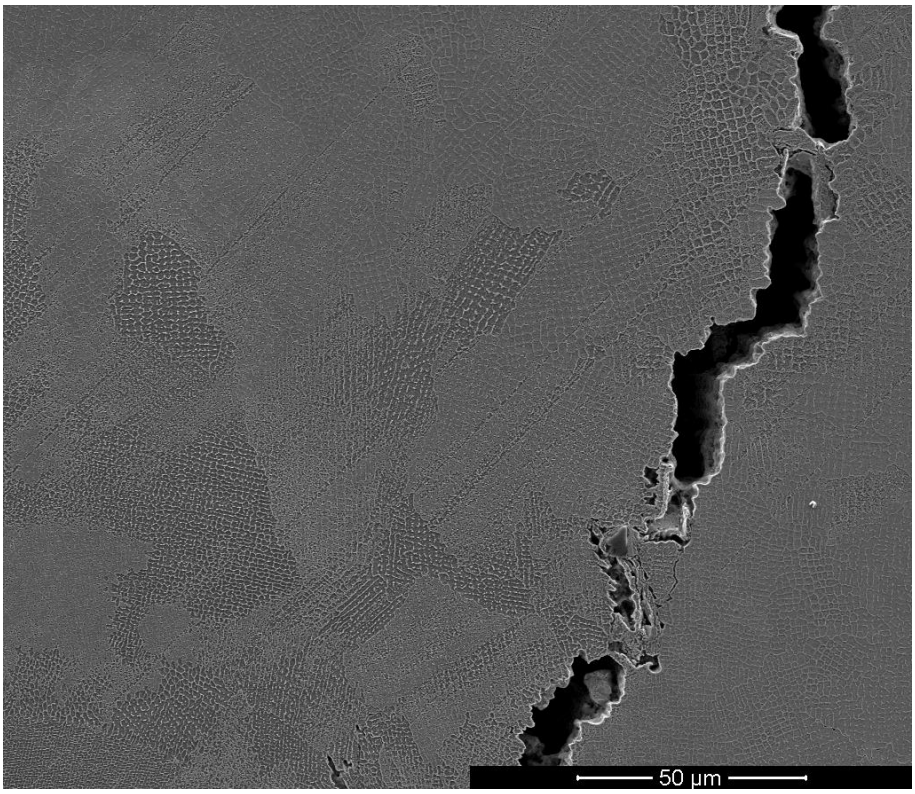

Figure 6.18 SEM image showing a zigzag-like crack in the high energy density samples. The crack direction generally follows grains orientation and build direction (X–Z plane).

6.4.2 Microstructural analysis

Typical columnar dendritic structures, such as IN713C, can also be observed in LR8 samples. As shown in Figure 6.19, the direction of the columnar structure strongly follows the build direction. The view from the X–Y plane in Figure 6.16, shows that the cells generally have a normal growth with a Feret diameter of approximately 1.9 µm. Therefore, from a 3D perspective, the cell in the as-built sample is a cylinder-like shape.

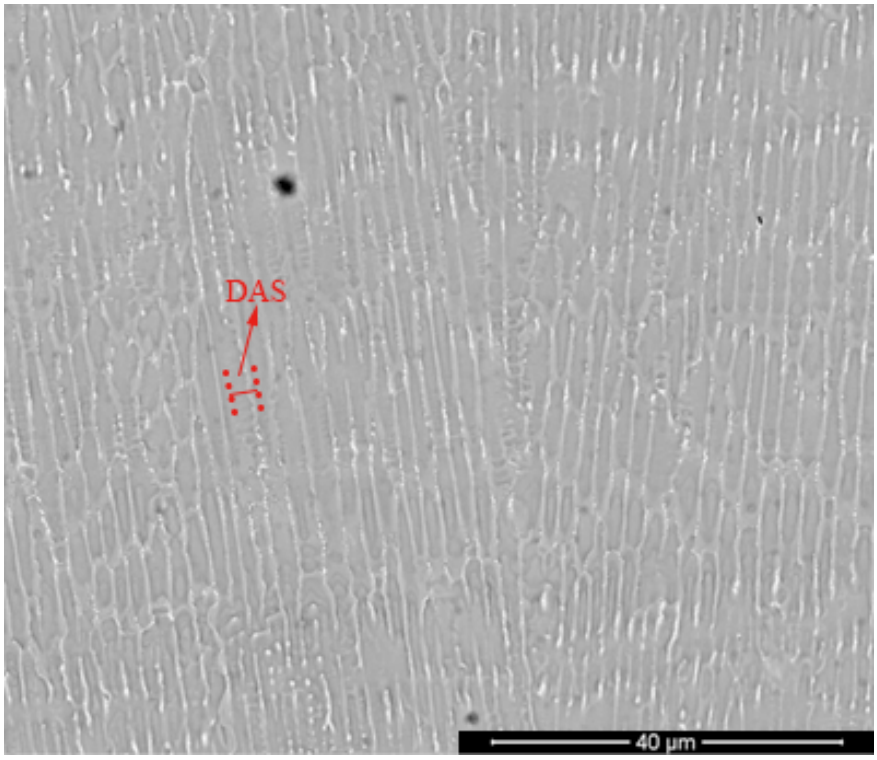

Figure 6.19 SEM image of the etched sample with highest density showing the columnar structure aligned in the build direction. Dendrite arm spacing (DAS) can be measured as shown in figure (X–Z plane).

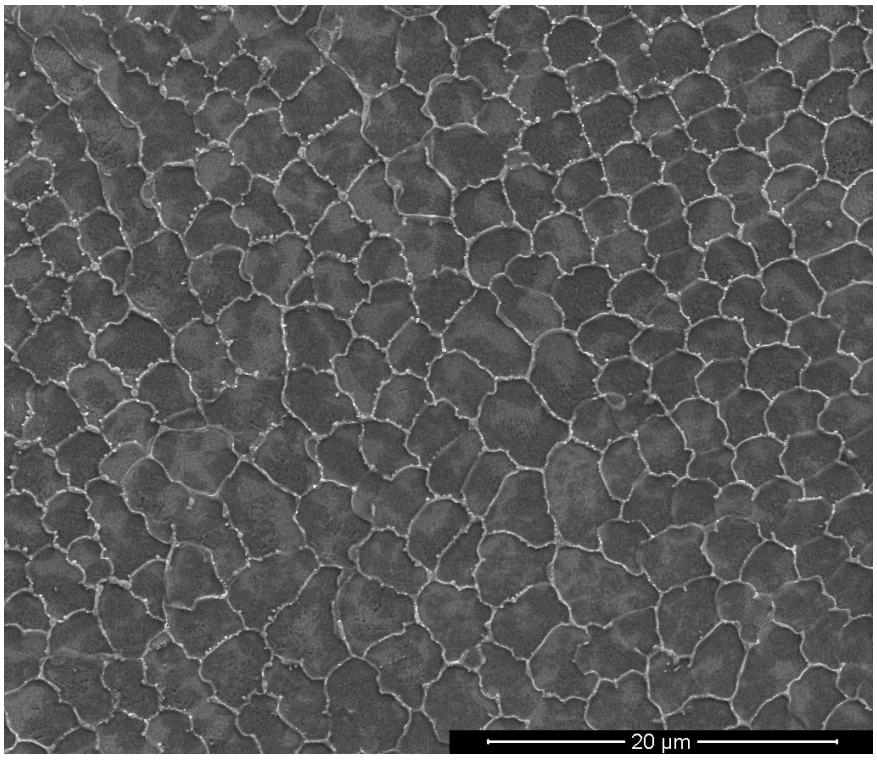

Figure 6.20 SE-SEM image of the etched sample with highest density showing the equiaxed structure at the centre of sample (X–Y plane).

An interesting texture can be observed at the overlapping area between spots. As shown in Figure 6.21, there is a clear transition of cell morphology. It can be the result of different cell growth orientations. A complex thermal flow profile can be formed when laser penetrating through metal powders. While the FCC grains have a preferential grain growth orientation during solidification. Therefore, the grain can grow generally toward the build direction but with a small tilt angle. The plan view of the built surface in Figure 6.21, is perpendicular to the build direction. While the growth orientation of cells can be at an angle to the plan view of built surface. The cross-section of interacted grains, therefore, exhibits a different level of the project area and cell size. The coarsen cells, with a DAS of 1.4-1.7 μm is about 60% larger than the fine cells.

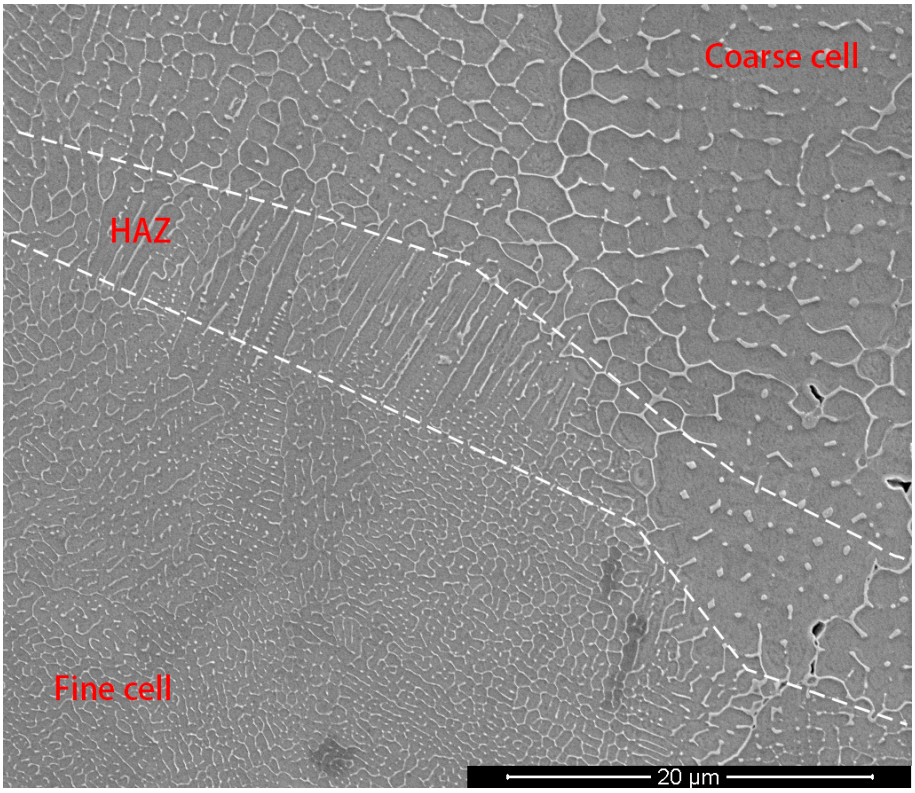

Figure 6.21 SE-SEM image of the etched sample showing the interacted grains (X–Y plane).

The morphology of the melting pool can be evidently observed, as the melting pool contour is labelled in Figure 6.22. Due to the massive overlapping, the melting pool can only be roughly measured, which is around 150–250 μm. Typically, the melting pool is shallow, while at the end of each hatch, the melting pool tends to form the keyhole

mode. The depth of melting pool at track end is about 80-100μm, which is much higher than the depth of melting pool at other location. When the laser returned to the next hatch, the reheating effect at the end of the hatches is higher than the other spots and causes keyhole melting.

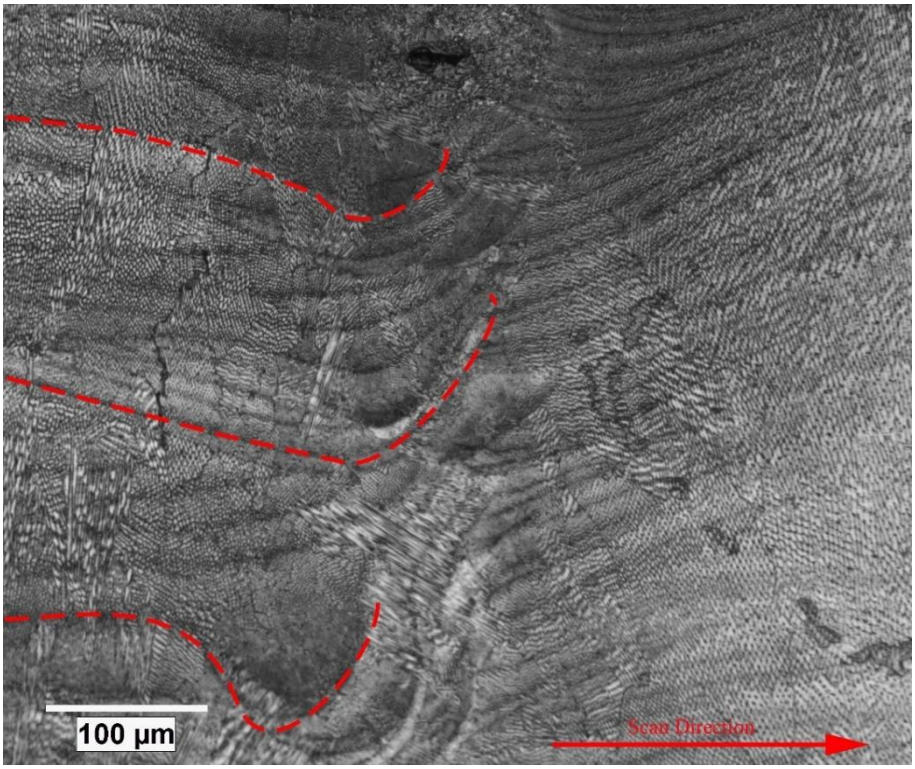

Figure 6.22 Melting pool geometry at the interaction area between hatches. The melt pool contours are labelled with red dash line.

The effect of processing parameters on microstructure can be revealed with the measurement of DAS, as shown in Figure 6.19. Two DAS prediction models (Travedi & Kurz-Fisher) in literature review Section 2.1.8 are used here to understand and interpret the experimental data obtained. In general, the DAS increases with the increase of energy density. As discussed in literature review Section 2.1.8, the DAS can be directly influenced by cooling rate and velocity. The thermal gradient (G) and solidification velocity (R) in these obtained from melting pool simulation. Owing to the increase in energy density, the cooling rate reduce and result in the coarsening dendrites. Figure 6.23 revealed the distribution of DAS as a function of G and R. The data point scatter is induced by the difference between the thermal condition of experiment and

theory. The assumption made for simulation as well as litretures are at thermal steady state condition. However in reality experiment, the thermal state is very complex. Meanwhile, the simulation does not include the undercooling phenomena which can have significant influence on the dendrite growth rate and DAS.

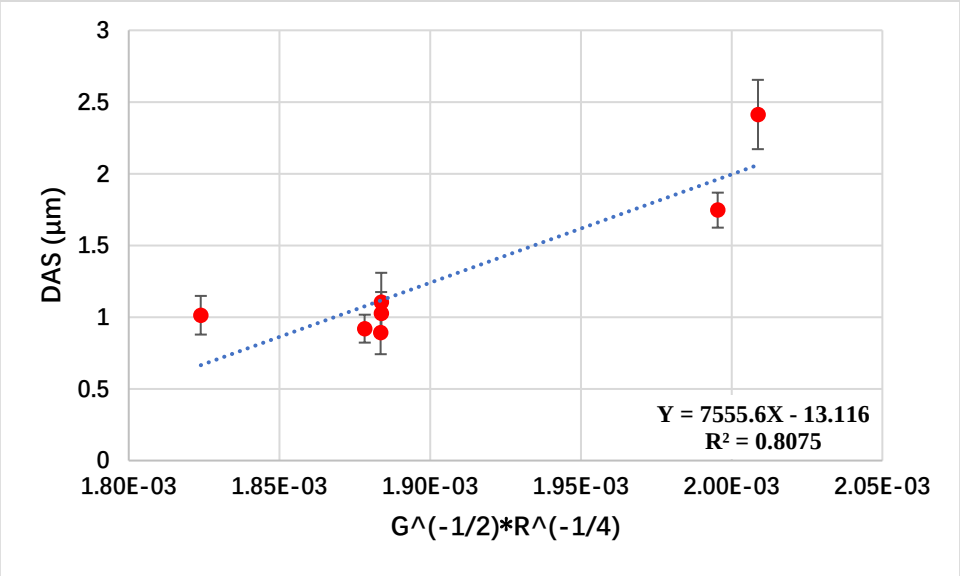

Figure 6.23 Plot of the measured DAS as the function of solidification rate (R) and thermal gradient (G) The linear fit line with correlation coefficient is shown in the plot.

The result shows a clear linear trend between DAS and the cooling rate (G*R) with a high correlation coefficient, R^2=0.81. The linear fit from obtained for the DAS data obtained experimentally when plotted against (G*R), shows a function common to both the Kurz and Fisher and Trivedi models, with the gradient, C = 7555. This gradient is of the same magnitude as that previously reported by Babu for Inconel 718 processed by laser and electron beam powder bed fusion, with the gradient, C = 3195 (Foster et al., 2018). Differing by a factor of 2.3, which can be accounted for in the differences in thermophysical properties of the two alloys specifically thermal diffusivity, surface energy and freezing range). and also, the limited range of data we have available.

In common with previous studies, it is found at the lower normalised energy densities investigated that the measured values fall close to the predictions provided by the Travedi model, but that as the normalised energy density rises above 20 the measurement DAS is better predicted by the Kurz-Fisher model. Hence, Travedi model

can be more accurate for fine dendrite prediction, while Kurz-Fisher model can be used for coarse dendrite prediction. However, owing to the potential inaccuracy from the assumption made in melting pool simulation to obtain the cooling rate value and the powder morphology, there still is a certain inconsistency between the predicted and measured value, as presented in Figure 6.24. Moreover, the DAS does not increase linearly with rising energy density, which means processing factors can have different weight in the effect of DAS the same as the discussion in Section 6.3.

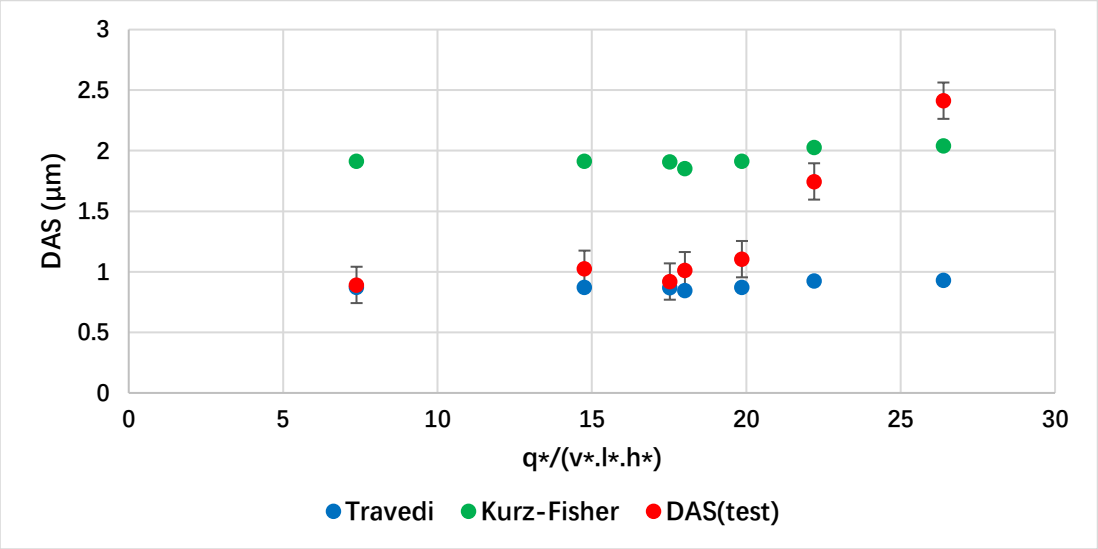

Figure 6.24 Measured and calculated DAS from parametric study, the solidification rate (R) and thermal gradient (G) at the back of a melting pool for Travedi and Kurz model are predicted using melt pool simulation.

The parameter in AM (Q/V) is a linear energy input. Therefore, to turn this into a volumetric energy the simplest means of doing so is to work with the concept of "aspirational" melt volume. This aspirational volume, which is the volume we would hope to melt fully can be defined by parameter we have control of during processing. In this study we choose the layer thickness (l) and the hatch spacing (h). The "volume" we would hope to melt per second therefore is given by V.l.h.

However, there are clear limitations of this approach. With the main problem for its use in the case of analysis of data from continuous laser experiments being hatch spacing (h). As the discussion in Section 6.2.1 proposed, the volume calculation can be invalid if the melting volumes are not predicted to be overlapped. Which also poses a problem

for V in the case of the pulsed laser, as both the point space and hatch space cannot be higher than 2 r_B. Clearly if a value of h > thermal diffusion distance or $2r_B$, the melting pools are disconnected and the hatch space as a melt dimension is physically meaningless.

There are better descriptions of the process that are in common use (King, 2014) but these require a knowledge of the melt pool and the thermal diffusivity of the alloy, which is at or close to the melting point, to use accurately and are therefore subject to their own limitations as predictive tools.

6.4.2.1 XRD result

Figure 6.25 presents the XRD result of the LR8 as-built samples. Notwithstanding the addition of a substantial amount of Co, the sample still only exhibited FCC structures without any additional structures and carbides. Thus, LR8 shares the same strengthening mechanism as IN713C. However, some of the γ and γ' peaks ((111), (200), (220)) in XRD results are highly overlapped among themselves which request high resolution technique to analysis.

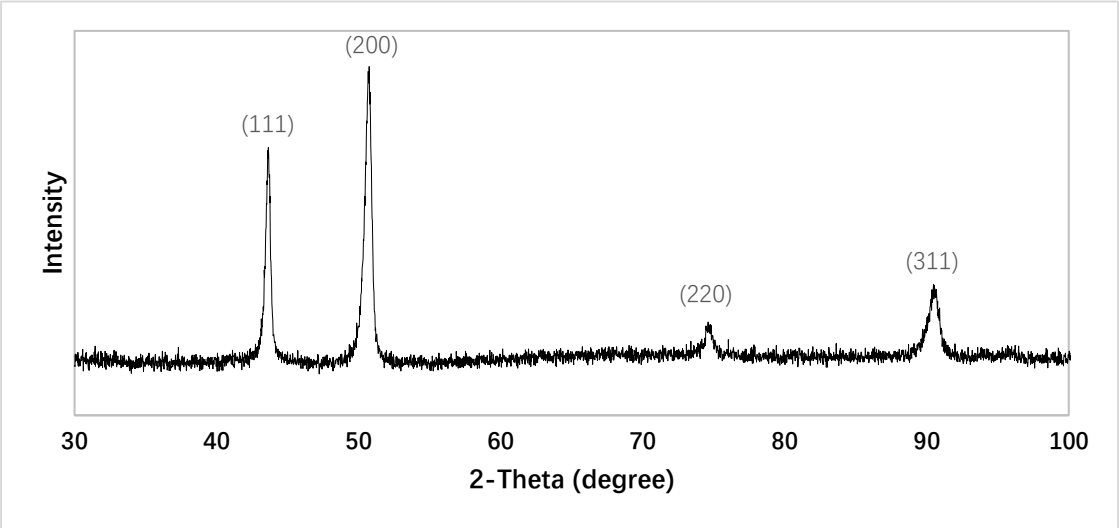

Figure 6.25 XRD profile of SLM as-built LR8: the texture peaks showing a typical nickel superalloy profile.

6.4.2.2 EDS result

The as-built sample was analysed via EDS. The results are depicted in Figure 6.26. It is evident that Ni and Co tend to concentrate at the centre of the cells, whereas an increased amount of Al, Mo, Ta, and Zr can be found to be precipitated at the cell boundaries. The precipitation of Mo, Ta, and Al indicated the formation of a second phase (γ' phase). Therefore, the existence of γ/γ' structure can be confirmed which shown that the peaks in the XRD pattern of the LR8 sample indicate the structure of a γ/γ' phases. However, the Based on the result from the melting pool simulation, with the processing parameter used for the highest density sample. The cooling rate is 2.18×10^5 K/s, while the cooling rate in IN713C samples and other literatures are in the range between 10^6 and 10^7. Owing to the relatively slow cooling rate and scan speed, the segregation pattern is closer to the casting Ni base superalloy. The high energy density and reheating effect at overlapping area provides a lower cooling rate to facilitate cubic like precipitation of the solution element in the interdendritic regions. The carbon concentration at certain locations near the grain boundaries indicated the formation of MC-type carbides. The amount of carbide can be very limited to extremely small sizes, which are undetectable via XRD.

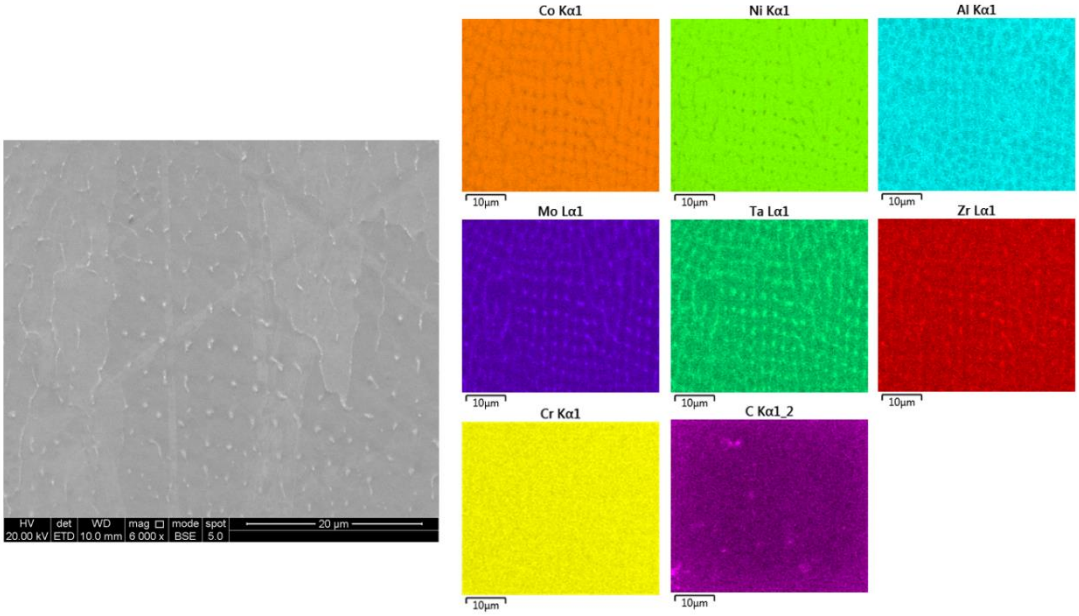

Figure 6.26 EDS mapping of the SLM as-built LR8 sample. The segregation pattern is more cubic like with slow cooling rate.

6.4.2.3 EBSD results

Figure 6.27 shows the EBSD inverse pole figure of the cross section along the build direction of sample 1. Grains generally have an average width of 55.3 μm, and the aspect ratio is about 4.8. Whereas the length of the grains is larger than the layer thickness, thereby indicating that grains grow across layers with no preferred crystallographic orientation. Although the grains are generally columnar along the build direction, the grain crystallographic orientations however are not perfectly aligned in the uniform orientations. The wide range of grain orientations can be the result from high residual stress associated with the relative high cooling rate. In the labelled area, grains have a smaller size and strong misorientation. This area is the interaction area of the two hatches, and the local heat energy is higher than that of the other locations. Therefore, grain refinement can occur at the interaction area. In general, more LAGBs can be found in LR8 as-build sample in comparison with the as-build IN713C samples, the misorientation angle distribution is closer to the HT IN713C sample. Previous reports show that grains in as-built AM-fabricated samples generally align with the build direction. However, in this sample, most grains showed orientations along <001><111>, while a few grains aligned along the <101> orientation, which could be induced by the close hatches that had a similar effect to the heat treatment process. Further investigation is necessary to understand the effect of processing parameters on grain orientation and size. The pole figure presented in Figure 4.20 also shows a strong off-axis orientation in {100} owing to the grain growth with repeat heating and fast cooling conditions. This also indicated that the grain structure did not have a preferable orientation. The grain structure is more equiaxed cubic like.

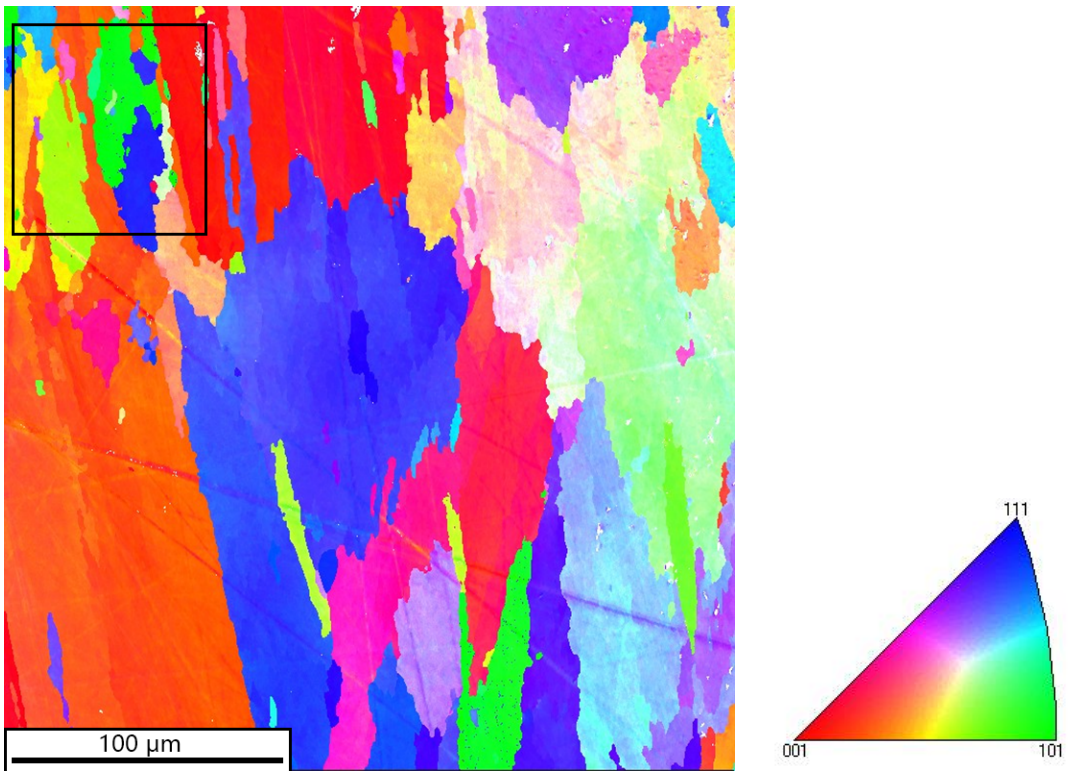

Figure 6.27 EBSD inverse pole figure (IPF) coloured map of the Y–Z plane of sample 1 from the parametric study. Fine grains can be observed in the labelled area.

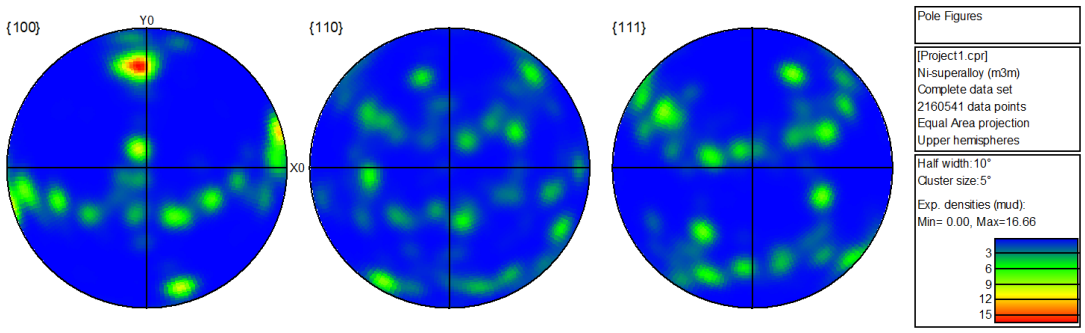

Figure 6.28 Pole figures of the texture of the Y–Z plane from the labelled area in Figure 6.27.

6.5 The reliability and reproducibility of coarse powder AM

The powder analysis result shows that the LR8 powder quality is not ideal for AM. By building a series of duplicate samples, the effect of powder quality on the repeatability of AM-fabricated parts can be more closely investigated. The process parameter is derived using the design of experiment method. The details of the processing

parameters used to produce samples for this analysis are presented in Table 6.4.

Table 6.4 Parameters used to produce samples to analyse the repeatability of SLM-fabricated LR8.

Sample ID	q	Q	v	h	q*/ (v*.l*.h*)	Q*/ (v*.l*.h*)
	(W)	(W)	(m/s)	(μm)		
1-A	190	114.0	2.67	30	1.989	1.19
1-B	190	114.0	2.67	30	1.989	1.19
2-A	190	142.5	1.33	30	3.979	2.98
2-B	190	142.5	1.33	30	3.979	2.98
3-A	190	130.6	1.82	20	4.377	3.01
3-B	190	130.6	1.82	20	4.377	3.01
3-C	190	130.6	1.82	20	4.377	3.01
4-A	190	114.0	1.6	10	5.968	3.58
4-B	190	114.0	1.6	10	5.968	3.58
5-A	190	142.5	1.33	10	11.936	8.95
5-B	190	142.5	1.33	10	11.936	8.95

The results in previous sections show that the part density indicates the overall part quality, as the level of defects and build failure can directly affect the relative density of the as-built parts. Figure 6.29 shows the effect of the parameters on the consistency of part density with different process parameters. In general, the results follow the same trend as in the previous section. The high energy density generally improves the quality of the built parts. The average difference in the relative density of each processing condition is quite significant (~4.0%). Comparatively, the relative density difference of the IN713C samples is approximately 0.5%. The nominal power for all samples is fixed at 190W, however the effective power is varied with the change of exposure time. It shows the complexity of the pulsed laser AM process, and many factors can impact build quality. Poor powder quality can lead to an unstable packing density during layer deployment, which is difficult to predict. Therefore, it can result in more uncertainty to the part quality and cause poor repeatability and reliability.

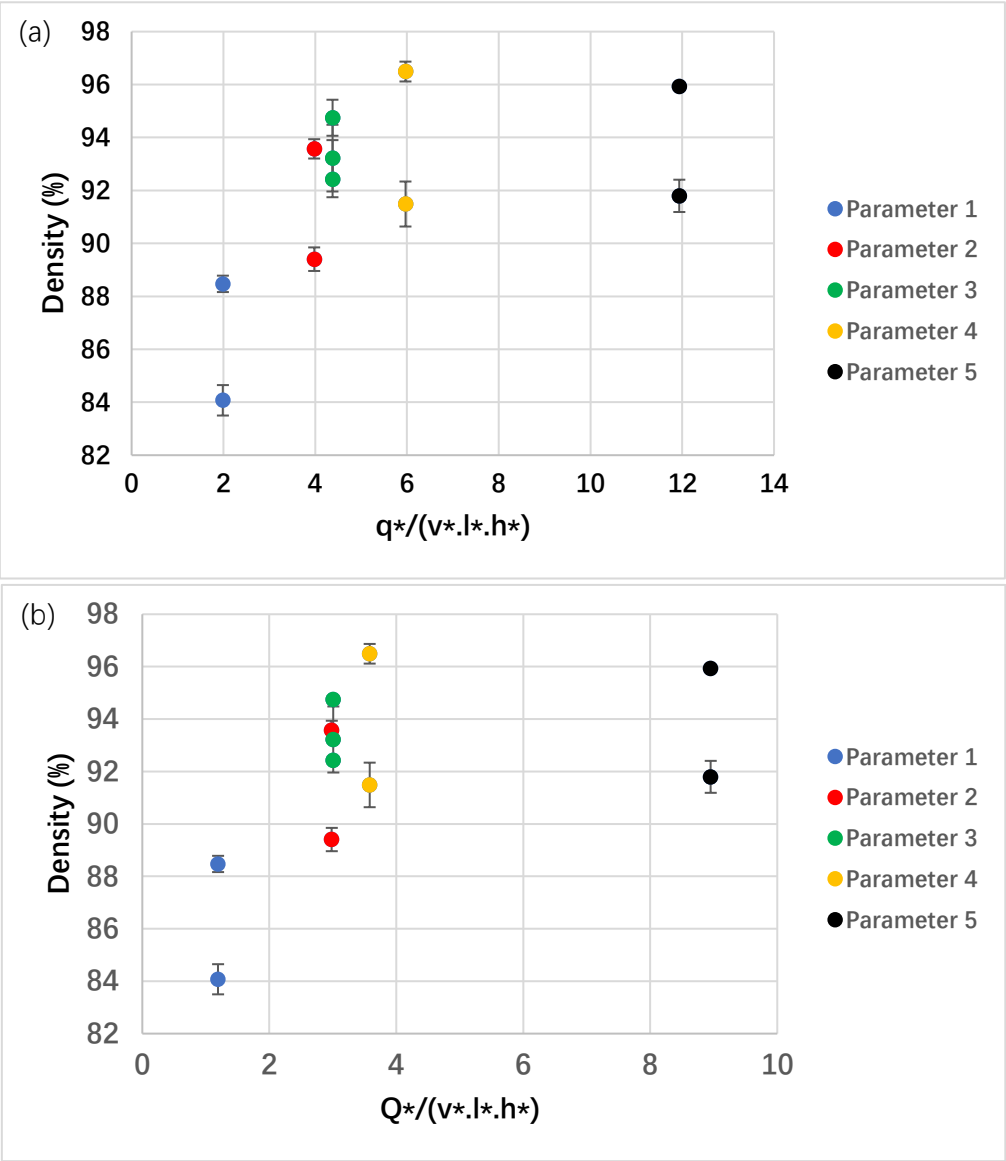

Figure 6.29 Plot showing the difference in part density with same normalised energy density. (a) Nominal power (b) Effective power. Plot demonstrated the poor repeatability and reliability using oversized powders.

6.6 Hardness tests

Figure 6.30 shows the effect of energy density on sample hardness, such that the sample exhibits higher hardness with increasing energy density. The gradient reduced when the energy density was over 15, which corresponded to the density graph where the LoF was eliminated and the samples had a near-full density (99%). The highest hardness is 370 HV, which is approximately the same as the previous IN713C result.

The hardness profiles of both along the building direction (X–Z plane) and laser travel

direction (X–Y plane) in the sample with the highest relative density is shown in Figure 6.31. Unlike the IN713C samples, there is no apparent trend of the hardness as more layers are deposited onto the substrates. The close hatch and scan strategy provide sufficient remelting effects; thus, the microstructure along the build direction is more consistent. The fluctuation of hardness across a layer (X–Y plane) can be induced by the fact that cells tend to have a preferred growth and crystallisation orientation along <001>.

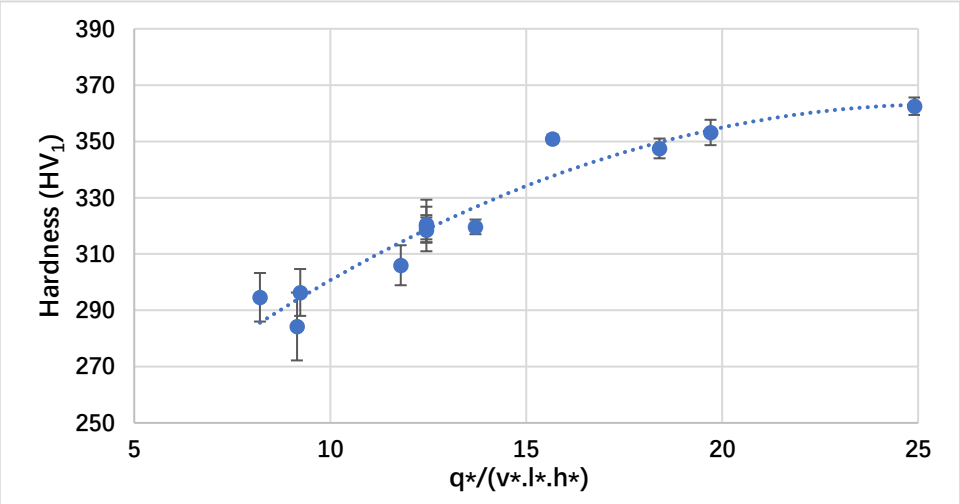

Figure 6.30 Measured hardness of SLM as-built LR8 samples versus normalised energy density.

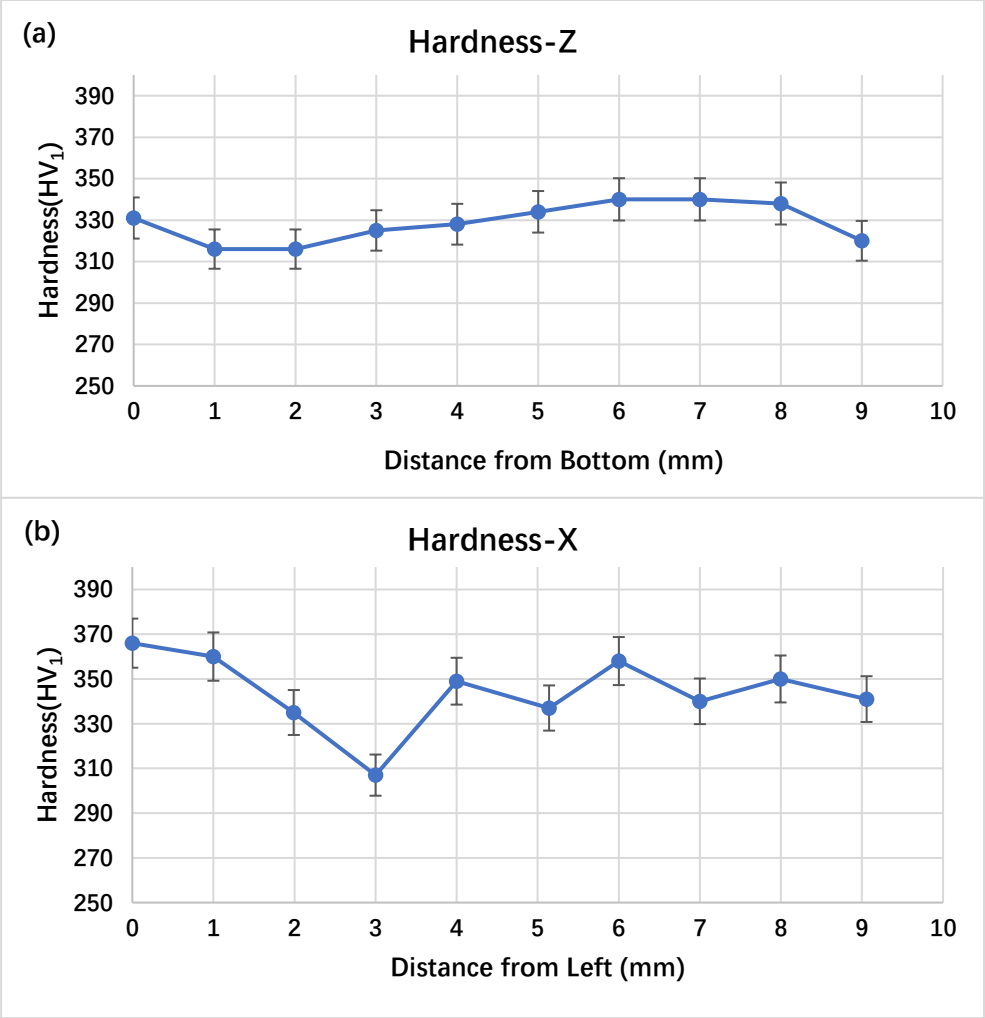

Figure 6.31 Hardness of sample 1 from parametric studies: (a) along build direction (Z) and (b) Horizontal direction (X).

6.7 Discussion

6.7.1 Determining a processing window for LR8

To understand the optimised processing window for LR8, the results of both density and defects need to be considered. All the density analysis of LR8 as-build sample with corresponding parameters is summarised into the contour map in Figure 6.32. Figure 6.32(a) shows the variation of the part density with normalised energy density and hatch space with the nominal power. The introduction of effective power (Q) and apparent power (Q_a) in Section 6.3 can qualify and include the effect of scan strategy in the processing map as well, as shown in Figure 6.32(b). The trend can be more evident with

a correction using effective power that a certain processing window can build a sample with an approximately fully dense level. For large particle LR8, the unit area heat input (Q*/v*l*) dominated the part quality, as the part density can only achieve near full dense when Q*/v*l*>8, Hatch space (h) can only be effective when the energy input is low. A small hatch space can provide a similar effect to remelting. This influence can also be related to the laser spot diameter. For the LR8 coarse powder, the density is higher when the hatch space is approximately 40% of the laser spot radius. Therefore, the constant local heat energy can effectively melt the oversized powder. As section 6.2.1 revealed, velocity (v) in pulsed laser system is a combination of point space(D) and exposure time(t). In general, the increase of point space will lead to a decrease of energy density therefore reduce the part density. The laser point space is fixed at 40μm for all experiments in this chapter to simplify the parametric study analysis. The effect of point space and exposure time with fixed velocity can be investigated in the future research.

Figure 6.33 shows the effect of normalised nominal and effective energy density on the different types of defects. Owing to the essential problem induced by oversize irregular power, the lack of fusion is dominant in most samples. It is hard to have a clear trend between energy density and the defect types. In conclusion, the optimised processing window can be predicted for poor powder quality LR8, as shown in Table 6.5. With the optimised processing parameters, the total number of defects can be minimised to approximately 0.25%. The main mechanism that dominates below the optimised condition is the keyhole pore due to the close hatch space and high energy input. With excess energy density, the part density did not show a significant drop. Therefore, LR8 has a better printability and tolerance compared with IN713C. The processing map can be more accurate with enriched data in the future research.

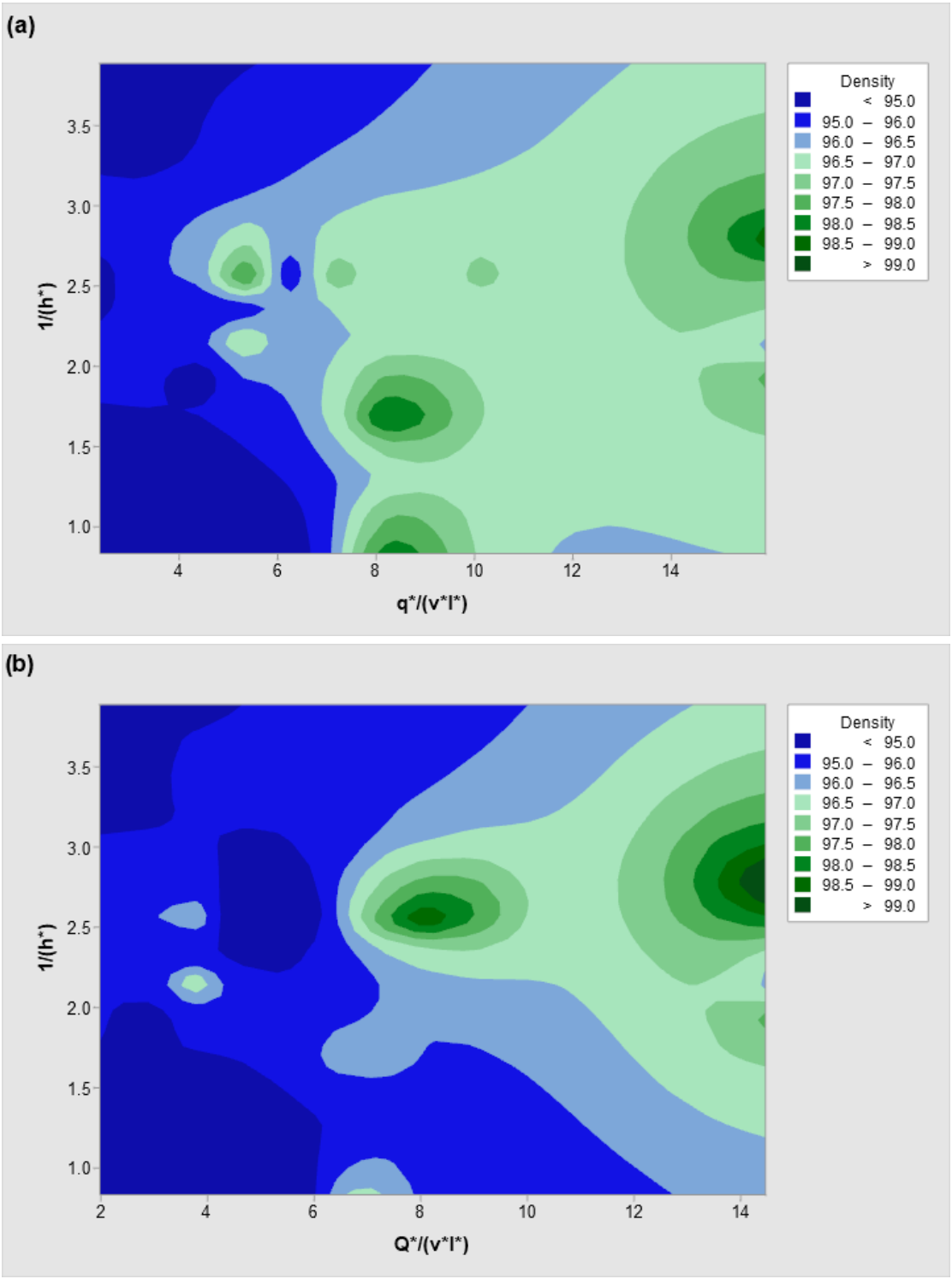

Figure 6. 32 Contour plot of the as-built part density on the normalised processing parameter map. (a) nominal power (q) before correction; (b) effective power (Q) after correction.

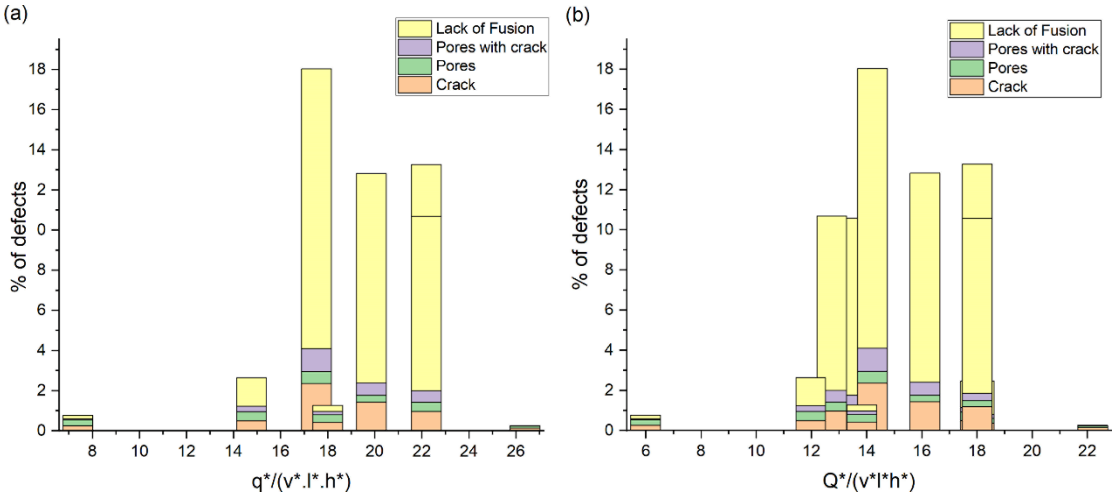

Figure 6.33 Plot showing the effect of normalised energy density on defect density. (a) nominal power (q) before correction; (b) effective power (Q) after correction Lack of fusion induced by large particle size contributed to a significant degree of uncertainty.

Table 6.5 Optimised processing window for large particle size LR8 with pulsed laser.

Power input	190 W
Exposure time	40–50 μs
Point space	40 μm
Scan speed	0.75–0.8 m/s
Hatch space	13–20 μm
Layer thickness	40 μm
Scan strategy	Stripe with no overlap

6.7.2 The effect of scan strategy

Different rotation angles indicated that the laser scan direction was varied between layers and caused a change in the thermal distribution. Therefore, with rotation angles of 45° and 66°, there are always layers whereat the scan tracks are not perpendicular to the edge; thus, the laser travel time varies across the layer. The surface therefore can have an uneven energy absorption, combined with the fact that large particles can lead to a rough surface and uneven distribution. The location, like the centre of part, has a

longer laser travel time and can have a lower residual temperature, so more porosity can occur at those locations. However, the location, such as the corner of a part, has a shorter laser travel time; hence, a high residual temperature can produce more hot cracking. The 90° rotation angle and stripe strategy can provide a constant laser travel time across a layer. Therefore, a better coverage of overlap for previous layers leads to more remelting. Thus, the uniform heat distribution can counter the uneven powder distribution to a certain degree. The analysis in Section 6.3 show that the effect of scan strategy can be represented using "apparent power" using the ratio between maximum hatch length and edge length. In general, the meander scan strategy is unsuitable for coarse powder (diameter > 80 μm) compared with the stripe strategy.

6.7.3 The effect of layer thickness

A considerable layer thickness that is greater than the maximum particle size can cause all particles to be deposited on the build platform. When the laser passes through, fully melting these large particles can be difficult, thereby inducing insufficient melting. Meanwhile, a relatively large layer thickness requires a large amount of energy to fully melt the powder. A 'keyhole' effect can occur. Based on the research of Abd-Elghany & Bourell (2012), an increasing layer thickness can lead to a decrease in part density and surface finishing quality.

Conversely, if the layer thickness is less than the maximum particle size, large particles can be removed from the layer and preferential deposition of fine particles can be achieved. The density of the manufactured parts and the surface finishing can be optimised, as the density of each layer can be maximised with finer powders. Thus, in general, a powder particle size ranging between 20–100 μm with a layer thickness between 20 and 60 μm is applied in the powder bed AM process.

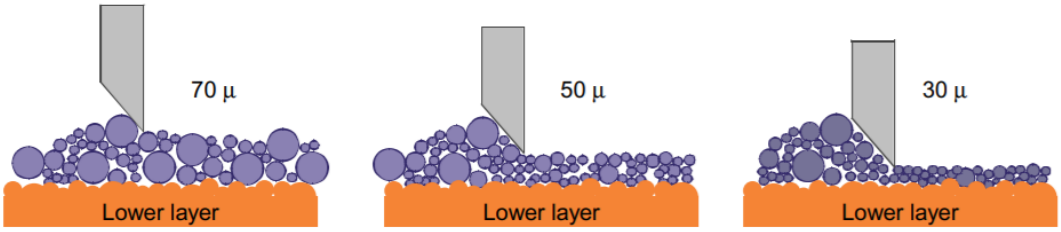

Figure 6.34 Schematic drawing for the effect of layer thickness and particle sizes on the spacing between particles, which induce porosity and reduce density. (Abd-Elghany & Bourell, 2012)

In this project, most powder particles are approximately 90–120 µm. The particle size distribution is very narrow and its size is relatively large. Thus, when the layer thickness is set to a small value, most of the powder is pushed away from the platform and causes an uneven deployment of powder particles; thus, some sites lack powder deployment, which can lead to an LoF and induce the formation of porosities, thereby reducing the part densities. If the layer thickness increases to a size similar to that of a powder particle, excess energy is required to fully melt the powder such that strong keyhole defects can occur in the manufactured parts.

Powder analysis shows that this batch of LR8 powder contains numerous internal porosities and cracks. The cracks inside the powder can be induced by non-uniform cooling during powder manufacturing. Porosity can be gas trapped inside the liquid metal and is sealed inside the powder during manufacturing.

It is known that small particles can efficiently fill vacuums between large particles, which can further reduce the potential porosity. However, extremely fine particles can reduce the flowability owing to the increasing attraction force between particles. Large particles tend to have low poor packing density, which exhibits porosities, and gas is easier to be trapped around the surface of particles, as presented in Figure 6.35. (Dawes, 2017) The maximum packing density can be achieved using a bi-modal distribution of both fine and coarse particles within relatively narrow size ranges.

The irregular shape of the powder can also cause defects in the as-built parts. Spherical particles tend to have better flowability; therefore, the powder can be more easily

deployed on the platform to increase the layer density. A layer of irregular particles can create more voids and gaps during deployment because the particles have increasing risk of mechanical interlocking and high fraction between particles. These irregular particles can also cause non-uniform heat absorption during melting owing to the complex surface reflectivity and absorptivity.

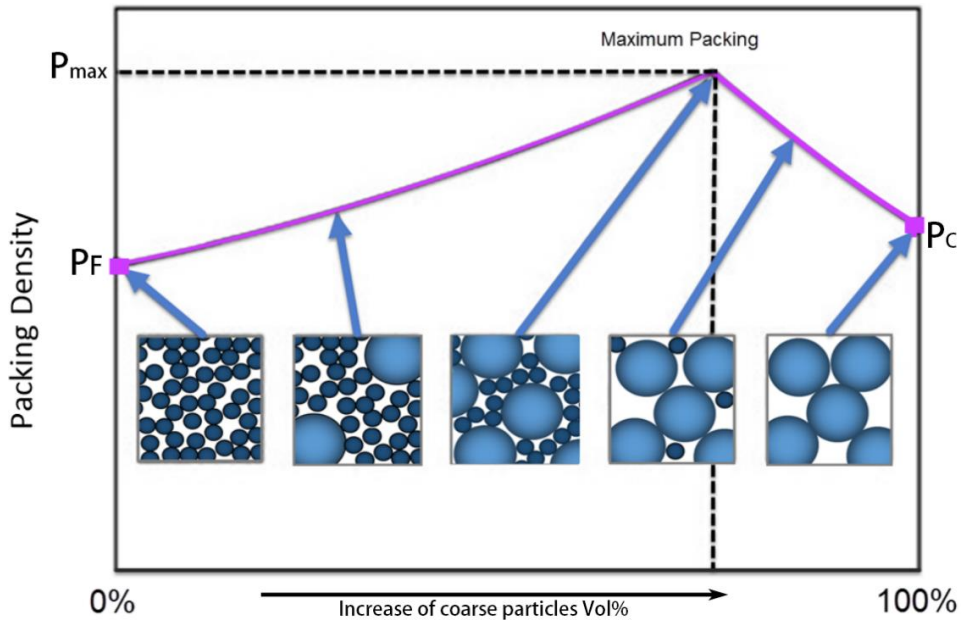

Figure 6.35 The relationship between coarse particles volume% and packing density. The maximum packing density can only be achieved with the distribution of both fine and coarse particles in a certain ratio. (Dawes et al., 2017)

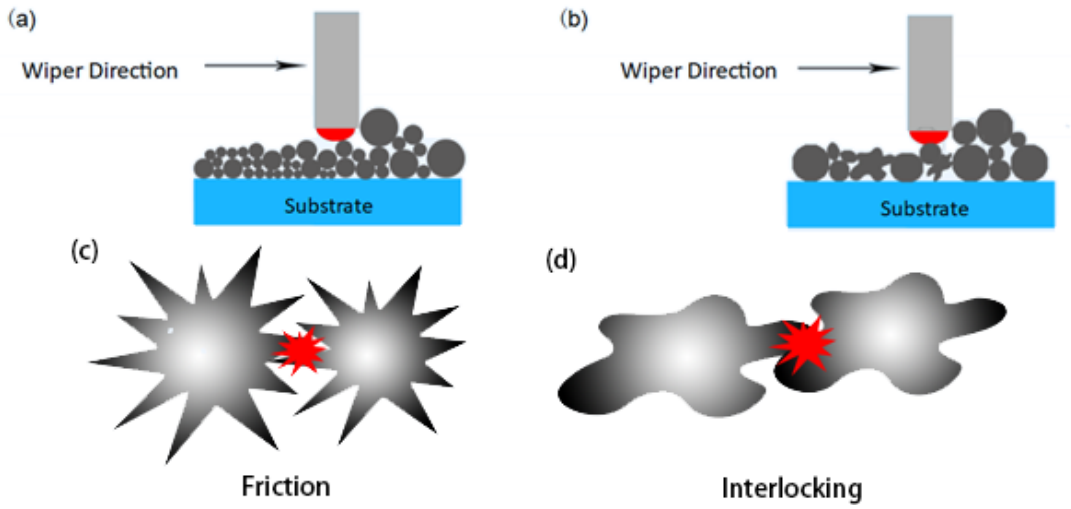

Figure 6.36 Schematic of the effect of particle quality on powder deployment. (a) Spherical powder flow (b) Irregular powder flow which increase the risk of (c) particle fraction and (d) mechanical interlocking.

During SLM, unmelted powders are generally recycled and introduced to the next build. However, several studies have shown that the recycled powder can cause a large deviation in the powder characteristics. The powder size distribution can be shifted to the large side and narrowed, as fine powder can be blown away during the building process. Meanwhile, fine powders can also attach to the chamber surface owing to the static effect. The morphology of the recycled LR8 powder is shown in Figure 6.37. Powders that are close to the heated body can be sintered together and cause the powder morphology to become less spherical. So, the recycled powder needs to be properly sieved before next build.

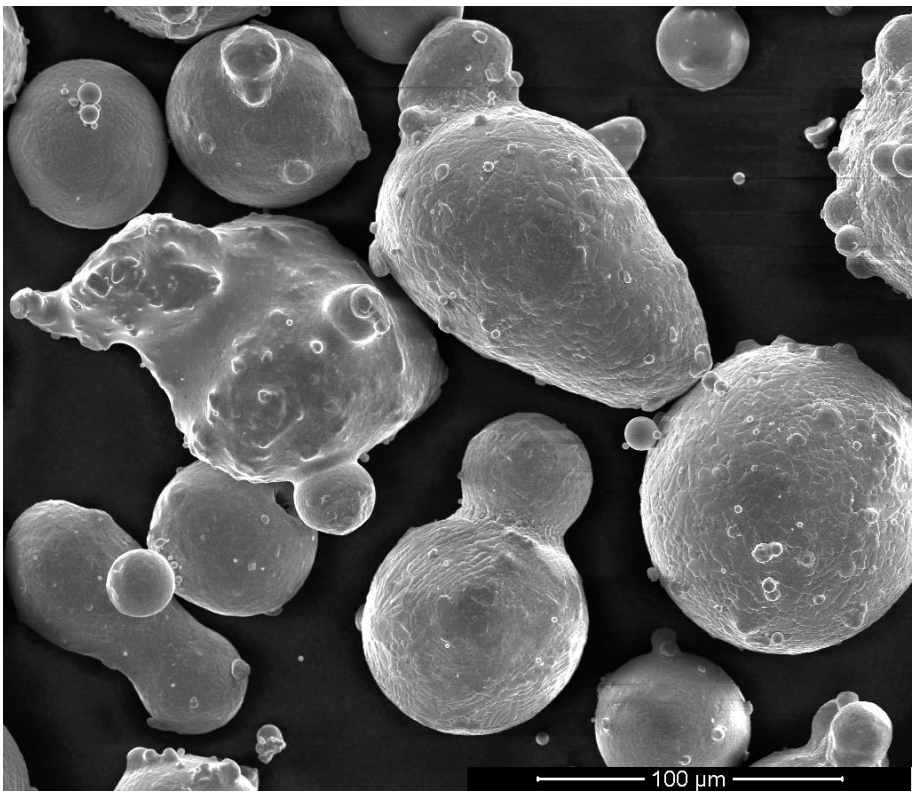

Figure 6.37 SEM micrograph of the LR8 powder after three builds. The fusing of powder particles can be observed.

In this project, powder particles have a wide distribution range, combined with the fact that several of the powders have large sizes and irregular shapes. Some of the particles have diameters larger than the laser spot size, which can result in an inconsistent density result. Therefore, the part with the same parameters can still have a large variation in the consolidation level and are difficult to predict, as presented in Section 6.5.

To overcome this issue, a close hatch space and low rotation angle need to be used. However, the close hatch space can also significantly increase the build duration. The large irregular powder could cause non-uniform heat distribution during laser scanning. Moreover, the frequency of internal defects can be a potential risk that induces defects in build parts. In theory, a large laser spot size combined with high unit energy input can be used to solve the problem associated with large particles, as the large spot size is able to sufficiently cover the size of powder. In conclusion, the oversized, irregular powder is not an optimised choice for AM with small laser spot size because of its poor repeatability and reproducibility.

6.7.4 The performance of the LR8 Ni superalloy

In general, the LR8 powder does not show a high crack susceptibility, similar to the Inconel series alloys, because of the lower content of the γ' precipitation element (Al+Ti), as only a few cracks can be found in all samples with different parameters. Thus, the LR8 powder shows better processability compared to IN713C. Moreover, compared with Ni-based superalloys, the additional amount of Co should provide a higher creep resistance and temperature performance, which requires further mechanical property research. It can be seen that the defect distribution is strongly affected by the uneven layer distribution due to the poor powder quality. Therefore, the LR8 component can be more durable than Inconel alloys in high-temperature environment applications. Owing to the higher density, the weight of LR8 components can be higher than that of Inconel alloys.

6.8 Summarising remarks

- LR8, as a new design material for AM, has shown a better processability in comparison with Ni-based alloys. A near-fully dense part can be built (99.5%).
- LR8 has a low crack susceptibility compared with IN713C. The defect mechanism dominates the highest-density sample as the keyhole porosity.
- Scan strategies show the influence on part quality. The concept of 'apparent power'

is introduce to quantify the effect of scan strategies on part density

- The microstructure of the as-built sample still shows typical elongated grains in AM-fabricated superalloys. The average size of the cellular dendrite is approximately 2 μm.
- The powder morphology has been shown to be an important factor in the part quality and finish. The powder morphology directly affects the packing density of the powder bed layer, thereby changing the densification level.
- A slow speed and close hatch can be beneficial to the AM of large powder particles. However, it can significantly increase the build duration.
- The variation in powder quality and morphology can lead to low repeatability. The use of recycled powder from previous builds can potentially increase the variation.
- The hardness test shows that LR8 has an equivalent level as IN713C. With better processability, the LR8 alloy has the potential to replace the commonly used commercial superalloy as an AM material.

Chapter 7 Overall Conclusion and Future Work

7.1 Conclusion

The results of the parametric studies in Chapters 4 and 6 show that SLM can be applied to the manufacturing of Ni superalloy components. However, the defects cannot be completely eliminated under the as-built condition. An optimised processing window can be obtained to produce near-fully dense parts. For high γ' precipitated alloys, such as IN713C, defects that can be found in the highest density sample are zigzag-like cracks on the grain boundaries. Therefore, the DDC and SAC can be responsible for defect formation. Further investigation showed that the factors that could affect defect formation are complex. The laser travel time combined with the energy input can be very effective towards controlling the heat flow and melting pool geometry. Therefore, the fundamental factors that control the defect formation and microstructure are the cooling rate and residual temperature. The energy density input should be varied with the size of the build parts to overcome the change in residual temperature owing to the laser travel time. Meanwhile, the difference between continuous laser and pulsed laser is revealed in Chapter 6, the effective power in pulsed laser system is significantly affected by the laser 'duty cycle', the parameter cannot be directly used across laser platform without conversion calculation.

The research presented in Chapter 6 revealed that the part quality and build repeatability could be highly related to the powder quality. The recycling of the powder could potentially increase the variation. A close hatch and slow scan speed can overcome this issue, but will significantly increase the processing duration. Ideally, the combination of large laser spot size and high laser power can be the best solution to process large particles AM. The laser scan strategy can directly affect the local energy input. Therefore, the concept of apparent power is introduced to qualified the effect of laser scan strategy. In general, the rotation of direction and overlap or gap of hatch can reduce the part quality. The research also shows that the Archimedes density test is a very efficient way to obtain a basic understanding of the defect level. Notably, less defects

existed in the part that had a density close to the powder pack density.

The SLM as-built sample has a distinctive microstructure compared to conventional casting. The elongated grains with a preferable growth direction along the build axis can be observed in all the SLM-fabricated samples. With the rapid solidification condition, fine cellular dendritic structures can be found in the grains. Only a single FCC γ phase was detected in the IN713C samples. No carbides nor other phases could be detected, as the solution element was difficult to precipitate with a high cooling rate. However, the limited data in Section 4.7.4 revealed that the effective heat treatment time may still be sufficient enough to initiate the recovery of material. Therefore, a minor amount of γ' with extreme fine size can exist in as-fabricated sample, which requires further TEM analysis to confirm. Hardness can be linearly dependent on cooling rate and in-situ heat treatment time. However, the limited experimental data is not enough to cover this discussion conclusively

The application of heat treatment can significantly alter the microstructure of the as-built samples. A γ/γ' matrix can be observed in all the heat treatment samples. The grain orientation is generally towards the build direction. The long-term ageing process led to a coarsening effect of the γ' particles and the dissolution of the carbide. The sizes of the γ' particles were more homogenous after long-term ageing. The fine cubic structure can only be observed in the sample solution heat treated above γ' solvus temperature and associated ageing sample. The γ' precipitates are larger and more irregular with a abnormal wide distribution when the solution heat treatment temperature below γ' solvus temperature. Thus, the γ' precipitate solvus temperature is a key threshold point in heat treatment. The γ' precipitates can only sufficiently dissolve into the matrix with a solution treatment temperature above the γ' solvus point. With a proper heat treatment, both desired microstructure and mechanical property can be effectively achieved. Heat treatment has a negligible influence on defect control. Further post-processing, such as HIP, can be necessary to completely eliminate internal defects.

The mechanical test shows that the as-built IN713C can provide a higher tensile stress level, but a poor ductility, compared with the conventionally cast material, while the hardness is virtually the same as that of the casting samples published in the literature.

The logarithmic dependence of hardness on effective heat treatment time is revealed. Heat treatment can significantly improve the mechanical properties of SLM-fabricated samples owing to the formation of γ' as a second phase to strengthen the structure. The heat-treated IN713C sample shows much better tensile and hardness properties than the conventionally cast sample. The mechanical properties in heat treated IN713C sample are directly influenced by the volume fraction as well as the size of γ' precipitates. The creep resistance requests further research due to the limited resource.

Furthermore, LR8 is a newly designed material for AM, and the reduction of Al and Ti composition to suppressed the crack susceptibility in the as-built part. Only a limited amount of keyhole and gas porosities can be detected in the near-fully dense sample (99.5%). Therefore, LR8 exhibits a significantly better printability compared to other γ'-hardened alloys. The hardness of the as-built LR8 sample is comparable to that of other Ni superalloys for aerospace applications.

In aerospace design, some components can have complex internal geometries, such as turbine disc and blade. The potential advantage of AM is the production of those components without expensive tooling and further machining. A viability experiment of SLM for the manufacture of complex geometry from the Ni superalloy IN713C was also conducted. As shown in Figure 7.1, the scale models of the turbine blade and compressor disc are successfully produced in one piece with AM. However, a commercially ready AM-fabricated IN713C component is still held by the high crack susceptibility. This thesis has shown evidence that crack formation and the microstructure can be regulated if the melting pool temperature can be dynamically controlled.

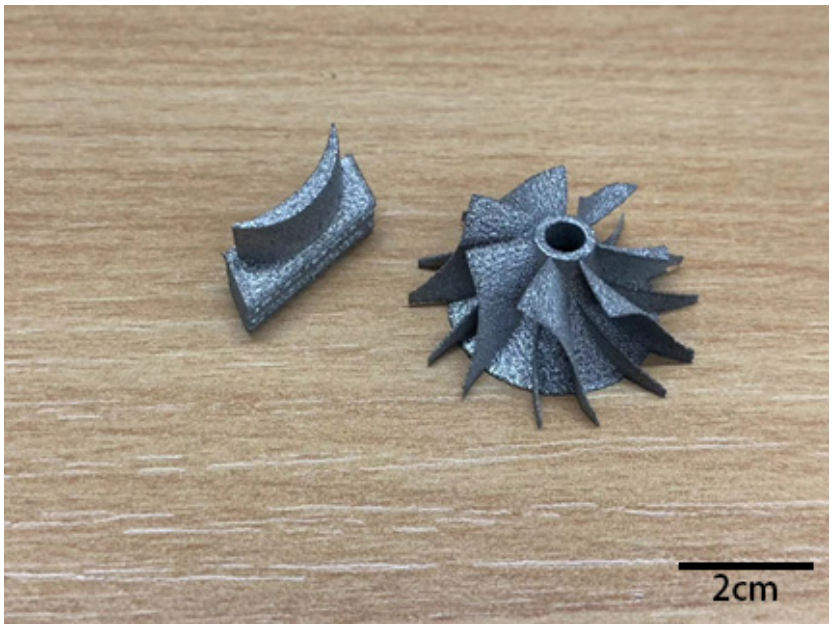

Figure 7.1 Scale model of the turbine blade and compressor disc using SLM-fabricated IN713C.

In general, SLM is a viable method to produce components, especially those with complex geometries. A more suitable material with a desirable powder quality can be beneficial for SLM commercial applications. Researchers must strive to further understand the complex factors that can affect the melting and solidification during SLM. Therefore, SLM technology can truly become a commercially feasible approach rather than a novel experimental technology.

7.2 Future work

7.2.1 Mechanical test at elevated temperature

Owing to the limitations of the build platform and the powder availability, the tensile properties of the vertical direction were not investigated. The elongated grain in the build direction means that less grain boundaries are perpendicular to the tensile direction, which can essentially act as the fracture initiation points. As the cracks generally follow the build direction, lower ductility can be expected.

The creep test or stress-rupture test can be performed to further analyse the mechanical properties of the SLM-fabricated sample. The test can determine the deformation rate over time at elevated temperatures and under a constant load. Meanwhile, the tensile

properties of the as-built and heat-treated samples at elevated temperatures can also be tested. The result can be used to further determine if the SLM-fabricated Ni superalloy is capable of replacing the conventional cast material for high-temperature aerospace applications.

7.2.2 The improvement of defect analysis

7.2.2.1 Machine learning script

In this thesis, the results show that the ML code fails to identify the difference between the LoF and keyhole porosity. To achieve better defect recognition, the code needs to be further trained to successfully identify different types of defects. First, more defect sample data need to be collected for different materials with variable parameters. Second, the defect parameter set can add more key particle measurements. For example, a threshold value of the defect area can be set to distinguish the LoF and keyhole porosity. The script should eventually be able to classify a wider list of defects, including the subdivision of cracks and porosity with less error.

7.2.2.2 3D analysis of defects

The defect analysis in this thesis also shows the limitation of 2D image defect analysis. The cross section of a sample may not comprehensively reflect the defect distribution in the entire sample. Therefore, the micro-CT technique can also be used in the future to visualise the 3D morphology and distribution of the defects. As presented in Figure 7.2, the internal defects a whole part can be revealed without damage the sample.

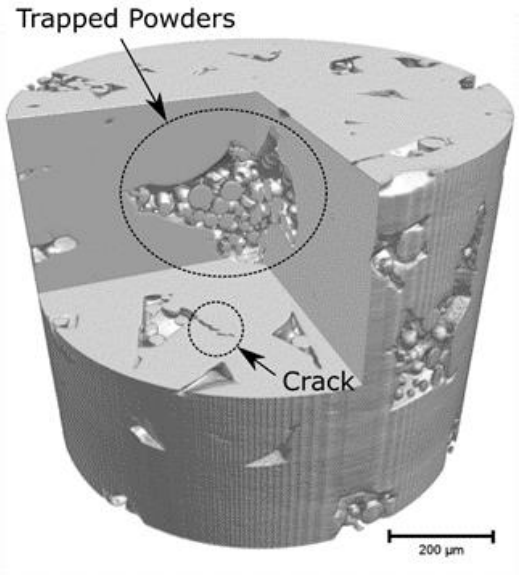

Figure 7.2 A three-dimensional image of AM part using the XCT technique. (Kim et al., 2017)

7.2.3 The effect of residual temperature

In the past, researchers have focused on defect and microstructural control with all the complex parameters. However, this thesis has already shown apparent evidence that processing parameters can directly change the residual temperature, while the residual temperature can then be directly related to the melting pool morphology. and therefore, influence the microstructure and internal defects. Therefore, future research on SLM can focus more on in-situ temperature monitoring to gain a better understanding of the temperature profile during laser scanning. Theoretically, if the residual temperature is maintained, the microstructure and defect level should be the same, even with different parameters.

7.2.4 The effect of in-situ heat treatment

Section 4.7.4 and 4.7.5 revealed the possibility that recovery and precipitation can occur in as-fabricated samples. The hardness can be linearly dependent on cooling rate and in-situ heat treatment time. However, the estimated value of activation energy of the γ' precipitation and the limited experimental data cannot provide a solid conclusion.

Therefore, the effect of in-situ heat treatment on the microstructure evolution in the AM as-fabricated samples can be investigated in the future research. The analysis can be carried out using numerical simulation of thermal cycling, combined with the TEM imaging to confirm the potential recovery and precipitation during AM.

7.2.5 Defect control during the building process

Based on the above-stated theory, an ML code can be applied to the Aconity SLM build program. With the pyrometer to monitor the residual temperature, it is possible to set the target processing temperature. After a layer is completed, the pyrometer data will be analysed by the program. If the temperature does not match the target, the power input and scan speed for the next layer can be adjusted by the script. Ideally, if the processing capacity is sufficiently high, the program can be capable of achieving real-time analysis, so the processing parameter can be continuously varied to maintain the target temperature within the part.

7.2.6 Powder preparation and storage

Poor powder quality shows a strong distraction in the parametric study of SLM and the repeatability in commercial building processes. Fine powder is necessary to obtain a better SLM build. Based on the result from the thesis and other literatures, the optimised powder for AM is spherical with a size range of 20–60 μm. With a better powder quality, an accurate processing window can be determined. The finer powder generally requires less energy input; thus, the build time can be significantly reduced by the fast scan speed and wide hatch space. Some powders show a minor binding phenomenon as the powder can contact moisture during storage and movement. The reuse of such a powder also causes it to become more irregular and coarser. Therefore, the powder should be carefully sieved and dried before being built. The maximum powder reuse time before the powder quality becomes unacceptable for SLM is also a topic worthy of attention to maximise the economic benefits of SLM.

7.2.7 The future investigation of coarse powders

Coarse powders are undesirable for AM; however, different processing methods can be considered. Spark plasma sintering (SPS) generally requires a powder size distribution ranging between 80 and 150 μm. The voids between particles can be eliminated under high pressure and temperature conditions; thus, the powder morphology will have a limited effect on the part quality. An early investigation was performed for the SPS LR8 superalloys, and owing to the different processing mechanisms, the microstructure of the SPS sample was completely different from that of the SLM-fabricated sample. The grain morphology can be more equiaxed-like, rather than elongated. Further investigation is necessary to fully understand the microstructure of the SPS sample and its mechanical performance.

References

Abd-Elghany, K., & Bourell, D. L. (2012). Property evaluation of 304L stainless steel fabricated by selective laser melting. Rapid Prototyping Journal, 18(5), 420–428.

Agazhanov, A. S., Samoshkin, D. A., & Kozlovskii, Y. M. (2019). Thermophysical properties of Inconel 718 alloy. Journal of Physics: Conference Series, 1382(1).

AMS 5391(2014): Nickel Alloy, Corrosion and Heat-Resistant, Investment Castings 73Ni-0.14C-4.5Mo-2.3Cb(Nb)-0.75Ti-6.0Al-0.010B-0.12Zr Vacuum Cast, As-Cast; Sae International: Warrendale, PA, USA,

Arısoy, Y. M., Criales, L. E., Özel, T., Lane, B., Moylan, S., & Donmez, A. (2017). Influence of scan strategy and process parameters on microstructure and its optimization in additively manufactured nickel alloy 625 via laser powder bed fusion. The International Journal of Advanced Manufacturing Technology, 90(5), 1393–1417.

ASM. (1992). ASM Handbook Volume 3: Alloy Phase Diagrams (10th edition), ASM International, USA.

ASTM, I. (2016). ASTM E8/E8M-16a: Standard Test Methods for Tension Testing of Metallic Materials. West Conshohocken, PA, USA: ASTM International.

ATI Metal. (2016). ATI 35N™ Alloy Technical Data Sheet. https://www.atimetals.com/Products/Documents/datasheets/nickel-cobalt/cobalt-based/ATI%2035N%20Datasheet.pdf

Atwood, R. C., Sridhar, S., Zhang, W., & Lee, P. D. (2000). Diffusion-controlled growth of hydrogen pores in aluminium–silicon castings: in situ observation and modelling. Acta Materialia, 48(2), 405–417.

Aydinöz, M. E., Brenne, F., Schaper, M., Schaak, C., Tillmann, W., Nellesen, J., & Niendorf, T. (2016). On the microstructural and mechanical properties of additively manufactured Inconel 718 superalloy under quasi-static and cyclic loading. Materials Science and Engineering: A, 669, 246–258.

Bean, G., Witkin, D. B., McLouth, T. D., & Zaldivar, R. J. (2018). The effect of laser focus and process parameters on microstructure and mechanical properties of SLM Inconel 718. Laser 3D Manufacturing V, February, 37.

Betteridge, W. (1984). Nickel and its alloys. Chichester, West Sussex, England: Ellis Horwood.

Bhadeshia, H. K. D. H. (2003), Nickel Based Superalloys, University of Cambridge, https://www.phase-trans.msm.cam.ac.uk/2003/Superalloys/superalloys.html

Bhadeshia, H. K. D. H. (1997). Recrystallisation of practical mechanically alloyed iron-base and nickel-base superalloys. Materials Science and Engineering: A, 223(1-2), 64-77.

Binczyk, F., & Śleziona, J. (2009). Phase transformations and microstructure of IN-713C nickel superalloy. Archives of Foundry Engineering, 9(2), 109-112.

Bish, D. L., & Post, J. E. (1989). Modern Powder Diffraction, The Mineralogical Society of America, Washington, ISBN 0-939950-24-3

Boig, Charlotte (2019) The Application of Additive Manufacturing to Nickel-Base

Superalloys for Turbocharger Applications. PhD thesis, University of Sheffield.

Boismier, D. A., & Sehitoglu, H. (1990). Thermo-Mechanical Fatigue of Mar-M247: Part 1—Experiments. Journal of Engineering Materials and Technology, Transactions of the ASME, 112(1): 68–79.

Booth-Morrison, C., Noebe, R., & Seidman, D. (2008). Effects of a Tantalum Addition on the Morphological and Compositional Evolution of a Model Ni-Al-Cr Superalloy. In Proceedings of the International Symposium on Superalloys.

Bor, H. Y., C. N. Wei, R. R. Jeng & P. Y. Ko (2008). "Elucidating the effects of solution and double ageing treatment on the mechanical properties and toughness of MARM247 superalloy at high temperature." Materials Chemistry and Physics 109(2-3):334-341

Boswell, J. H., Clark, D., Li, W., & Attallah, M. M. (2019). Cracking during thermal post-processing of laser powder bed fabricated CM247LC Ni-superalloy. Materials and Design, 174, 107793.

Brinegar, J., Mihalisin, J.R., & VanderSluis, J. (1984). The Effects of Tantalum for Columbium Substitutions in Alloy 713C. Superalloys, 53-61.

Cahn, R.W., Haasen, P., & E. J. Kramer (1993) Materials Science and Technology. Volume 6 – Plastic Deformation and Fracture of Materials. p. 311.

Cahn, R.W., Jones, H., (1999). Non-equilibrium processing of materials, 1st Edition. Elsevier.

Calignano, F. (2014). Design optimization of supports for overhanging structures in aluminum and titanium alloys by selective laser melting. Materials & Design, 64, 203–213.

Callister, W. D. (1997). Materials science and engineering: An introduction (Vol. 9). New York: John Wiley & Sons

Çam, G., & Koçak, M. (1998). Progress in joining of advanced materials. International Materials Reviews, 43(1), 1–44.

Campbell, J. (2015). Complete Casting Handbook: Metal Casting Processes, Metallurgy, Techniques and Design: Second. Birmingham: Elsevier Ltd.

Carter, L. N., Attallah, M. M., & Reed, R. C. (2012). Laser Powder Bed Fabrication of Nickel-Base Superalloys: Influence of Parameters; Characterisation, Quantification and Mitigation of Cracking. 577–586.

Carter, L. N., Martin, C., Withers, P. J., & Attallah, M. M. (2014). The influence of the laser scan strategy on grain structure and cracking behaviour in SLM powder-bed fabricated nickel superalloy. Journal of Alloys and Compounds, 615, 338-347.Carter, L.N (2013). Selective laser melting of nickel superalloys for high temperature applications. PhD Thesis, University of Birmingham. Birmingham, UK.

Chang, S. H. (2012). Effects of γ′ Precipitation on the Structure and Properties of 713LC Superalloy via HIP Treatment. Materials Transactions, 53(2), 446-452.

Chen, H. L., Doernberg, E., Svoboda, P., & Schmid-Fetzer, R. (2011). Thermodynamics of the Al3Ni phase and revision of the Al–Ni system. Thermochimica acta, 512(1-2), 189-195.

Christofidou, K. A., Hardy, M. C., Li, H. Y., Argyrakis, C., Kitaguchi, H., Jones, N.

G., ... & Stone, H. J. (2018). On the effect of Nb on the microstructure and properties of next generation polycrystalline powder metallurgy Ni-based superalloys. Metallurgical and Materials Transactions A, 49(9), 3896-3907.

Collins M.G, Lippold J.C. (2003). An investigation of ductility dip cracking in nickel-based filler materials - Part I. Welding Journal, 82: 288-s to 295-s

Collins M.G, Ramirez A.J, Lippold J.C. (2004), An investigation of ductility-dip cracking in nickel-based weld metals - Part III. Welding Journal 83: 39-s to 49-s

Cooper, D. E., Blundell, N., Maggs, S., & Gibbons, G. J. (2013). Additive layer manufacture of Inconel 625 metal matrix composites, reinforcement material evaluation. Journal of Materials Processing Technology, 213(12), 2191–2200.

Cornish, L., Potgieter, J., Maledi, N., & Sephton, M. (2010). The Platinum Development Initiative: Platinum-Based Alloys for High Temperature and Special Applications: Part IV. Platinum Metals Review, 54 (2).

Cui, C., Tian, C., Zhou, Y., Jin, T. and Sun, X. (2012). Dynamic Strain Aging in Ni Base Alloys with Different Stacking Fault Energy. CD room Superalloy (2012) E1

Cunningham, R., Zhao, C., Parab, N., Kantzos, C., Pauza, J., Fezzaa, K., Sun, T. & Rollett, A. (2019). Keyhole threshold and morphology in laser melting revealed by ultrahigh-speed x-ray imaging. Science, 363 (6429), 849-852.

CustomPartNet, (2016), Rapid Prototyping-Selective Laser Sintering, http://www.custompartnet.com/wu/selective-laser-sintering

Darmawan, A., Siswanto, W. A., Febrianto, B., & Sujitno, T. (2012). The Influences of Ion Implantation Doses to Commercially Pure Titanium Surface Hardness. National Conference RAPI XI

Davis, J. R. (Ed.). (1997). ASM specialty handbook: heat-resistant materials. ASM International.

Dawes, J., Langley, C., & Clayton, J. (2017). Optimizing Metal Powders for Additive Manufacturing: Exploring the Impact of Particle Morphology and Powder Flowability. Metal Powder Report, 69(5), 1–5.

Doherty, J. E., Kea, B. H., & Giamei, A. F. (1971). On the origin of the ductility enhancement in Hf-doped Mar-M200. JOM, 23(11), 59–62.

Donachie, M. J., & Donachie, S. J. (2002). Superalloys a technical guide, ASM international. The Materials Society, Materials Park, Ohio.

Dye, D., Hunziker, O., & Reed, R. C. (2001). Numerical analysis of the weldability of superalloys. Acta Materialia, 49(4), 683–697.

Eisenhut, M.; Langefeld, B. (2013). Additive Manufacturing: A Game Changer for the Manufacturing Industry; Roland Berger Strategy Consultants GmbH: Munich, Germany

Engler-Pinto, C. C., C. Noseda, M. Y. Nazmy & F. Rezai-aria (1996). "Interaction between creep and thermo-mechanical fatigue of CM247LC-DS." Superalloys 1996, 319-325

Fairbank, G. B. (2003), Development of platinum alloys for high-temperature service, PhD Thesis, University of Cambridge, Cambridge, UK

Federal Aviation Administration (FAA), (2012), Airplane Flying Handbook, U.S. Government Printing Office, Washington D.C.: U.S. FAA-8083-3A

Foster, S. J., Carver, K., Dinwiddie, R. B., List, F., Unocic, K. A., Chaudhary, A., & Babu, S. S. (2018). Process-Defect-Structure-Property Correlations During Laser Powder Bed Fusion of Alloy 718: Role of In Situ and Ex Situ Characterizations. Metallurgical and Materials Transactions A: Physical Metallurgy and Materials Science, 49(11), 5775–5798.

Freeman Felicity, (2018) Structuring Difference: The Additive Manufacture of Spatially & Functionally Differentiated Microstructures. PhD thesis, University of Sheffield.

Freeman Felicity, (2019). "ACONITY_Continuous_Eagar_withHatches.m", "RENISHAW_StationaryPulsed_Eagar_withHatches.m"

Galizoni, B. B., Couto, A. A., & Reis, D. A. P. (2019). Heat Treatments Effects on NickeI-Based Superalloy Inconel 713C. Defect and Diffusion Forum, 390, 32–40.

Gasko, K. L., Janowski, G. M., & Pletka, B. J. (1988). The influence of γ-γ′ eutectic on the mechanical properties of conventionally cast MAR-M247. Materials Science and Engineering: A, 104, 1–8.

Goldstein, J. I., Newbury, D. E., Michael, J. R., Ritchie, N. W., Scott, J. H. J., & Joy, D. C. (2017). Scanning electron microscopy and X-ray microanalysis. Springer.

Gordon, A. P., Trexler, M. D., Neu, R. W., Sanders Jr, T. J., & McDowell, D. L. (2007). Corrosion kinetics of a directionally solidified Ni-base superalloy. Acta materialia, 55(10), 3375-3385.

Han, P. (2017). Additive design and manufacturing of jet engine parts. Engineering, 3(5), 648-652.

Harada H., Yamazaki M., Koizumi Y., Sakuma N., Furuya N., Kamiya H. (1982) Alloy Design for Nickel-Base Superalloys. High Temperature Alloys for Gas Turbines. Springer,

Harrison, N. J., Todd, I., & Mumtaz, K. (2015). Reduction of micro-cracking in nickel superalloys processed by Selective Laser Melting: A fundamental alloy design approach. Acta Materialia, 94, 59-68.

He, L. Z., Zheng, Q., Sun, X. F., Guan, H. R., Hu, Z. Q., Tieu, A. K., ... & Zhu, H. T. (2005). Effect of carbides on the creep properties of a Ni-base superalloy M963. Materials Science and Engineering: A, 397(1-2), 297-304.

Hemsworth, B., Boniszewski, T., & Eaton, N. F. (1969). Classification and definition of high-temperature welding cracks in alloys. Metal Construction, 1(2), 5-16.

Henderson, M. B., Arrell, D., Larsson, R., Heobel, M., & Marchant, G. (2004). Nickel based superalloy welding practices for industrial gas turbine applications. Science and technology of welding and joining, 9(1), 13-21.

Higginson, R. L. (2002). Worked Examples in Quantitative Metallography. Leeds: CRC Press LLC.

Hunt, J.D. (1984) Steady State Columnar and Equiaxed Growth of Dendrites and Eutectic. Materials Science Engineering, 65, 75-83.

Hunziker, O., Dye, D., Roberts, S. M., & Reed, R. C. (1999). A coupled approach for the prediction of solidification cracking during the welding of superalloys. In Fifth International Seminar on the Numerical Analysis of Weldability (pp. 299-319).

ImageJ Documentation Webpage (2020), http://rsbweb.nih.gov/ij/docs/index.html.

INCO (1968), Engineering Properties of ALLOY 713C, The Nickel Institute, https://nickelinstitute.org/media/4686/ni_inco_337_engineering713.pdf

InsideMetalAdditiveManufacturing, (2015), Scanning patterns in SLM, https://www.insidemetaladditivemanufacturing.com/blog/-scanning-patterns-in-slm

Ion, J. C., Shercliff, H. R., & Ashby, M. F. (1992). Diagrams for laser materials processing. Acta metallurgica et materialia, 40(7), 1539-1551.

Jackson, M. A., Groeber, M. A., Uchic, M. D., Rowenhorst, D. J., & Graef, M. De. (2014). H5Ebsd: an Archival Data Format for Electron Back-Scatter Diffraction Data Sets. Integrating Materials and Manufacturing Innovation, 3(1), 44–55.

Jarrett, R. N., Collier, J. P., & Tien, J. K. (2012). Effects of Cobalt on the Hot Workability of Nickel-Base Superalloys. 455–466.

Kadlec, K. (2009). P3.5 - Non-contact Measuring the Surface Temperature of Chemical Sensors. Proceedings SENSOR 2009, Volume II, 335-340.

Karthikeyan, S., Unocic, R. R., Sarosi, P. M., Viswanathan, G. B., Whitis, D. D., & Mills, M. J. (2006), Modeling microtwinning during creep in Ni-based superalloys, Scripta Materialia, 54(6), 1157-1162,

Kathryn Baker, (2020), "all_models_visualisation.R"

Kim, D., Choi, Y., Kim, Y., & Jung, S. (2015). Characteristics of Nanophase WC and WC-3 wt% (Ni, Co, and Fe) Alloys Using a Rapid Sintering Process for the Application of Friction Stir Processing Tools. Advances in Materials Science and Engineering, 2015, 343619.

Kim, F. H., Garboczi, E. J., Moylan, S. P., & Slotwinski, J. (2017). Investigation Of Pore Structure and Defects of Metal Additive Manufacturing Components Using X-Ray Computed Tomography. , 3rd International Conference on Tomography of Materials and Structures, Lund, SE.

Kim, I. S., Choi, B. G., Hong, H. U., Yoo, Y. S., & Jo, C. Y. (2011). Anomalous deformation behavior and twin formation of Ni-base superalloys at the intermediate temperatures, Mater. Sci. Eng. A 528, 7149–7155.

King, W. E., Barth, H. D., Castillo, V. M., Gallegos, G. F., Gibbs, J. W., Hahn, D. E., Kamath, C., & Rubenchik, A. M. (2014). Observation of keyhole-mode laser melting in laser powder-bed fusion additive manufacturing. Journal of Materials Processing Technology, 214(12), 2915–2925.

Kotval, P. S., Venables, J. D., & Calder, R. W. (1972). The role of hafnium in modifying the microstructure of cast nickel-base superalloys. Metallurgical and Materials Transactions B, 3(2), 457–462.

Kruth, P. M. J., Mercelis, P., & Kruth, J. (2006). Residual stresses in selective laser sintering and selective laser melting. Rapid prototyping journal.

Kumar, A. (2016). Synthesis and Characterization of TiO2-GeO2-Azobenzene nanocomposite as photoanode for Dye Sensitized Solar cells and optoelectronic devices applications. PhD Thesis, Pondicherry University, India.

Kurz, W., & Fisher, D. J. (1981). Dendrite growth at the limit of stability: tip radius and spacing. Acta Metallurgica, 29(1), 11-20.

Kurz, W., & Fisher, D. J. (1989). Fundamentals of Solidification, 3rd Edition. Trans

Tech Publications, Aedermannsdorf, Switzerland.

Kurz, W., & Trivedi, R. (1994). Rapid solidification processing and microstructure formation. Materials Science and Engineering: A, 179, 46-51.

Lapin, J., Gebura, M., Bajana, O., Pelachova, T., & Nazmy, M. (2009). Effect of size and volume fraction of cuboidal γ' precipitates on mechanical properties of single crystal nickel-based superalloy CMSX-4. Kovove Materialy, 47, 129–138.

Li, Z., Li, B. Q., Bai, P., Liu, B., & Wang, Y. (2018). Research on the thermal behaviour of a selectively laser melted aluminium alloy: Simulation and experiment. Materials, 11(7), 1172.

Lippold, J. C., Kiser, S. D., & DuPont, J. N. (2013). Welding metallurgy and weldability of nickel-base alloys. John Wiley & Sons.

Lippold, J. C., Sowards, J. W., Murray, G. M., Alexandrov, B. T., & Ramirez, A. J. (2008). Weld solidification cracking in solid-solution strengthened Ni-base filler metals. Hot Cracking Phenomena in Welds, 147–170.

Liu, S., Yu, H., Wang, Y., Zhang, X., Li, J., Chen, S., & Liu, C. (2019). Cracking, Microstructure and Tribological Properties of Laser Formed and Remelted K417G Ni-Based Superalloy. Coatings, 9(2), 71.

Losert, W., Shi, B., & Cummins, H. (1998). Evolution of Dendritic Patterns during Alloy Solidification: From the Initial Instability to the Steady State. Proceedings of the National Academy of Sciences of the United States of America, 95(2), 439-442.

MacKay, R. A. & M. V. Nathal (1990). "AB coarsening in high volume fraction nickel-base alloys." Acta Metallurgica et Materialia 38(6): 993-1005.

Masoumi, F., Shahriari, D., Jahazi, M., Cormier, J., & Devaux, A. (2016). Kinetics and Mechanisms of γ' Reprecipitation in a Ni-based Superalloy. Scientific reports, 6, 28650.

Matysiak, H., Zagorska, M., Balkowiec, A., Adamczyk-Cieslak, B., Cygan, R., Cwajna, J., Nawrocki, J., & Kurzydłowski, K. J. (2014). The microstructure degradation of the in 713C nickel-based superalloy after the stress rupture tests. Journal of Materials Engineering and Performance, 23(9), 3305–3313.

McFalls, T. (2018). The effect of hydrogen on gas porosity in Laser Powder Bed Fusion of AlSi10Mg. Master's Thesis, University of Tennessee, USA

Mousavizade, S., & Malek Ghaini, F. (2011). Effect of preweld surface modification using friction stir processing of in738 superalloy on the liquation cracking of autogenous laser welds. Metallurgical and Materials Engineering, 18(1), 43-52.

Nathal, M. V.; Maier, R. D.; Ebert, L. J. (1982) The Influence of Cobalt on the Tensile and Stress-Rupture Properties of the Nickel-Base Super-Alloy MAR-M247. Metallurgical Transactions A, 13(10), 1767-1774

Nathal, M. V.; Maier, R. D.; Ebert, L. J. (1982) The Influence of Cobalt on the Microstructure of the Nickel-Base Super-Alloy MAR-M247. Metallurgical Transactions A, 13(10),1775-1783

Odabaşı, A., Ünlü, N., Göller, G., & Eruslu, M. N. (2010). A study on laser beam welding (LBW) technique: effect of heat input on the microstructural evolution of superalloy Inconel 718. Metallurgical and Materials Transactions A, 41(9), 2357-

2365.
Oxford Instruments NanoAnalysis. (2019). SEM Transmission Kikuchi Diffraction (TKD) Method Using EBSD Detector and AZtecHKL Software. https://www.azonano.com/article.aspx?ArticleID=3795.
Pacurar, R.; Pacurar, A. (2016) Applications of the selective laser melting technology in the industrial and medical fields. In New Trends in 3D Printing; Shishkovsky, I.V., Ed.; INTECH: Rijeka, Croatia,
Pandey, M. C., Taplin, D. M. R., Ashby, M. F., & Dyson, B. F. (1986). The effect of prior exposure-time on air-environment/creep interactions. Acta Metallurgica, 34(11), 2225-2233.
Pratt & Whitney's Aircraft (1965). Engineering Properties of Alloy 713C (Material Engineering Section); East Hartford, CT, USA.
Qi, H., Azer, M. N., & Ritter, A. (2009). Studies of standard heat treatment effects on microstructure and mechanical properties of laser net shape manufactured INCONEL 718. Metallurgical and Materials Transactions A: Physical Metallurgy and Materials Science, 40(10), 2410-2422.
Rawlings, R. D., & Staton-Bevan, A. E. (1975). The alloying behaviour and mechanical properties of polycrystalline Ni3Al (γ′ phase) with ternary additions. Journal of Materials Science, 10(3),
Raza, S. S. (2015). Superalloys: an introduction with thermal analysis. Journal of Fundamental and Applied Sciences, 7(3), 364-374.
Reed, Roger C. (2006), The Superalloys: Fundamentals and Applications. Cambridge University Press, Cambridge, UK:
Ricks, R. A., Porter, A. J., & Ecob, R. C. (1983). The growth of γ′ precipitates in nickel-base superalloys. Acta Metallurgica, 31(1), 43-53.
Rifai, M. A., M. A. Abdou, G. M. Ali & M. A. Bayoumi (1985). "Effect of particle size of precipitate on the strength of gamma prime- hardened alloys." Modelling, simulation & control. B 2(1): 51-63.
Rivera, O., Allison, P., Jordon, J., Rodriguez, O., Brewer, L., Mcclelland, Z., Whittington, W., Francis, D. K., Su, J., Martens, R., & Hardwick, N. (2017). Microstructures and mechanical behavior of Inconel 625 fabricated by solid-state additive manufacturing. Materials Science and Engineering A, 694, 1.
Rolls-Royce Inc, (2017), LR8 Data Sheet
Sames, W. J., List, F. A., Pannala, S., Dehoff, R. R., & Babu, S. S. (2016). The metallurgy and processing science of metal additive manufacturing. International Materials Reviews, 61(5), 315–360.
Sames, W. J., Medina, F., Peter, W. H., Babu, S. S., & Dehoff, R. R. (2014, November). Effect of process control and powder quality on Inconel 718 produced using electron beam melting. In 8th Int. Symp. Superalloy 718 Deriv (pp. 409-423).
Sandvik Osprey Ltd. (2015), IN713C Data Sheet. Sandvik Osprey Ltd.
Sehitoglu, H., & Boismier, D. A. (1990). Thermo-mechanical fatigue of mar-M247: Part 2-Life prediction. Journal of Engineering Materials and Technology, Transactions of the ASME, 112(1), 80-89.
Shi, X., Ma, S., Liu, C., Chen, C., Wu, Q., Chen, X., & Lu, J. (2016). Performance of

high layer thickness in selective laser melting of Ti6Al4V. Materials, 9(12), 1–15.
Simkovich, G., & Whitney, E. J. (2001). Superalloys with improved oxidation resistance and weldability, U.S. Patent No. 6,177,046. Pennsylvania State University, PA, USA.
Sims, C. T. (1966). A contemporary view of nickel-base superalloys. JOM, 18(10), 1119-1130.
Sims, C. T., Stoloff, N. S., & Hagel, W. C. (Eds.). (1987). superalloys II (Vol. 8). New York: Wiley.
Sing, S. L., Yeong, W. Y., & Wiria, F. E. (2016). Selective laser melting of titanium alloy with 50 wt% tantalum: Microstructure and mechanical properties. Journal of Alloys and Compounds, 660, 461–470.
Smallman, R. E., & Ngan, A. H. W. (2014). Phase Diagrams and Alloy Theory. Modern Physical Metallurgy, 43-91.
Sola, A., & Nouri, A. (2019). Microstructural porosity in additive manufacturing: The formation and detection of pores in metal parts fabricated by powder bed fusion. Journal of Advanced Manufacturing and Processing, 1(3), e10021.
Sowa, R., Arabasz, S., & Parlinska-Wojtan, M. (2016). Classification and microstructural stability of high generation single crystal Nickel-based superalloys. Zaštita materijala, 57(2), 274-281.
Strondl, A., Lyckfeldt, O., Brodin, H., & Ackelid, U. (2015). Characterization and Control of Powder Properties for Additive Manufacturing. JOM, 67(3), 549–554.
Su, X., & Yang, Y. (2012). Research on track overlapping during Selective Laser Melting of powders. Journal of Materials Processing Technology, 212(10), 2074–2079.
Sun, F., Gu, Y. F., Yan, J. B., Xu, Y. X., Zhong, Z. H., & Yuyama, M. (2016). Creep deformation and rupture mechanism of an advanced wrought NiFe-based superalloy for 700° C class A-USC steam turbine rotor application. Journal of Alloys and Compounds, 687, 389-401.
Syed A.M. Tofail, Elias P. Koumoulos & Amit Bandyopadhyay, (2018), Additive manufacturing: scientific and technological challenges, market uptake and opportunities, Materials Today, 21(1), 22-37.
Tancret, F., Bhadeshia, H. K. D. H., & MacKay, D. J. C. (2003). Design of a creep resistant nickel base superalloy for power plant applications: Part 1 - Mechanical properties modelling. Materials Science and Technology, 19(3), 283–290.
Tenbrock, C., Fischer, F. G., Wissenbach, K., Schleifenbaum, J. H., Wagenblast, P., Meiners, W., & Wagner, J. (2020). Influence of keyhole and conduction mode melting for top-hat shaped beam profiles in laser powder bed fusion. Journal of Materials Processing Technology, 278, 116514.
Thomas, M., (2018) “defect_type_KNN_Batch_processing.R.”.
Thomas, M., Baxter, G. J., & Todd, I. (2016). Normalised model-based processing diagrams for additive layer manufacture of engineering alloys. Acta Materialia, 108, 26–35.
Thompson, S. M., Bian, L., Shamsaei, N., & Yadollahi, A. (2015). An overview of Direct Laser Deposition for additive manufacturing; Part I: Transport phenomena,

modeling and diagnostics. Additive Manufacturing, 8, 36–62.

Tian, C., Han, G., Cui, C., & Sun, X. (2015). Effects of Co content on tensile properties and deformation behaviors of Ni-based disk superalloys at different temperatures. Materials & Design, 88, 123-131.

Tian, S. G., D. Xia, T. Li, F. L. Meng, M. G. Wang & X. F. Yu (2008). "Influence of element W and microstructure evolution on lattice parameters and misfits of nickelbase superalloys." Journal of Aeronautical Materials 28(4): 12-16.

Tiearney, T.C., & Grant, N.J. (1982). Measurement of Structural Parameters Important in Creep of Ni-Mo and Ni-W Solid Solutions. *Metallurgical Transactions A, 13*, 1827-1836.

Tin, S. (2001). Carbon additions and grain defect formation in directionally solidified nickel-base superalloys. University of Michigan.

Uddin, S. Z., Murr, L. E., Terrazas, C. A., Morton, P., Roberson, D. A., & Wicker, R. B. (2018). Processing and characterization of crack-free aluminum 6061 using high-temperature heating in laser powder bed fusion additive manufacturing. Additive Manufacturing, 22, 405-415.

Verma, K., & Garg, H. K. (2012). Underwater welding-Recent trends and future scope. International Journal on Emerging Technologies, 3(2), 115-120.

Wang, X., Carter, L. N., Pang, B., Attallah, M. M., & Loretto, M. H. (2015). Microstructure and yield strength of SLM-fabricated CM247LC Ni-Superalloy. Acta Materialia, 128, 87–95.

Wang, X., Gong, X., & Chou, K. (2017). Review on powder-bed laser additive manufacturing of Inconel 718 parts. Proceedings of the Institution of Mechanical Engineers, Part B: Journal of Engineering Manufacture, 231(11), 1890-1903.

Wohlers, T. T. (2015). Wohler's report 2015 - 3D printing and additive manufacturing state of the industry. Annual Worldwide Progress Report. Wohlers Report 2015, 32–42.

Yilmaz, N., & Kayacan, M. Y. (2018). On The Relation Between Cooling Rate and Parts Geometry in Powder Bed Fusion Additive Manufacturing. Academic Perspective Procedia, 1(1), 223–231.

Yoo, B. K., Choi, H. K., Park, H. I., & Jeong, H. Y. (2020). The Effect of Heat Treatment on the Microstructures and Mechanical Properties of Inconel 713C Alloy Vacuum Investment Castings. Journal of Korea Foundry Society, 40(2), 16-24.

Young, G. A., Capobianco, T. E., Penik, M. A., Morris, B. W., & McGee, J. J. (2008). The mechanism of ductility dip cracking in nickel-chromium alloys. Welding Journal (Miami, Fla), 87(2), 31–43.

Yusof, F., & Jamaluddin, M. F. (2014). 6.07 - Welding Defects and Implications on Welded Assemblies (S. Hashmi, G. F. Batalha, C. J. Van Tyne, & B. B. T.-C. M. P. Yilbas (eds.); pp. 125–134). Elsevier

Zadorozne, N. S., Giordano, C. M., Rodríguez, M. A., Carranza, R. M., & Rebak, R. B. (2012). Crevice corrosion kinetics of nickel alloys bearing chromium and molybdenum. Electrochimica Acta, 76, 94–101.

Zenou, M., & Grainger, L. (2018). 3 - Additive manufacturing of metallic materials (J. Zhang & Y.-G. B. T.-A. M. Jung (eds.); pp. 53–103). Butterworth-Heinemann.

Zhang, J. X., Murakumo, T., Harada, H., Koizumi, Y., & Kobayashi, T. (2004). Creep deformation mechanisms in some modern single-crystal superalloys. Superalloys, 2004, 189-195.

Zhang, J., Li, J. G., Jin, T., Sun, X., & Hu, Z. (2010). Effect of Mo concentration on creep properties of a single crystal nickel-base superalloy. Materials Science and Engineering: A, 527, 3051–3056.

Zhang, Q. (2011). The microstructure and properties of powder HIPped nickel-based superalloy CM247LC. PhD Thesis, University of Birmingham. Birmingham, UK.

Zhang, Y., Chen, G., Mao, S., Zhou, C., & Chen, F. (2017). Optimization of hybrid laser arc welding of 42CrMo steel to suppress pore formation. Applied Physics A, 123(6), 389.

Appendix A. Defect image analysis image threshold setting

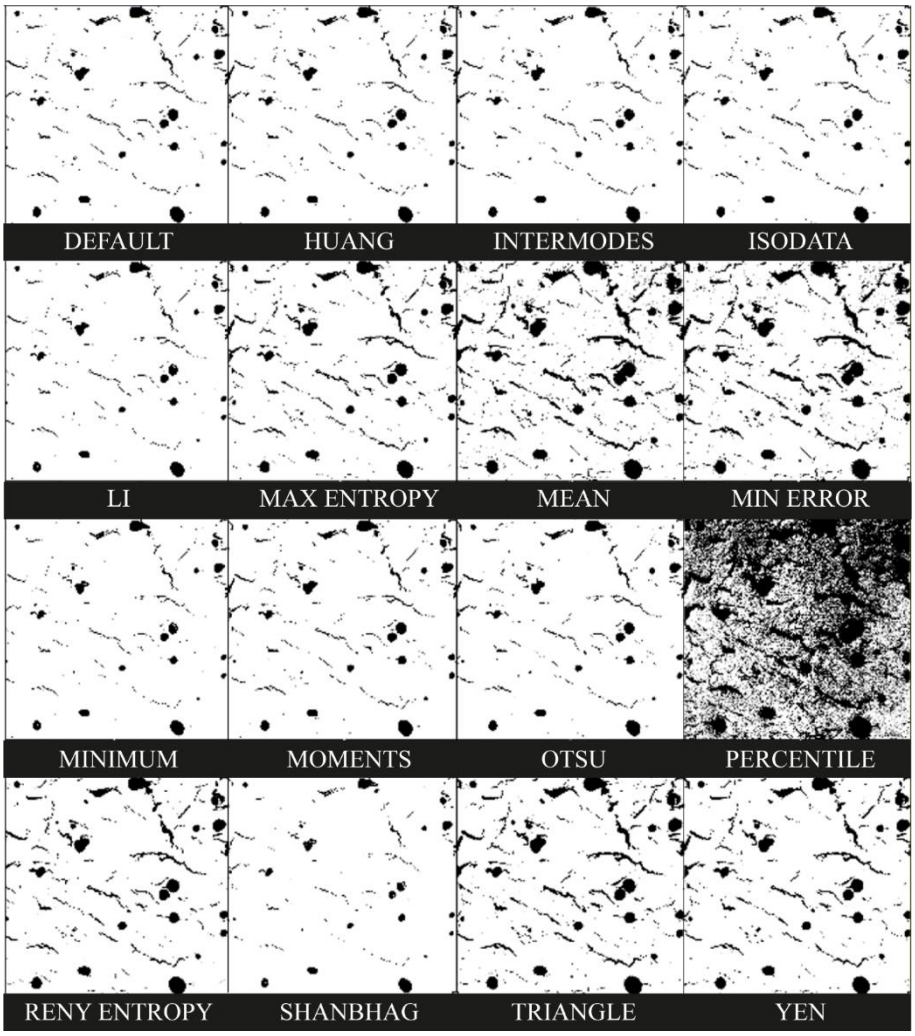

Figure A1. The result with different threshold methods in ImageJ. "Default" was used in this project

Appendix B. Stress-strain curves of tensile test samples for heat treated condition

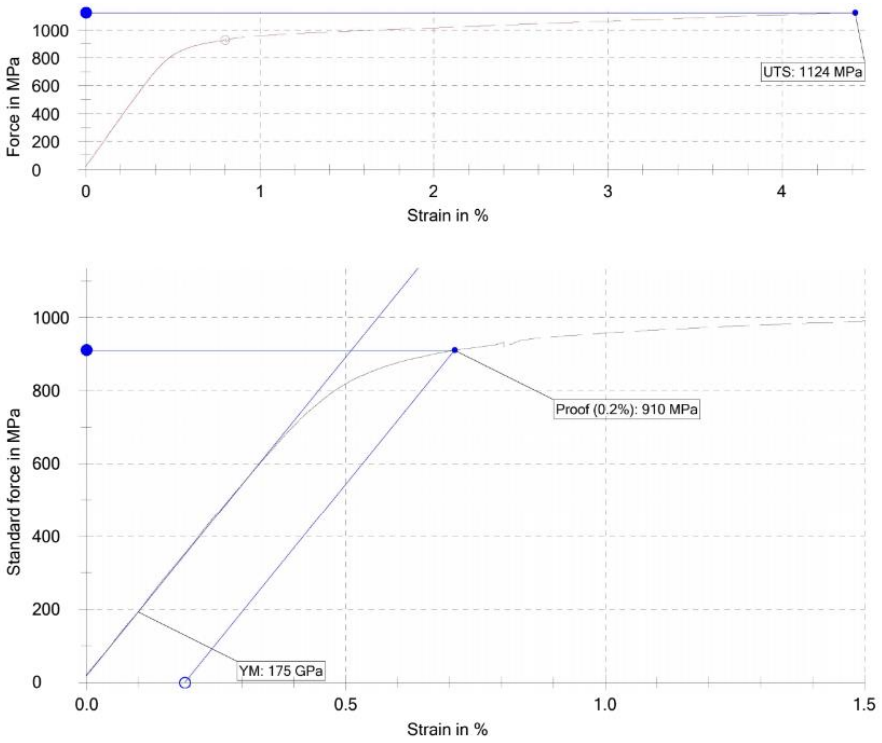

Figure B1. The stress-strain curve of HT1 sample (1176°C/2h).

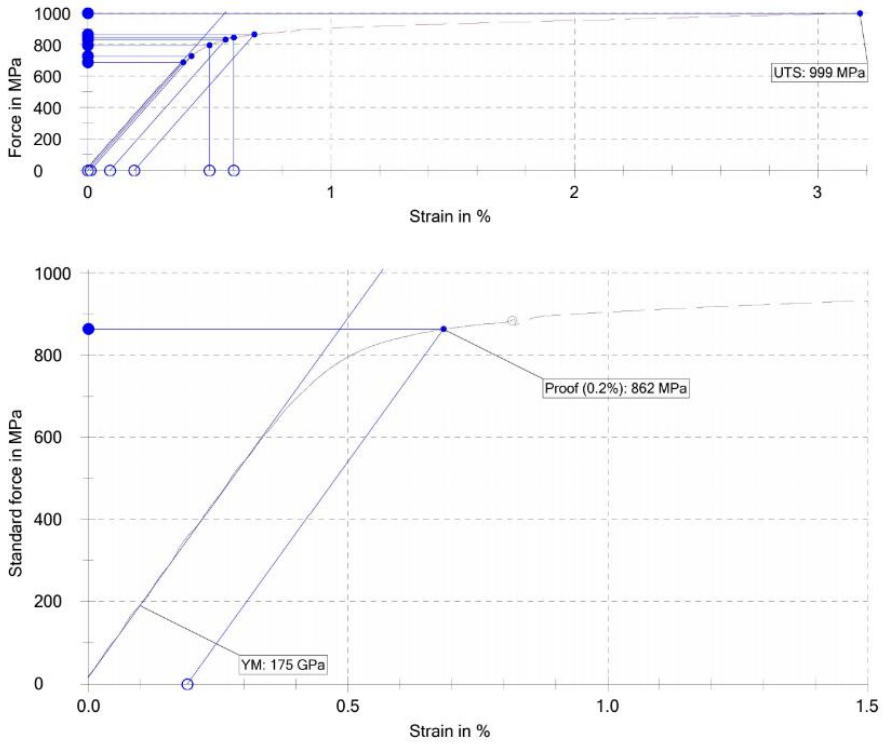

Figure B2. The stress-strain curve of HT2 sample (1176°C/2h+895°C/16h).

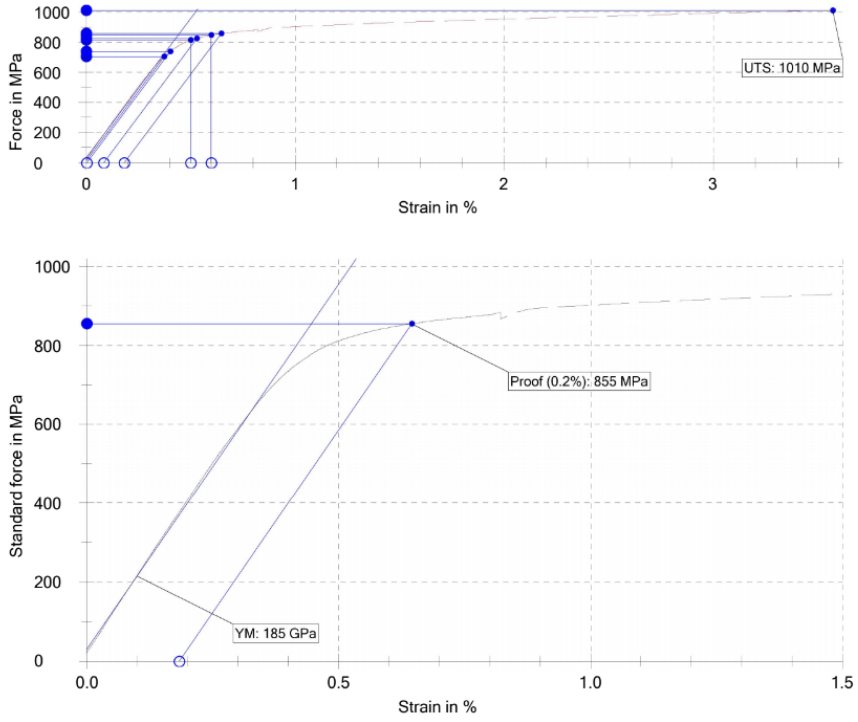

Figure B3. The stress-strain curve of HT3 sample (1076°C/2h).

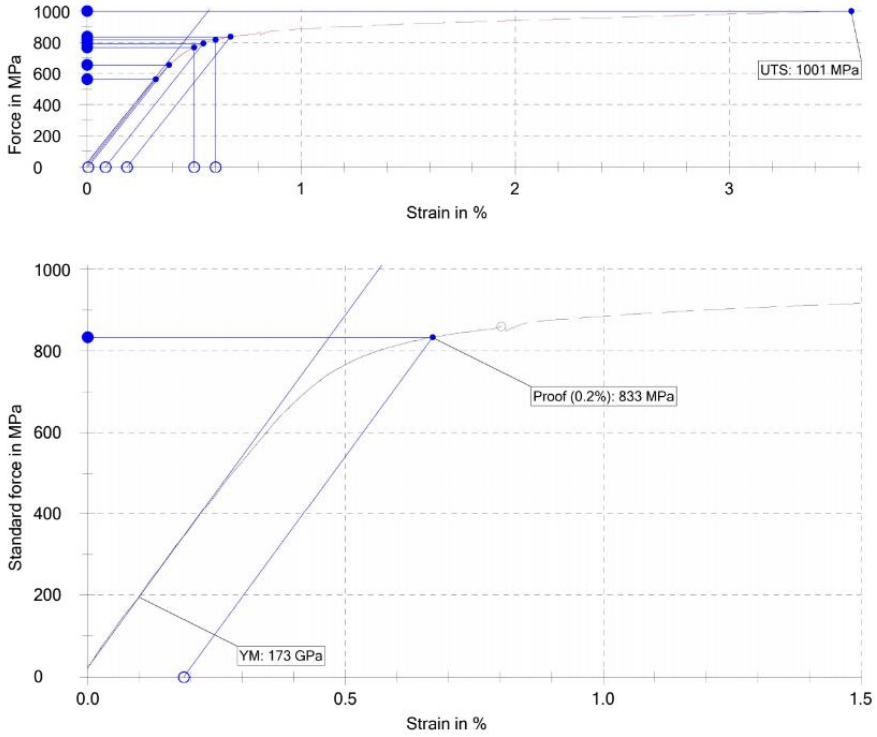

Figure B4. The stress-strain curve of HT4 sample (1076°C/2h+795°C/16h).

Appendix C. Spark plasma sintering of Nickel-based alloys

Table C1 Early investigation parameter used for the SPS LR8 sample.

Sample ID	Heat rate (k/min)	Pressure (MPa)	Dwell temperature (°C)	Dwell time (min)
1	100	50	1000	2.5
2	100	50	1000	5

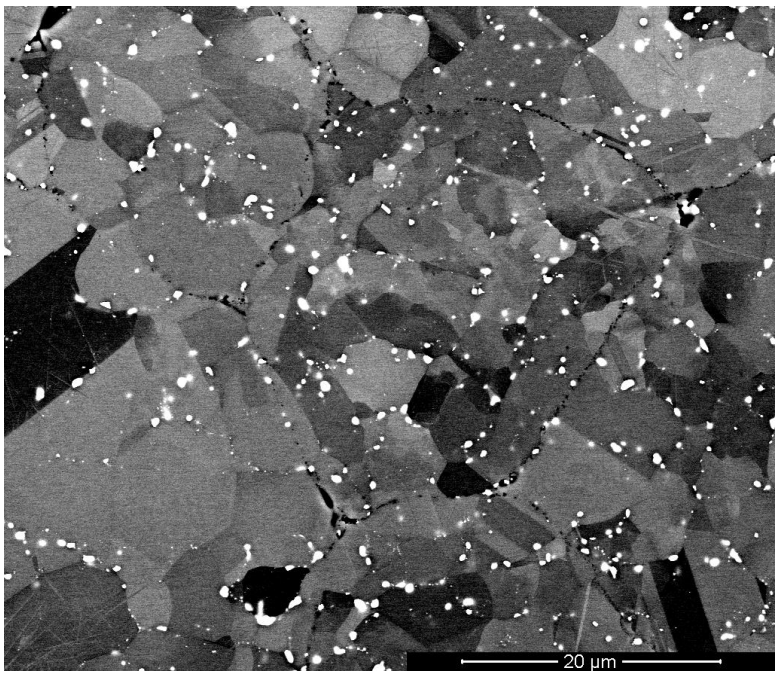

Figure C1 SEM micrograph of SPS LR8 alloys showing a completely different microstructure compared with the SLM as-built LR8. White particle can be the carbide segregation